WARWICK
THE UNIVERSITY OF WARWICK

A Thesis Submitted for the Degree of PhD at the University of Warwick

Permanent WRAP URL:
http://wrap.warwick.ac.uk/81815

Copyright and reuse:
This thesis is made available online and is protected by original copyright.
Please scroll down to view the document itself.
Please refer to the repository record for this item for information to help you to cite it.
Our policy information is available from the repository home page.

For more information, please contact the WRAP Team at: wrap@warwick.ac.uk

warwick.ac.uk/lib-publications

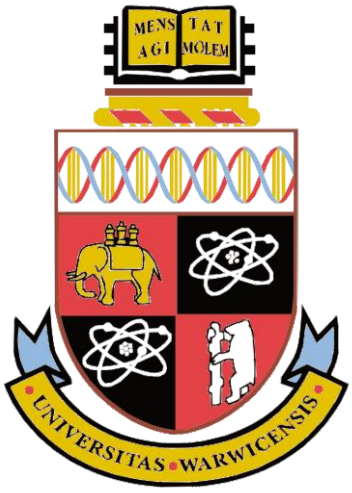

Quantifying solute mixing across low velocity emergent real vegetation shear layers

Patrick Oakley West

Thesis
Submitted in fulfilment of the requirements for the degree of
Doctor of Philosophy

University of Warwick, School of Engineering

June, 2016

Contents

List of Tables

List of Figures

List of Publications

West, P., Hart, J. H., Guymer, I. and Stovin, V. 2016. Development of a laboratory system and 2D routing analysis to determine solute mixing with aquatic vegetation. Hydrodynamic and Mass transport at Freshwater Aquatic Interfaces, *GeoPlanet: Earth and Planetary Sciences*, 34th International School of Hydraulics, pp. 49-61.

Acknowledgements

I am grateful to Professor Ian Guymer for his supervision and friendship; his attention to detail and passion for understanding the natural world has, I hope, brought out the best in me. I am indebted to him for guiding me as a scientist and will think fondly of our discussions in all of my pursuits.

I am grateful for the advice from my friend Laurie Laybourn. My successes in academia were made possible thanks to our comradery and his infectious vision to make the world a better place.

I owe much to Catherine Archer for her support and commitment. I am proud of the woman she has become and her dedication to being a good person has kept me going.

Finally, I wish to thank my parents. To my mother, the kindest person I know; and my father, the smartest person I know.

Declaration

I declare that the work in this thesis has been composed by myself and no portion of the work has been submitted in support of an application for another degree or qualification of this or any other university or other institute of learning. The work has been my own except where indicated and all quotations have been distinguished by quotation marks and the sources of information have been acknowledged.

Nomenclature

Abbreviations

ADE	Advection Diffusion Equation
ADV	Acoustic Doppler-shift Velocimetry
FDM	Finite Difference Model
LIF	Laser Induced Velocimetry
OFDM	Optimized Finite Difference Model
UVP	Ultrasound Velocity Profiling

Roman Symbols

A	Cross-sectional area [m^2]
a	Frontal area per unit volume [m^{-1}]
C	Concentration [ppb]
C_D	Bulk drag coefficient [-]
C_f	Bed friction coefficient [-]
c_1	Flux gradient model cut-off criteria 1 [-]
c_2	Flux gradient model cut-off criteria 2 [-]
d	Vegetation stem diameter [m]
D_{ij}	Turbulent Diffusion Coefficient Scalar [m^2/s]
D_{peak}	Peak transverse mixing coefficient [m^2/s]
D_x	Longitudinal scalar mixing coefficient [m^2/s]
D_y	Transverse scalar Mixing Coefficient [m^2/s]
D_z	Vertical Turbulent Diffusion Coefficient [m^2/s]
e	Molecular Diffusion Coefficient [m^2/s]
f	Ultrasound frequency [s^{-1}]
f_D	Average drag per unit length of stem [kg/s^2m]
G	External momentum source [m/s^2]
g	Acceleration due to gravity [m/s^2]
H	Depth of flow [m]
h	Height of vegetation [m]
$\boldsymbol{i}$	Unit vector in the x direction
$\boldsymbol{J}$	Concentration flux [$m^{-2}s^{-1}$]

$\boldsymbol{j}$	Unit vector in the *y* direction
$\boldsymbol{k}$	Unit vector in the *z* direction
k_e	Kinetic energy [J]
L	Interior adjustment length for deflecting velocity around a patch [m]
L_0	Upstream deceleration length [m]
l_c	Mixing length scale [-]
N	Stem population density per unit area [m^{-2}]
n	Median filter parameter [-]
p	Instantaneous pressure [N/m^2]
Q	Channel discharge [m^3/s]
Re	Reynolds number [-]
Re_d	Stem Reynolds number [-]
r	Longitudinal vegetation stem spacing [m]
S	Bed slope [-]
s	Transverse stem spacing [m]
s_c	Ultrasound measurement channel spacing [m]
t	Time [s]
t_N	Nominal retention time [s]
t_{ml}	Mixing layer width [m]
U	Temporal, depth-average longitudinal velocity [m/s]
U_c	Temporal averaged, area mean, upstream longitudinal velocity [m/s]
U_{outer}	Outer region temporal mean longitudinal velocity [m/s]
U_{inner}	Inner region temporal mean longitudinal velocity [m/s]
U_1	Temporal mean longitudinal vegetation velocity [m/s]
U_2	Temporal mean open-channel longitudinal velocity [m/s]
U_i	Interfacial temporal mean longitudinal velocity [m/s]
U_m	Matching velocity for hyperbolic shear layer profiles [m/s]
ΔU	Velocity shear [m/s]
$\boldsymbol{u}$	Velocity vector ($u\boldsymbol{i} + v\boldsymbol{j} + w\boldsymbol{k}$) [m/s]
u	Instantaneous longitudinal velocity [m/s]
u^*	Bed shear velocity [m/s]
V	Volume [m^3]
v	Instantaneous velocity in the *y* direction [m/s]
W	Vegetation patch width [m]

w Instantaneous velocity in the z direction [m/s]

x Distance in the direction of primary flow [m]

y Transverse distance in the direction of primary flow [m]

y_i Location of vegetation interface [m]

y_{peak} Location of peak transverse mixing coefficient [m]

z Vertical distance in the direction of primary flow [m]

Greek Symbols

α Total light attenuation coefficient [m^{-1}]

α_w Light attenuation coefficient in water [m^{-1}]

δ_o Open channel vortex penetration distance [m]

δ_v Vegetation vortex penetration distance [m]

E Molecular diffusion coefficient [m^2/s]

ε_0 Light attenuation coefficient extinction rate [ppb^{-1}]

η Vegetation porosity (1- Φ) [-]

λ Ultrasound Wavelength [m]

μ Dynamic fluid viscosity [Ns/m^2]

σ Standard Deviation [-]

σ^2 Variance [-]

ν Kinematic fluid viscosity [Ns/m^2]

ν_T Eddy viscosity [m^2/s]

ρ Fluid density [kg/m^3]

Φ Solid volume fraction [-]

τ Shear stress tensor [N/m^2]

ϑ Arbitrary physical quantity [-]

Abstract

The efficacy of pond treatment systems is dependent on the internal hydrodynamic and mixing interactions between aquatic vegetation and the adjacent flow. In attempting to improve pollution degradation and reduce the effects of hydraulic short circuiting, an understanding and quantification of these interactions was sought for seasonal changes in vegetation growth. Controlled laboratory studies were conducted using detailed Laser Induced Fluorometry (LIF) and Ultrasound Velocity Profiling (UVP) techniques to quantify mixing across vegetated shear layer, emergent Cattail reeds (*Typha latifolia*).

An Optimised Finite Difference Model (OFDM) was developed to predict the best fit downstream concentration distributions given the input profiles of transverse mixing coefficient, $D_y(y)$. The model provided strong fitting in artificial vegetation (R^2 = 0.977 and 0.969 for high and low density rigid cylinders). A good fitting was also made for the winter reeds (R^2 = 0.976); although the physical application of conventional shear layer theory failed to significantly improve predictions in the summer season reeds above those of a simple discontinuity functionality describing $D_y(y)$. The form of the lateral variation in transverse mixing coefficient was confirmed in the artificial vegetation studies where peak mixing is enhanced by shear layer vortices. However, in real vegetated shear flows, the heterogeneities in stem morphology and distribution render the relative magnitude of shear layer mixing diminished when compared to other regions of the flow.

It is shown that, while the OFDM provides good predictions of concentration distributions when using a physically justified profile of the transverse mixing coefficient, a discrete step formulation is sufficient for describing mixing in real vegetated shear flows. This study shows therefore, that, while shear layer mixing is dominant in artificial, uniform vegetation, transverse mixing in real vegetated flows is dominated by complex geometries, localised shear processes and bed roughness effects.

Introduction

Preface and motivation

Global water resources face growing challenges in the 21st Century. A changing climate, irrespective of anthropogenic causes, has the potential to impact upon transnational water resources (Arnell, 2004). One impact will be the effect on the intensity and frequency of precipitation (Jeppesen, 2009, Sexton and Harris, 2015; Murphy et al., 2009). Increase in rainfall and the frequency of storm events will elevate the risks of flooding (Murphy et al., 2009) – increasing sediment runoff (Jeppesen et al., 2009) and enhancing nutrient loading (Arnell, 1999). Conversely, lower precipitation and droughts (Murphy et al., 2009) will reduce the dilution of contamination while potentially increasing abstraction demand (Arnell and Delaney, 2006) for agricultural purposes. Demand for water quantity may also increase as domestic and agricultural supplies adjust to expanding populations, increased meat consumption (FAO, 2009) and domestic water footprint (Ercin and Hoekstra, 2012). These stresses on water as a resource may lead to higher consumer costs, greater instability in global food markets and degradation of ecosystem services and environmental amenities.

A range of stakeholders therefore have an interest in the future of water resources. Water utility managers require information regarding the travel time and quality of contaminated water entering water courses; where increased turbidity and contamination of abstracted water entails greater treatment costs. Environmental managers require information regarding pollution run-off from urban areas, highways and agricultural land to maintain standards; while agriculturalists and industrialists must comply with environmental regulation and permitting.

A variety of methods have been proposed for protecting and improving the sustainable use of water resources. Reducing consumption is a clear immediate option; however, socio-

political implementation is difficult and potentially slow. Adaptation to changes and unpredictability in the quality and quantity of water resources is currently favorable – permitting transition from old to new practices. Technological improvements in water treatment can reduce, or at least maintain, the costs of meeting water quality standards; while agricultural adaptations to crop characteristics can be improved through biological innovations. A pertinent approach is the integration of hydrological processes and features into urban and agricultural environments. Swales and natural drainage systems are being increasingly used to manage flood events (Persson et al., 1999); while pond and wetland features have the potential to intercept contamination en route to vulnerable water courses. Whatever the options, it is clear that a strategic combination of approaches is needed to successfully cope with the current and future demands on water resources.

Research focus – treatment ponds

In theory, ponds and wetlands are suitable, low cost and low maintenance (Koskiaho, 2003) installations for reducing contamination loading from urban and agricultural environments (Dieberg et al., 2005). Flow velocity is reduced as the water spreads out in the larger detention area (Koskiaho, 2003), reducing the downstream concentration through dispersion and bio-chemical degradation. The treatment efficacy can be described using a 'hydraulic retention time'. This is the mean time taken for a pollution event to completely pass through the installation. However, the 'nominal retention time' is the time taken for the installation to discharge its entire volume. Retention times for treatment ponds have often been quoted using the hydraulic retention time due to the ease of measurement and estimation. In practice, the flow field is non-uniform such that the true nominal retention time is often overestimated (Kadlec and Knight, 1996; Wong et al., 1998). The discharge of contamination in a time shorter than the predicted nominal retention time is referred to as short-circuiting and

represents a current problem for designers and modelers of treatment ponds (Mitsch, 1992; Persson et al., 1999; Dieberg et al., 2005; Lightbody et al., 2008).

The mixing properties of ponds are affected by the presence of vegetation; where variation in depth, geometry and drag leads to preferential flow paths and non-uniform flow fields. The increased drag caused by the vegetation leads to lower velocity within the vegetation; slowing contaminant advection and enhancing bio-chemical degradation through extended contact with organic surfaces (Nepf, 1999). Further, heterogeneities in morphology and porosity and the presence of patches and borders can improve mixing through enhanced turbulence (Ghisalberti and Nepf, 2005; Okamoto et al., 2012). Improving treatment efficacy is, therefore, reliant upon the quantification of the mixing processes associated with the interaction between the vegetation and adjacent flows and the quantification of morphologically heterogeneous flows.

The objectives of this research were to quantify the mixing characteristics across patches of emergent, real vegetation and to investigate these during the seasonal growth of cattail reeds (*Typha latifolia*); simulating natural pollution treatment ponds. Secondly, the application of current theoretical understandings developed in idealized conditions was evaluated for real vegetation. Finally, the quantification of the transverse mixing between vegetated borders and the adjacent flow using a novel application of a finite difference model was compared to existing approaches to improve the understanding of mixing in real vegetation.

1. Literature Review

This literature review chapter is divided into three sections. The first section provides a background description of the problems of hydraulic short-circuiting prevalent in pond and wetland treatment systems and the relevant and necessary mathematical constructions required to characterize the flow dynamics of vegetated flows. Secondly, the velocity and flow field associated with aquatic vegetation is discussed with regards to the mean velocity profiles and the effects of vegetated shear layers. Finally, solute mixing in vegetated flows is described – comparing recent advances and limitation when characterizing a spatially variable mixing coefficient.

1.1. Background Description

The research presented in this thesis relies on the assumption that the pollutant in question is completely water soluble and/or neutrally buoyant and that the movement of the pollutant is concomitant with the local flow of water. Secondly, the degree of mixing of a pollutant is dependent upon the hydrodynamic characteristics and, while it is acknowledged that wind shear effects contribute to mixing, the flow system is treated with a "fixed lid" approximation under uniform, steady-flow conditions. Both of these assumptions infer that the quantification of the hydrodynamics is sufficient for characterizing the mixing of a pollutant.

1.1.1 Hydraulic retention and short-circuiting

The reduction of pollution in the pond effluent to an acceptable concentration is dependent on the rate of bio-chemical degradation and the total time that the compromised water is detained (Wahl et al., 2010). In turn, these are affected by the rate and magnitude of mixing within the system; which is determined by the influence of geometry, type and distribution of vegetation on the hydrodynamics (Koskiaho, 2003). The treatment efficacy of ponds has been characterized using a hydraulic retention time (Persson et al., 1999); which quantifies the average time that a parcel of pollution spends within the system. However, the nominal retention time, t_N (= V/Q), defined as the time taken for the system to discharge its entire volume, is more frequently used to quantify the treatment efficacy given its ease of calculation over the hydraulic retention time (Holland *et al.* 2004). Geometric and bathymetric heterogeneities within the pond induce preferential flow paths, re-circulations and stagnant regions, often leading to hydraulic short-circuiting; where the hydraulic retention time is shorter than the nominal retention time.

Figure 1.1a demonstrates the effects of varying vegetation density on the flow path. If the vegetation is dense, water may fail to penetrate and deflect around the vegetation leading to short-circuiting. Conversely, if the vegetation is sparse, water may travel rapidly between the vegetation elements and discharges before adequate treatment processes can occur.

Fluorescent tracer studies (e.g. Figure 1.1b) are a common approach for quantifying the hydraulic retention time. A tracer is injected upstream of the pond and the effluent concentration is recorded with time; where the centroid of the resultant residence time distribution provides an estimate of the hydraulic retention time if the time of injection is known. Figure 1.1c presents an idealised (black line) residence time distribution and corresponding cumulative residence time distribution (dotted line) for the system. Included are distributions indicative of short-circuiting (red line) and enhanced mixing (green line).

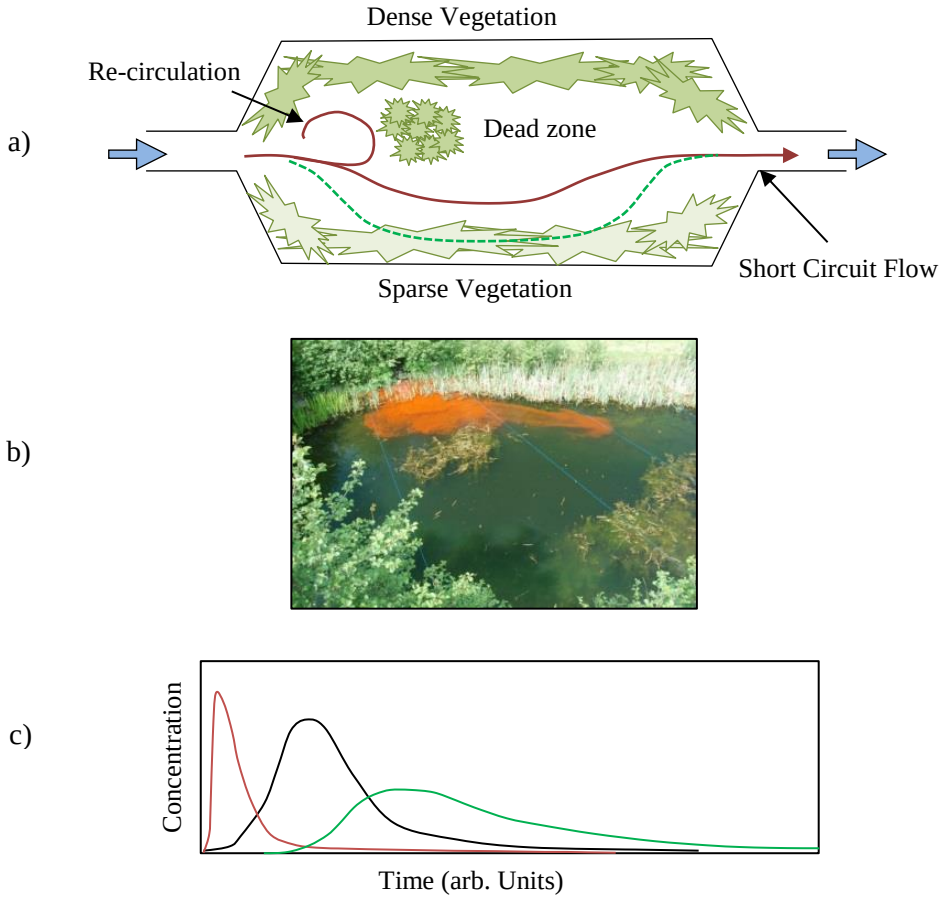

Figure 1.1: a) Plan view of pond-short circuiting (red line) and flow through less dense vegetation (dotted line). b) Photograph of fluorescent tracer visualizing flow paths (courtesy of I. Guymer). c) Theoretical residence time distribution (black) for a pond with short-circuiting (red) and enhanced mixing (green).

The hydrodynamic effect of aquatic vegetation demands a consideration of three flow-environments relating to emergent vegetated ponds. Firstly, in large patches or regions far enough away from the open flow, the vegetation can be considered as full cross-sectional, or 'full vegetation', and the flow properties are spatially uniform when averaged over a scale larger than the spacing between stems. Secondly, in border regions (see Figure 1.1a) the adjacent open flow interacts with the immediate vegetation interface – known as the 'mixing layer' and the mixing is spatially non-uniform. Finally, in the region sufficiently far from the vegetation interface, known as the 'open channel' region, the flow is analogous to open channel flow and the flow properties are spatially uniform. These three regions are, collectively, referred to as a "vegetated shear layer".

1.1.2 Mathematic construction for mixing

In this thesis, "mixing" is treated as the aggregate effect of the processes that contribute to the spread of a pollutant in time and space. In vegetated flows it becomes difficult to experimentally distinguish between the different contributors to mixing and for practical applications is not necessary. For an isotropic, homogenous fluid, mixing is therefore defined as the aggregation of molecular diffusion (Brownian motion), turbulent diffusion (small scale eddy turbulence), mechanical diffusion (porous obstructions), differential advection (bed shear effects) and shear layer mixing (large scale vortices). Moreover, here, and in the subsequent mathematical description, it is assumed that turbulent-advective models – namely the advection diffusion equation – are suitable formulations for describing the solute mixing characteristics of vegetated and partially vegetated flows. However, it is still important to understand and account for the relative contributions to mixing that the individual processes make and, as such, this mathematic constructions aims to provide an explanation of these mechanisms. In addition, flow velocity in ponds is here characterized as flow where the temporal and spatial mean velocity, U, is not in excess of 0.5m/s and the stem Reynolds number, Re_d, typically ranges from 50 to 5,000 (Nepf et al., 1997; Kadlec, 1990; King et al., 2009; Lightbody et al., 2008).

The physical system and quantity decomposition

The flow system is defined using the conventional Cartesian notation where x represents the distance in the longitudinal direction aligned with the direction of primary flow. The horizontal and vertical distances are denoted by y and z, respectively, such that x, y and z are orthogonal to one-another and the position of a point, χ, within the system can be defined as $\chi = (x, y, z)$. The instantaneous velocity vector – defined as the rate of change of distance – of point χ is defined as $\boldsymbol{u} = u\boldsymbol{i} + v\boldsymbol{j} + w\boldsymbol{k}$, where u, v and w are the magnitudes of the instantaneous velocity in the x, y and z directions, respectively, and $\boldsymbol{i}$, $\boldsymbol{j}$ and $\boldsymbol{k}$ are the unit

vectors in the conventional directions. The concentration, C, may also vary with space and time such that $C = f(x, y, z, t)$. In this formulation, the stem diameter, d, of the vegetation is assumed to be constant with depth such that the vegetation may be characterized by the population density per unit area, N, and the solid volume fraction, Φ (= $N\pi d^2/4$) and porosity, η (= $1 - \Phi$).

Following the conventional Reynolds time decomposition (e.g. Raupach and Shaw, 1982; Nikora, 2007) the instantaneous velocity components and concentration may be given as a summation of the temporal mean (overbar) and fluctuation from the mean (prime), e.g.:

$$u = \bar{u} + u'$$
$$v = \bar{v} + v'$$
$$w = \bar{w} + w'$$
$$C = \bar{C} + C'. \qquad \textbf{Equation 1.1}$$

In heterogeneous flows such as those associated with porous media, the velocity field is non-uniform with space and time and is highly three-dimensional (White and Nepf, 2007). For example, within a patch of vegetation the flow is forced between the plant elements leading to a local spatially and temporally heterogeneous velocity field at the stem scale, where the velocity is expected to be greater between the stems than behind the individual wakes (e.g. Serra et al., 2004). The Reynolds averaged equations are impractical in these situations (Nikora, 2004); therefore, it has become conventional to apply a volumetric or area averaging technique as a suitable method for managing the spatial variations in the temporal time series (Wilson and Shaw, 1977; Raupach, 1996; Nikora, 2005; King et al., 2012). Subsequent decomposition of the time-averaged physical quantity, say ϑ, (e.g. Equation 1.1) yields a spatial average and deviation from the spatial average (double-prime);

$$\bar{\vartheta} = \langle\bar{\vartheta}\rangle + \langle\bar{\vartheta}''\rangle. \qquad \textbf{Equation 1.2}$$

The Momentum Equation

The fluid momentum associated with vegetation and vegetation borders has generally been treated as turbulent flow within, and adjacent to, porous media (e.g. White and Nepf, 2007;

Wilson and Shaw, 1977; Nepf, 2004). It is important to distinguish between the sources and sinks of momentum associated with vegetated flows when creating a mathematical description. In aquatic vegetation and borders, turbulence is generated at the scales of the vertical shear, the stem diameter or spacing (Nepf et al., 1997) and at the scale of shear-layer vortices under certain flow conditions (e.g. Ghisalberti and Nepf, 2002). The Navier-Stokes equation, or the momentum equation, describes the movement of incompressible, viscous fluid substances (Nikora, 2007):

$$\frac{\partial \boldsymbol{u}}{\partial t} + (\boldsymbol{u}.\nabla)\boldsymbol{u} - \upsilon\nabla^2\boldsymbol{u} = -w\nabla + \boldsymbol{G} \qquad \textbf{Equation 1.3}$$

where the kinematic viscosity of water, w, is the specific thermodynamic work and $\boldsymbol{G}$ is an external source. The terms in Equation 1.3 represent, respectively from left to right, variation, convection, diffusion and internal and external sources. Note that the diffusion term can be interpreted as the difference in velocity at a point and the mean velocity and thus the viscosity acts to diffuse momentum.

Given the complex, three-dimensional nature of the flow and the spatial and temporal heterogeneity at both the small time-scale and spatial scale of the vegetation stems, decomposition of the Navier-Stokes equation using the Reynolds decomposition, or Reynolds averaging, yields a more suitable description of the momentum and continuity equations for vegetated flows. However, vegetated flows have been treated as two-dimensional problems by a number of Authors (White and Nepf, 2007; Nepf, 2004; Nepf and Vivoni, 2000) where depth-averaging of the decomposed Navier-Stokes equation is more practical for shallow flows. The time-, spatial- and depth-averaged physical quantities, ϑ, are first represented using the subscript notation e such that;

$$\langle\bar{\vartheta}\rangle_e = \frac{1}{h}\int_0^h \langle\bar{\vartheta}\rangle \mathrm{d}z, \qquad \textbf{Equation 1.4}$$

where the depth of flow, h, is assumed to remain constant in both time and all space. Assuming the continuity that $\partial U/\partial x = 0$, the decomposition and subsequent depth-averaging

(e.g. Equation 1.4) of Equation 1.3 yields the two dimensional, shallow water momentum equation (Nepf, 2004):

$$\rho\Lambda\frac{\partial\langle\bar{u}\rangle_e}{\partial t}+\rho\frac{\partial\eta\langle\bar{v}\rangle_e\langle\bar{u}\rangle_e}{\partial y}=-\rho g\frac{\partial\eta\langle\bar{h}\rangle_e}{\partial x}+\mu\frac{\partial^2\eta\langle\bar{u}\rangle_e}{\partial y^2}+\frac{\partial\eta\langle\tau_{xy}\rangle_e}{\partial y}-f_i \qquad \textbf{Equation 1.5}$$

$$\langle\tau_{xy}\rangle_e=-\rho\langle\overline{u'v'}\rangle_e-\rho\langle\bar{u}''\bar{v}''\rangle_e-\rho\langle[\langle\bar{u}\rangle-\langle\bar{u}\rangle_e][\langle\bar{v}\rangle-\langle\bar{v}\rangle_e]\rangle_e,$$

where f_i is the non-time varying external force, μ is the dynamic viscosity, g is the acceleration due to gravity, and τ_{xy} is the total shear stress tensor containing Reynolds and dispersive stresses and the additional contribution from the depth variations in the mean flow. For emergent vegetated flows, if sufficient time-averaging is taken to remove all temporal fluctuations in the physical quantities, Raupach and Shaw (1981) showed that, under uniform flow conditions, the Reynolds equation reduces to a balance of gravitational and pressure forces, Reynolds stress, dispersive stress, viscous stress and drag forces, giving:

$$0=-gS+\frac{\partial\tau_{xy}}{\partial y}-f_m \qquad \textbf{Equation 1.6}$$

$$\tau_{xy}\equiv\nu\frac{\partial U}{\partial y}-\langle\overline{u'v'}\rangle-\langle\bar{u}''\bar{v}''\rangle, \qquad \textbf{Equation 1.7}$$

where f_m is the drag force per unit fluid mass, U is the depth-averaged temporal mean longitudinal velocity and dh/dx has been substituted for the bed slope, S. The mean shear stress, τ_{xy}, is the sum of the viscous stress, the Reynolds stress, and the dispersive stress due to the heterogeneity of the time averaged velocity profile between vegetation stems. Note that the drag force is a summation of the form (pressure) and viscous drag forces.

The vegetation flow system is schematically depicted in Figure 1.2. Firstly, in uniform emergent flow conditions, i.e. deep within a vegetated region, the dominant source of drag is the vegetation elements and, when averaged over a length scale larger than the stem spacing, the contributions from Reynolds and dispersive stress are negligible (King et al., 2012). Thus, assuming that $\partial U/\partial t$ (e.g. uniform flow) with no vertical gradients, Equation 1.6 reduces to a balance between gravitational force, gS, and canopy drag, $C_D a$, (Nepf et al., 1997);

$$-gS = \frac{1}{2} C_D \langle \bar{u} \rangle |\langle \bar{u} \rangle| \qquad \textbf{Equation 1.8}$$

where the mean or bulk vegetation drag coefficient per unit volume, C_D [-], is a quantification of the resistance to flow by the vegetation on an incoming volume of water (Shucksmith et al., 2011); a [m^{-1}] (= Nd) is the frontal facing area of vegetation per unit volume, (e.g. Luhar et al., 2008) and the vertical line signify the magnitude of the velocity, such that the temporal area mean velocity, U, can be approximated as;

$$U = \sqrt{\frac{2gS}{C_D a}} \qquad \textbf{Equation 1.9}$$

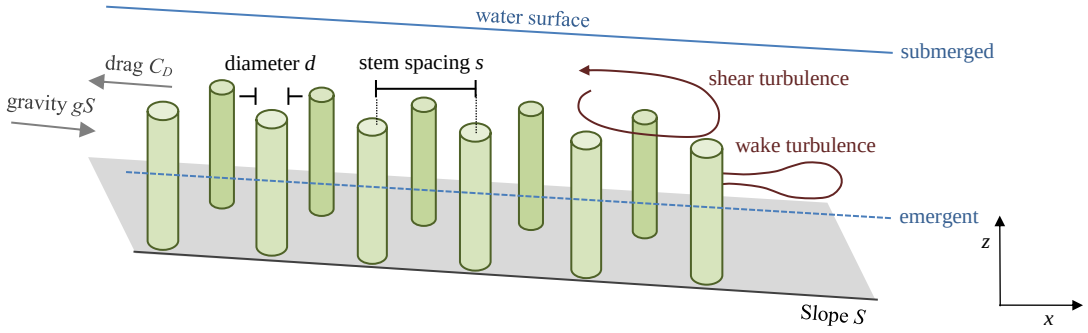

Figure 1.2: Vegetated flow for submerged and emergent conditions.

Note that the C_D is a function of stem Reynolds number and therefore velocity. Further, the equality in Equation 1.9 assumes a quadratic law between velocity and drag (e.g. Koch and Ladd, 1997). Tanino and Nepf (2008) conducted mean drag investigations in a random array of emergent rigid vegetation for various stem Reynolds numbers, Re_d. The spatially-averaged drag coefficient was defined as:

$$C_D \equiv \frac{\langle \bar{f}_D \rangle}{\rho U^2 \langle d \rangle / 2} \qquad \textbf{Equation 1.10}$$

where the denominator is the average drag in the direction of the primary flow per unit length of stem, f_D. The relationship between C_D and Re_d for different vegetation solid volume fractions, Φ, is presented in Figure 1.3. The drag coefficient is a strong function of Re_d – in some cases reducing by approximately 50% for a tenfold increase in Re_d. As the fractional volume of space occupied by the vegetation increases the incoming flow loses an increasing

amount of energy in momentum loss by the intercepting stems thus reducing the impact velocity. The profiles of C_D versus Re_d for each value of Φ deviate from one another as the stem Reynolds number exceeds 100. For any given value of Φ, the energy that is lost to the drag force exerted by the by the vegetation decreases for increasing values of Re_d, i.e. the drag coefficient is greatest at lower Re_d and for high stem densities.

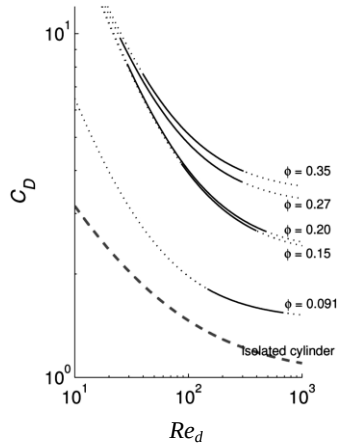

Figure 1.3: Experimental values of vegetation drag coefficient, C_D, compared to stem Reynolds number, Re_d, for different solid volume fractions, Φ. Tanino and Nepf, 2008a.

In this thesis flow in submerged cross-sectional uniform vegetation and emergent partial vegetation (e.g. borders) is considered to exhibit many analogies to one-another – such as the dominant contributions to turbulence and the form of the mean longitudinal velocity profile – and is often referred to as a "vegetated shear layer". The literature review below discusses both physical systems in light of these comparisons.

In the partially vegetated scenario, the momentum equation requires consideration of the Reynolds stress term as it is non-negligible and lateral gradients are more important. Assuming that the dispersive stress and viscous stress are negligible compared to turbulent stress (term iii) and the canopy drag (term iv) and adopting the new notation for the spatial and temporal, area mean velocity, U (King et al., 2012);

$$\frac{D\langle\bar{u}\rangle}{Dt} = gS - \frac{\partial}{\partial z}\langle\overline{u'v'}\rangle + \frac{1}{2}C_D U^2 \qquad \textbf{Equation 1.11}$$

(i) (ii) (iii) (iv)

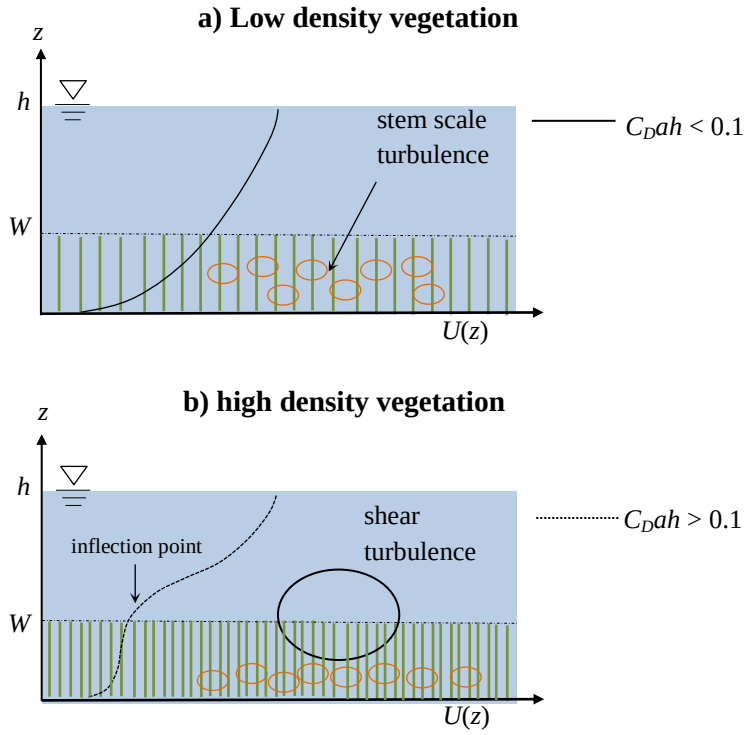

Figure 1.4: Visualisation of vertical profiles of temporal mean longitudinalvelocity, $U(z)$, and turbulent scales for a) high and b) low density partial vegetated flows.

Figure 1.4 demonstrates the two canopy density criteria defined by Nepf et al. (2007). For small values of drag, $C_Dah < 0.04$, Nepf et al., (2007) found that the momentum transport (iii) dominates drag (term iv) and the flow resembles a boundary layer (Figure 1.4a). However, for higher values of canopy drag, $C_Dah > 0.1$ (Poggi et al., 2008), the drag dominates the momentum transport. In this case, the longitudinal velocity within the canopy can reduce to such an extent that the flow resembles a mixing layer (Figure 1.4b). In the low density case (Figure 1.4a) the vegetation is a poor sink of momentum and the systems behaves as a boundary layer. In the high density case (Figure 1.4b) the vegetation is a strong sink for momentum and Equation 1.11 is applicable. Figure 1.4 shows that the major contribution to turbulence within the vegetation is due to the wake effect of the individual stem elements since the density of stems prevents the development of larger scale eddies. In borders of vegetation, the shear layer region generates large scale turbulence due to the Kevin-Helmholtz

instability and Reynolds stress is maximized at the location of the discontinuity between the vegetation and the adjacent open-flow.

Turbulence energy

The turbulent kinetic energy budget, k_e, for vegetated flows is (Raupach et al., 1996);

$$\frac{\partial \overline{k_e}}{\partial t} = \underbrace{P_s}_{\text{shear production}} + \underbrace{P_w}_{\text{wake production}} + \underbrace{P_b}_{\text{buoyant production}} + \underbrace{T_t}_{\text{turbulent transport}} + \underbrace{T_p}_{\text{pressure transport}} - \underbrace{\Omega_d}_{\text{dissipation}} \qquad \textbf{Equation 1.12}$$

showing that, under uniform flow conditions, the shear, wake and buoyant production and turbulent and pressure transport are balanced by the energy dissipation. Similarly, the spatial and temporal Reynolds decomposition of the kinetic energy budget can be used to account for the production and dissipation of energy in vegetated flows.

In the full vegetation case, the absence of vertical gradients implies that the turbulent kinetic energy budget become as balance between stem wake production, P_w, and dissipation, Ω_d, e.g. $P_w = \Omega_d$; where the dissipation rate scales inversely with the stem diameter and thus the kinetic energy can be predicted from the vegetation characteristics and temporal mean velocity, U. In the partial vegetation the turbulent kinetic energy budget is governed by wake and shear production, P_s. The turbulence created by these two mechanisms has different length scales (e.g. Figure 1.4b) and thus alters the pathways of energy dissipation. In dense canopies the mixing layer turbulence scales with the drag length, $(C_D a)^{-1}$ and thus $C_D ad/1\text{-}\Phi$ is a measure of the separation between the shear kinetic energy and wake kinetic energy.

King et al. (2012) developed a k-ε turbulence model of vegetated flows to incorporate variations in vegetation morphology. The Authors use the averaging schemes proposed by Raupach and Shaw (1982) and those later developed by Raupach, Coppin and Legg (1986) to produce a model of canopy flow that assumes the dispersive stress (the extra term found by Raupach and Shaw, 1982) is significantly less than the Reynolds stress for canopy densities of $ah > 0.1$. Figure 1.5 schematically illustrates the energy pathways. King et al. (2012) assumed that, for $C_D ah/(1\text{-}\Phi) \geq 0.1$, the vegetation is sufficiently dense and eliminates vertical shear.

Experimental verification of the model was conducted on a range of rigid cylinder with (N = 1290, 645, 315,158 stems/m^2, U = 0.011 – 0.107 m/s and Re_d = 36-1388) and on field site Eurasian Watermilfoil (*Myriophyllum spicatum*) (N = 500 stems/m^2, U = 0.007-0.111 m/s, Re_d = 30-319).

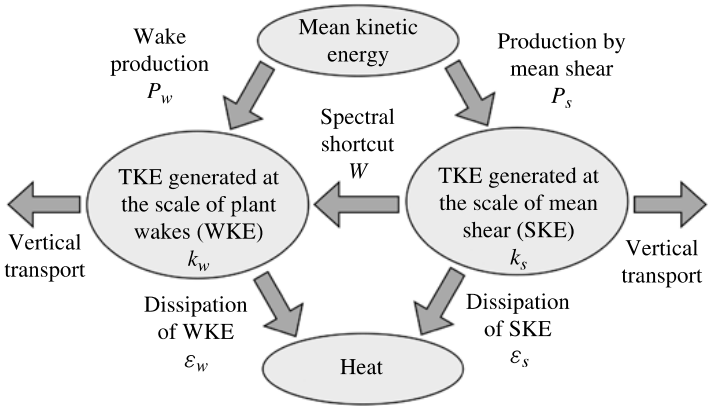

Figure 1.5: Diagram of kinetic energy flow paths in aquatic vegetation. King et al., 2012.

Diffusion and Advection

A pollutant will diffuse due to random molecular motion (Brownian motion); where the rate of change in concentration at point χ is proportional to the gradient of the concentration flux, $\boldsymbol{J}_{\text{diff}} = -\nabla C$, (note that we assume that $\nabla(\nabla \cdot C) = \nabla^2 C$) where the coefficient of proportionality is the Molecular Diffusion Coefficient, ε (Fick, 1855);

$$\frac{\partial C}{\partial t} = \varepsilon \nabla^2 C$$

$$\frac{\partial C}{\partial t} = \varepsilon \left(\frac{\partial^2 C}{\partial x^2} + \frac{\partial^2 C}{\partial y^2} + \frac{\partial^2 C}{\partial z^2} \right) \qquad \textbf{Equation 1.13}$$

When subject to the velocity field $\boldsymbol{u} = u\boldsymbol{i} + v\boldsymbol{j} + w\boldsymbol{k}$, the total concentration flux, $\boldsymbol{J}$, contains additional components due to the advection from velocity gradients, $\boldsymbol{J}_{\text{adv}}$, such that $\boldsymbol{J} = \boldsymbol{J}_{\text{adv}} + \boldsymbol{J}_{\text{diff}}$;

$$\frac{\partial C}{\partial t} = \varepsilon \nabla^2 C - \nabla.(\boldsymbol{u}C) + R \qquad \textbf{Equation 1.14}$$

where $\boldsymbol{J}_{\text{adv}} = \boldsymbol{u}C$ and R is a source term. This equation is often referred to as the continuity equation or the Advection-Diffusion Equation (ADE).

Turbulent Diffusion and Differential Advection

Fluctuations in the velocity field known as turbulence cause a pollutant to mix by increasing the distance between adjacent particles over time leading to, what is referred as, turbulent diffusion. Boundary roughness and flow obstructions generate turbulence increasing the rate of mixing relative to molecular diffusion. These random, small-scale velocity fluctuations are generated through velocity shear; where obstructions, such as vegetation stems, and bed irregularities generate turbulence at the scale of the obstruction. Further, long-term spatial variation in the velocity field also leads to mixing and is caused by the difference in advection of one fluid parcels from another – referred to as differential advection. Dead zone storage also promotes mixing (Beer and Young, 1983), where the trapping of parcels and subsequent release increases the dilution in concentration. The aggregate effect of molecular diffusion, turbulent diffusion and differential advection is, hereafter, referred to as "mixing" and is characterized using a mixing coefficient D [m^2/s]. Although conventionally referred to as "dispersion" (e.g. Fischer et al., 1979), "mixing" is appropriate for vegetated flow as two additional processes contribute to the spread of a pollutant. Recall that mixing arises from "the spatial heterogeneity in the velocity field" (Taylor, 1953) and the magnitude of mixing is related to the degree of the shear velocity, u^* (Rutherford, 1994).

In vegetated flows the velocity field may vary due to the local spatial and/or temporal variations in morphology and the spatial variations in stem density per unit area, N. These features of vegetated flows therefore generate mixing via long-term velocity shear (e.g. differential advection), small-scale velocity field heterogeneities (e.g. turbulent diffusion) due to bed roughness and stem-obstructions and an additional contribution from the flow path tortuosity leading to a specific form of differential advection – known as mechanical diffusion (discussed in more detail below).

Kolmorgorov (1931, 1933) showed that "…the diffusion of matter in a turbulent velocity field with independent properties satisfies the diffusion equation…" (in Fischer et al., 1979)

only if the motion of the particles is considered as a series of independent random steps happening over a sufficient time scale, such that, in Cartesian coordinates;

$$\frac{\partial C}{\partial t} + \boldsymbol{u} \cdot \nabla C = \frac{\partial}{\partial x}\left(D_{xx}\frac{\partial C}{\partial x}\right) + \frac{\partial}{\partial}\left(D_{yy}\frac{\partial C}{\partial y}\right) + \frac{\partial}{\partial}\left(D_{zz}\frac{\partial \mathrm{C}}{\partial z}\right) + \frac{\partial}{\partial}\left(D_{xy}\frac{\partial C}{\partial y}\right) + \frac{\partial}{\partial}\left(D_{xz}\frac{\partial C}{\partial z}\right) + \text{similar terms} \quad \textbf{Equation 1.15}$$

where D_{xx}, D_{yy}, D_{zz}, etc. are the tensor components of the turbulent diffusion coefficients. In uniform flow conditions (e.g. open channel flow), averaged over a length scale greater than that of the dominant scale of turbulence and over a sufficient time-scale such that the turbulent diffusion can be considered "Fickian" diffusion (e.g. the concentration flux is proportional to the concentration gradient), the double-average advection-diffusion equation (Equation 1.14) reduces to the well-known formulation (Fischer et al., 1979) – assuming that the coordinate axes coincide with the principle axis of the flow and thus the flow cross variances are zero;

$$\frac{\partial C}{\partial t} + u\frac{\partial C}{\partial x} + v\frac{\partial C}{\partial y} + w\frac{\partial C}{\partial z} = D_x\frac{\partial^2 C}{\partial x^2} + D_y\frac{\partial^2 C}{\partial y^2} + D_z\frac{\partial^2 C}{\partial z^2}, \quad \textbf{Equation 1.16}$$

where D_x, D_y and D_z are the longitudinal, transverse and vertical scalar mixing coefficients, respectively, and incorporate the effects of molecular diffusion, differential advection and turbulent diffusion; assuming that the mixing coefficients do not varying with space and time. Here the tensor subscripts (e.g. Equation 1.15) are dropped and replaced with the scalar notations for the *x*, *y* and *z* directions given that, for example, the longitudinal change in concentration due to the transverse concentration flux is expected to be negligible and cannot be measured experimentally, e.g. D_{xy}. Note that, if the scalar mixing coefficients do vary spatially, then Equation 1.16 becomes;

$$\frac{\partial C}{\partial t} + u\frac{\partial C}{\partial x} + v\frac{\partial C}{\partial y} + w\frac{\partial C}{\partial z} = \frac{\partial}{\partial x}\left(D_x\frac{\partial C}{\partial x}\right) + \frac{\partial}{\partial y}\left(D_y\frac{\partial C}{\partial y}\right) + \frac{\partial}{\partial z}\left(D_z\frac{\partial C}{\partial z}\right) \quad \textbf{Equation 1.17}$$

Averaging the Advection-Diffusion Equation

Applying this double-averaged techniques to the advection diffusion equation, in Cartesian coordinates, (Nikora, 2007) yields;

$$\frac{\partial\langle\overline{C}\rangle}{\partial t}+\langle\overline{u}_j\rangle\frac{\partial\langle\overline{C}\rangle}{\partial x_j}=\frac{1}{\eta}\frac{\partial}{\partial x_j}\eta\langle\varepsilon\overline{\frac{\partial C}{\partial x_j}}\rangle-\frac{1}{\eta}\frac{\partial\eta\langle\widetilde{u}_j\widetilde{C}\rangle}{\partial x_j}-\frac{1}{\eta}\frac{\partial\eta\langle\overline{u'_jC'}\rangle}{\partial x_j}$$

$$-\frac{1}{\eta}\frac{1}{V_0}\underbrace{\iint_{S_{\text{int}}}\left(\varepsilon\frac{\partial C}{\partial x_j}\right)n_j\mathrm{d}S}_{S}+\langle\overline{F}\rangle \qquad \textbf{Equation 1.18}$$

where u_i is the i-th component of the velocity vector; V_0 is the total volume of the averaging domain; $\boldsymbol{n}$ is the inwardly directing unit-vector normal to the bed surface; S_{int} is the extent of water-bed interface bounded by the averaging domain; η is the spatial porosity (or 1-Φ); and F is the source or sink of the pollutant. The subscript "s" denotes the superficial time average when the averaging time interval includes both periods when the spatial points are intermittently occupied by fluid and when they are occupied by roughness elements (e.g. stems). The wavy overbar denotes the double average (overbar and angled brackets) and time average (overbar) values.

The double-averaged advection diffusion equation contains important additional terms when compared to conventional Reynolds averaging:

- a dispersive pollutant flux due to the correlation of spatial variations in the time-averaged fields;
- and the diffusive flux at the water-bed surface interface.

Practical methods for calculating mixing coefficients

In large channels, D_x was shown to be related to the bed-shear velocity, u^*, through $D_x = 5.93hu^*$ (Elder, 1959) assuming that the vertical profile of temporal mean, longitudinal velocity, $U(z)$, is logarithmic. Furthermore, Rutherford (1994) showed that transverse mixing is an order of magnitude smaller than longitudinal mixing giving $D_y = 0.134hu^*$. However, Elder (1959) and Rutherford (1994) assumed a logarithmic form for the vertical variation in mean longitudinal velocity, $U(z)$, and, as will be shown, is not applicable given the non-logarithmic nature of $U(z)$ in aquatic vegetation.

The spatial and/or temporal observations of a tracer concentration can be used to calculate the scalar mixing coefficient for a given direction in the flow and many studies have

employed the advection diffusion equation to measure and predict them (Deng et al., 2002; Stovin et al., 2008; Boxall and Guymer, 2007; Shucksmith et al., 2010; Seo et al., 2006; Murphy et al., 2007; Ghisalberti and Nepf, 2005). Longitudinally – assuming that the random particle walk generate Gaussian distributions and therefore a linear increase in variance with time and space – the rate of change in variance with time can be used to calculate the longitudinal mixing coefficient, D_x, through (Taylor, 1953);

$$D_x = \frac{1}{2}\frac{\mathrm{d}\sigma_x^2}{\mathrm{d}t} \qquad \textbf{Equation 1.19}$$

Subsequently, in the transverse case, the spatial change in concentration variance at successive longitudinal locations can be used to calculate the transverse mixing coefficient, D_y;

$$D_y = \frac{U}{2}\frac{\mathrm{d}\sigma_y^2}{\mathrm{d}x} \qquad \textbf{Equation 1.20}$$

where U is the temporal and spatial mean longitudinal velocity.

Many examples pollution events can be considered as continuous injections – such as chemical outflows or the confluence of two rivers – and may be located in regions where the scale of turbulence varies laterally such that the transverse mixing coefficient is not spatially constant. In these conditions one can assume that $\partial C/\partial t = 0$ and $D_y = f(y)$; therefore, assuming a vertically well mixed source e.g. $\partial C/\partial z = 0$, the advection diffusion equation (Equation 1.17) can be reduced to;

$$\mathrm{h}(y)U(y)\frac{\partial C(x,y)}{\partial y} = \frac{\partial}{\partial y}\left(h(y)D_y(y)\frac{\partial C(x,y)}{\partial y}\right), \qquad \textbf{Equation 1.21}$$

where h is the flow depth and $U(y)$ is the transverse profile of temporal mean longitudinal velocity. This expression for the steady-state injection enables the transverse variation in scalar transverse mixing coefficient to be determined.

Two additional contributions to mixing are associated with vegetated or porous media flows. Mechanical diffusion is a product of the flow path tortuosity caused by the physical obstruction of the vegetation stems (Nepf, 1999). When a stem is encountered a particle is deflected laterally around the stem either to the left or the right; leading to differential

advection as multiple particles all take different length routes. Over a sufficient number of deflections and therefore over a sufficient longitudinal distance, the lateral spread in the particles is assumed to be Gaussian. Secondly, shear layer dispersion is of the same order as depth limited differential advection but is associated with shear layer velocity inflection – such as that seen in vegetation patches and borders.

1.2 The Mean Flow and Velocity

Velocity characteristics in emergent and submerged vegetated channels have been investigated by a number of Authors (Shucksmith et al., 2010; Lightbody and Nepf, 2006b; Nepf, 1999; Nepf and Vivoni, 2000; Ghisalberti & Nepf, 2007). In full cross-sectional emergent vegetation, the balance of pressure gradient and drag results in vertical profiles of mean longitudinal velocity and Reynolds stress that reflect the morphology of the vegetation elements. In shear layers, the lateral profiles of longitudinal velocity and Reynolds stress are determined by the vegetation drag and density and the effect on shear layer vortices. This section details the generation, magnitudes, and forms of vegetation flow structures and reviews current theoretical and experimental advances.

1.2.1 The vegetated flow system

The two emergent vegetated scenarios are shown in profile and plan in Figure 1.6. Upstream of the leading edge of the vegetation the spatial and temporal depth-averaged longitudinal velocity is denoted by U_c. In Figure 1.6a the full vegetation cross-section shown in green has a spatial and temporal depth-averaged longitudinal velocity denoted by U_1; where the width of the vegetation, W, is considered sufficiently large that any boundary effects are neglected. Within the vegetation, the scaling of Reynolds number calculation using the convention flow depth to scale the turbulence is nonsensical as turbulence is generated at the scale of the stem

wakes (Nepf and Vivoni, 2000). As such, Stem Reynolds number, $Re_d = Ud/\nu$, is considered a more appropriate method for assigning Reynolds number.

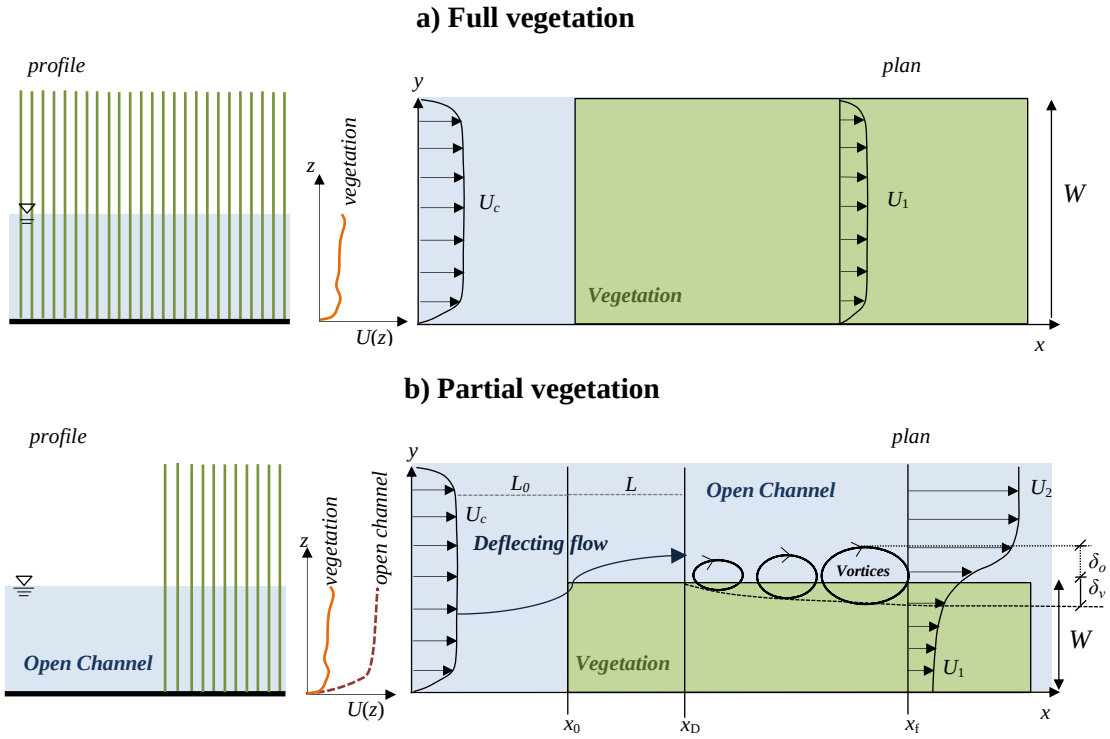

Figure 1.6: Flow in emergent vegetation in the a) full and b) partial scenario given in profile (left) and plan (right).

In the partial vegetation scenario (Figure 1.6b) the depth-averaged, temporal mean longitudinal velocity deep within the vegetation and open channel are defined as U_1 and U_2, respectively. The lateral drag discontinuity is found at the interface between the vegetation and the open channel, $y = y_i$, and induces a flow preference within the open channel increasing U_2 relative to U_c; while the increased friction due to the vegetation reduces U_2 relative to U_c such that the velocity difference, $\Delta U = U_2$-U_1, may cause an inflection in the transverse profile of depth-averaged, temporal mean longitudinal velocity, $U(y)$; generating interfacial shear layer vortices in specific situations (discussed below). In this scenario the system may be divided into three regions of flow; the vegetated region, $0 < y < y_i - \delta_v$, characterised by U_1, the open channel region, $y > y_i + \delta_o$, characterised by U_2, and the mixing layer region, $y_i - \delta_v < y < y_i + \delta_o$.

The locations at which the upstream flow deflects around the vegetation and then becomes stable (i.e. $\partial U(y)/\partial x = 0$) are dependent on the resistance of the vegetation (Rominger and Nepf (2011). The divergent flow decelerates after deflection around the vegetation up to a distance known as the interior adjustment length, L, from the leading edge, scaling with C_D and a (Rominger and Nepf, 2011) and occurs at the location $x = x_D$, where:

$$x_D = 2(C_D a)^{-1} \quad \textbf{Equation 1.22}$$

Zong and Nepf (2011) found that x_D extended to up to 2 m in a sparse patch (a = 4 m^{-1}) and up to 3 m in a dense patch (a = 20 m^{-1}). Similarly, Rominger and Nepf (2011) investigated the flow associated with emergent shear layers to parameterise L and the upstream deceleration length, L_0, for different blockage factors and drag. Zong and Nepf (2011) defined dense and sparse patches as $aW < 0.1$ and $aW > 0.1$, respectively. Dense patches are defined as systems where the vegetation flow is decelerated sufficiently such that an inflection point occurs in the transverse profile of depth-average, temporal mean velocity (e.g. Figure 1.6b). Further, high and low flow blockage was defined as:

- High blockage flow causes a pressure increase at the leading edge of the patch that scales as $\Delta p \sim \rho u_0^2$ with $C_D aW \geq 2$.
- Low blockage flow leads to an insignificant pressure drop at the leading edge thus $\Delta p = 0$ and $C_D aW < 2$.

Rominger and Nepf (2011) provided empirical scaling for L and L_0;

High and low blockage $$L_0 = (4.0 \pm 0.7) W \quad \textbf{Equation 1.23}$$

High blockage $$L = (3.0 \pm 0.3) \left[\frac{2}{C_D a} \left(1 + (C_D a W)^2 \right) \right] \quad \textbf{Equation 1.24}$$

Low blockage $$L = (7.0 \pm 0.4) W \quad \textbf{Equation 1.25}$$

The empirical relationships between the upstream deceleration and interior adjustments lengths and the vegetation characteristics are required when designing physical experiments that demand uniform, steady flow condition.

1.2.2 Vegetated shear layers

Beyond the stabilisation limit x_D and in the presence of sufficient drag, the discontinuity in drag between the vegetation and open channel leads to vortex generation along the vegetation/open-channel interface. These vortices grow in magnitude downstream until they reach a fixed size at a distance $x = x_f$ (Zong and Nepf, 2011) and the region encompassing the vortices at the maximum scale, $y_i - \delta_v < y < y_i + \delta_o$, is referred to as the "mixing layer". The scale of these vortices is set by the ΔU and the magnitude of the vegetation drag, $C_D a$. White and Nepf (2007) found that the vortex penetration into the patch, δ_v, and open channel, δ_o, is inversely proportional to the vegetation density and bed friction, C_f, respectively; giving:

$$\delta_v \sim 0.5(C_D a)^{-1} \quad \textbf{Equation 1.26}$$

$$\delta_o \sim \frac{H}{C_f} \quad \textbf{Equation 1.27}$$

Measurements of transverse profiles of temporal mean longitudinal velocity by Zong and Nepf (2010) for both dense and sparse vegetation highlighted the change in velocity and Reynolds stress at the vortex penetration location. When the patch width is larger than the penetration scale ($W > \delta_v$), a two-zone system is created with a region of high exchange at the boundary (within δ_v) and one of lower exchange deeper within the vegetation. The region between the two penetration distances, δ_v and δ_o, is characterised by an increase in mixing and is, therefore, referred to as the *mixing layer*, with width $t_{ml} = \delta_v + \delta_o$.

Under mixing layer conditions, the mass exchange between the vegetation and the free flow is controlled by the magnitude of shear layer vortices. Within the mixing layer, shear turbulent kinetic energy is converted into wake turbulent energy via the energy cascade shown in Figure 1.5. Ghisalberti and Nepf (2004) presented lateral profiles of longitudinal velocity in shear layer vegetation to evaluate this energy balance. Profiles of Reynolds stress were used to show that maximum stress is located at the vegetation interface and the velocity shear was shown to have a positive correlation with plant density, *ad*, (goodness of fit, $R^2 = 0.98$). The vegetation drag increases with vegetation density, reducing U_1 increasing ΔU. Further, the fraction of the

shear layer within the canopy decreases with the stem frontal area per unit volume, *a*, as the increases density provides a strong energy sink reducing vortex penetration.

Ghisalberti and Nepf (2004) developed a numerical model to predict $U(y)$ by dividing the mixing layer into two regions – open channel and vegetation, where:

Vegetation

$y_i - \delta_v < y < y_i$

$$\frac{\partial}{\partial y}\left[\left(\frac{\partial U}{\partial y}\right)^2\right]=\frac{1}{l_c^2}\left(\frac{1}{2}C_D U^2\text{-}gS\right) \qquad \textbf{Equation 1.28}$$

Open channel

$y_i < y < y_i + \delta_o$

$$\mathrm{U}(y)=U_h+\frac{2\sqrt{gS}}{3(0.95t_{ml})}\left\{(\delta_v\text{-}h)^{3/2}\text{-}(\delta_v\text{-}y)^{3/2}\right\} \qquad \textbf{Equation 1.29}$$

where U_i is the interfacial longitudinal velocity and l_c is the mixing length scale, $\alpha l_c/t_{ml} = 0.22\pm0.01$, and α is the penetration ratio. Equation 1.28 was solved numerically while its counterpart above the canopy was solved analytically to obtain Equation 1.29. Ghisalberti and Nepf (2004) report a good fit ($R^2 > 0.93$) between the predicted and experimental velocity profiles.

White and Nepf (2008) successfully predicted $U(y)$ in emergent shear layer vegetation. Velocity and shear stress measured in rigid cylinders were compared to a semi-empirical model based on the shear layer vortex-induced exchange. Velocity was described in two parts to account for the asymmetry in the profile about the inflection point. Figure 1.7 provides a schematic description of White and Nepf's formulation. Firstly, the constant velocity of the free channel and vegetation zones, U_1 and U_2, were described using a force balance, e.g.,

$$U_1=\sqrt{\frac{2gS}{C_D a}} \qquad \textbf{Equation 1.30}$$

and

$$U_2=\sqrt{\frac{2gSH}{c_f}} \qquad \textbf{Equation 1.31}$$

Secondly, the velocity profile describing the mixing layer region was also separated into two parts, in accordance with Ghisalberti and Nepf (2004). A hyperbolic tangent shear

function was employed to predict $U(y)$ from within the vegetation, U_{inner}, up to a matching point, y_m ($dU_{inner}/dy = dU_{outer}/dy$), where;

$$U_{inner}(y) = U_1 + U_s\left(1+\tanh\left(\frac{y-y_i}{\delta_v}\right)\right) \qquad \textbf{Equation 1.32}$$

where y_0 is the location of the inflection point and U_s is the slip velocity, $U_s = U(y_0) - U_1$. Note that δ_v is described above in Equation 1.32 for sparse canopies ($C_D ah < 1$) while for dense canopies the dependence of δ_v becomes independent of the canopy drag and scales as $\delta_v = 1.8d$ (White and Nepf, 2008).

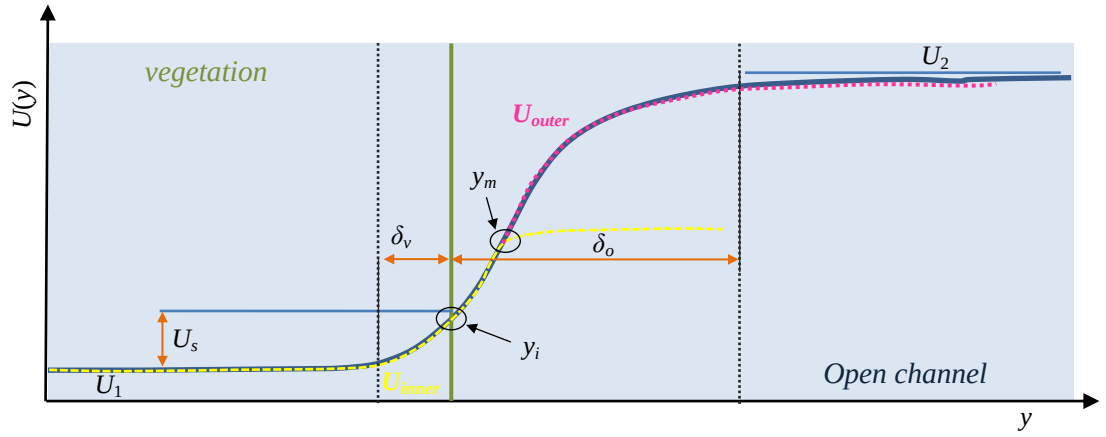

Figure 1.7: Construction of transverse profile of spatial average, temporal mean longitudinal velocity (blue) for shear layer emergent vegetation; using a hyperbolic prediction for the inner region (Equation 1.32) (yellow) and quadratic prediction for outer region (Equation 1.33) (magenta) that meet at y_m. The interface (green) is located at y_i.

In the outer mixing layer region the velocity profile was derived from the balance of pressure gradient and the lateral shear stress. Under the assumption of a constant eddy viscosity the momentum balance in the outer shear layer region can be written as;

$$-gS = \nu_t \frac{d^2 U_{outer}}{dy^2} - \frac{c_f}{2H} U_{outer}^2 \qquad \textbf{Equation 1.33}$$

where ν_t is the eddy viscosity. The solution to Equation 1.33 for the outer shear layer velocity profile, U_{outer}, was shown to be a quadratic function of U_2, δ_o and the matching velocity, U_m ($=U(y_m)$), between the inner and outer shear layer regions:

$$U_{outer} = U_m + (U_2 - U_m)\left[\frac{y-y_m}{\delta_o} - \frac{1}{4}\left(\frac{y-y_m}{\delta_o}\right)^2\right] \qquad \textbf{Equation 1.34}$$

The description of U_{inner} and U_{outer} enabled the Author's to predict $U(y)$ across the mixing layer.

The empirical success of White and Nepf (2008) is useful when describing the hydraulic features of shear layer vegetation. Their approach was derived for homogeneous vegetation and may encounter short-comings when applied to real vegetation – where C_D and c_f are non-uniform. The formulation requires a vegetation velocity, U_1, which is the spatial average over the length scale greater than the stem spacing. Moreover, the stem spacing in the formulation is smaller than the length scale δ_v such that the heterogeneities in the velocity field between stems may be omitted. This simplification may not apply to flow fields in real vegetation where $s \ \delta_v$. Further, prediction of δ_v and δ_o are required to complete $U(y)$.

1.2.3 Velocity in real vegetation

Velocity profiles in real vegetation have been predominantly quantified in the full vegetation scenario. Shucksmith *et al.* (2010) investigated the velocity and mixing properties of real vegetation (Carex and Reeds) in both full emergent and submerged scenarios. Vertical profiles of temporal mean longitudinal velocity, $U(z)$, were collected during the growth of the vegetation – from 2 to 52 weeks. Peak velocity reduced with plant age, suggesting that the older plants exert a greater drag on the flow. However, the two species were characterised by age rather than morphology; preventing quantitative comparisons to be made. Figure 1.8 presents the velocity profiles for the Carex and Reed study. Note that a logarithmic profile was recorded for the bare channel base test. The profiles confirm that the dominance of the vegetation drag over the bed roughness results in profile shapes depends on the vertical variation in plant morphology.

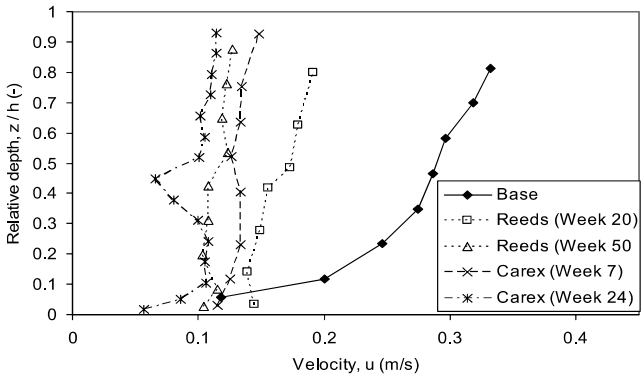

Figure 1.8: Vertical profiles of temporal mean longitudinal velocity measured in Reeds and *Carex*. Shucksmith et al., 2010.

Lightbody and Nepf (2006b) attempted to predict $U(z)$ in emergent salt marsh vegetation and showed that the form of velocity is affected by the stems morphology; where Figure 1.9 provides profiles of $U(z)$ measured by Lightbody and Nepf (2006a) in a matrix of three common salt marsh species; *Alisma gramineum*, *Atriplex portuloides* and *Spatina alterniflora*.

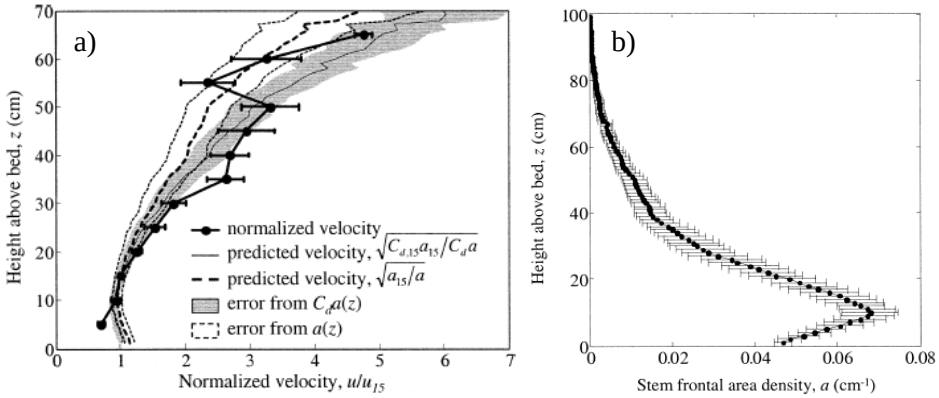

Figure 1.9: a) Measured and predicted profiles of $U(z)$ (normalised by the velocity at 15 cm from the bed) and b) frontal area per unit volume variation with height for emergent saltmarsh vegetation. Lightbody and Nepf, 2006b.

In steady, uniform flow, $U(z)$ was characterised using the stem morphology, e.g.;

$$\mathrm{U}(z) = \sqrt{\frac{2g\partial\eta/\partial z}{C_D(z)/a(z)}} \qquad \textbf{Equation 1.35}$$

where $C_D(z)$ and $a(z)$ are the vertical profiles of drag and frontal area per unit volume, respectively. Mean stem diameter and stem frontal area per unit volume were calculated using fields samples and image analysis. Velocity profiles measured in the real vegetation were then compared to those proposed using Equation 1.35. Figure 1.9a compares the measured (black circles), predicted (black line) and predicted with constant C_D (dotted line) profiles while

Figure 1.9b gives an example of $a(z)$ showing decreasing vegetation density with height as the stems reduce in diameter. The two approaches used to estimate the variations in $U(z)$ (e.g. $C_D = f(z)$ and $C_D \neq f(z)$) were successful in predicting the profile shape; although normalisation did not yield successful predictions of the velocity magnitude. Further, no quantification of the fit between model and predictions was given and, despite the models success, physical measurements were required to characterise the vegetation demanding experimental time.

Nepf and Vivoni (2000) also reported vertical profiles of mean longitudinal velocity collected in both emergent and submerged flexible, randomly distributed artificial vegetation. Although artificial vegetation was used, the mechanical properties were matched to simulate natural stems and the distribution was generated randomly using computer software. Controlled laboratory experimentation was conducted for a range of submergence ratios, W/h; where The temporal mean profiles of $U(z)$ are given in Figure 1.10 for W/h = 1.0 and 2.75. In the emergent scenario, plant morphology, rather than bed shear determines $U(z)$; while in the submerged scenario $U(z)$ exhibits an inflection about the interface and the shear layer effects dominate the profile shape. Note that, beyond the extent of the mixing layer vortices, within the vegetation (denoted in Figure 1.10 by h_p) $U(z)$ is similar to that of the emergent case, e.g. $U(z) \approx U_1$. Reynolds stress (open circles) was also shown to peak at the top of the vegetation concurrent with the velocity inflection point.

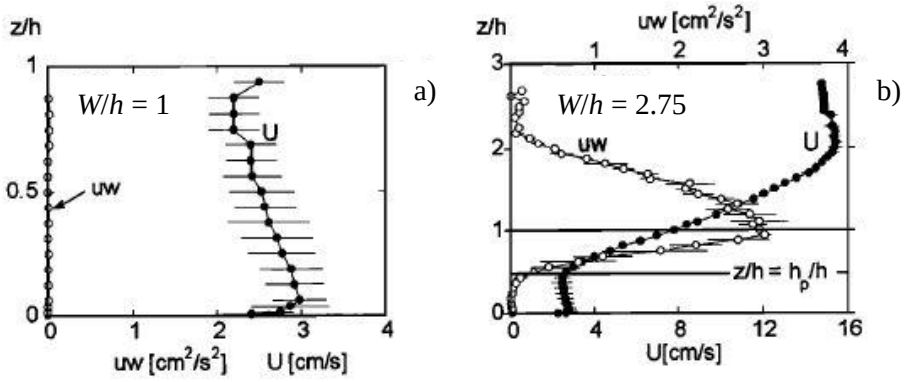

Figure 1.10: Measured profiles of $U(z)$ and Reynolds stress (uw) for emergent and submerged simulated real vegetation for a) W/h = 1 and b)W/h = 2.75 – where and h_p is the penetration depth of turbulent vortices. Nepf & Vivoni, 2000.

Nepf and Vivoni (2000) showed that lateral profiles of longitudinal velocity in shear layer vegetation can be characterised using three regions of flow. In the open channel region, sufficiently far from the vegetation interface, the flow is not influenced by the mixing layer vortices and $U(z) \approx U_2$ where $U(z)$ is approximately logarithmic for $W/h >> 1$. Conversely, in deep or dense vegetation, the mixing layer vortices do not penetrate completely where $U(z)$ is set by the balance between potential gradient and the sum of the canopy and bed drag (Carollo et al., 2002). Between these two zones the mixing layer is characterised by an inflection in $U(z)$ and enhanced turbulence at the interface. Reynolds stress is maximized in the center of the vortex layer and, therefore, turbulent exchange is the dominant transport process for the entire shear layer.

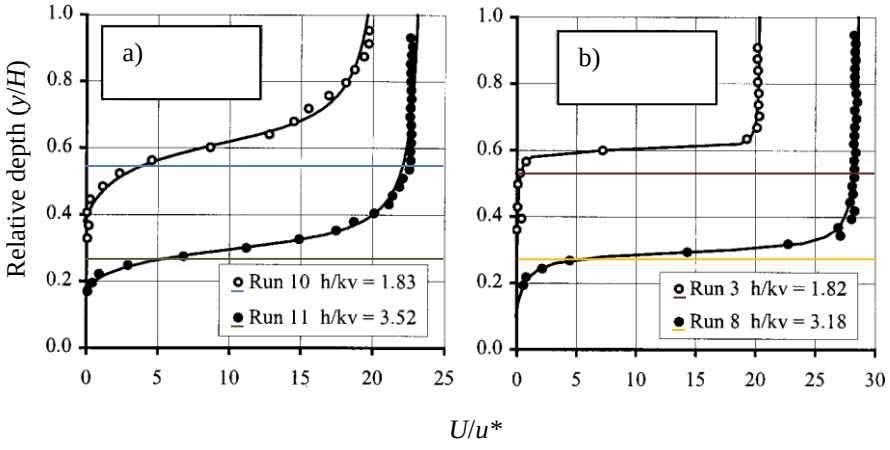

Figure 1.11: Measured profiles of $U(z)$ in submerged real vegetation for a) 28,000 and b) 44,000 stems/m^2 for submergence ratios (h/k_v) interface height is given by the coloured lines. Carollo et al., 2002.

In submerged vegetation the shape and degree of inflection in $U(z)$ has been shown by a number of authors to be dependent upon the submergence ratio (Nepf and Vivoni, 2000; Nepf, 2012; Carollo et al., 2002; Nepf et al., 2007). Carollo et al., (2002) measured and predicted velocity profiles in shear layer real vegetation (*Loietto*, *Festuca rubra* and *Poa prantensis*) for different densities and submergence ratios. Nepf and Vivoni's (2000) distinction of three regions was confirmed in all cases; however, the location of the logarithmic zone was only affect by the submergence ratio – whereas, the inflection shape was altered by the vegetation density. The shape and magnitude of $U(z)$ were well predicted; where the two sets of profiles

in Figure 1.11 support the notion that increasing drag (N = 28,000 stems/m^2 to 44,000 stems/m^2) notably accentuates the degree of inflexion in $U(z)$ – also reported by Ghisalberti and Nepf (2004).

It was noted by Nepf and Ghisalberti (2008) that the generation of shear layer vortices only occurs once the momentum absorption (i.e. drag) of the vegetation is sufficiently large to induce a critical velocity shear. Over a sufficient length of vegetation these vortices will grow to a fixed size and penetration (Nepf, 2012) when the energy dissipation balances with the shear production. This balance between momentum and absorption was shown by Nepf et al., (2007) to yield an empirical ratio between δ_v, and the canopy width, W, as a function of drag and frontal area density, e.g.,

$$\frac{\delta_v}{W} = \frac{0.23 \pm 0.06}{C_D a W} \qquad \textbf{Equation 1.36}$$

Equation 1.36 implies that the vegetation with a greater drag will act as a greater sink of momentum and arrest the penetration of vortices into the canopy.

1.2.4 Summary of the velocity field in vegetation

Aquatic vegetation increases drag relative to the channel bed such that the lateral profile of mean longitudinal velocity is non-logarithmic (see Figure 1.10 and Figure 1.11). In laterally uniform vegetation, the drag is constant with location and the velocity is constant both laterally and vertically when averaged over a distance greater than the stem spacing. However, in vegetated shear layers the disparity in drag between the adjacent flow and the vegetation leads to an inflection in the lateral profile of velocity. Upstream flow is deflected leading to velocity shear and generating interfacial vortices via the Kelvin-Helmholtz instability in conditions of sufficient drag - where the vortex penetration is inversely proportional to the vegetation drag. Reynolds stress is maximized at the location of the drag discontinuity and the magnitude, shape and location of the velocity inflection are determined by the relative magnitudes of the vegetation drag and by the submergence ratio.

Deep within the vegetation, the flow is analogous to a fully vegetated channel; where the temporal mean, longitudinal velocity is spatially constant and is set by the balance between gravitational potential and vegetation drag, e.g. $U \neq f(y, z) = U_1$. It will be shown in the following section that the mixing in this region is set by the turbulence caused by the vegetation elements and mechanical diffusion. Similarly, in the open channel region the mean velocity is spatially constant, set by the balance between bed drag and gravitational potential, e.g. $U \neq f(y, z) = U_2$, where $U_2 > U_1$. Finally, the velocity profile across the mixing is asymmetric (e.g. $\delta_v \neq \delta_o$) and δ_v and δ_o are set by the canopy drag, $C_D a$, and the bed friction, C_f, respectively.

Flow fields have been described and predicted for artificial vegetation with uniform morphologies in the majority of cases. Information is lacking regarding the mean velocity characteristics of real vegetation for a range of morphologies and seasons. There is also a paucity of evaluations of theoretical descriptions developed in idealised, artificial flow conditions applied to real vegetation flows. Real vegetated shear layers have been poorly documented and the application of models such as White and Nepf (2008) have not been extensively applied to them – in particular, mixing layer features have not been described.

1.3 Mixing

1.3.1 Spatially variable mixing

Central to the quantification of mixing in vegetated shear layers is the application of models capable of describing large scale spatial heterogeneities in the mixing field. Boxall and Guymer (2003) adapted the discretized zonal model proposed by Chickwendu (1986) to predict the longitudinal mixing coefficient, D_x, for a channel with a simulated naturally deposited bed-form. The effects of lateral heterogeneity in the mean longitudinal velocity

profile were modelled by modifying Chickwendu's (1986) expression for the discretization of primary velocity for application in the horizontal plane.

Figure 1.12a shows the associated error in D_x for the meandering channel between various location in the sinuosity. It was found that, when using the modification, the prediction of D_x was dependent on the accurate measurement and sensitivity of the transverse mixing coefficient, D_y (Figure 1.12b). Furthermore, a change in D_x was observed over the channel meander cycle as the dominant mixing process changes from longitudinal to transverse. Predicted values of D_x were found to be within 20% of the measured values; however, error of up to 50% was recorded in some cases.

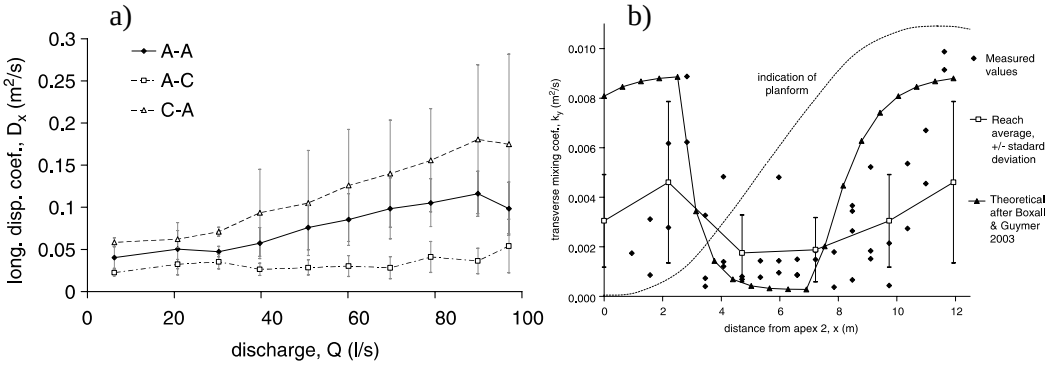

Figure 1.12: a) Experimental mixing coefficients in a meandering channel for a) D_x against discharge and reach location and b) D_y against distance from the meander apex. Boxall and Guymer, 2007.

Seo et al. (2006) combined the method of moments and a stream tube approximation to quantify transverse mixing in meandering rivers; where variations in velocity and water depth, as well as bank reflection, made a continuous injection unfavourable rendering instantaneous release preferable. Seo et al. (2006) modelled the system using the two-dimensional Advection-Diffusion formulation. A novel aspect was to transform the Cartesian coordinate system into one as a function of partial discharge, tracer dosage and channel form; where;

$$D_y = \frac{U}{2}\frac{\mathrm{d}\sigma_y^2}{\mathrm{d}x} \qquad \textbf{Equation 1.37}$$

becomes,

$$\frac{\partial\theta}{\partial x} = \frac{\partial}{\partial q}\left(E_y \frac{\partial\theta}{\partial q}\right) \qquad \textbf{Equation 1.38}$$

where q is the cumulative flow discharge, θ is the dosage of tracer, defined by the integral of $C(x, y, t)$ with respect to time, and E_y is the diffusion factor, defined as $E_y = uh^2 D_y \Psi$, where U is the cross-sectional averaged velocity and Ψ is a dimensionless shape-velocity factor; defined as:

$$\Psi = \frac{1}{Q}\int_0^Q h^2 U dq \qquad \textbf{Equation 1.39}$$

where Q is the total discharge. Normalisation of θ and q transforms Equation 1.38 into

$$\frac{\partial S}{\partial x} = \frac{E_y}{Q^2}\frac{\partial^2 S}{\partial \Lambda^2} \qquad \textbf{Equation 1.40}$$

where $\Lambda \equiv q/Q$; $S \equiv \theta/\Theta$; with Θ equivalent to the integral of the dosage θ with respect to Λ. The transformation conducted to obtain Equation 1.40 maintains a fixed partial discharge of q to a particular streamline and effectively modelled a meandering channel as straight – since the coordinate system translates across the lateral reach depending on the flow.

Lateral measurements of tracer concentration were recorded at three downstream sites of varying sinuosity. A routing procedure was applied to provide a stronger fit for the observed lateral distribution in concentration; where Equation 1.40 was evaluated for E_y to give;

$$E_y = \frac{Q^2}{2}\frac{d\sigma_\eta^2}{dx}\frac{1}{[1-(1-\Lambda_0)S_1-\Lambda_0 S_0]} \qquad \textbf{Equation 1.41}$$

where Λ_0 is the centroid of the S-Λ distribution (S_0, S_1 are normalised dosages at the left and right bank).

The routing procedure calculated an optimal value of D_y by finding the best-fit downstream concentration profile using the upstream observations. The procedure then varied the input parameters, namely E_y and Λ in this case, to acquire a profile fit which best matched the observed profile. The transverse mixing coefficients using the stream-tube approximation were compared to the method of moment. The Authors report success using the routing technique when compared to the method of moments approach. Values of $D_y/hu^* = 0.24$-0.85 were reported and were in agreement, in magnitude, with those calculated using the method of moments.

The optimisation of D_y using a routing procedure is potentially applicable to vegetated flows where similar detailed lateral concentration distributions can be measured at multiple transverse locations. However, the approach provided by Seo et al. (2006) does not take account of the effects of spatially variable mixing coefficients and is, therefore, not applicable to heterogeneous flow fields.

Kay (1987) provided an analytical description of the two-dimensional concentration distribution associated with a compound channel system with laterally varying transverse mixing coefficient, $D_y(y)$. Mixing associated with a lateral-depth discontinuity and gradient were modelled by analytically solving the two-dimensional ADE equation for spatially variable velocity and mixing fields;

$$\frac{\partial}{\partial x}\left(hU(y)C(x,y)\right) - \frac{\partial}{\partial y}\left(hD_y(y)\frac{\partial C(y)}{\partial y}\right) = M\delta(x)\delta\left(y - y_0\right) \qquad \textbf{Equation 1.42}$$

where M is the mass of substance injected at a discrete location. The system was modelled under two scenarios. Firstly, a lateral discontinuity in channel depth was constructed with two distinct flow regions; where U_1 and U_2 are the depth-mean velocities in the deep flow and in the shallow flow, respectively (Figure 1.13a). The transverse mixing coefficients for the deep and shallow regions, D_1 and D_2, were input into the model and, after applying mass conservation across the discontinuity, Kay (1987) showed that regions of higher concentration are expected to persist for longer within the shallow region.

Secondly, a laterally sloping channel was constructed where $U(y)$ and $D_y(y)$ were related to the channel depth through the proportionalities $u \propto h^{1/2}$ and $D_y \propto h^{3/2}$ (Figure 1.13b). A graphical representation of the dimensionless concentration distribution from the sloping beach is given in Figure 1.14; where the colouring denotes concentration and $y = 0$ is the location of the steady injection point.

Kay's (1987) inclusion of U, D_y, $h = f(y)$ improved the description of the concentration distribution compared to the step case. The approach is a useful foundation for understanding and predicting mixing in regions of laterally variable velocity and transverse mixing; as the

analytical solution allows the downstream two-dimensional concentration distribution to be simulated for any input lateral profiles of U and D_y. The results do not, however, incorporate shear layer turbulence effects or secondary flows. Therefore, Kay's (1987) solution cannot be used to precisely quantifying mixing associated with vegetated shear layers – where $U \propto h^{1/2}$ and $D_y \propto h^{3/2}$. The applicability of the analytical solutions presented in Kay (1987) is revisited in the following section to evaluate a flux-gradient approach.

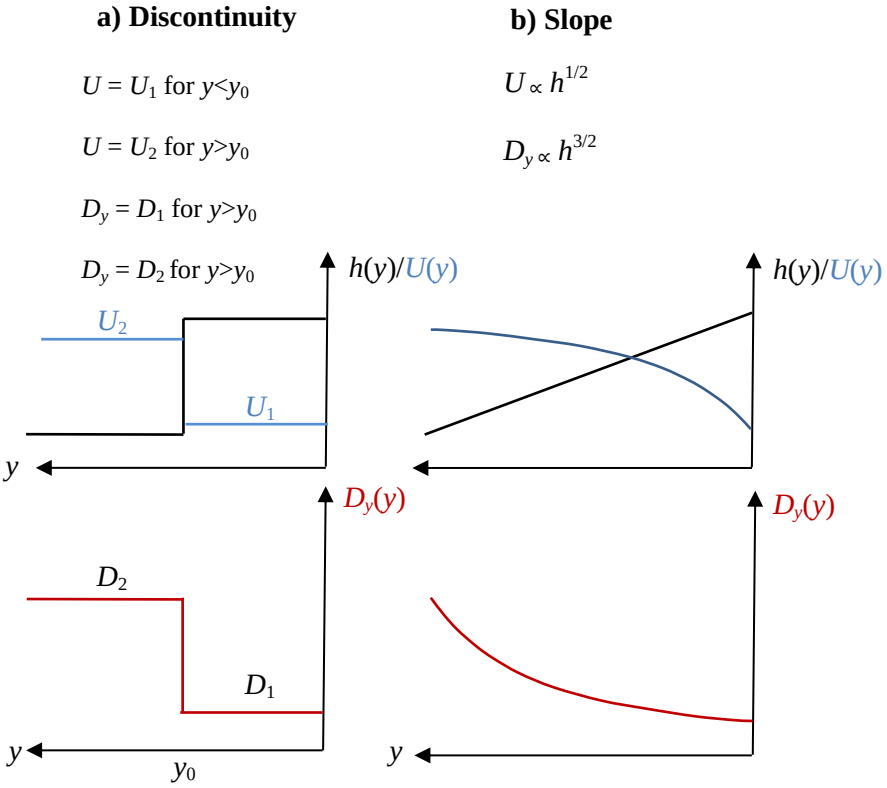

Figure 1.13: Transverse bed depth a) discontinuity and b) slope scenario used to model concentration distribution from a steady point source in Kay, 1987; depicting depth (black line), velocity (blue line) and transverse mixing coefficient (red line).

Despite the differences in hydrodynamic scale between ponds and large fluvial channels, the studies of Seo et al. (2006) and Kay (1987) provide valuable experimental and analytical techniques applicable when quantifying mixing in vegetated shear layers and other non-uniform flow fields. The routing procedure provided by Seo et al. (2006) gives an example of mixing coefficient optimisation; while Kay's (1987) analytical solution and velocity field formulation is analogous to shear layer vegetation and may be used in the velocity description defined by White and Nepf (2008) to construct a model of shear layer mixing.

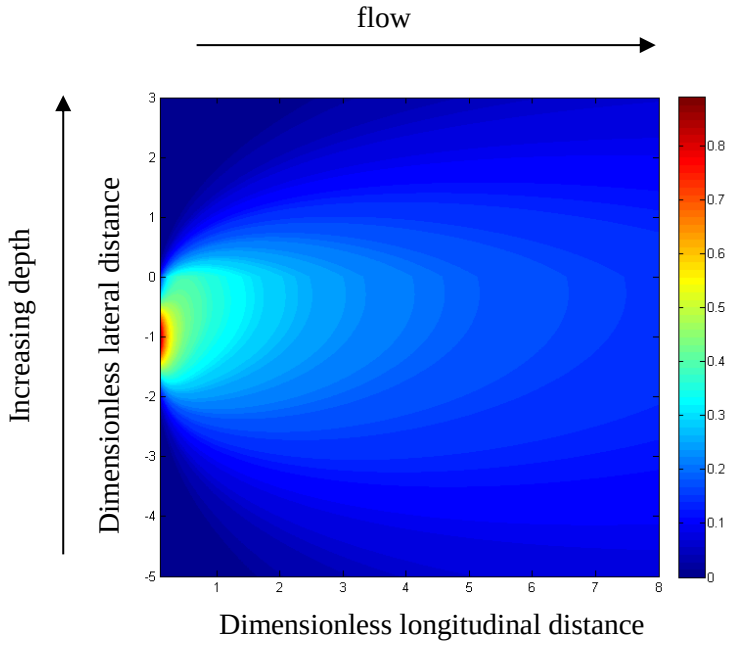

Figure 1.14: Graphical representation of dimensionless concentration distribution from a steady source at a laterally sloping compound channel. Kay, 1987.

1.3.2 Mixing in aquatic vegetation

This sub-section reviews mixing in vegetated flows. In similarity with the mean velocity field, the rate of solute mixing is dependent on the vegetation geometry and morphology. In full vegetation, mixing is dominated by the mechanical action of the stem wakes and the effects of bed shear are negligible. However, in shear layer vegetation, mixing is dominated by the large-scale interfacial coherent vortices (Murphy et al., 2007; Ghisalberti and Nepf, 2005).

Nepf et al. (1997) developed a random walk model to describe the enhanced turbulence caused by the mechanical action of stem wakes in artificial, emergent, laboratory vegetation – using a scanning laser light sheet and video image analysis assume that the tracer concentration was linearly proportional to the fluorescent intensity at a particular point. This assumption does not take into account the attenuation of laser light by the tracer and is a potential shortcoming of the experimental accuracy. The model described the Fickian diffusion of solute flow paths around vegetation stems and the effect of flow tortuosity and the lateral concentration distribution was statistically described using a Gaussian distribution.

Huang et al. (2008) investigated the mixing characteristics of shallow real emergent everglade vegetation. The study site was populated with a variety of aquatic plants species with a range of stem densities, where N = 2200, 92, 20, 16, 12, and 8 stems/m^2 and $2.1 < U < 3.8$ cm/s for *Elocharis elongate*, *Cladium jamaicense*, *Eleocharis cellulose*, *Sagittaria lancifolia*, *Bacopa carolinia*, and *Panicum hemitomon*, respectively (see Appendix I for species identification). Trace particle injection was made using a horizontal line source of latex microspheres to eliminate the apparent effects of transverse mixing. The ADE equation was employed to model the continuous injection of the spheres;

$$\frac{\partial C}{\partial t} = U\frac{\partial C}{\partial x} + D_x\frac{\partial^2 C}{\partial x^2} + \frac{\partial}{\partial z}\left(D_z\frac{\partial C}{\partial z}\right) - \lambda_c C \qquad \textbf{Equation 1.43}$$

where λ_c is the rate of particle capture or deposition coefficient. A finite element method was then used to solve Equation 1.43 to model the downstream concentration profiles. Figure 1.15 shows the comparison between measured and predicted concentrations with time for a range of injection and sampling depths. The parameters D_x, D_z, and λ were optimised by minimising the sum-of-squared differences between observations and predictions. Longitudinal mixing coefficients were reported between 0.21 cm^2/s (R^2 = 0.953) and 48.5 cm^2/s (R^2 = 0.926).

Huang et al. (2008) successfully capture the plateau concentration of the profiles but do not accurately describe the arrival and decent concentration trend; although, the modelled profiles remain above a goodness of fit of $R^2 > 0.89$. Huang et al. (2008) attempted to analytically model the vertical profile of mean longitudinal velocity using depth-wise measurements of the frontal area per unit volume, $a(z)$, (c.f. Lightbody and Nepf, 2006b) in combination with a wake zone formulation described by Nepf (2004). Huang et al. (2008) do not report total success in their overall predictions; with values of D_x differing by an order of magnitude between those calculated and predicted. The underestimation of the mixing coefficient was partially attributed to non-idealized plant morphologies that lead to heterogeneity in plant shape with depth. This has the potential to increase longitudinal mixing both through wake scale processes and by increasing the velocity shear. Measurement error is not provided

limiting the extent to which one may criticise the modelling technique. Furthermore, the density of measurements over a 2000 second timescale (Figure 1.15) does not necessarily provide sufficient temporal resolution. However, such an experiment provides field values of velocity and mixing coefficients.

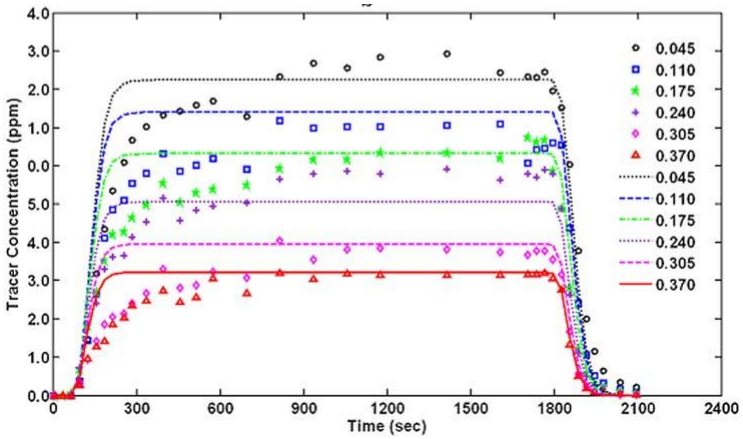

Figure 1.15: Measured (symbols) and predicted (lines) concentration profiles in everglade vegetation. The key refers to the sampling extraction depth in meters. Huang et al., 2008.

There is a paucity of research characterising mixing in real vegetated flows under the control of laboratory experimentation. Field studies in real vegetated environments provide useful flow parameterisation, but are not as reproducible or reliable as laboratory conditions; which permit the controlled adjustment of variables – such as velocity and flow depth – and allow for the elimination of external variables, such as wind shear.

Nepf (1999) employed a continuous tracer to quantify transverse mixing in with both field (smooth Cordgrass, *Spartina alterniflora*) and laboratory (artificial cylinders) experiments. Nepf (1999) attempted to account for the relatively high transverse mixing in emergent real vegetation, despite the low Reynolds numbers ($Re_d < 200$), using a theoretical description of mechanical diffusion (e.g. Nepf et al., 1997). Fundamental to the formulation was that the turbulent budget becomes a balance between wake production and viscous dissipation (see Nepf et al., 1997). Secondly, it was assumed that the characteristic length scale of turbulence was set by the vegetation geometry; i.e. stem diameter, *d*. The turbulent kinetic energy per unit volume *k* was related to the vegetation characteristics through;

$$\frac{\sqrt{k}}{U} = \alpha_1 (\overline{C_D} ad)^{1/3} \qquad \textbf{Equation 1.44}$$

where α_1 is a scale coefficient.

The net transverse mixing was modelled as a summation of turbulent diffusion and mechanical diffusion (Figure 1.16); where the turbulent diffusion is linked to the stem characteristics through Equation 1.44. Mechanical diffusion is determined by the "…variability in the flow paths imposed by the tortuosity of the pore spaces…" (Nepf, 1999) and was modelled statistically as a series of collisions with the stems – where the final position of particles (or tracer) from their original point can be described using a Gaussian distribution. As such, mechanical diffusion scales with the vegetation density, *ad* and thus, total transverse mixing was shown to be described through,

$$\frac{D_y}{Ud} = \alpha_1 (\overline{C_D} ad)^{1/3} + \left(\frac{\beta^2}{2}\right) ad \qquad \textbf{Equation 1.45}$$

where β is a scale factor related to the distance a particle travels in a unit time Δt and the first and second terms represent the contributions from turbulent and mechanical diffusion, respectively.

Tracer injections in a laboratory array of emergent randomly distributed cylinders were visualised with a horizontal light sheet and video imaging. The array density ranged from N = 200-2000 stems/m^2 and $Re_d > 200$. In the region $\mathrm{Re}_d < 200$, the viscous drag becomes dominant and the assumption of a balance between wake production and viscous dissipation becomes invalid (e.g. Equation 1.44). Mean vegetation drag, velocity, turbulent intensity and transverse mixing were measured for a range of flow conditions. The laboratory investigations show that the bulk drag coefficient, C_D, decreases with increasing array density, *ad* (e.g. Tanino and Nepf, 2008b). A Gaussian functions fitted the steady-state concentration distributions to yield values of D_y.

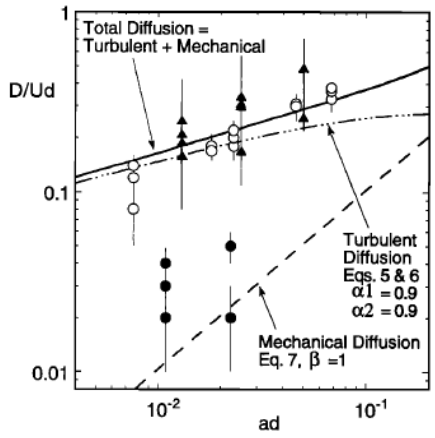

Figure 1.16: Laboratory observations of D_y for emergent vegetation for Re_d=400-2000 (open circles) and Re_d=60-90 (solid circles), fitted to model curves for mechanical (dashed lines) and turbulent (dashed-dotted line) diffusion (e.g. Equation 1.45). Marsh field study data, Re_d = 300-600, is given by the solid triangles. The sum of both diffusion processes is given as a solid black line. Nepf, 1999.

Complementary field experiments using a continuous Rhodamine dye injection were used to calculate D_y in real emergent salt marsh vegetation, *Spartina alterniflora*. Stem Reynolds number, Re_d, in the field ranged from 200-600, for U = 3.0-7.4 cm/s, and N = 96, 196, and 370 stems/m^2. Figure 1.16 shows how the contribution to total transverse mixing from mechanical and turbulent diffusion changes for different vegetation densities. The figure aggregates the transverse mixing results from the laboratory and field studies. Despite successful model predictions of turbulent intensity, drag and mixing, the study fails to make any comment or suggestions regarding the transverse mixing in emergent vegetation where Re_d is less than 200. Moreover, real shear layer conditions were not investigated.

Serra et al. (2004) constructed a model of randomly distributed emergent vegetation to simulate a known field site and fluorescent tracer injections were conducted and the lateral concentration distributions were recorded using laser fluorescence and camera visualisation. Serra et al. (2004) quantified the spatially homogeneous transverse mixing coefficient by fitting a Gaussian distribution to the stead-state, mean lateral concentration distributions downstream of a continuous tracer injection point. Channel flow was adjusted such that U = 0.1 - 1.0 cm/s and Re_d = 10 - 100. Transverse mixing coefficients were reported between 0.05 m^2/s, for Re_d = 10 (Φ = 0.2), and 0.32 m^2/s, for Re_d = 80 (Φ = 0.2). Serra et al. (2004) reported a discrepancy between their measured transverse mixing coefficients and those

provided by Nepf (1999). The discrepancy was attributed to the differences in solid volume fraction between the two experiments and the potential impact on the wake shedding from the vegetation elements.

Serra et al. (2004) provided valuable experimental techniques for observing mixing in full vegetated systems. However, a number of limitations in the experimental accuracy are apparent. Despite the employment of a laser fluorescence and camera visualisation system, the reported lateral concentration resolution (approximately 40 data points), particularly in the regions of maximum concentration gradient, may limit the reliability in the calculation of D_y. Secondly, the fitted Gaussian distribution used to calculated D_y does not show a strong fit in matching the concentration gradient – limiting precision.

Shucksmith et al. (2010) also investigated longitudinal mixing in a controlled laboratory channel using emergent and submerged real vegetation. They sought to elucidate the effects of species, age and submergence on the total longitudinal mixing using *Carex* and *Phragmites australis* (common reeds, Appendix I). The vegetation was cultivated *in situ* and, as such, did not represent true natural growth. In the emergent scenario it was found that vegetation caused a reduction in shear dispersion thus reducing longitudinal mixing when compared to the bare channel. The change in D_x in the *Carex* vegetated system (Figure 1.17a) was un-noticeable with plant age whereas D_x reduced with age in the *Reed* system as the plant density increased. In the submerged case, it was shown that the degree of longitudinal mixing was dependent on the submergence ratio as this variable leads to a longitudinal velocity differential between the open channel and wake zones. No relationships were found when scaling the emergent conditions to the parameters Uh, u^*h and the spatial average Reynolds stress. Values of D_x/hu^*_i were observed to decrease with plant age and therefore, vegetation resistance (see Shucksmith et al., 2010 – Fig. 10b).

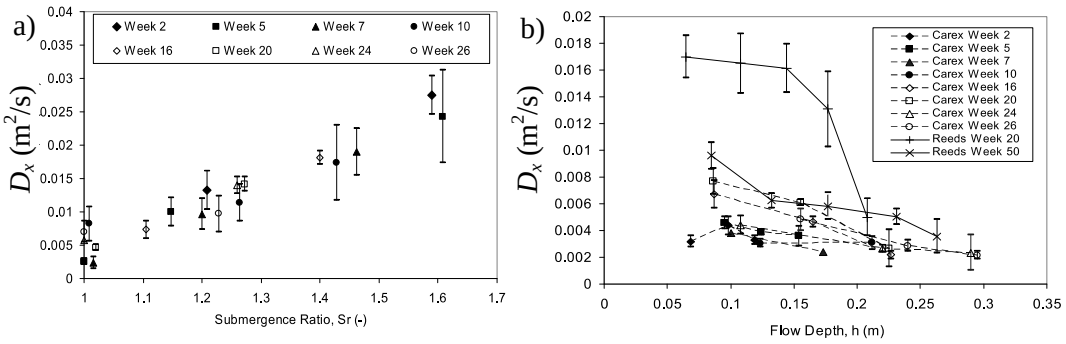

Figure 1.17: Longitudinal mixing coefficient measured during the vegetation growth for a) *Carex* with submergence ratio, *W/h*, and b) *Carex* and Reeds (*Phragmitis australis*) with depth. Shucksmith et al., 2010.

Lightbody and Nepf (2006b) used a continuous dye injection source (see Nepf, 1999) in order to calculate the vertical mixing coefficient in emergent salt marsh vegetation, *Spartina alterniflora*. The Authors compared the results of a numerical discussed by Lightbody and Nepf (2006a) to measurements. It should be noted that tracer field measurements employed a submersible fluorometer where the probe was passed directly through the tracer plume – potentially leading to unwanted mixing.

The triple integral equation predicting the depth average longitudinal mixing coefficient from the vertical profile of temporal mean stream-wise velocity, $U(z)$, first proposed by Fischer et al. (1979, pp. 94, Eq. 4.48), was modified with the consideration that the vertical mixing coefficient, D_z, can be described as a function of the stem density and drag; $D_z = {}_1(C_D ad)^{1/3} Ud$, e.g. Nepf (1999). A key assumption was that, for $Re_d < 10{,}000$, the drag coefficient is not a strong function of stem density or Reynolds number and is constant with depth. Total longitudinal mixing was considered as a summation of the mechanical dispersion (D_m) and depth shear dispersion (D_h). In the Fickian limit, the mechanical dispersion was approximated as;

$$D_m = \frac{1}{2} C_D^{3/2} ud \qquad \textbf{Equation 1.46}$$

When combined with the depth-shear dispersion, the total longitudinal mixing, in the near field, as a function of the canopy characteristics C_D, a and d was presented as,

$$\frac{D_x}{U_r d} = \left(\frac{D_z}{U_r d}\right)\left[\left(\frac{\partial}{\partial z}\sqrt{\frac{C_{D,r}a_r}{C_D a}}\right)\right]^2 x^2 + C_D^{3/2} \qquad \textbf{Equation 1.47}$$

where r, U_r, a_r, are the depth, temporal mean longitudinal velocity and frontal area per unit volume at the injection point, respectively; and the second term represents the mixing at the stem-scale (see Lightbody and Nepf, 2006b, p. 219-221 for full derivation). Continuous tracer release through a horizontally orientated needle allowed for the vertical diffusivity to be estimated. Flow velocity was recorded between 1 - 6 cm/s; although values of 24 cm/s occurred during tidal events. Instantaneous tracer release and an increase in variance method was used to calculate the longitudinal mixing coefficient.

The vertical diffusivity was predicted within error of the observations. Figure 1.18 shows the comparison between observed and predicted longitudinal mixing coefficients for the saltmarsh field experiment – where the two series having a correlation of $R^2 = 0.59$. The large error bars demonstrate the models limitations, especially at larger values of D_x, and are attributed to uncertainty in the stem diameter and D_z. It was found that $D_x = 4 – 27$ cm^2/s for U = 1-28 cm/s and that D_x/Uh = 0.8, 17 and 9 for *Atriplex porlutiodes*, *Alisma graminium* and *Spartina alterniflora*. It is stated that the over prediction of D_x may be attributed to the lack of consideration for non-vertical components of stem morphology – potential horizontal stem components may enhance lateral mixing thus reducing the observed value of D_x compared to the predictions. The Authors demonstrate the applicability of using the vertical variation in the frontal area per unit volume in predicting vertical velocity profiles in real vegetation. However, the large error associated the calculated and predicted values of D_x indicate that the precise characterisation of the vegetation morphology and drag coefficient is fundamental for accurate predictions of mixing.

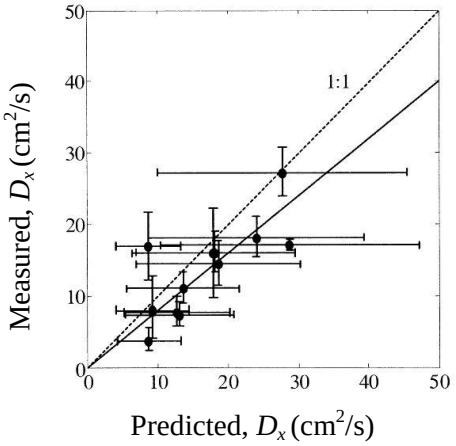

Figure 1.18: Predicted Longitudinal Mixing Coefficients (Equation 1.47) are compared to observed values in emergent Saltmarsh. Lightbody and Nepf, 2006b.

Lightbody and Nepf (2006b) and Tanino and Nepf (2008b) state that the dominant component of D_x in emergent vegetation is that caused by turbulent diffusion (for $\Phi < 0.1$) and scales with the stem diameter and U through:

$$D_x = 0.2Ud \qquad \textbf{Equation 1.48}$$

In the dense vegetation, when the stem spacing is less than the stem width, $s < d$, the turbulent diffusion dominance reduces and when the solid volume fraction increases above 0.1, mixing due to vertical heterogeneity in the velocity profile becomes more important (Nepf, 2012).

Tanino and Nepf (2008) reassessed the linear contribution of mechanical and turbulent diffusion (e.g. Nepf, 1999) for randomly distributed emergent vegetation. A key criterion was that the size of turbulent eddies greater than or equal to the length scale of the stem diameter contribute significantly to transverse mixing. An expression for D_y defined by the random array's parameters was derived giving:

$$\frac{D_y}{Ud} = \gamma_1 \frac{4}{\pi} \Phi \left\langle \frac{\sqrt{k_t}}{\langle \bar{u} \rangle} \right\rangle P_{S_{nc}<r^*} \frac{\langle s_n^2 \rangle_{s_{nc}<r^*}}{d^2} + \gamma_2 P_{s_{nc}<5d} \frac{\pi}{4096} \left(\frac{d^2}{k_p} \right)^{3/2} \frac{1-\Phi}{\Phi^2} \qquad \textbf{Equation 1.49}$$

where k_t is the turbulent kinetic energy per unit mass; r^* is the minimum distance between cylinder centers that permits the pore space constrained by them to contain eddies of the length scale $O(d)$; s_{nc} is the center-center distance to the nearest element neighbour with $s_n = s_{nc} + d$ where s_n is the surface-to-surface distance; γ_1 and γ_2 are scaling constants; k_p is the permeability; and $P_{Snc<r^*}$ and $P_{Snc<5d}$ are the fractions of cylinders with a nearest neighbour

farther than r^* and $5d$, respectively. The distance $5d$ is taken as the maximum centre-to-centre distance over which cylinder-cylinder interaction takes place (see Appendix in Tanino and Nepf, 2008b).

Two-dimensional velocimetry and laser induced fluorometry was conducted to determine the dependence of D_y on Φ, for $\Phi = 0.01$-0.35. Longitudinal and transverse velocity was measured simultaneously; while Rhodamine WT was illuminated using a laser light sheet downstream of a continuous injection, and the concentration was inferred from greyscale resolutions using a video camera (Figure 1.19a).

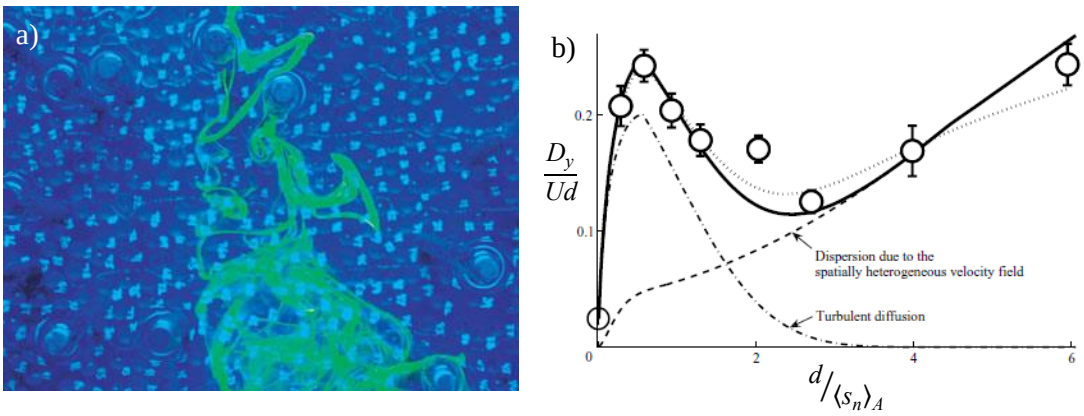

Figure 1.19: a) Random emergent cylinder flow visualization shown for $\Phi = 0.010$, $Re_d = 880 \pm 40$. b) Normalised D_y is compared to theoretical predictions; where Equation 1.49 (solid line) is compared to the linear superposition (dotted) of the turbulent diffusion (dotted-dashed) and shear dispersion (dashed) proposed by Nepf (1999). Tanino and Nepf, 2008b.

The transverse mixing coefficient was then calculated using $D_y/Ud = (1/2d)\mathrm{d}\sigma^2/\mathrm{d}x$. Figure 1.19b shows the comparison between the observed transverse mixing coefficients and those predicted using Equation 1.49. Three mixing regimes were identified. Firstly, D_y increases rapidly as the ratio if the stem diameter to mean spacing, $d/\langle s_n \rangle_A$, (0 to 0.5) increases (for $\Phi = 0$ to $\Phi = 0.031$). Secondly, D_y decreases in the intermediate zone (from $\Phi = 0.031$ to $\Phi = 0.2$). Finally a slower increase in D_y was observed as Φ exceeds 0.20. This non-linear trend between D_y and Φ were attributed to the relative contributions from turbulent diffusion and shear dispersion and were successfully predicted using the linear combination proposed in Equation 1.49. Despite the predictive success of the model, the approach relies on a detailed knowledge of the vegetation distribution and mean steam diameter. These parameters are

harder to define in real, heterogeneous vegetation and justify the requirement for experimentation using live vegetation.

There are potential experimental limitations to the methodological approach in Tanino and Nepf (2008b). Firstly, the visual matching of tracer injection velocity to local velocity is inaccurate and demands greater precision to attain reliability. Secondly, potential laser power reduction due to attenuation from the water or Rhodamine tracer is not mentioned. Spatial reduction of laser power along the beam length may result in inaccurate concentration profile, reducing the precision in calculating D_y.

In shear layer emergent vegetation Zong and Nepf (2010) described the turbulent diffusivity in the outer patch region using:

$$D_{to} = \beta \Delta U t_{ml} \qquad \textbf{Equation 1.50}$$

where β is an empirical constant (O = 0.02) for rigid vegetation of solid volume fractions of 0.01 - 0.04 (Ghisalberti and Nepf, 2005). Note that Patil and Singh (2011) found that β = 0.013. The corresponding transverse mixing coefficient in the inner patch region – where KH-vortices do not penetrate – is similar to Equation 1.50:

$$D_v = 0.17 U_1 d \qquad \textbf{Equation 1.51}$$

Murphy et al. (2007) attempted to model the longitudinal mixing coefficient in partial vegetation consisting of rigid cylinders. The *N*-zonal model proposed by Chickwendu (1986) was adapted into that of two zones – representing the vegetation and open channel – to give:

$$D_x = \frac{\left(\frac{h}{W}\right)^2 \left(\frac{W\text{-}h}{W}\right)^2 (U_2\text{-}U_1)^2}{\varepsilon_z} + \left(\frac{h}{W}\right) D_{xv} + \left(\frac{W\text{-}h}{W}\right) D_{xo} \qquad \textbf{Equation 1.52}$$

where h is the vegetation height, W, ε_z is a vertical exchange coefficient between zones and D_{xv} and D_{xo} are the longitudinal mixing coefficients for the vegetated and open-channel zones, respectively. The first term in Equation 1.52 represents the exchange between the relatively fast zone and the slow zone. The second and third terms represent the longitudinal mixing in the canopy and free-flow, respectively. Murphy et al. (2007) built on the concepts of turbulent exchange and diffusion exchange to develop two conditions describing the vertical exchange

coefficient, ε_z. Firstly, under turbulent exchange, ε_z may be approximated as $\Delta U/40h$; and secondly, for diffusion limited exchange, ε_z is limited by wake zone diffusivity (Ghisalberti and Nepf, 2005) such that $\varepsilon_z = D_w/h^2$; where D_w is the wake zone mixing coefficient given by $D_w = 0.17Ud$.

Tracer tests were conducted in a laboratory channel made up of submerged solid cylinders for ad = 0.015 and 0.048 and U_1 = 0.7 - 9.9 cm/s and U_2 =1.6 - 18.7 cm/s. Depth-averaged Rhodamine concentration was measured using a pulley system that recorded at a higher rate than that of the passage of dye and the method of moments was employed to calculate the depth mean D_x. Satisfactory prediction (R^2 = 0.89) of the depth-average longitudinal mixing coefficients were made using Equation 1.52. The depth-average D_x was observed in the range 50 – 450 cm^2/s. It was shown that, as the submergence ratio approaches 2.7, the shear dispersion in the open flow becomes dominant over that of the exchange zone. For $W/h < 3$ the inefficient exchange within the upper canopy dominates the total mixing. Further, in sparse vegetation, mixing is dominated by vortex exchange as less momentum is lost to the canopy and therefore the vortex penetration is greater. Finally, in dense canopies, vortex momentum is lost to the canopy leading to shallower penetration and therefore, stem-scale turbulent exchange dominates.

In vegetated shear layers, mass exchange between the vegetation and the free flow is controlled by the shear layer vortices. Ghisalberti and Nepf (2005) use image analysis to measure vertical steady-state concentration distributions from a trace injection made at the vegetation interface. The steady state vertical profiles of concentration for the six downstream locations are given in Figure 1.20a. Ghisalberti and Nepf (2005) found that the exchange between the canopy and the free flow increased in the more dense cases – since the denser canopies generated vortices with a greater rotational speed leading to more rapid canopy flushing; where the exchange velocity is proportional to the velocity shear, ΔU. The Authors evaluated a two-box model and a flux-gradient approach in describing the results presented by Ghisalberti and Nepf (2004) (see section 1.3).

The Authors state that the use of a constant exchange velocity and therefore, a two box model (such as Murphy et al., 2007) is valid when the exchange zone encompasses a large proportion (70-90%) of the entire canopy – since a uniform concentration can be achieved relatively quickly across the canopy. However, as the canopy density increases, vortex penetration reduces as does the rate of renewal. As such, the spatially variable advection diffusion equation (Equation 1.17) was discretised to provide a "flux gradient model" vertical variation in vertical mixing coefficient, $D_z(z)$;

$$D_z(z)=\frac{\Delta\left(\int_0^z U(z)C(z)\mathrm{d}z\right)}{\langle\partial C/\partial z\rangle_z \Delta x} \qquad \textbf{Equation 1.53}$$

where $\Delta x = x_B - x_A$. Values of $D_z(z)$ were calculated by considering mass balance between adjacent downstream locations e.g. the depth integrated mass at location *A* is equal to the sum of the depth integrated mass at location *B* and the net flux. Figure 1.20b shows the collapse of D_z for different densities when normalised by $\Delta U t_{ml}$.

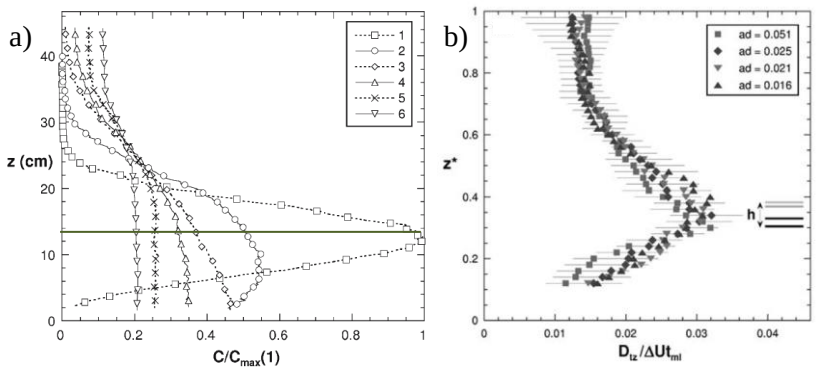

Figure 1.20: a) Vertical profiles of steady-state concentration measured in shear layer vegetation for increasing downstream distance, x = 19, 54, 92, 150, 250 and 380 cm. Vegetation height is given by the green line. b) Vertical profiles of vertical mixing coefficient for different vegetation densities, *ad*, by Ghisalberti and Nepf, 2005.

The model provides a useful descriptive form of lateral mixing associated with vegetated shear layers. Ghisalberti and Nepf state that, the peak later turbulent diffusion coefficient, or mixing coefficient, D_{peak}, is related to $\Delta U t_{ml}$ through:

$$D_{peak}=0.032\Delta U t_{ml} \qquad \textbf{Equation 1.54}$$

Okamoto et al. (2012) also quantified $D_z(z)$ in shear layer of cylinders by employing instantaneous, simultaneous measurements of velocity fluctuations and concentration field. Turbulent diffusion was evaluated using a quadrant conditional analysis where a similar form

for $D_z(z)$ as Ghisalberti and Nepf (2005) was observed (Figure 1.21). Like Ghisalberti and Nepf (2004, 2005), Okamoto et al. (2012) do not extend their shear layer analysis to real vegetation. Further, the analytical methods (flux gradient model and quadrant analysis, respectively) do not compute a value of D_z at a given location assuming that the measurements at the point are correct. The following chapter evaluates the application of the flux-gradient model. It will be shown in the Analysis Chapter that a finite difference model reduces the uncertainty in D_z by performing an optimised routing procedure.

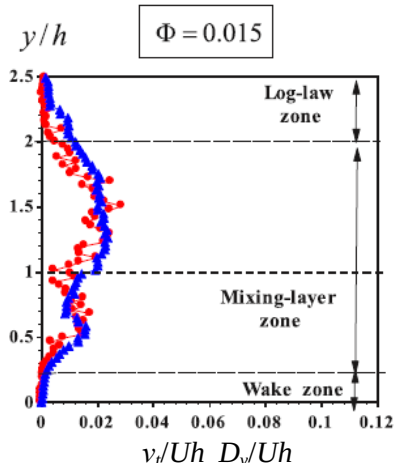

Figure 1.21: Vertical profiles of vertical mixing coefficient (red circles) and eddy diffusivity (blue triangles) measured in submerged cylinders by Okamoto et al., 2012.

1.4 Conclusions

Velocity and drag has been well characterised for fully-vegetated wetland environments (Nepf, 1997; Lightbody and Nepf, 2006a; Shucksmith et al., 2010 & 2011a; Tanino and Nepf, 2008a)); and some research has focused on using plant morphology for predicting velocity fields (e.g. Lightbody and Nepf, 2006a; Shucksmith et al., 2011b). Longitudinal mixing and the bulk effects of the shear layer on retention times have been investigated for artificial vegetation (e.g. Murphy et al., 2007; Nepf et al., 2007) ; while some Authors have attempted to shed light on the spatial variability in the lateral mixing in homogeneous, artificial vegetation (Ghisalberti and Nepf, 2005; and more recently, Okamoto et al., 2012).

However, spatially variable mixing is poorly quantified for real vegetation. There is a paucity of information regarding the changes during plant growth; where Shucksmith et al., (2010 & 2011) provided measurements of longitudinal mixing only for vegetation grown in the laboratory and Nepf (1999) provided field data only. The lateral mixing at the vegetation/open-channel interface – such as the perimeter of ponds or patches of vegetation – is poorly reported in the literature; particularly for spatially heterogeneous morphologies associated with real vegetation. This leaves a lack of understanding about the exchange of contamination between the open channel and the vegetated regions – key in predicting and improving the efficacy of pond treatment systems. There is a paucity of characterisation of velocity and mixing using naturally cultivated vegetation using controlled laboratory experimentation. Moreover, the shear layer environment in real vegetation has not been compared to theoretical understandings developed in artificial vegetation (e.g. Ghisalberti and Nepf, 2005; Okamoto et al., 2012).

Research proposal

The aims of this research were to improve the flow dynamics and mixing across real, emergent vegetation shear layers. A desire was to characterise and quantify the form of transverse mixing over the seasonal growth of real vegetation – namely *typha latifolia* (or cattail reeds) – providing accessible information for practitioners. Secondly, the accepted theoretical consensus regarding vegetated shear layers developed under idealized, artificial vegetation was applied and compared to real vegetation with similar density and morphology. Finally, the novel application of a finite difference model and optimised routing technique was evaluated for artificial and real shears layers – providing scaling for mixing in real vegetation.

2. Methodology

2.1.1 Introduction

This chapter describes the techniques employed to quantify the mixing in shear layer emergent vegetation. Section 2.2 describes the laboratory system. Section 2.3 details the experimental operations for the artificial vegetation while Section 2.4 and 2.5 detail the velocity measurements and Rhodamine tracing, respectively. Section 2.6 provides the equivalent experimental setup for the real vegetation including a detailed description of characterising the real vegetation (see Appendix III) and challenges when employing ultrasound velocimetry. Finally, section 2.7 provides a summary of the experimental test conditions.

Difficulties and shortcomings in the measurement techniques were encountered during the data collection. As such, the experimental methods describe a development in the entire procedure with notable methodological differences between some of the vegetated cases.

Quantifying spatial variations in transverse mixing for partially vegetated emergent vegetation was achieved using Rhodamine dye tracing in combination with ultra-sound velocity measurements. As shown in the Literature Review, dye tracing and velocity measurements are common methods for elucidating the hydrodynamic characteristics of vegetated flows. Four vegetation types were investigated: high density and low density artificial vegetation and naturally cultivated *typha* harvested in winter and spring to compare real vegetation at the extremes of growth. The following nomenclature is employed to distinguish between experimental sets, types and trials:

- ***Scenario*** –describes the vegetation configuration only i.e. full vegetation, partial vegetation or open bare channel; e.g. 'The full vegetation scenario' encompasses all tests conducted with vegetation covering the full width of the channel.
- ***Type*** – describes the specific type of vegetation that was employed e.g. high density artificial.
- ***Case*** – describes the specific discharge for a given test e.g. 1.00 l/s.
- ***Test*** – describes an individual experimental run. In the full vegetation scenario, ten repeat tests were conducted in order to obtain average hydraulic characteristics; 'test 1' would therefore specify the first trace test conducted for the specific scenario, type and case.

Three channel scenarios were investigated:

- Bare channel
- Full vegetation
- Partial vegetation

A range of discharges was preselected in order to produce the suitable temporal mean longitudinal velocities that have previously been observed in operational treatment ponds and wetlands (e.g. Nepf, 1999; Lightbody and Nepf, 2006a; Lightbody et al., 2008; see Literature Chapter). Note that the bare channel and full vegetation scenarios were employed to quantify the transverse mixing in approximately spatially uniform flows required for the mixing analysis of shear layer (discussed further in the Analysis Chapter).

2.2 The laboratory System

The controlled laboratory tests were conducted at the School of Engineering, University of Warwick, UK. A 24 m long, recirculating horizontal flume was employed to simulate typical flow conditions found in pond environments. Figure 2.1 shows a side view of the installation.

The flat flume was 0.99 m wide and could be filled to a maximum flow depth of 0.60 m and was manufactured from smooth, opaque Perspex. Channel discharge was maintained with a hydraulic pump – controlled with a manual valve – that fed water from a reservoir directly into the channel inlet before a set of flow expander. The inlet flow passed through two sets of flow straighteners after the settling basin (Figure 2.1); an aluminium sheet, 0.20 m downstream of the inlet, with an array of holes (diameter = 0.05 m) and a dense array of horizontal tubes, 0.05 m in diameter and 0.05 m in length, 0.5 m from the aluminium sheet.

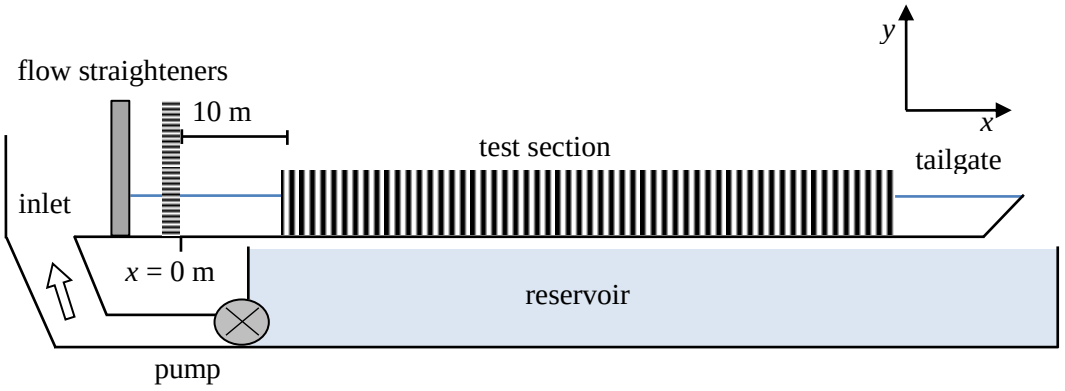

Figure 2.1: Side view of the horizontal laboratory flume.

The reservoir had a maximum capacity of approximately 18,000 litres; however, frequent reservoir renewal was necessary as the flume operating volume was almost a third of the total combined volume (flume and reservoir) and the background tracer concentration quickly increased to an unacceptable level during testing.

Flow discharge could be varied between 0.50 to 12.00 l/s and was measured using an *in situ* electromagnetic flow-meter (Siemens SITRANS F M MAG 6000, Figure 2.2a). Care was taken to ensure that the channel discharge remained constant while the required flow depth was adjusted and the flow depth was controlled with a downstream tail-gate located at the channel outlet. Precise measurements of flow depth were made using a Vernier gauge accurate to 1×10^{-4} m (Figure 2.2b).

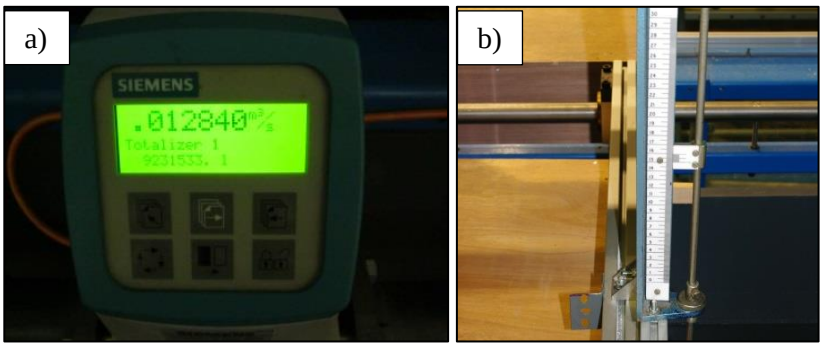

Figure 2.2: a) Image of Siemens electromagnetic flow-meter and b) Vernier gauge used to measure flow depth.

2.3 Artificial Vegetation Testing

An array of artificial vegetation was constructed using 200 mm long, 4 mm diameter plastic straws inserted into 0.6 m x 0.3 m Perspex boards, fixed to the channel bed from x = 10.0 m downstream of the second set of flow-straighteners. Two artificial vegetation types were employed: firstly, the *high density* type had a stem density, N, and frontal area per unit volume, a, of 1594 stems/m^2 and 0.064 cm^{-1}, respectively; while for the *low density* N = 398 stems/m^2 and a = 0.026 cm^{-1}. The vegetation solid volume fraction, Φ, is the total fractional space occupied by vegetation within the water column (Shucksmith et al., 2011), where;

$$\Phi = N\pi(d/2)^2 \qquad \textbf{Equation 2.1}$$

and was 0.02 and 0.005 for the high and low densities types, respectively. Such densities were chosen as they are representative of real vegetation those found ponds (Koskiaho, 2003; Nepf, 1999; Huang et al., 2008; Lightbody and Nepf, 2006a). Both types were aligned in the longitudinal direction and were staggered in the transverse direction (e.g. Figure 2.3a). The stems were separated by r = 0.025 m and 0.050 m in the x direction and l = 0.026 m and 0.052 m in the y direction for the high and low density types, respectively.

2.3.1 Full artificial vegetation

The full-vegetation configuration was employed to simulate a spatially uniform hydrodynamic environment that is characteristic within a patch of vegetation i.e. where the dominant source of turbulence is the stem wakes. This statement is a simplification of complex hydrodynamic phenomena but is used as a test case and starting point for quantifying mixing. The flow field and mixing properties of the full-vegetation configuration were considered spatially uniform across the channel – when averaged over the spacing between stems – and along the length of the test section. Spatially extensive measurements of hydraulic parameters were still measured to assess the validity of this statement. Figure 2.3b shows the configuration of the full artificial vegetation; the leading edge of the vegetation was located at x = 10 m and extended to x = 15.2 m.

Rhodamine tracer injections were made within the vegetation at the channel centreline, upstream of two observation locations, or "windows", installed 1.0 and 2.0 m downstream of the injection point, and 2.8 m and 3.8 m downstream of the vegetation leading edge. The windows were constructed such that the vegetation array maintained its correct geometry from one side of the window to the other; requiring only a single transverse line of stems to be removed. The observation windows also served as velocity measurement locations, where the absence of vegetation permitted the unattenuated propagation of ultrasound. The same range of discharges was used for both density types and the depth was maintained at 0.1500 m in order to isolate the hydrodynamic effects of a change vegetation density.

a) **Artificial vegetation geometry**

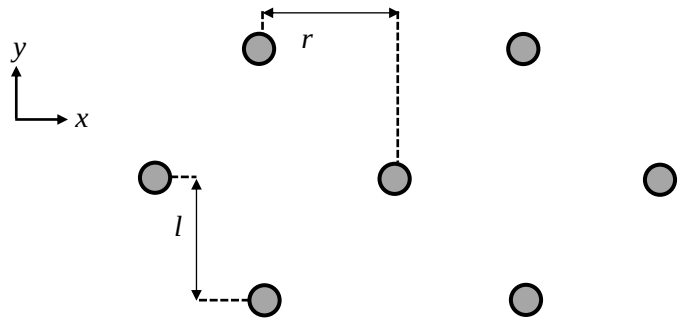

b) **Full vegetation schematic plan view**

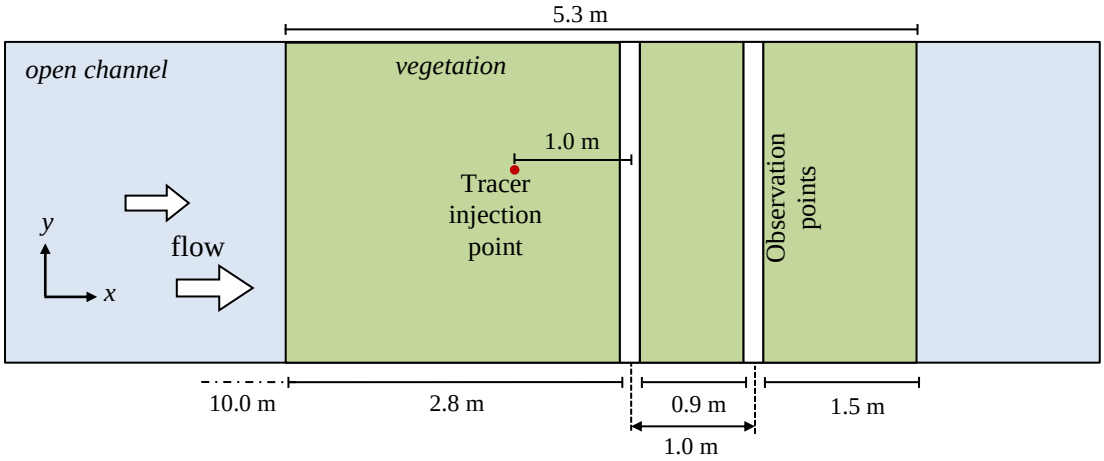

Figure 2.3: a) Artificial stem geometry and b) plan view of the full vegetation scenario.

2.3.2 Partial artificial vegetation

Figure 2.4a shows how the artificial stems were reassembled to form an emergent, partially vegetated array simulating a vegetated shear layer. The array was 7.50 m long and 0.60 m wide, positioned against the right-hand channel wall such that the vegetation and open channel occupied the regions $0 < y \leq 0.60$ m and $0.60 < y \leq 0.99$ m, respectively (Figure 2.4b). The array geometry was orientated in the same manner as described above in Figure 2.3a. Note that the channel walls were made of the same material as the vegetation boards and therefore had the same roughness coefficient.

The leading edge of the array was located at $x = 6.4$ m and sufficient vegetation was installed upstream of the tracer injection point such that the flow was uniform, i.e. $\partial/\partial x = 0$.

Rominger and Nepf (2011) discus, in depth, the effect of vegetation density and drag on the flow deviation associated with borders of porous obstructions (see Literature Review, section 1.2). Preliminary measurements of transverse profiles of temporal mean, longitudinal velocity, $U(y)$, at successive downstream locations confirmed that the flow became stable approximately 2.0 m downstream of the leading edge ensuring that the tracer and velocity measurements were in regions on stable flow.

a) **Partial vegetation laboratory example**

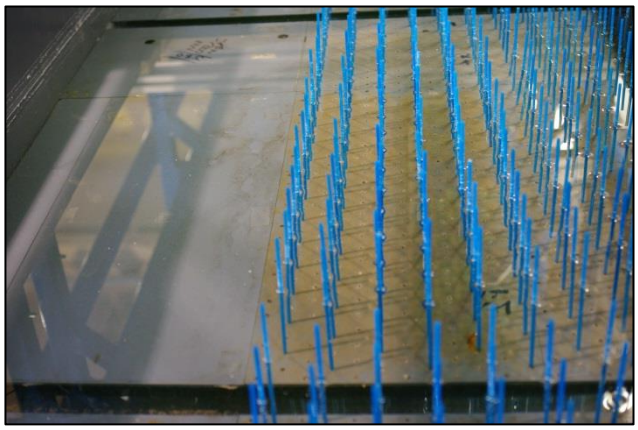

b) **Partial vegetation schematic plan view**

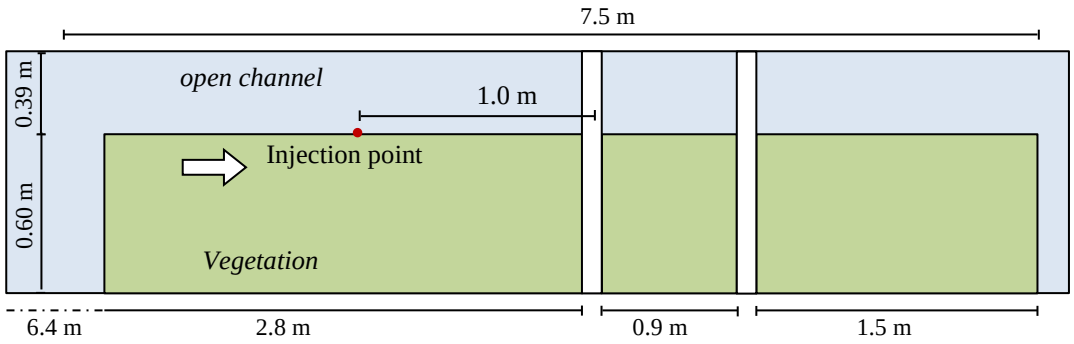

Figure 2.4: a) Downstream looking image and b) plan view of the partial vegetation scenario.

2.4 Velocity Measurements

Instantaneous velocity was measured using Acoustic Doppler-shift Velocimetry (ADV) and spatial profiles of velocity (vertical and horizontal) were enabled using Ultrasound Velocity

Profiling (UVP). Ultrasound is advantageous over other measurement techniques as it causes minimal disturbance to the flow field caused by the obstructive nature of measurement probes, e.g. electromagnetic velocity measurements. Further, the assembly of transducer equipment is practically straightforward compared to laser Particle Imaging Velocimetry (PIV) and the technique is potentially more precise than surface PIV which can be perturbed by surface tension and wind shear.

2.4.1 Principles of ADV and ultrasound velocity profiling

UVP relies on the principles of Doppler frequency shift (Met-flow, 2000). A submersible ultra-sound transducer was used to emit pulses of ultrasound within the water column; whose orientation depended on the direction of the measured velocity. The ultrasound pulse propagates through the water, at wavelength λ and speed c (=1484 m/s in water), until it is reflected from an object within the water column. The reflected pulse returns towards the transducer at a shifted frequency, f_d, inversely proportional to the component of the velocity, $\boldsymbol{v}$, at which the object is moving relative to the receiver; e.g. if a higher frequency return signal is received then the velocity component normal to the transducer must be positive. This frequency shift, known as Doppler shift, enables the magnitude of the velocity, u, of the moving particle to be determined, where:

$$u = f_d \frac{\lambda}{2} \sin\theta \qquad \textbf{Equation 2.2}$$

where θ is the angle between the direction of propagation and the direction of u. UVP measuring techniques require seeding of the water column to act as reflective media. In turn the quality of the signal is partly dependent upon the seeding density within the water column and represents a drawback of UVP techniques. Neutrally buoyant seeding was chosen such that density effects –rising or sinking – did not perturb the results.

Figure 2.5a shows the propagation of ultrasound through a medium with a given temporal mean longitudinal velocity profile $U(y, z)$. The beam is orientated at an angle θ to the

perpendicular direction of the component of the velocity and thus the instantaneous component *u* can then be calculated using a trigonometric correction.

Profiles of velocity are enabled by transmitting pulses of ultrasound at delayed time intervals and recording the return frequency from multiple locations, or "channels", along ultrasound beam length (Figure 2.5b). The velocity at each channel is then calculated from the shifted frequencies of the sampling range, *w*, and thus the instantaneous velocity at multiple channels can be recorded simultaneously to provide a velocity profile. The distance *w* and the spacing between channels, s_c, can be prescribed and determine the spatial resolution of the profile.

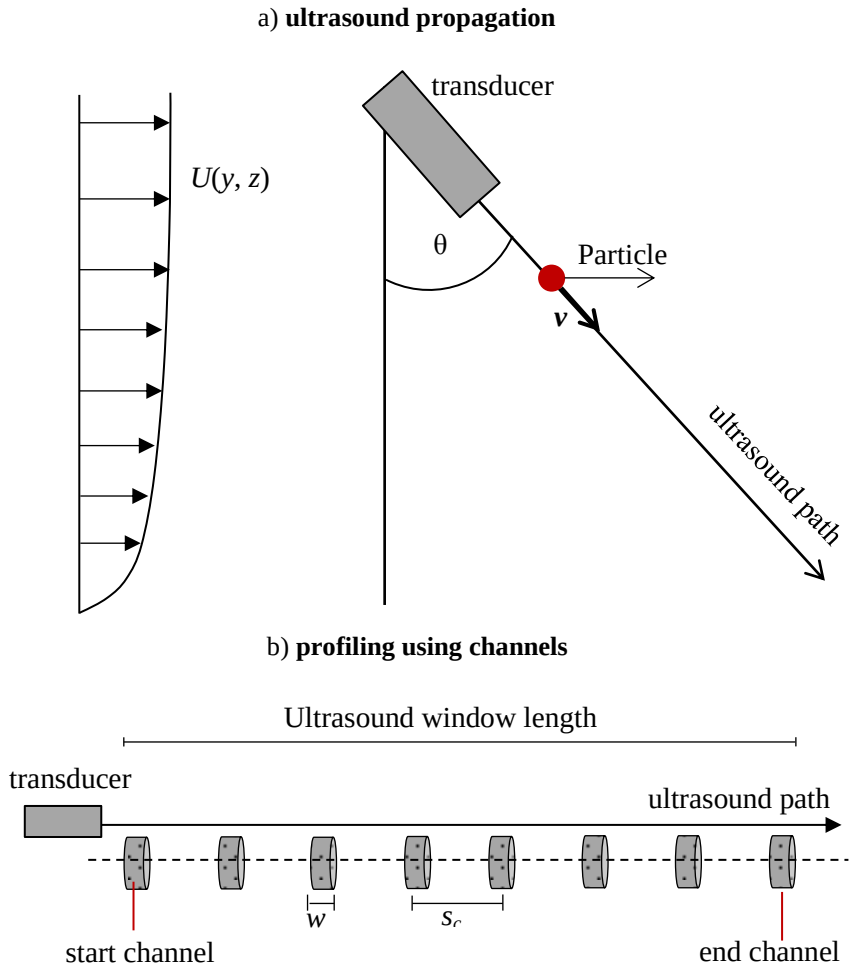

Figure 2.5: a) UVP transducer direction of the ultrasound beam is set at the angle θ relative to the perpendicular of the component of velocity that is to be measured. b) Schematic example of the method for velocity profiling, discretizing the ultrasound beam into channels of a given width *w* and spacing s_c.

Optimisation of the ultrasound beam properties and seeding characteristics improves accuracy. Firstly, the ultrasound frequency is adjusted depending on the desired value of w and the expected magnitude of u; i.e. higher frequencies (> 4 MHz) are suitable for smaller seeding particles. Secondly, the sampling properties, such as rate and spacing, are adjusted to meet the measurement requirements; such as velocity uncertainty (e.g. error), area of interest (measurement location within the beam length) and/or memory limitations. For example, when recording over, say, 200 channels, i.e. 200 measurement points, an increase in the sampling window reduces the spatial resolution as s_c increases. Thirdly, the size of the reflective seeding particles must be of the same order of magnitude as the ultrasound wavelength ensuring maximal reflection and minimal scatter.

2.4.2 Measurement apparatus and procedure

The implementation of UVP represents a methodical development of the experimental procedure. Different velocity measuring arrangements were employed during the testing and are described below alongside each test. One of two UVP devices was used; either the *Vectrino II* velocity profiler (Nortek™) or the *UVP-DUO* (Met-Flow™).

Device 1: Vectrino II profiler (Nortek™)

The *Vectrino II* profiler records the three-dimensional components of the instantaneous velocity over a 35 mm sampling window with maximal spatial resolution of 1 mm. Figure 2.6 shows the *Vectrino II* profiler sampling region located 40 mm from the transducer head. Profiles of velocity were recorded at the flow mid-depth given the limited sampling range. The flow mid-depth compromises vertical or transverse detail vertical and time constraints[1]. Note that the *Vectrino II* accurately recorded bed distance providing precise locations of the profile in z.

[1]Vertical profiles of longitudinal velocity late recorded showed that the channel mean longitudinal velocity is within 5% of the mid-depth, temporal average.

Schematic profile of the *Vectrino II*

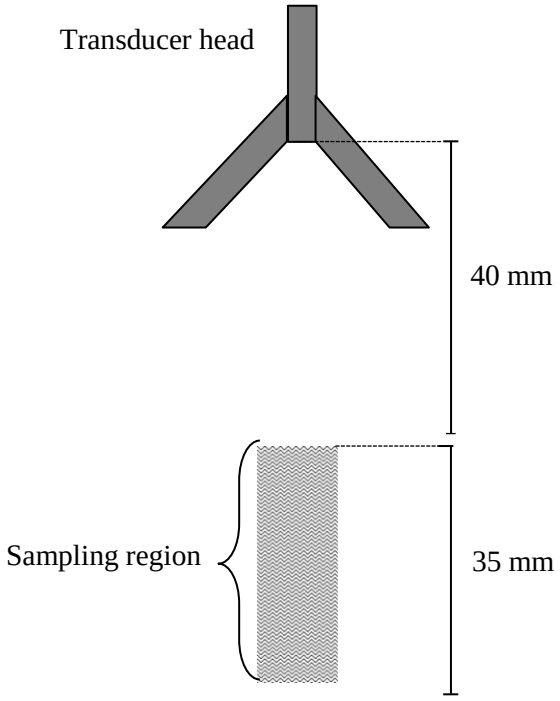

Figure 2.6: schematic illustration of the *Vectrino II* velocity profiler and sampling region.

Velocity was measured at the upstream observation window providing sufficient space for the transducer head and the uninterrupted propagation of ultrasound – where it was assumed that $\partial U/\partial x = 0$. In the full vegetation scenario, vertical profiles of velocity profiles were recorded at the flow mid-depth at ten transverse locations; while in the partial vegetation scenario, 16 transverse locations were chosen to increase the spatial resolution across the vegetation interface.

Device 2: UVP-DUO Profiler

The *UVP-DUO* velocity profiler was employed to overcome the limitations in ultrasound window length associated with the *Vectrino II*. The *UVP-DUO* measures instantaneous scalar velocity over a sampling window length of up to 2.00 m and the number of channels, n_c, channel distance, s_c, and width, w, are adjustable. A variable array of *UVP-DUO* transducers was employed depending on the experimental scenario. Figure 2.7a shows how transducers were inserted into the channel walls at the flow mid-depth. In the full artificial vegetation

cases, vertical profiles of instantaneous longitudinal velocity, $u(z)$, were measured at four transverse locations (y = 0.135, 0.385, 0.440 and 0.660 m) at the upstream observation window, and were inserted into the channel bed – minimising flow field disturbance – at an angle of 12° to the channel bed normal (Figure 2.8). Velocity was measured at a range of frequencies between 13 and 25 Hz depending on the device parameters – deemed sufficient high for recording the expected turbulent fluctuation – until a minimum of 2000 samples were collected.

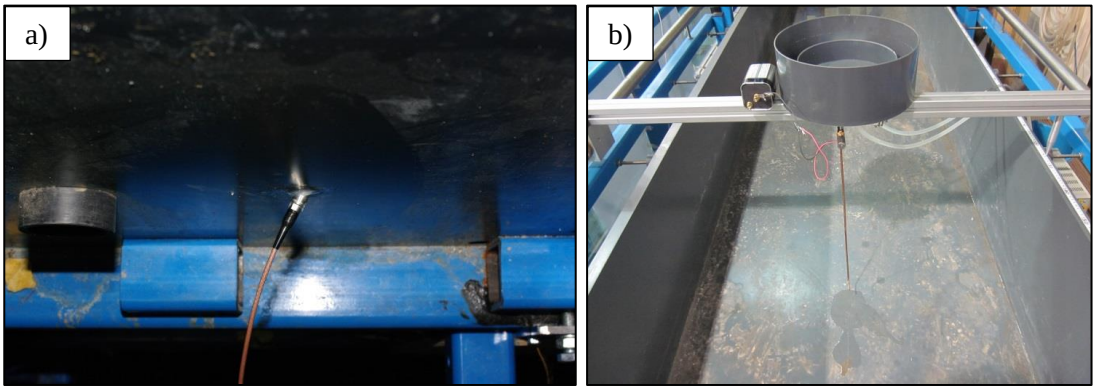

Figure 2.7: a) *UVP-DUO* transducer probe installed at the flow mid-depth in the side of the flume wall. b) Photograph of the constant-head Rhodamine tracer injection system with solenoid valve.

Velocity profiling procedure

The water column was heavily seeded with almost neutrally buoyant Telamin particles with density and diameter of approximately 1007 kg/m^3 and 10 µm, respectively, which was coated in a surfactant (wetting agents Tetanel® Mirasol and conventional soap) to improve solution. Without such a coating, the particles' hydrophobicity caused them to remain on the water surface; and at lower velocities ($u \leq 5$ mm/s), the particles would deposit onto the channel bed required regular stirring to promote re-suspension between tests. Recirculating pumps were also installed in the reservoir to maintain sufficient seeding density. It should be noted that the validity of the velocity measurements was dependent on the seeding density per unit volume. If the velocity sampling channel is temporarily void of particles then the ultrasound reflects poorly and the signal intensity reduced. As the spacing between velocity sampling channels

decreases the density of seeding must be increased to ensure that there are sufficient particles present within each velocity measurement location.

Table 2.1: Summary of the velocity measurement configuration for each test.

Vegetation type	Scenario	Ultrasound Device	No. probes	Sample frequency (Hz)	No. Channels	Total samples
High density artificial	Full	*Vectrino II*	1	50	35	9000
	Partial	*Vectrino II*	1	50	35	7500
Low density artificial	Full	*UVP-DUO*	8	13-25	600	2000
	Partial	*UVP-DUO*	4	13-25	600	2000
Winter *Typha*	Full	*UVP-DUO*	8	13-25	169	7000
	Partial	*UVP-DUO*	2	13-25	500	10,000
Summer *typha*	Full	*UVP-DUO*	4	13-25	500	6000
	Partial	*UVP-DUO*	4	13-25	800	4000

Table 2.1 provides a summary of the velocity measurement procedure for each vegetation type and test scenario. Longitudinal velocity was measured in the low density artificial vegetation using an array of 8 *UVP-DUO* probes and represents the final stage of the velocity measurement development (Figure 2.8). Four transverse pointing transducers were installed within the channel walls, at mid-depth; 2 at the upstream and 2 at the downstream observation windows. The remaining four transducers were installed across the channel within the bed pointing vertically at the upstream observation window. This array enabled instantaneous longitudinal velocity to be measured simultaneously with the Rhodamine tracing.

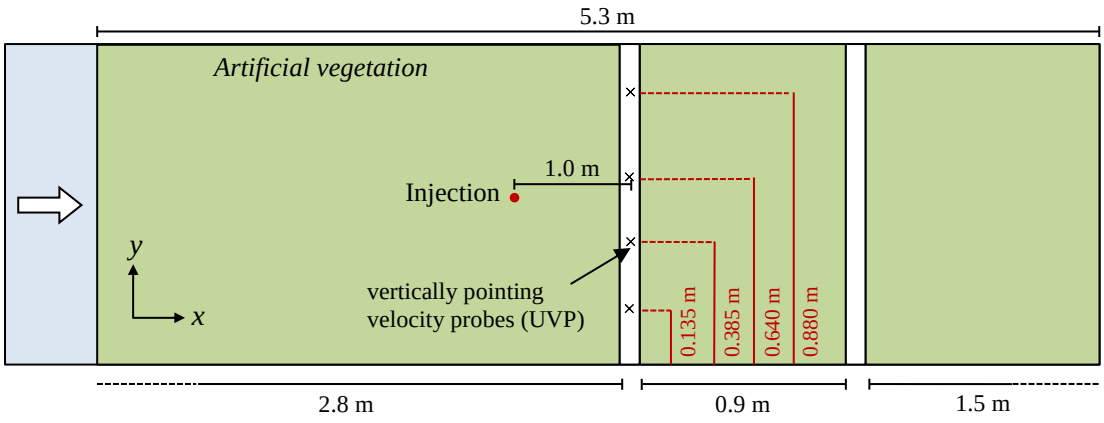

Figure 2.8: Full artificial vegetation channel plan. The crosses denote the locations of the vertically point UVP probes employed to measure longitudinal velocity in the low density cases.

2.5 Rhodamine Dye Tracing

Solute mixing was investigated with the use of Rhodamine 6G fluorescent dye. Rhodamine was injected into the channel using a vertical source. A copper pipe with 14, 0.8 mm diameter holes with 10 mm spacing injected the dye such that injection excluded the bed and directly at the water surface. The pipe was connected to a constant header tank located directly above the flume (Figure 2.7b). It was assumed that the vertical source lead to a rapidly vertically well-mixed tracer thus eliminating the observational effects of vertical mixing. A point laser beam was then employed to image the tracer positioned at the flow mid-depth point transverse across the flow. Laser Induced Fluorometry (LIF) was then employed as a method of tracer visualisation.

LIF relies on the principles of dye fluorescence. Laser light is directed at a volume of dye and a proportion of the light power is absorbed and then re-emitted by the dye – known as fluorescence; where the peak fluorescence of a substance is at a specific wavelength. Lasers beams are characterised by a narrow bandwidth and are more suitable than conventional lighting sources for exciting fluorescent tracers. Rhodamine 6G has a peak excitation of 532 nm; therefore, a green 200 mW (λ = 532 nm) laser (CNI 200 mW, 532 nm DPSS laser. Model: MGL-III-532-200 with PSU-III-FDA power supply) was employed to deliver a narrow coherent beam of light at the flow mid-depth pointing transversely through the water column. The fluorescence of Rhodamine 6G is proportional to the concentration of dye up to a saturation limit of approximately 1000 parts per billion (ppb). Beyond a certain concentration of tracer molecules, the light intensity of the observed fluorescence will quench as the neighbouring molecules obscure the fluorescent light.

A bespoke LIF array was constructed at the two transverse observation locations downstream of the injection point. Figure 2.9 shows the locations of the two laser beams at both LIF measurement sites. The lasers were directed perpendicularly into the flow at the flow

mid-depth through two small glass windows made in the channel wall (Figure 2.10). A second glass window installed into the channel bed allowed the full 0.99 m length of the beam to be observed; where a camera (Point Grey 1.3MP On Semi VITA CMOS 1/2" Monochrome, Global 2) was mounted below the glass window. The camera was focussed manually until an image, positioned at the same depth as the laser beam, was clearly visible. The camera CCD display was 1280 x 1024 pixels wide and the entire beam could be included within its field of view. A wide-angle lens was used with the camera in order to image the full beam length. A glass filter was mounted on top of the camera to filter only the light emitted by the Rhodamine dye. Camera observations of fluorescent intensity detected minimal light in the absence of any tracer awarding reliability to the filters.

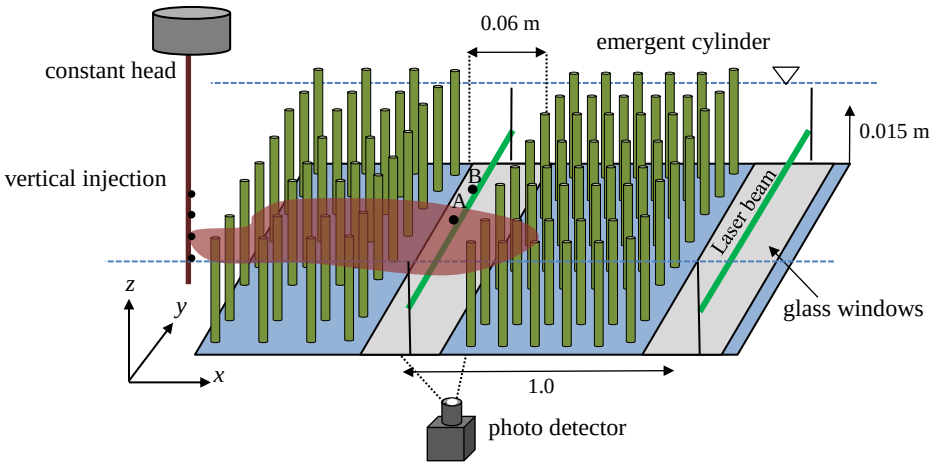

Figure 2.9: Schematic diagram of emergent, full-cross-sectional vegetation with LIF windows. Note that the cylinder diameter and density are not to scale to the channel width.

The camera was positioned such that the laser beam was horizontal in the camera image and was aligned to within one pixel accuracy using a target; aligning both cameras precisely in the *x* and *y* directions. Geometric distortion was minimised by orientating the camera such that the vertical co-ordinate (in pixels) of the beam remained constant along the beam length. Grey-scale images of the laser beam were recorded at 5 Hz on an 8-bit setting; where absolute black was recorded as 0 and absolute white, or saturation, was recorded as 256. This frequency was deemed sufficiently high to capture temporal variations in concentration as the tracer passed through the beam and did not demand excessive computational memory.

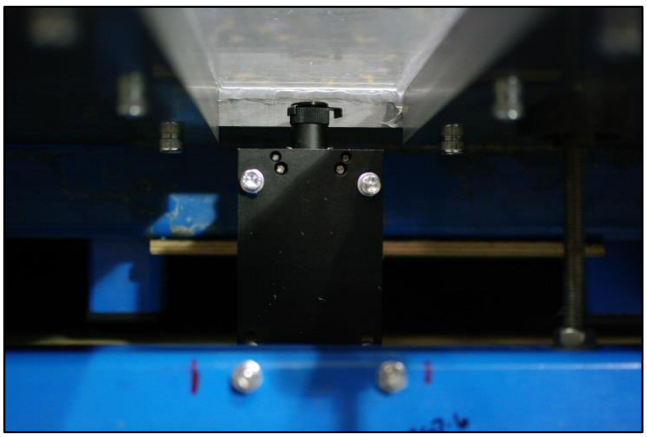

Figure 2.10: Image of the laser directed perpendicular through the glass window at the flow mid-depth.

The entire flume was covered in black-painted wooden boards to minimise background noise from lighting and the passage of objects by the test sections. Blackout conditions also helped to maintain a constant background light intensity level; improving data repeatability and maximising the resolution in tracer concentration. The laser-camera system was calibrated for a desired range in Rhodamine concentration. A maximum concentration of 50 ppb was chosen as this minimised the disparity in density between the dye and the surrounding water; mitigating for disparities in buoyancy. Further, a weak peak concentration reduced the non-linear effects of laser attenuation due to localities of strong dye. Camera shutter speed was adjusted such that the maximum prescribed concentration of 50 ppb approached the saturation level (256) of the CCD screen. Thus, the resolution in concentration was approximately given by the ratio of peak calibration concentration to camera-bit setting e.g. 50/256 = 0.2 ppb. Both LIF detection sites were simultaneously calibrated to attain correct mass balance between the two observation windows.

Two injection methods were employed. Firstly, five-second ‘pulse’ injections were made 1 m upstream of the first observation window. The pulse injections were repeated 10 times to quantify the spread and reproducibility of the data. Secondly, continuous dye injections were made for 10 minutes to simulate steady state conditions. The steady state injection eliminated the observational effects of longitudinal mixing and allowed only the effects of transverse mixing to be observed. In short, the two injection approaches were employed to observe either

2-dimensional mixing (i.e. both longitudinal and transverse) or 1-dimensional (i.e. transverse mixing) as functions of time.

In the full-vegetation scenario, tracer was injected at the channel centreline (y = 0.495 m) 1.8 m downstream of the vegetation leading edge (shown in Figure 2.8) and the concentration was measured in the transverse plain at 1.0 and 2.0 m downstream. Care was taken to ensure that the tracer was not injected directly behind or in front of a vegetation element – as such an upstream stem was removed to minimise the initial disruption caused by stem eddy shedding. In the partial vegetation scenarios, the tracer was injected at the interface between the vegetation and the open channel (y = 0.660 m), 4.9 m downstream of the vegetation leading edge; where Figure 2.4b shows the location of the injection point relative to the vegetation leading edge and observation windows. The vertical injection pipe was positioned a few millimetres into the open channel side of the interface to avoid ejection of dye directly behind a stem. Similarly, concentration was measured transversely 1 m and 2 m downstream of the injection point.

2.5.1 LIF calibration

The 2 m test section was isolated using baffles and filled with a known concentration of dye. Images were taken simultaneously at each camera section for 5 minutes providing 1500 images of the laser beam. The mean intensity at every pixel along the beam was then calculated from the average of the 1500 images. This was then repeated for 10 different concentrations from 0 ppb - 50 ppb in 5 ppb intervals. A correlation between intensity and concentration was made for the full range of known concentrations. This relationship allows the pixel intensity as measured by the camera to be converted into parts per billion. The difference in absolute power between the upstream and downstream lasers meant that a conversion from intensity to concentration was necessary.

Two additional constraints had to be taken into account: firstly, the laser power was strongly attenuated across the channel width. The Beer-Lambert Law[2] was applied to the exponential decay in laser power to provide a linear calibration. Secondly, the attenuation of laser power was also a function of local Rhodamine concentration. Figure 2.11 is an example of laser attenuation due to a local-high concentration of Rhodamine. In the example the laser beam is directed vertical with regards to the page. The Rhodamine trace in the middle of the channel is excited by the laser, as indicated by the bright spot in the centre of the cloud. The laser beam towards the top of the image is significantly reduced in intensity due to the attenuation. The high concentration of the trace absorbs laser powering resulting in weak beam intensity at the top of the image.

In instances where the spatial concentration distribution of tracer is non-uniform, the Beer-Lambert description of power decay cannot be used. Therefore, each calibration concentration had to be repeated for a range of initial laser powers – that is, the power immediately at the glass interface. A pixel-by-pixel decay model (Ferrier et al., 1993) was used to calibrate intensity to concentration; where the intensity as measured at a pixel was dependent on the concentration, and power leaving the previous pixel. Thus, an average calibration relationship was obtained for both LIF windows to accurately convert pixel intensity recorded along the length of the laser beam into absolute Rhodamine concentration. The LIF calibration procedure is detailed in greater depth in Appendix II.

Such a procedure allowed the measured concentration distribution along the length of the laser beam to be converted into parts per billion either as a calibration for each pixel or using a mean distribution. The benefit of using a calibration for each pixel is that any defect to the glass, or filter, causing erroneous data points can be corrected for (assuming that the cameras are kept in their exact calibration position). On the other hand, calibration using a mean distribution allows for undesired movements to camera without the need for a re-calibration. It

[2]J.H. Lambert, *Photometria sive de mensura et gradibus luminis, colorum et umbrae* [Photometry, or, On the measure and gradations of light, colors, and shade] (Augsburg ("Augusta Vindelicorum"), Germany: Eberhardt Klett, 1760).

was, therefore, deemed more suitable to use the mean calibration method to mitigate for alignment problems and impurities on the window surface.

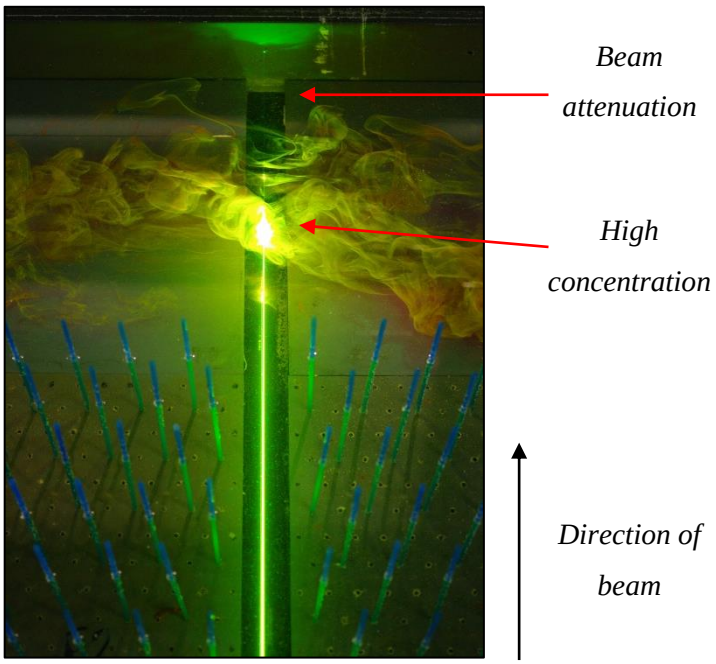

Figure 2.11: Example image of laser beam attenuation due to the spatially non-uniform concentration of Rhodamine 6G.

2.6 Real Vegetation Investigations

The aim of the second experimental part was to quantify the mixing characteristics of real vegetation shear layers. The natural geometric and morphological heterogeneity of real vegetation could not easily be replicated in the laboratory with the use of plants cultivated 'in-house'. Therefore, two real vegetation types were supplied directly to the University of Warwick; winter *typha* (Cattail reeds), harvested in February 2015, and summer *typha*, harvested in August 2015. This section describes the changes to the experimental method required for the real vegetation cases and sets out a method for describing and quantifying the geometric characteristics of real vegetation.

2.6.1 Vegetation installation

A 1 x 10 m long section of the flume was vegetated with living *typha latifolia*. The vegetation was grown in the UK for two years under normal growing conditions –defined here as external environmental conditions without human influence over the level of precipitation, competition or sun-light. The vegetation was supplied by *Salix*© specialising in the cultivation of aquatic vegetation for installation in pond and wetlands. The vegetation was grown in rope matting and could be easily manoeuvred or transported without harming the root system or plant structure. Figure 2.12 provides a close-up image of the vegetation root structure and matting used to hold the sections together.

The central 10 m of the 24 m long flume was planted with the real vegetation (Figure 2.13) and was secured to the channel bed using manufactured steel spikes that prevented the vegetation from floating and allowed the mats to be flattened to a near constant-level bed. The vegetation roots were approximately 100 mm thick and ranged from ~50 mm to ~150 mm. The remaining 14 m (10 m upstream and 4 m downstream of the test section) of the channel was raised using polystyrene boards to produce a continuous level bed along the entire flume length.

Figure 2.12: Cross-section image of the real vegetation root system.

2.6.2 Channel plan

The real vegetation was installed such that the upstream leading edge was located 5.0 m downstream of the flow straighteners (Figure 2.13). Figure 2.14 provides examples of the winter and summer *typha* in both the full (a & c) and partial (b & d) vegetation scenarios. The upstream LIF window was located 6.0 m downstream of the vegetation leading edge and 1.0 m downstream of the Rhodamine injection point. The downstream LIF window was located a further 1.0 m downstream of the first window with a remaining 3.1 m of vegetation downstream such that the whole measurement section was 10.0 m long.

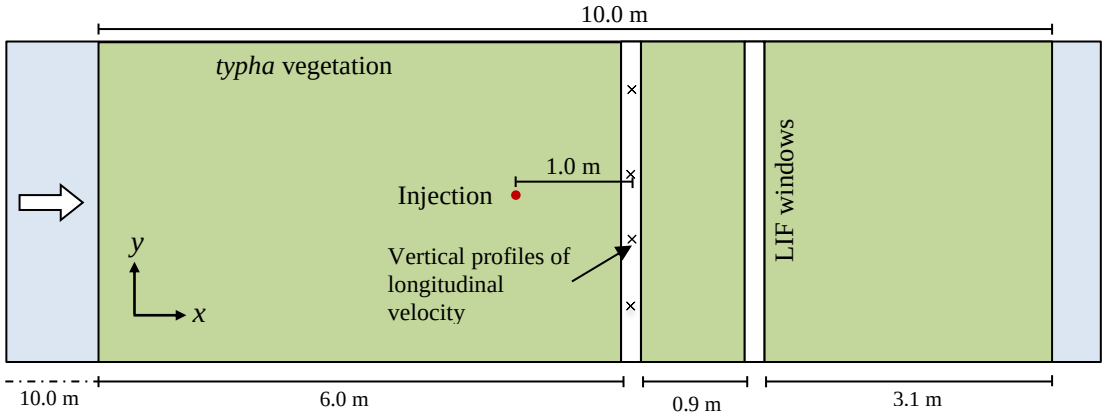

Figure 2.13: Full vegetation channel configuration for the real vegetation test cases.

The partially vegetated scenario was then enabled by cropping the vegetation along the channel centreline ($y = 0.495$) such that the region $y > 0.495$ m was open channel and the vegetation was cropped at the stem root to retain the real vegetation bed. Finally, the full open channel scenario was enabled by cropping the remaining vegetation to leave the bare vegetation bed.

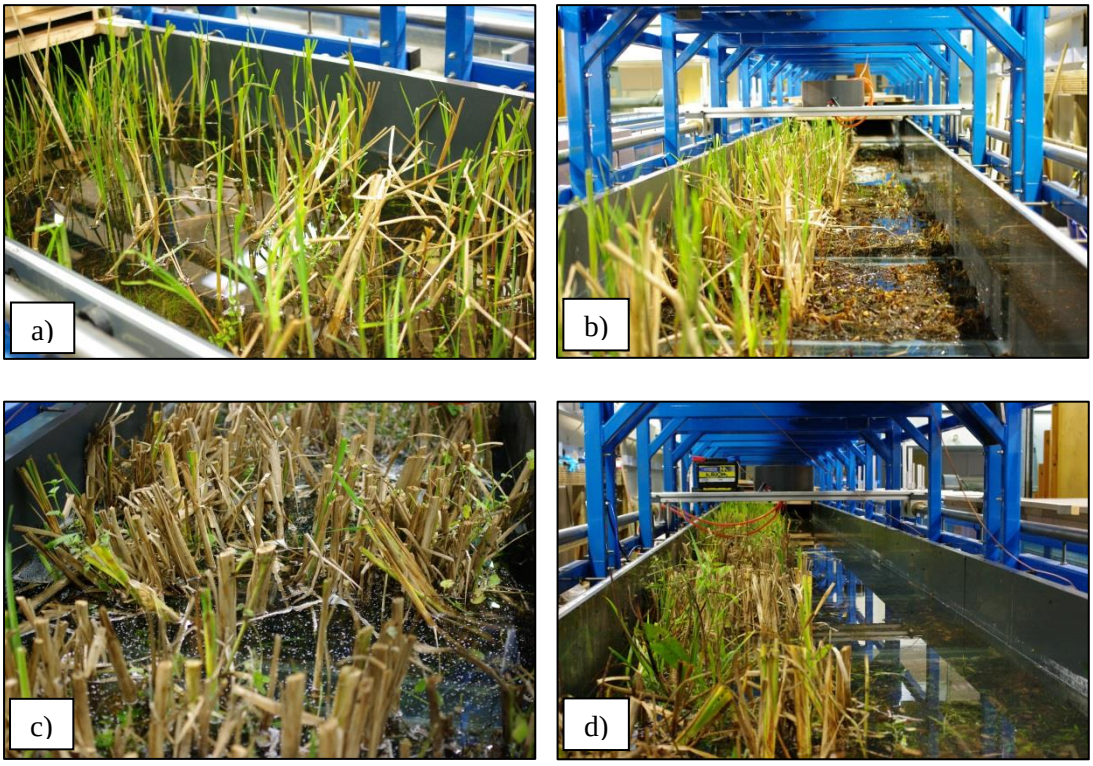

Figure 2.14: Real *typha* vegetation shown for winter a) full and b) partial and summer c) full and d) partial scenarios.

2.6.3 Real vegetation characterisation

The real vegetation characteristics (morphology and geometry) were quantified to facilitate statistical comparison between seasons and types using the following characteristics:

- Population stem density per unit area, *N*;
- Stem diameter, *d*;
- Frontal area per unit volume, *a*.

The stem population density was measured by counting the number of stems in a known plan area of 0.5 m^2. This was repeated at up to 10 random locations to provide an accurate estimation of the mean population density. The mean stem diameter was calculated by measuring the stem diameter approximately at the channel mid-depth (75 mm) of at least 100, randomly chosen stems. The diameter was recorded using digital Vernier gauge callipers accurate to 0.01 mm. The stems were oval in shape and therefore the diameter in the plane perpendicular to the direction of mean flow was measured where possible. Finally, the frontal

area per unit volume was estimated from cross-section images taken of the vegetation in-front of a clear white board with a scale. Image processing of the cross-sections is described in more detail in Appendix III.

2.6.4 Velocity measurements in real vegetation

Figure 2.14 shows that the diameter and spacing of the *typha* was non-uniform with location and depth. The random morphology and distribution of the real vegetation meant that measurements of velocity would provide only an approximation of the temporal mean velocity field; bringing into question what were the desired outcomes of measuring the temporal mean vertical or transverse profiles of longitudinal velocity? Despite the insight gained from measuring accurate vertical velocity profiles within emergent, real vegetation, the experimental aims were to quantify the transverse mixing associated with shear layer, real vegetation. Therefore, a general understanding and quantification of a mean longitudinal velocity was sufficient when relating to transverse mixing coefficients.

Moreover, a mean longitudinal and transverse velocity could be calculated from observing the spatial and temporal concentration distributions of pulse injections of tracer in the full vegetation scenario. The mean velocity was calculated using the travel time between centroids of the upstream and downstream concentration distributions. This 'travel time' velocity was – in the full vegetation scenario – a more representative calculation of the channel mean than limited vertical or transverse velocity profiles, as the tracer experienced an average velocity field on its advection from the upstream to the downstream measurement points.

Full Vegetation

In the full vegetation scenario, vertical profiles of longitudinal velocity, $u(z)$, were measured at a 8 random location in the winter *typha* (Figure 2.15a) and 4 set locations in the summer *typha* (Figure 2.15b). In the winter *typha* type, $u(z)$ was measured from the channel surface

using the *UVP-DUO* probes. The *typha* vegetation was characterised by clumps of vegetation interspersed with sparse, open patches; as such, 4 random transverse locations were selected within both the upstream and downstream observation windows. In the summer *typha*, $u(z)$ was measured using 4 *UVP-DUO* pointing vertically from the channel.

a) **Winter *typha* full vegetation velocity measurement**

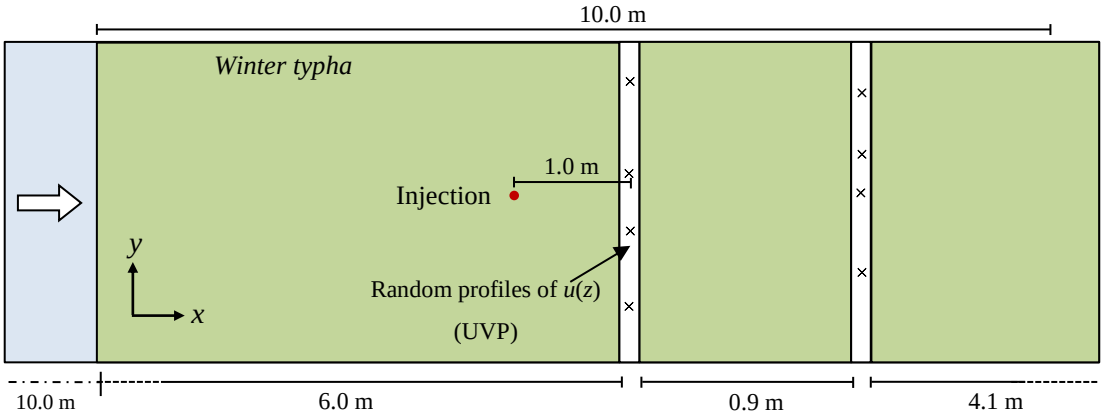

b) **Summer *typha* full vegetation velocity measurement**

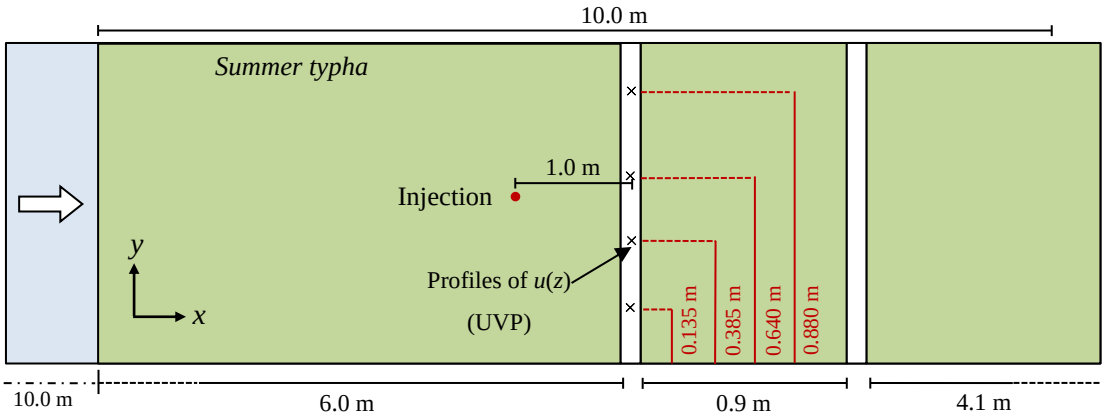

Figure 2.15: Full vegetation channel configuration for the *typha* vegetation tests for a) winter and b) summer types.

Partial Vegetation

In the winter *typha* partial vegetation scenario, two transverse profiles of longitudinal velocity, $u(y)$, were measured at the upstream and downstream observation windows using a single *UVP-DUO* probe installed at the channel mid-depth (Figure 2.16). In the summer *Typha* partial vegetation scenario, upstream and downstream transverse velocity profiles were measured using an array of 4 *UVP-DUO* transducers. A transducer was installed either side of

the channel within the walls of the flume in the vicinity of each observation window. Measurement limitations meant that a complete transverse profile of $u(y)$ had to be created by superimposing the incomplete profiles recorded from either side of the channel. Transducers were installed such that the beams from opposing sides of the channel overlapped at the channel centre line (y = 0.495 m).

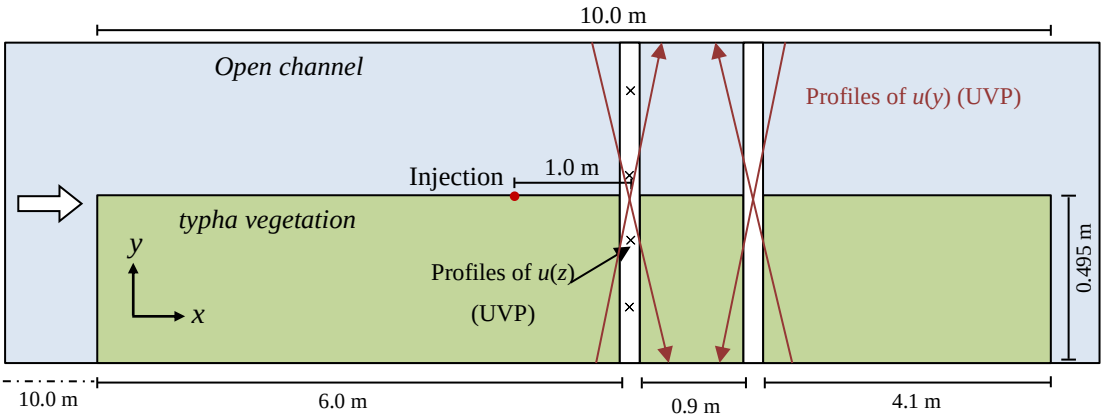

Figure 2.16: Partial vegetation channel configuration for the *typha* vegetation.

2.6.5 Fluorescent tracing in real vegetation

The same injection procedure used in the artificial vegetation tests was employed for the real vegetation. Pulse injections were made at the channel centreline (y = 0.495 m), 1.0 m upstream of the first observation window in the full vegetation scenario. In the partial scenario, the injection point was located at the interface between the vegetation and the open channel (y = 0.495 m). Constant injections were made for 10 minutes to ensure steady state concentration distributions. Continuous and pulse injection were also tests in the open channel scenario to quantifying the mixing properties of the real vegetation bed.

2.7 Test Conditions

Five discharge cases were investigated for each vegetation scenario (full-vegetation, partial-vegetation and bare channel) and vegetation type (high density artificial, low density artificial, winter *typha*, and summer *typha*). The desired discharge for each test was determined iteratively by observing the temporal spatial mean longitudinal velocity within the three distinct flow regions. Firstly, a preliminary velocity investigation was made in the full-vegetation configuration using the high density artificial vegetation as a base case. Vertical profiles of longitudinal velocity, $u(z)$, was recorded for 5 minutes at 50 Hz at the channel centreline using the *Vectrino II* UVP for five discharges: 1.0, 1.5, 2.0, 2.5 and 3.0 l/s. The mean longitudinal velocity was observed in the range of 0.5 - 2.0 cm/s – typical values for flow within real aquatic vegetation (Lightbody et al., 2008). Note that the downstream tailgate had to be adjusted for each discharge to maintain a channel depth at the upstream observation window of 0.150 m. The flow depth was measured relative to the surface of the glass window at the upstream measurement site creating a constant reference point across all experiments.

It was desirable to vary the discharge between scenarios such that the mean longitudinal velocity within the vegetation in the partial vegetation scenario was similar to the mean longitudinal velocity measured in the equivalent full vegetation scenario for the same vegetation type. Velocity was again recorded in the partial vegetation configuration at $y = 0.25$ m at the upstream observation window. The channel discharge was altered until the mean longitudinal velocity approximately matched that measured in the full vegetation scenario. This was repeated for 5 discharges to obtain a relationship between discharge in the partial vegetation scenario and mean longitudinal velocity deep within the vegetated portion of the flow. The corresponding 5 discharges to be used within the partial vegetation configuration were 3.35, 4.25, 5.25, 6.35 and 7.35 l/s.

The two sets of discharges were maintained for the four vegetation types in order to assess the mixing characteristics of different types of vegetation under the same flow conditions. The channel depth was also maintained at 0.150 m for all types to reduce the number of variables acting on the system. Table 2.2 summarises the test conditions for the artificial vegetation types; where Q is the channel discharge, H is the flow depth measured at the upstream observation window, a is the frontal area per unit volume, and Φ is the solid volume fraction of the vegetation elements. The test conditions for the real *typha* vegetation cases are summarised in Table 2.3.

Table 2.2: Artificial Vegetation test summary.

Parameter	**High Density Tests**									
	Full vegetation					Partial vegetation				
	1	2	3	4	5	1	2	3	4	5
Q (l/s)	1.00	1.50	2.00	2.50	3.00	3.35	4.25	5.22	6.35	7.45
h (m)	0.1496	0.1503	0.1500	0.1502	0.1499	0.1499	0.1503	0.1499	0.1504	0.1498
a (cm^{-1})	0.064	0.064	0.064	0.064	0.064	0.064	0.064	0.064	0.064	0.064
Φ (-)	0.020	0.020	0.020	0.020	0.020	0.020	0.020	0.020	0.020	0.020

Parameter	**Low Density Tests**									
	Full vegetation					Partial Vegetation				
	1	2	3	4	5	1	2	3	4	5
Q (l/s)	1.00	1.50	1.99	2.49	2.99	3.35	4.25	5.22	6.35	7.45
h (m)	0.1504	0.1504	0.1500	0.1501	0.1502	0.1496	0.1503	0.1499	0.1503	0.1498
a (cm^{-1})	0.016	0.016	0.016	0.016	0.016	0.016	0.016	0.016	0.016	0.016
Φ (-)	0.005	0.005	0.005	0.005	0.005	0.005	0.005	0.005	0.005	0.005

In the full vegetation configuration, 10x pulse injections lasting 5 seconds were made to observe mixing both longitudinally and transversely for all 5 flow cases. This was repeated for the second vegetation density. In the partial vegetation configuration, continuous injections of Rhodamine tracer were made for 10 minutes to attain steady state conditions. 10 minutes was long enough to capture sufficient images to obtain an accurate average concentration distribution.

Table 2.3: Real *typha* vegetation test summary.

Parameter	**Winter *typha***									
	Full vegetation					Partial vegetation				
	1	2	3	4	5	1	2	3	4	5
Q (l/s)	1.00	1.50	2.00	2.50	3.02	3.34	4.25	5.23	6.35	7.46
h (m)	0.1496	0.1503	0.1503	0.1501	0.1501	0.1499	0.1503	0.1499	0.1504	0.1498

Parameter	**Summer *typha***									
	Full vegetation					Partial vegetation				
	1	2	3	4	5	1	2	3	4	5
Q (l/s)	1.00	1.50	2.00	2.50	3.00	3.35	4.25	5.22	6.35	7.25
h (m)	0.1496	0.1503	0.1500	0.1502	0.1499	0.1499	0.1503	0.1499	0.1504	0.1498

3. Flux Gradient Analysis of Spatially Variable Transverse Mixing

This chapter evaluates a potential method for quantifying the lateral variation in transverse mixing for spatially variable flow fields – such as those associated with partially vegetated channels. The prediction of the fate of pollutants in vegetated shear layers demands that the lateral variation in transverse mixing coefficient, $D_y(y)$, be accurately calculated. However, standard statistical procedures employing the rate of change of spatial variance in concentration (e.g. Fischer et al., 1979 and Equation 1.20) assume a spatially constant mixing coefficient mixing the solute in a Gaussian distribution; thus yielding a spatially averaged solution.

Ghisalberti and Nepf (2005) presented a discretized solution to the depth-averaged advection diffusion equation (Equation 1.17) evaluated for $D_y(y)$ between two longitudinally-adjacent, transverse profiles of tracer concentration, downstream of a vertically well mixed, continuous source. Ghisalberti and Nepf (2005) state that the mass of solute at the upstream slice, dy, at measurement location A, must equate to the mass of the same slice at a downstream measurement location, B, and any mass that has exited the volume through mixing. The rate of loss of mass is therefore proportional to the transverse concentration gradient and the transverse mixing coefficient of that particular slice. It is assumed that the transverse variation in mixing coefficient and U are longitudinally uniform such that $\partial/\partial x = 0$; where $D_y(y)$ is calculated using;

$$D_y(y) = \frac{\Delta\left(\int_0^y U(y)C(x,y)\mathrm{d}y\right)}{\Delta x \left|\left\langle {}^{\partial C}/_{\partial y}\right\rangle\right|_y} \qquad \textbf{Equation 3.1}$$

where $C(x, y)$ is the profile of steady-state concentration and the denominator, $\langle \partial C/\partial y \rangle_y$, is the mean transverse concentration gradient of the adjacent concentration profiles, $[(\partial C/\partial y_A)+(\partial C/\partial y_B)]/2$.Ghisalberti and Nepf(2005) stipulate two constraining criteria for the application of Equation 3.1: firstly, the expression may only be applied in locations where the mean transverse concentration gradient does not change beyond a given factor between adjacent longitudinal locations, i.e. $c_1 = (\partial C/\partial y)_B/(\partial C/\partial y)_A \leq 3$; ensuring that the mean transverse concentration gradient is sufficiently representative of the gradient at both A and B. Secondly, the transverse concentration gradient at any transverse location at B must not be significantly smaller than the maximum concentration gradient at A, i.e. $(\partial C/\partial y)_B > 0.05*\max(\partial C/\partial y)_A$ where $c_2 = (\partial C/\partial y)_B/\max(\partial C/\partial y)_A = 0.05$.

The applicability of Equation 3.1 was evaluated for three analytical scenarios: 1) spatially uniform flows i.e. $U, D_y \neq f(y)$, 2) a lateral discontinuity in depth, or *step*, with two distinct flow zones; U_1 and D_1 for the deep zone and U_2 and D_2 for the shallow zone (e.g. Kay, 1987), and 3) a transversely sloping channel with a continuously varying transverse mixing coefficient and velocity. The constraining criteria, c_1 and c_2, were evaluated for every transverse location to investigate the applicable range of the method.

3.1.1 Evaluation 1 – spatially uniform flow conditions

Firstly, the transverse concentration distribution downstream of a steady-source was simulated for an environment with spatially uniform transverse mixing, i.e. $D_y, U, H \neq f(y, x, z)$, using the analytical solution for a continuous point source injection (Fischer et al., 1979). A 1.0 m wide channel uniform longitudinal velocity and transverse mixing coefficient, $U = 0.0029$ m/s and $D_y = 2.0\text{x}10^{-5}$ m^2/s, was simulated. The downstream concentration distributions at 1.0 and 2.0m were then calculated for every 1 mm across the flow (Figure 3.1) using;

$$C(x, y) = \frac{K}{\sqrt{4\pi D_y x U}} \exp\left[\frac{-(y^2 U)}{4 D_y x}\right] \qquad \textbf{Equation 3.2}$$

where K is the mass injection rate.

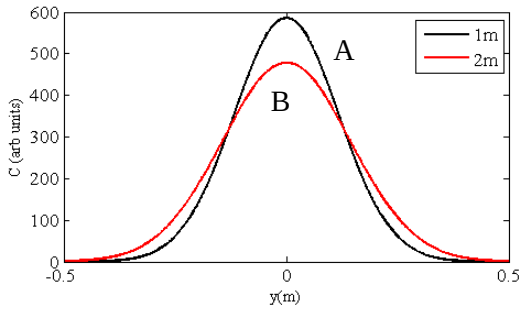

Figure 3.1: Upstream (1 m) and downstream (2 m) steady-state concentration for a point source in uniform flow predicted using the analytical solution to the Advection Diffusion Equation.

Secondly, the restraining criteria were evaluated for the concentration profiles in Figure 3.1. Figure 3.2a provides the calculated transverse profile of c_1; where the constraining limit of 3 is marked with the blue horizontal line. The values of c_1 exceeding the constraint are the locations where Equation 3.1 cannot be evaluated. Figure 3.2b provides the calculated transverse profile of c_2; where the minimum change in $\partial C/\partial y$ is given by the horizontal lines. Values of c_2 within the horizontal lines are also locations where Equation 3.1 cannot be evaluated.

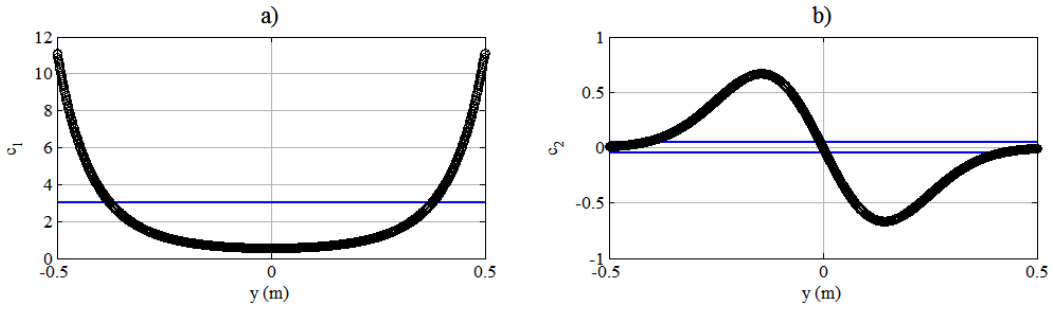

Figure 3.2: Flux-Gradient Model constraining criteria: a) the fractional change in gradient c_1 (black circles) where the horizontal line indicates the maximum permitted value; and b) the mean concentration gradient, c_2, where the region between the blue lines indicates the violating values.

Figure 3.3a gives the location where the constraining criteria are violated (grey shading) when compared to the transverse concentration distributions; while the calculated profile of transverse mixing coefficient is shown in Figure 3.3b – where the grey shading shows the locations where the constraining criteria are violated. Recall that the spatially uniform input value of D_y was 2.00×10^{-5} m^2/s. The calculated transverse profile of D_y shows an approximate

recovery of this value in the locations that do not violate the constraining criteria; where the mean value of D_y in these regions is 1.973x10^{-5} m^2/s – accurate to 97.3%.

The flux gradient approach does not recover the constant analytical input value of D_y. The restraining criteria limit the application of Equation 3.1 at locations where the fractional change in gradient is too small and where the change in gradient is too large. Despite these limits, the calculated values of D_y tend towards the analytical input (2.00x10^{-5} m^2/s) at locations sufficiently far from the influence of the violating locations and the mean value of D_y in the valid locations (between the shaded areas) recovers the input values to within 97%.

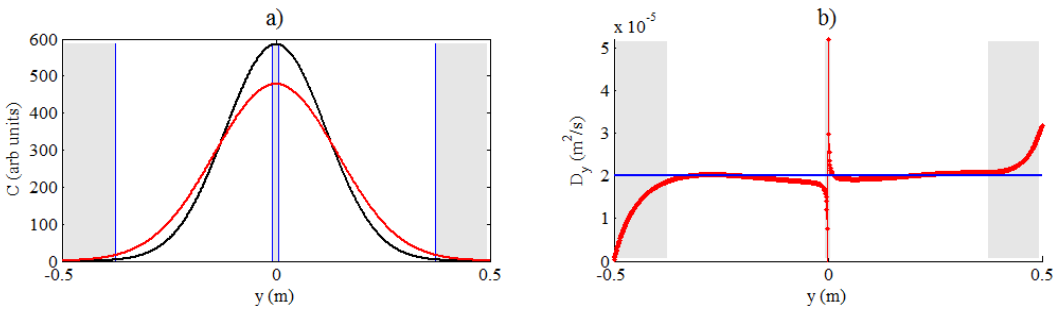

Figure 3.3: Flux-Gradient constraining criteria visualised against a) the concentration profiles and b) the calculated profiles of $D_y(y)$; where the grey shading indicates violating regions and the horizontal blue line is the analytical input of D_y.

3.1.2 Evaluation 2 – discontinuity in transverse mixing coefficient

The second evaluation of the flux gradient approach was the calculation of $D_y(y)$ for a lateral discontinuity in transverse mixing simulated using a depth discontinuity. Kay (1987) derived an analytical solution for predicting the concentration from a continuous injection at a transverse depth discontinuity (see section 1.3, Figure 1.13) where two adjacent flow regions were created with defined values of D_y, U and h. Figure 3.4 gives an illustration of the defined system for the step model showing the input values for the deep region (-0.5 m < y < 0 m), $D_y = D_1$, $h = h_1$ and $U = U_1$, and the shallow region (0.5 m > y > 0 m), $D_y = D_2$, $h = h_2$ and $U = U_2$. Kay (1987) suggested relationships between the depth of flow and the values of D_y and U where $U \propto h^{1/2}$ and $D_y \propto h^{3/2}$; as such the values of D_y and U were calculated for the shallow region using the input values for the deep region.

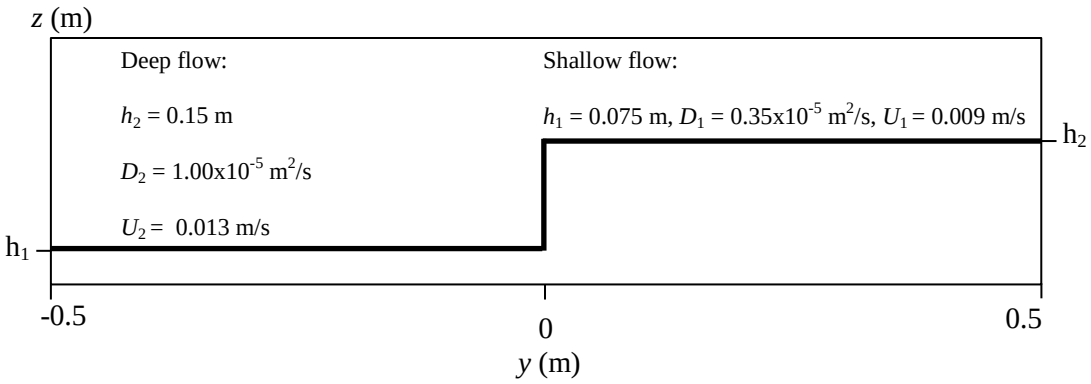

Figure 3.4: Theoretical design and hydraulic parameters for the depth discontinuity, or step, model.

The transverse concentration distributions from a continuous source located at the discontinuity (y = 0 m) were predicted downstream at 1 and 2 m and are shown in Figure 3.5a. The depth of flow, velocity and transverse mixing coefficient for the deep region were input as 0.15 m, 0.013 m/s and 1.00x10^{-4} m^2/s, respectively. The depth of flow in the shallow region was input as 0.075 m; where the velocity and transverse mixing coefficients were 0.009 m/s and 0.35x10^{-5} m^2/s using the above proportionalities. The constraining criteria, c_1 and c_2, are graphically illustrated in Figure 3.5b & c, where blue horizontal lines indicate the criteria limits.

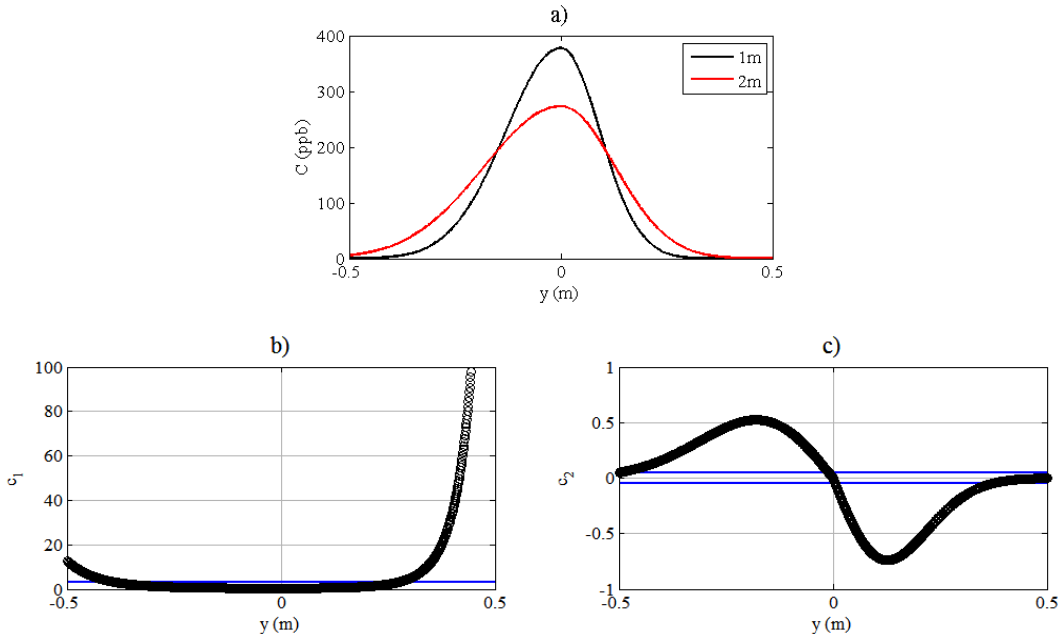

Figure 3.5: Depth-discontinuity results using Kay (1987) for a) the predicted concentration distributions and the evaluation of the flux-gradient constraining criteria b) c_1 and c) c_2 (black circles); where the horizontal blue lines indicate the criteria thresholds.

Figure 3.6a shows the locations in violation of the constraining criteria compared to the simulated concentration distributions. Similarly to the spatially uniform case, the criteria exclude those regions at the peak concentration – where the change in gradient is minimal – and in the regions where the fractional change in gradient between adjacent measurement locations exceeds a factor of 3 – predominantly in the limits of y. The profile of $D_y(y)$ calculated using Equation 3.1 is presented in Figure 3.6b; where regions in violation of the constraining criteria are given by the grey shading. The horizontal blue lines denote the input values of $D_y(y)$ for the different flow zones.

The profile of $D_y(y)$ indicates that there are two distinct mixing zones, but does not recover the discontinuity between the zones. The analytical approach approximately recovers the values of D_1 and D_2; the peak mixing coefficient in the deep zone ($y < 0$ m) is $1.007\text{x}10^{-5}$ m^2/s while the minimum value in the shallow zone ($y > 0$ m) is $0.355\text{x}10^{-5}$ m^2/s – matching closely the input values of 1.00 and $0.35\text{x}10^{-5}$ m^2/s, respectively. The mean values of D_y in the valid regions for the two zones are, however, 9.214 & $0.413\text{x}10^{-5}$ m^2/s.

The approach fails to match the $D_y(y)$ at the discontinuity – where the small change in transverse concentration gradient (<0.05) causes the prediction of D_y to blow up. For the given input conditions (D_1, u_1 etc.) the constraining criteria limit the application of the model to less than 70% of the total channel width.

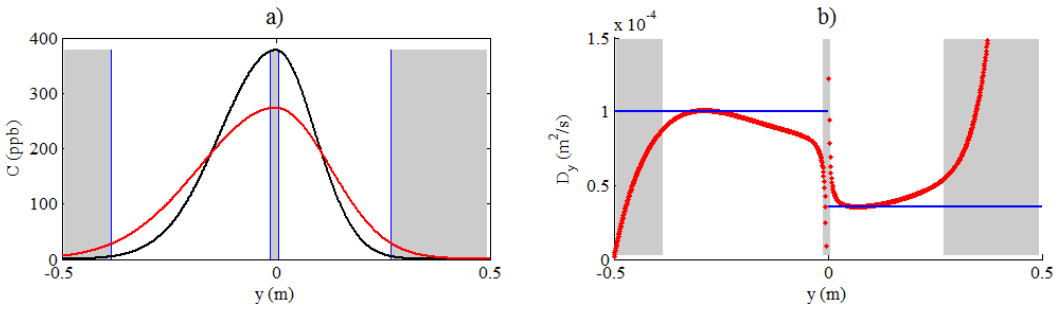

Figure 3.6: Flux-Gradient Model constraining criteria are compared to a) the concentration profiles and b) the calculated profile of $D_y(y)$ (red points) (horizontal blues lines indicate the input profile) for the step analytical solution; where the grey shading indicates violating regions.

3.1.3 Evaluation 3 – transverse sloping bed

The third evaluation of the flux-gradient approach was of a laterally sloping channel using an analytical solution given by Kay (1987); where D_y and U are continuous functions of y. A 0.5 m wide, transversely sloping channel was constructed with maximum and minimum depths of 0.15 m and 0 m, respectively. The maximum velocity, at the deepest point, was set to 0.07 m/s. The injection point was positioned at the channel centreline (y = 0.25 m) where the input D_0, the value of D_y at y = 0.25 m, was 2.40x10^{-5} m^2/s. The profiles of $U(y)$ and $D_y(y)$ were then calculated using the proportionalities described above ($U(y) \propto h^{1/2}$ and $D_y(y) \propto h^{3/2}$) – Figure 3.7 gives the profiles of U and D_y for the constructed channel.

Lateral profiles of concentration were calculated for x = 1 and 2 m (Figure 3.8). The concentration profiles show a stronger skew towards the shallower flow than the step channel case due to the greater difference in maximum and minimum transverse mixing coefficients. The model constraints were evaluated for the predicted concentration profiles; the results of which are show in Figure 3.9a & b, respectively, for the criteria, c_1 and c_2. The regions violating the constraints (grey shading) are compared to the raw transverse concentration profiles, shown in Figure 3.10a. The predicted profile $D_y(y)$ using Equation 3.1 is compared to the input profile in Figure 3.10b (Figure 3.7b shows the functionality of the input D_y compared to the channel depth). The constraining criteria significantly reduce the locations where the analysis is applicable compared to the spatially uniform and step channel cases. When the downstream concentration profile spreads beyond the transverse limits of the upstream profile, the fractional change in transverse concentration gradient causes the first criteria to be exceeded. This is visible in Figure 3.9a where the value of c_1 rapidly increases in the region y < 0.17 m causing the grey shaded region in Figure 3.10a to be located closer to the peak concentrations.

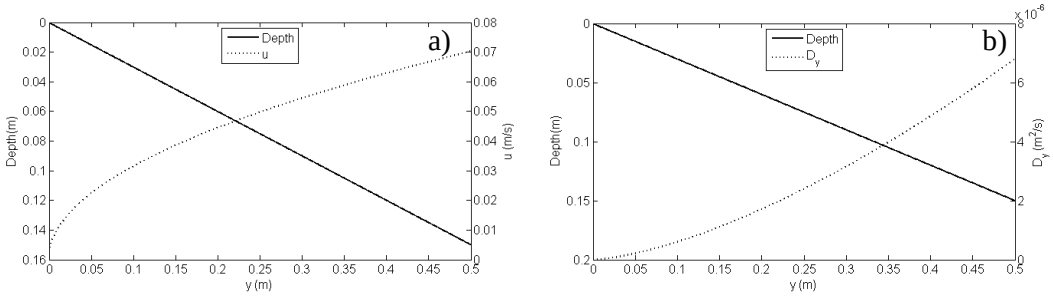

Figure 3.7: Transverse profiles of a) velocity and b) transverse mixing coefficient for the sloping channel formulation; where the depth is given by the solid line.

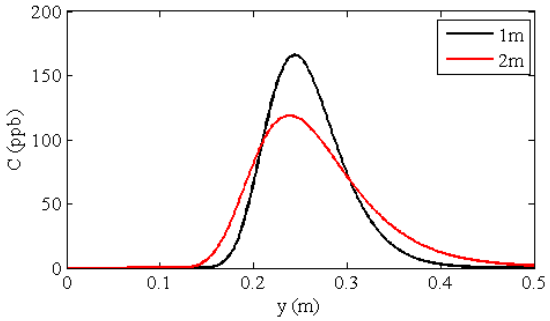

Figure 3.8: analytical steady-state concentration distributions using the sloping channel solution by Kay, 1987.

The predicted profile of $D_y(y)$ using Equation 3.1 (Figure 3.10b) shows that the modelling approach has difficulty when recovering values of D_y of a similar magnitude to the input. The predicted profile is similar in general trend to the input –showing an increasing value of D_y towards the deeper flow – but fails to provide values in the same order of magnitude.

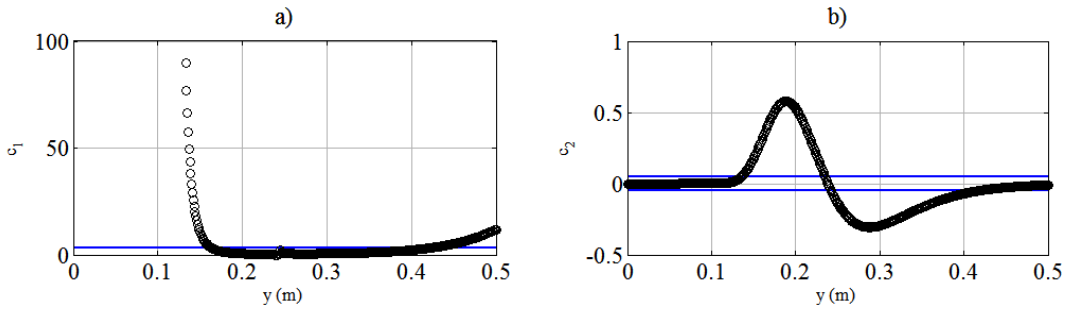

Figure 3.9: Flux-gradient analysis constraining criteria: a) the fractional change in gradient c_1 (black circles) where the horizontal line indicates the maximum permitted value; and b) the mean concentration gradient, c_2, where the region between the blue lines indicates the violating values, for the sloping channel formulation.

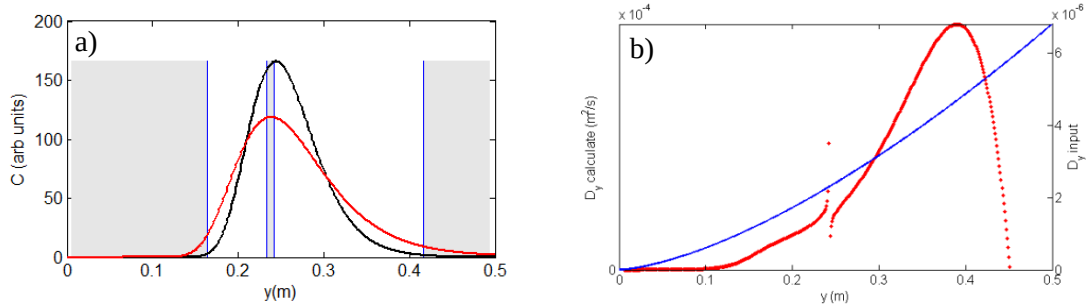

Figure 3.10: Constraining criteria are compared to the a) steady-state concentration profiles and b) the calculated profile of $D_y(y)$; where the grey shading indicates the violating regions and the analytical input is given by the blue line.

Conclusion

The calculation of a spatially variable transverse mixing coefficient proposed by Ghisalberti and Nepf (2005) using a flux-gradient analysis (Equation 3.1) fails to accurately recover the profile magnitude and shape of the input analytical solutions. It is, therefore, not applicable to real vegetated shear layer systems where the lateral concentration gradient, $\partial C/\partial y$, changes sign frequently due to erroneous data points and local heterogeneities. Note that the application to real data measured in laboratory conditions is evaluated in the Analysis Chapter.

4. Experimental Results

This chapter presents the results of the velocity and tracer measurements for the full and partial vegetation scenarios for the four vegetation types. The results are divided into four sections to facilitate comprehension and comparison between types. Firstly, the measured and calculated vegetation characteristics are compared in Section 4.1. Section 4.2 and 4.3 present the velocity processing and filtering techniques, respectively, employed to provide the final mean velocity profiles given in Section 4.4. Finally, section 4.5 presents the calibrated tracer results and should be viewed with Appendix IV and the accompanying disc which provides all of the raw tracer results.

4.1 Vegetation Characteristics

The real vegetation was characterized using the methods detailed in Appendix III. Stem population density per unit volume, N, stem diameter, d, and cross-sectional images were collected for the winter and summer season *typha*. Characterisation of the artificial vegetation did not required measurement given the geometric and morphological uniformity.

Table 4.1 provides the measured and calculated characteristics for the winter and summer *typha*. Stem diameter and density were measured at 10 longitudinal locations within the test section to estimate their variability; as such, the mean characteristic and standard deviation are presented. Note that the frontal area per unit volume was calculated for every 10 cm longitudinal section of the real vegetation. At least 130 stem diameters were measured for both types – where Figure 4.1 shows the distribution in stem diameter as a histogram for the

a) winter and b) summer seasons. Note that the solid volume fraction, Φ, for the real vegetation was calculated for each of the 6 sampling locations using the fractional volumetric occupation of the stems; where the stem diameter, d, was assumed to be vertical uniform, such that $\Phi = Nd^2\pi/4$ and the porosity, or void fraction, is $1 - \Phi$. The average diameter was thicker in the summer after the growing season and the range in diameter was also greater.

Table 4.1: Measured real vegetation characteristics with standard deviation.

Characteristic ± σ	Winter *typha*	Summer *typha*
Stem density, N (stems/m^2)	161 ± 72	192 ± 14
Mean stem diameter, d (mm)	8.38 ± 7.50	19.38 ± 9.08
Solid Volume Fraction, Φ(-)	0.012 ± 0.003	0.037 ± 0.012
Porosity, λ (-)	0.988 ±0.003	0.965 ± 0.012
Frontal area per unit volume, a (cm^{-1})	0.0278 ± 0.0073	0.0379 ± 0.0066

The solid volume fraction is only an estimation for the real vegetation given that: a) the calculation of d is an average of 130 stems, measured at the channel mid-depth; b) the mean stem diameter assumes a constant value with depth (where Figure 4.1c & d show the vertical variation of a with depth for the winter and summer, respectively); and c) the calculation of the total volume of vegetation assumes cylindrical stems – however the real diameter varied with depth. The non-cylindrical nature of the stems was mitigated for, in part, by measuring the stem diameter in the transverse plane, i.e. normal to the direction of primary flow. An example of the winter *typha* test section is shown in Figure 4.2a. The stems were sparsely distributed ($\langle N \rangle$ = 161 stems/m^2) compared to the two artificial types and the summer *typha*. The image shows the presence of dead matter and leaf litter on the channel bed as well as new stems (green shoots) distributed among the previous year's mature stems (light brown). A relatively large range in the stem diameter was recorded where d = 8.38 ± 7.50 mm. The range is attributed to the distinct difference in diameter between the mature stems and the new

shoots; where the minimum and maximum measured diameters were approximately 3.00 and 25.00 mm, respectively.

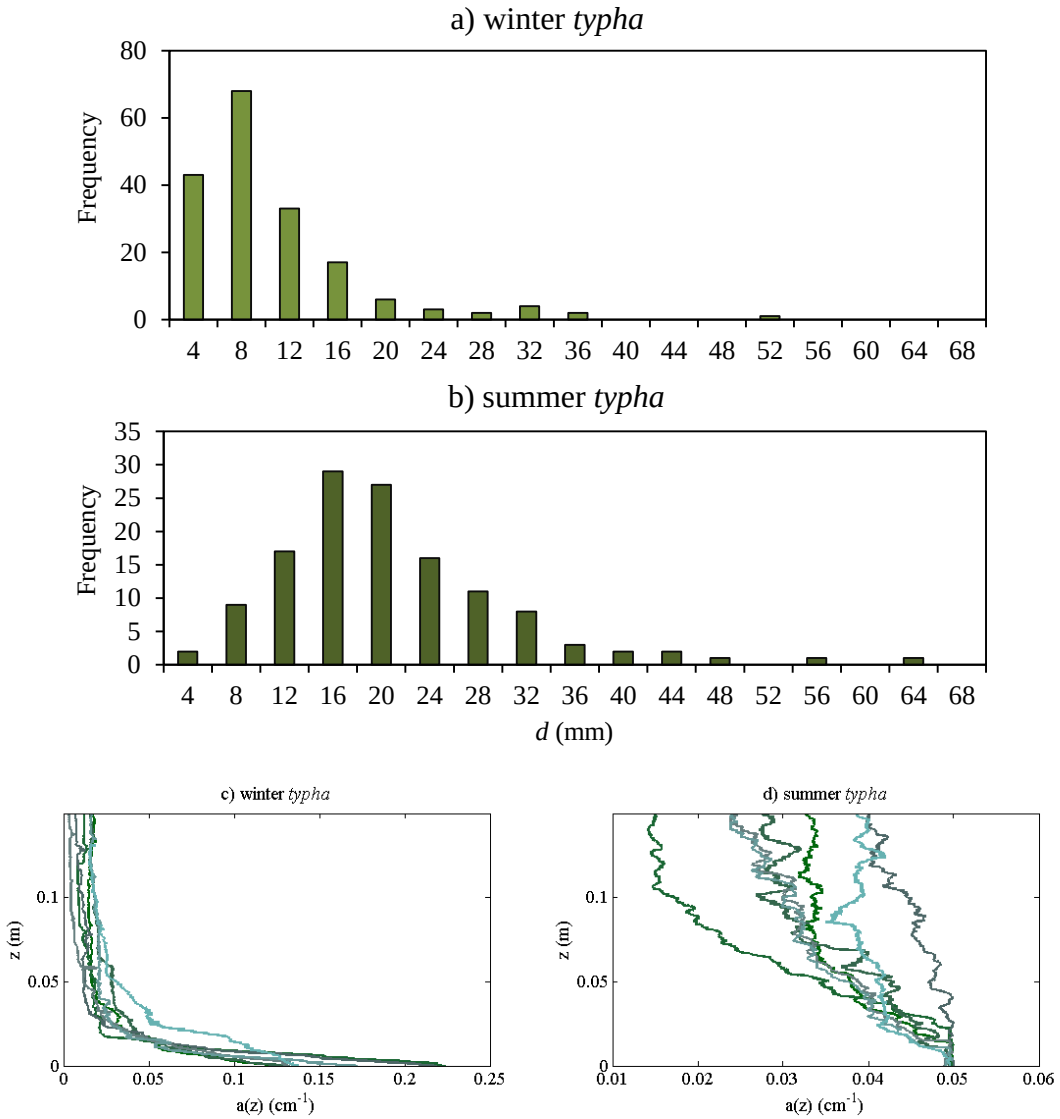

Figure 4.1: Histograms of the stem diameter frequency for the a) winter and b) summer *typha* and variation in frontal area per unit volume with depth, $a(z)$, for c) winter and d) summer.

Table 4.2: Comparison of all vegetation characteristics.

Parameter ± σ	High Density Artificial	Low Density Artificial	Winter *typha*	Summer *typha*
Diameter, d (mm)	4.00	4.00	8.38 ± 7.50	19.38 ± 9.08
Stem density, N (stems/m^2)	1594	398	161 ± 72	192 ± 14
Solid Fraction, Φ	0.020	0.005	0.012 ± 0.003	0.037 ± 0.012
Frontal area per unit volume, a (cm^{-1})	0.064	0.016	0.0278 ± 0.0073	0.0379 ± 0.0066

Figure 4.2b shows the full vegetation test section for the summer *typha*. The stems were more densely populated than the winter type (N = 192 stems/m^2) and the installation was more uniformly distributed with a standard deviation of only ±14 stems/m^2 – compared to the winter *typha* density variation of ±72 stems/m^2. The mature stems in the summer case had a large mean stem diameter (d = 19.38 ± 9.08 mm) and a smaller deviation (e.g. Figure 4.1b). As such, the density and diameter, the summer *typha* was considered more uniform than the winter type. Table 4.2 provides a comparison of characteristics between the artificial and real vegetation types.

The larger solid volume fraction in the summer, Φ = 0.037 compared to 0.012 in winter, is attributed to the greater mean stem diameter and population density. The summer *typha* was the most occupying vegetation type, while the winter *typha* had an intermediary solid volume fraction between the high and low density artificial types – Φ = 0.02 and 0.005, respectively. However, the frontal area per unit volume of the summer *typha* is comparable to that of the winter type suggesting that the thicker stems have a greater spacing between them than in winter – although the winter *typha* was more uniform with depth (Figure 4.1c). This also implies that the population density between types may be more comparable than appears in Table 4.2. Moreover, there may have been comparable regions between the two seasons given the standard deviation in N.

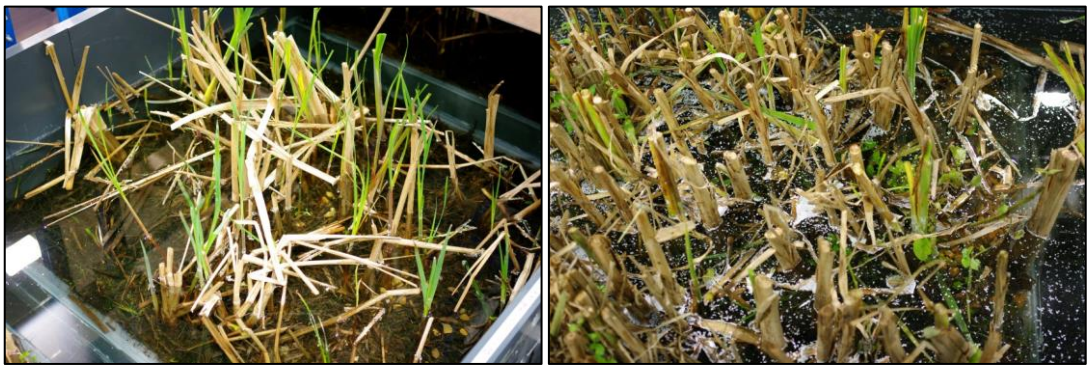

Figure 4.2: Image of the a) winter and b) summer *typha* test section in the full vegetation scenario.

4.2 Determining the Spatial Limits of Acceptable Velocity Data

4.2.1 Introduction

The temporal mean-longitudinal velocity profiles measured using the *Metflow UVP* probes exhibited data that were considered erroneous in the extreme spatial limits of the profile i.e. at the near-probe location and at the channel surface. Unreliable mean vertical or transverse profiles of longitudinal velocity, $U(y)$ and $U(z)$, limit the precision of spatial-average velocity calculation and further flow characterization. Two anomalies were apparent in the temporal mean vertical profiles of velocity recorded from both the bed and surface mounted transducers. Firstly, the velocity recorded adjacent to the UVP transducer tended towards 0 mm/s – even in locations of relatively high velocity. It is not known whether the disturbance was caused by the physical obstruction of the device or measurement limitations at close proximity to the transducer. Secondly, velocity recorded in the vicinity of the channel surface also reduced towards zero when measured from the channel bed.

This section describes a supplementary test that was conducted to define the regions of the mean velocity profiles that were considered erroneous and therefore, viable for discarding prior to further averaging and analysis.

4.2.2 Supplementary investigations

The low-density, emergent, artificial vegetation (N = 398 stems/m^2) was installed in a 0.300 m wide, tilting Armfield flume with a uniform flow depth, h = 0.1500 mm. Vertical profiles of stream-wise velocity were recorded using the 4 MHz *Metflow UVP* probes at 30 Hz until 5000 samples were collected (~170 s). Velocity channel spacing, w, was 0.74 mm intervals. The transducer angle to the bed normal was constrained at 10° by a pre-existing inspection hole

drilled into the bed of the flume. Vertical profiles of longitudinal velocity, $u(z)$, collected between the emergent rigid straws were then compared for three measurement cases, as shown in Figure 4.3.

In case 1, $u(z)$ was recorded using a bed-mounted probe submerged beneath the defined channel bed (z_{probe} = -1.4 mm) where the immediate water column above the probe was unobstructed, i.e. a clear water column – and is referred to as the *bed profile*. In case 2, a second transducer was inserted into the flow, beneath the water surface (z = 145 mm), directly in the path of the ultrasound beam emitted from the bed-mounted probe. The same velocity profile in case 1 was then measured with the presence of this new *obstruction* (light grey rectangle in Figure 4.3) and is referred to as *bed + obstruction*. Finally, in case 3, $u(z)$ was recorded from the water surface using the newly inserted upstream probe to compare the surface and bed profiles; referred to as the *surface profile*. In all cases, an upstream straw was removed to provide access for the transducer and prevent unwanted sound reflections.

The *surface cut-off* distance, d_s, was defined as the distance from the water surface to the first point at which the temporal mean velocity deviates by two standard deviations, σ_U, from the local spatial mean (defined below). The *near-probe cut-off* distance, d_p, was defined as the distance between the transducer head and the point at which the mean velocity lies within two standard deviations of the local spatial mean. The values of d_s and d_p were determined to define the spatial limits of acceptable data along the UVP profiles.

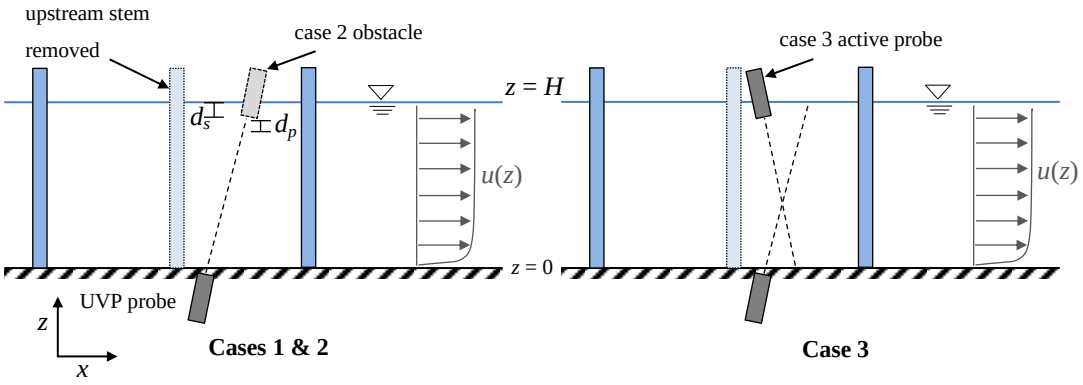

Figure 4.3: The experimental setup in the 300 mm wide flume to test the *Metflow UVP* profile validity.

4.2.3 Velocity profile truncation results

Vertical profiles of the temporal mean, longitudinal velocity are presented in Figure 4.4 for Q = 2.27 l/s. The brown, blue and dotted lines indicate the channel bed, water surface, and transducer locations, respectively. The area mean longitudinal velocity in the example (Q/A) is 50.4 mm/s; and is recovered well using the UVP probes. Figure 4.4a shows that there was not a significant difference in profile shape between the bed profile and bed + obstacle cases (black and green data points). The two bed cases provide an example of the measurement difficulties close to the water surface. The surface profile indicates that the velocity measurement does not become valid until approximately 6.56 mm from the transducer head (Table 4.3). The shaded regions in Figure 4.4b & c represent two spatial standard deviations from the mean velocity calculated in the range 110 < z < 130 mm. The penultimate data point contained within the shaded region closest to the surface or the probe was then used to calculate the distance d_s or d_p.

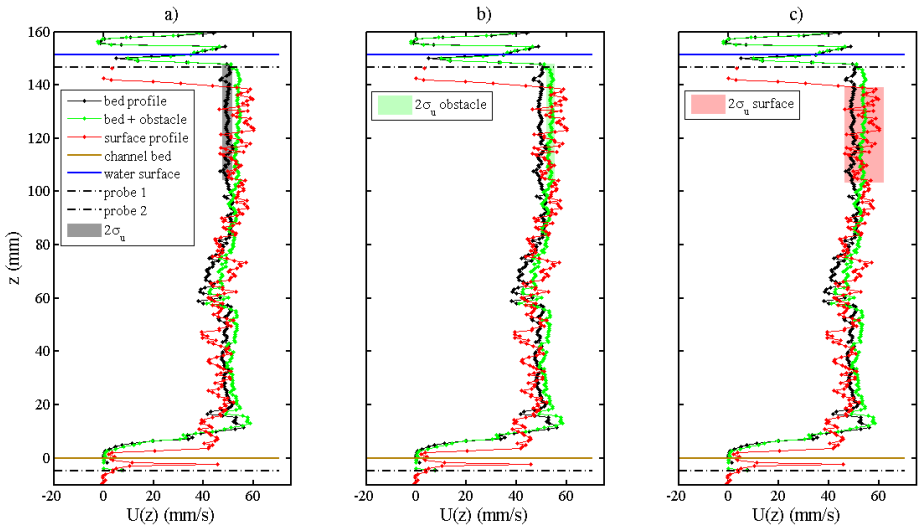

Figure 4.4: Mean vertical profiles of velocity for 2.27 l/s measured in the low density, emergent artificial vegetation for a) case 1, b) case 2 and c) case 3 in the supplementary testing. The shaded regions indicate two standard deviations from the local mean.

There is also a disparity in shape between the profiles measured from the bed (green and black) and the surface (red) in the region of the channel bed (8 mm ≥ z ≥ 0 mm). Given that the velocity is expected to be zero at the channel bed, one cannot conclude with certainty, that

the profile shape measured at the bed is attributed to a measurement limitation or a physical phenomenon.

It can be seen that the defining criteria for d_p is reached at approximately $z = 140$ mm; where the *surface profile* (red data) is contained within the red shaded region (within two standard deviations of the local mean). The *surface cut-off* distance can be seen between the *probe 2* location and the *water's surface* location (150 mm $\geq z \geq$ 147.5 mm). The test cases presented were then repeated for two further channel discharges to elucidate the effects of mean flow velocity on the calculation of d_s and d_p and provided a more accurate definition of the acceptable velocity window (Table 4.3). The distances d_s and d_p do not differ, within measurement accuracy and error, between the two bed-mounted probe tests and there is no correlation with discharge.

Further, given the range in values of d_s and d_p ($d_s = 3.75 \pm 1.38$ mm, $d_p = 6.56 \pm 0.66$ mm) and considering their respective standard deviation, values of 5.1 mm and 7.1 mm are suitable for d_s and d_p, respectively. There was, however, variability in the nature of the cut-off distances apparent for the real velocity profile data and thus, a near profile cut-off distance of 10 mm was chosen to ensure that no erroneous data was included in further analysis. These cut-off values represent a range of confidence over which the mean vertical profiles will not contain erroneous data allowing depth-average values of velocity to be accurately calculated.

Table 4.3: Profile cut-off distances from the surface and transducer are given for four test discharges. The mean cut-off distances can be used to define the acceptable region of the velocity profile data.

Discharge (l/s)	Velocity (Q/A) (mm/s)	Surface cut-off d_s (mm ± σ)	Near-probe cut-off d_p (mm ± σ)
0.91	20.2	4.5	6.92
1.36	30.2	2.3	5.84
2.27	50.4	5.3	6.20
2.27 (repeat)	50.4	2.9	7.29
mean	-	3.75 ± 1.38	6.56 ± 0.66

The new cut-off limits for the UVP vertical profiles were applied to the mean velocity data recorded in the low density, full artificial vegetation scenario for $Q = 2.00$ l/s. The comparison

between pre- and post-cut-off profiles is presented in Figure 4.5 for vertical profiles of temporal mean longitudinal velocity. Despite the loss of information at the channel bed and surface, the final profile describes the general trend in mean velcoity well. Further, the impact on the calculated depth-mean longitudinal velocity is minimal given that the velocity profiles in emergent cyclinders are approximately uniform with depth; where U = 15.4 and 14.2 mm/s for the cropped and un-cropped profiles, respectively.

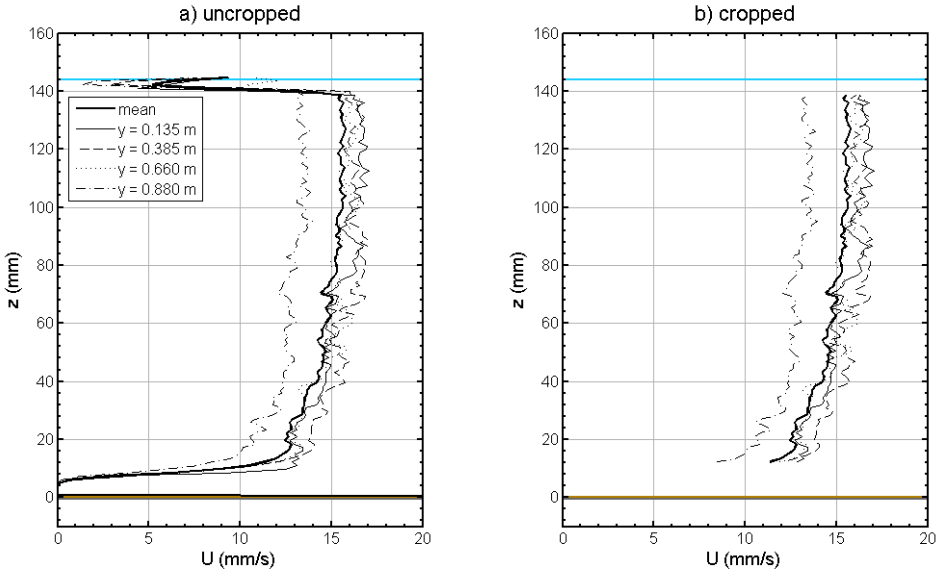

Figure 4.5: Comparison of uncropped and cropped mean vertical profiles recorded in the full, low density, artificial vegetation at 2.00 l/s using the spatial limits of acceptable velocity data. The water surface, channel bed and probe location are indicated by the blue, brown and grey lines, respectively.

4.3 Velocity Filtering Evaluation

This section details the filtering technique applied to the raw longitudinal velocity to minimise the effects of erroneous data and "spikes". Four filtering methods were compared to assess the impact of the propagation of data spikes. The processing of the velocity profiles highlights some of the limitations of ADV and validates the characterisation using bulk flow statistics.

4.3.1 Introduction

For comparative reasons, it is necessary to describe the flow characteristics of a test using a bulk parameter such as the temporal and/or spatial average velocity from a range of velocity time series[3]. Further, the temporal and spatial average longitudinal velocity profile (e.g. $U(y)$ or $U(z)$) is commonly presented to provide information regarding the flow dynamics and characteristics of a particular system, e.g. the flow profile associated with a vegetation stem.

Paramount to characterization using averaged velocity profiles is an appropriate and precise method for processing the raw velocity time series data. Raw time series data can be averaged without any processing but may not be an accurate representation of the system in which it was recorded. Erroneous data, such signal reflections and bias all contribute to what is known as data spikes. Detecting and mitigating against erroneous data propagation is, therefore, an important part of the raw data processing.

Both ADV instruments (*Vectrino II* and the *Metflow UVP*) collected raw data that contained data spikes to a certain degree. The processing of this raw data time series is referred to as *filtering.* As such, a description of the raw data output for the two instruments and a comparative analysis of the potential velocity filtering methods are given below.

4.3.2 Raw data collection

Recall that the *Vectrino II* collected 3-dimensional velocity records over a 35 mm profile range between 1 and 200 Hz (Figure 4.6a). The *Metflow UVP* was used to collect 1-dimensional velocity time records over a prescribed profile range in (Figure 4.6b) between 1 and 30 Hz depending upon the flow conditions; where the minimum sampling time was set by the beam length, channel spacing and width. Figure 4.6a & b shows the configuration of the ADV instruments. The *Vectrino II* had a measurement precision of 0.05 mm/s and the

[3]Here the spatial and temporal average longitudinal velocity, or simply *mean velocity* is averaged over multiple locations along the profile length. This mean, therefore, requires the spatial averaging of several velocity time series.

Metflow UVP had a precision set by the operation parameters – approximately 0.6 mm/s in all cases. Figure 4.6c gives examples of 3 time records of longitudinal velocity, $u(t)$, along the same ultrasound beam profile using the *Metflow* device; where erroneous data is visible at 50, 60, 80 and 125 s.

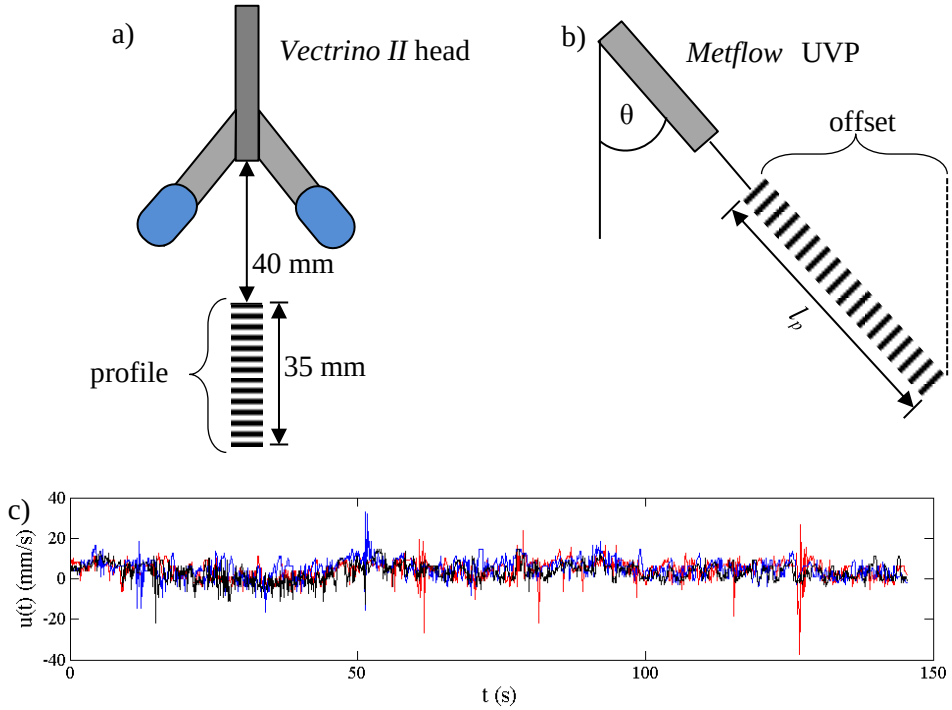

Figure 4.6: Measurement window of the a) *Vectrino II* and b) The *Metflow UVP* profilers. The *Metflow UVP* records velocity over a profile length l_p mounted at an angle θ to the direction of flow. c) Example longitudinal velocity time record from the *Metflow UVP* at three locations.

4.3.3 Erroneous data and spikes

"Spikes" is used here to describe any data that may be considered erroneous and was identified as data that deviated significantly from the velocity trend or local temporal mean. In some cases spikes were recorded at values up to 10 times the temporal mean. These values were not accounted for but may be attributed to the measurement system, e.g. poor data collection in regions close to the transducer head, of poor seeding density, or in regions of significant reflection due to complex bed geometry.

Figure 4.7 gives an example of spikes events recorded in a longitudinal velocity time series using the Metflow UVP probes (blue circles), highlighting the difficulty in distinguishing

spikes from the surrounding acceptable data. The occurrence of erroneous data of this type was prevalent in locations of strong ultrasound echo, from the channel bed, surface or adjacent obstacles and signal interference.

Erroneous data also presented as 'zero value' data point readings and reduced the magnitude of the temporal mean velocity. Zero-value noise is attributed to the absence of, or reduction in sufficient seeding particles in the measurement volume. ADV techniques rely on the presence of seeding particles within the sampling volume during the measurement. If the ultrasound beam samples a volume void of seeding particles then the apparatus returns a reading of 0 m/s. This phenomenon is aggravated when the sampling rate is increased and the density of seeding is sub-optimal; since the ultrasound pulse is more likely to sample in an empty volume.

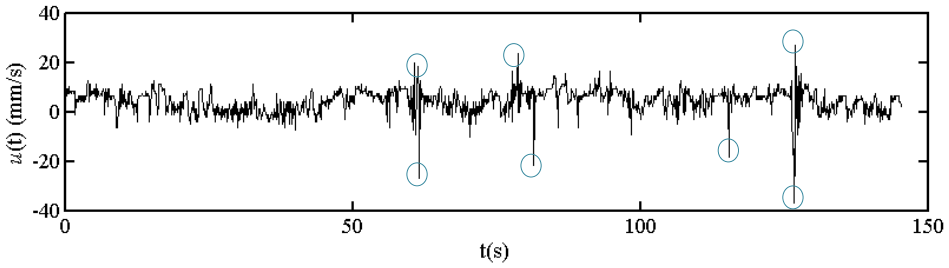

Figure 4.7: Examples of spikes (blue circles) in the velocity time series, $u(t)$.

4.3.4 Filtering methods for velocity data

Data filtering will inherently remove real data; however, the degree and impact of this depends on the chosen technique and on the volume of data collected. All filtering methods therefore seek to accurately distinguish between what is noise and what is real data; where a compromise must be made between vigilant spike removal and distortion to the valid results. Four data filtering methods were compared; the removal of zero-values (no-zero), standard deviation filtering (STD), median filtering (MED), and phase space filtering (PS) – where the time series shown in Figure 4.7b was used as the filtering test example.

a) No-zero filtering

The most basic filtering technique is the removal of the zero-value velocity recordings. This method is only appropriate for filtering velocity recorded in the primary flow direction, where stationary particles in the longitudinal direction are not expected. Zero velocity values could be replaced with a velocity reading from the adjacent time step; however, here the zero velocity readings are simply ignored in the calculation of the temporal mean. Sufficient data collection ensures that the omission of these values did not have a substantial impact on the accuracy of the temporal mean velocity. However, zero-value filtering still requires the removal of data spikes; where approximately 5% of the raw velocity data contained zero-value readings.

b) Standard deviation filtering

The standard deviation filter creates two thresholds about the temporal mean velocity, U, given the temporal standard deviation, σ_u. The standard deviation and U of the raw time series are first calculated. Every time record at each spatial location along the velocity profile is then filtered according to the threshold criterion, $n_{std} = 2\ \sigma_u$; if $u(t) > U + 2\sigma_u$ or $u(t) < U - 2\sigma_u$ then a value of '0' is returned. An example of the final standard deviation of the filtered time series is plotted in Figure 4.8a for increasing values of n_{std}. The standard deviation increases with n_{std} until all of the raw data is contained. The filter threshold of $n_{std} = 2$ was selected as this includes 95% of the data – assuming that the data probability distribution is Gaussian. The standard deviation of the raw velocity time series Figure 4.7b is 4.44 mm/; while the standard deviation of the equivalent time series after the $\pm 2\sigma_u$ threshold was applied is 3.79 mm/s.

Figure 4.8b shows the original raw time series with the inclusion of the $+2\sigma_u$ and $-2\sigma_u$ filter thresholds and the filtered time series is shown in Figure 4.8c. In the example given there are 54 zero velocity recordings (1500 total samples) before filtering and 101 zero velocity recordings after filtering implying that 47 data points violated the filter criteria. The temporal mean velocity for the raw and filtered velocity data are 4.44 and 4.53 mm/s, respectively. In

this example the temporal mean velocity of the filtered data is higher than the pre-filtered as the large negative values of velocity have been omitted. The standard deviation filter is a useful technique as the limits of the filter are specific for each time series (since U and σ_u are calculated individually). It is also computationally less demanding than other filtering techniques (see below). The method does, however, assume that the data probability distribution is Gaussian and that 95% of the data lies within $\pm 2\sigma_u$. Further, the method of calculating the pre-filtered mean velocity includes the erroneous data and inaccurately affects the absolute value of the standard deviation.

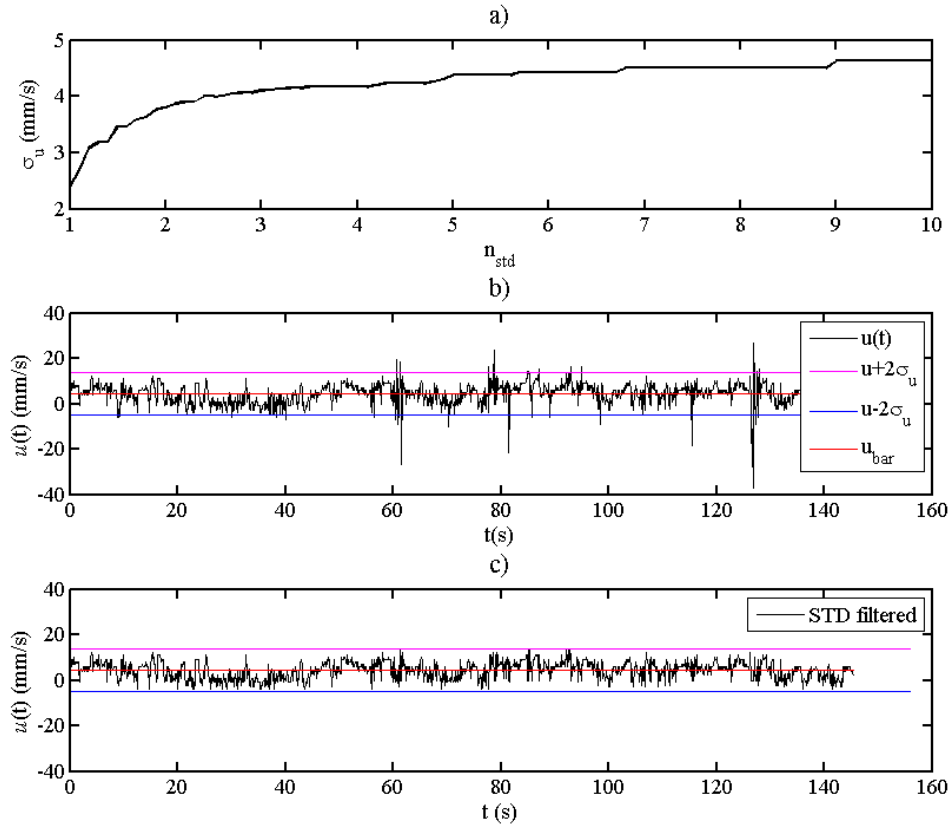

Figure 4.8: a) The effect of increasing the STD filter threshold, n_{std}, on the standard deviation, σ_u, of the velocity time series. The example raw velocity time series data file is plotted b) without filtering including the $\pm 2\sigma_u$ limits and c) after STD filtering.

c) Median filtering

The median filter technique computes the local median value of a number of data points within the time series. Similarly to a running average technique, the median filter replaces the value of u_i with the median value of u_{i-n} - u_{i+n}, where n_m is the specified range over which the

median is calculated, or *median filter parameter*. The technique is commonly used in image analysis in 2-dimensions to reduce signal noise whilst retaining important local information (Justusson, 1981). A running average would not be applicable in this application, as erroneous data would alter the local average around that point and the data would be smoothed.

The median is computed as the middle value of the range of numbers specified by n_m. For example, if the range of numbers for $n_m = 5$ were [0 7 3 3 4] then the median is 3, as this is the middle number between 0 and 7. Note that, if n_m is an even integer then the median is taken as the mean of the middle two numbers. Running median filters are advantageous as the general trends are not lost even if a significant spike occurs within the range of n_m. For example; let $n_m = 5$, and the data = [3 3 4 16 3]. The median of this set is still 3 despite the data spike of 16. Reducing the range of n_m has the effect of retaining data close in magnitude to that of a spike but may also allow "groups" of noise to pass through the filter.

Figure 4.9a shows how the standard deviation, σ_u, of the filtered series decreases as the median filter parameter is increased. The standard deviation will naturally decrease as the range over which the median filter operates increases as more data points are replaced by an increasingly less local median. A median filter parameter of $n_m = 5$ was chosen as a suitable value as it retains appropriate turbulent information. Higher values of n_m would reduce the reliability of the turbulent statistics; while a smaller value of n_m would potentially increase the number of spike events in the filtered profile.

The test raw velocity time series (Figure 4.7b) was filtered using $n_m = 5$ and the resultant filtered time series is plotted in Figure 4.9b. The temporal mean velocity calculated from the median filtered time series is 4.6 mm/s. The mean velocity using the median filter method is comparable to the values calculated without any filtering (4.4 mm/s) and with the standard deviation filter (4.5 mm/s). The result shows that the MED filter technique significantly reduces the appearance of data spikes. The technique does, however, incur a degree of data smoothing that the STD technique does not provide. It must be noted that, when the

measurement error is considered (±0.37 mm/s), the difference in mean velocity calculated between the no-zeroes, STD and MED techniques is insignificant.

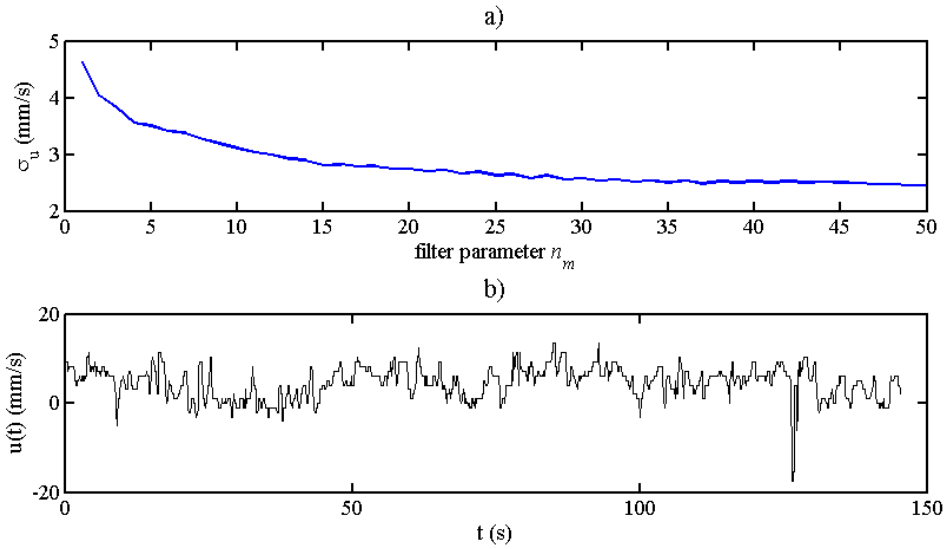

Figure 4.9: Median filter results for a) change in standard deviation of the velocity time series with increasing MED filter parameter, n_m, and b) median filtered velocity times series using n_m = 5.

d) Phase Space filtering

The Phase Space filtering (PS) technique operates using a similar principle to the STD filter approach (Goring and Nikora, 2002). A 3-dimensional-filter space is constructed for each velocity time series. This 3-dimensional space, known as *phase space*, is generated by computing the first and second time derivatives of the velocity data, du/dt and d^2u/dt^2. The velocity, u, is then plotted in phase space against du/dt and d^2u/dt^2 to improve visualization of the erroneous data; where the higher frequency spike data appears further from the cluster. Data that is considered a spike has a relatively large first and second derivative and, therefore, becomes more distinguishable from the valid data within phase space.

Goring and Nikora (2002) developed the technique and showed that "valid" data grouped together as a cloud in phase space (Figure 4.10a). A three-dimensional ellipsoid defined by statistical criteria is constructed to encompass the valid data cloud. The dimensions of the ellipsoid in Figure 4.10a are calculated using the maximum expected values, M, of u, du/dt and d^2u/dt^2. These expected values, like the STD technique, are calculated from their respective standard deviations and rely on the principle that, if a statistically significant

number of data have been collected, the maximum expected value of a data set is a multiple of the standard deviation i.e. $M = \sigma (2 \ln m)^{1/2}$, where m is the number of data collected.

Goring and Nikora's development was to increase the precision of the technique by making the process iterative. Data falling outside the constructed ellipse (red dots in Figure 4.10a) were discarded and the process was repeated. The iterations continued until all of the filtered data remained within the ellipsoid limits. Goring and Nikora (2002) suggest a linear interpolation method for replacing the identified noise. However, in this approach these values are replaced with values of 0 mm/s and are subsequently omitted during averaging e.g. zero-value filtering. The relatively large sample size enabled these values to be discarded and eliminated the potentially inaccurate process of interpolation.

The test raw velocity time series (Figure 4.7b) was filtered using the PS technique and is presented in Figure 4.10b. The temporal mean velocity after filtering is 4.59 mm/s. The data series in Figure 4.10b shows the retention of some spikes; however they do not exceed the maximum and minimum expected values. In this example, the iterative PS filtering technique discarded 54 data points – 7 more than the STD filter – and performed 5 iterations before all of the data remained within the statistical limits of the ellipsoid.

PS filtering is more accurate than the MED filter approach as it eliminates the effects of local data smoothing. Further, the construction of phase space provides a more rigorous assessment of erroneous data. Defining the data cut-off limits is subjective for the STD and MED filter approaches; through either the $2\sigma_u$ range or given by the limits of the median filter parameter n_m. However, the PS filter defines these limits more accurately through the iterative process.

a) **Phase Space visualization**

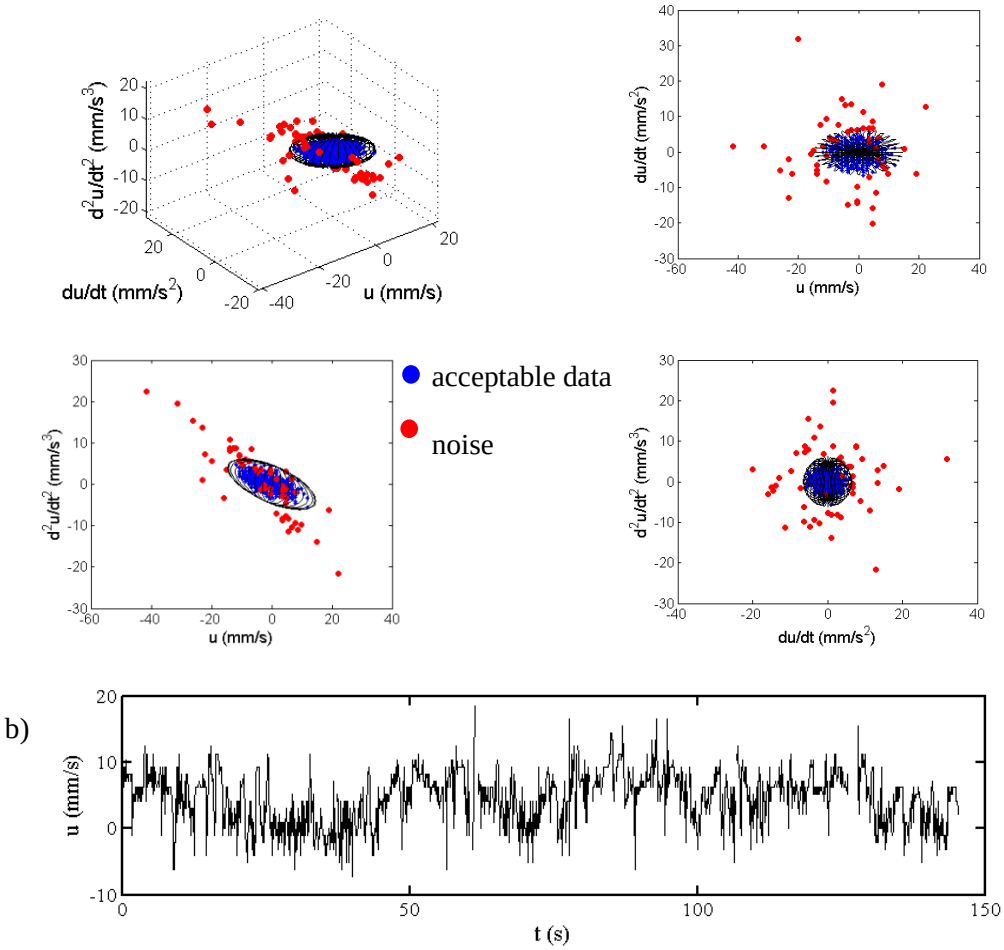

Figure 4.10: a) Three-dimensional visualization of the phase space filtering method plotting $u(t)$ against the du/dt and d^2u/dt^2. b) The phase space filtered data.

e) Filtering conclusions

A comparison between the STD, MED and PS velocity filtering techniques was made and is shown in Table 4.4. The data was calculated using the depth-mean velocity values measured using the *Metflow UVP* profiler in the low density, full artificial vegetation cases. The mean velocities are, therefore, the mean depth-average of four vertical profiles recorded across the channel (see section 4.4 and Figure 2.15b).

The STD filter allows the largest amount of data to pass through since the filter boundaries are calculated using the data that is considered noise; the noise affects the mean and therefore, the standard deviation. The velocity calculated using the MED filter method, U_{MED}, is comparable to the STD method. Reducing large spikes by computing the local median was

shown to have a similar impact on the depth mean velocity as using a cut-off defined by the standard deviation of the data. All of the depth mean velocities calculated using Phase Space technique, U_{PS}, are lower than U_{STD} and U_{MED} implying that fewer velocity spikes are passed through the filter. Figure 4.11 compares the filtered velocity time series for the three filtering methods.

Table 4.4: Comparison of the area mean velocity (Q/A) to depth-mean velocity for the standard deviation (STD), Median (MED) and Phase Space (PS) filtering techniques.

Q (l/s)	$U_{Q/A}$ (mm/s)	U_{STD} (mm/s)	U_{MED} (mm/s)	U_{PS} (mm/s)
1.00	6.7	6.7	6.6	6.4
1.50	10.1	12.6	12.6	11.7
2.00	13.5	15.9	16.0	15.4
2.50	16.8	20.7	20.7	19.9
3.00	20.2	24.3	24.4	23.6

Figure 4.12 compares the filtered profiles supporting the differences between techniques given in Table 4.4. The temporal mean longitudinal velocity using the phase space filter (triangles) is reduced relative to the Median (black circles) and Standard Deviation (diamonds) filters. The difference in profile trend is minimal across all filter techniques and the absolute difference in velocity at any given location within the profile is no more than 3 mm/s. The velocity profiles for all three filtering methods are very similar considering that the measurement error in velocity is (± 0.37 mm/s).

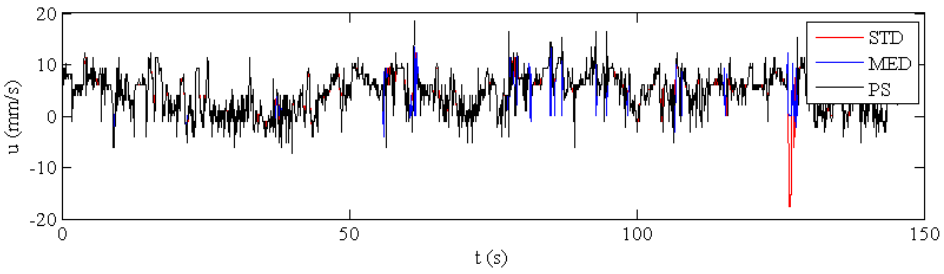

Figure 4.11: Comparison of the three filtering techniques for the original times series recorded in the low density artificial vegetation.

The standard deviations, σ_u, of the test velocity time series using the three filtered methods (*STD*, *MED* and *PS*) are compared in Table 4.5 with the standard deviation prior to filtering,

σ_{raw}. The standard deviation from the *PS* filtering is the second largest after the raw data, suggesting that the data is sufficiently filtered minimizing the loss of turbulent characteristics.

The *STD* and *MED* methods both show respective reductions in the value of σ_u, suggesting that turbulent information is sacrificed to reduce the occurrence of noise. The median filter method replaces spike data with the local median and thus shows the biggest reduction in σ_u. Given the considerations for spike reduction, discharge recovery and turbulence retention, the *PS* filtering technique was selected as the appropriate data filtration method prior to analysis and presentation.

Table 4.5: The standard deviation of the filtered time series given in Figure 4.7b for different filtering techniques.

σ_{raw} (mm/s)	σ_{STD} ($\pm 2\sigma_{raw}$) (mm/s)	σ_{MED} ($n_m = 5$) (mm/s)	σ_{PS} (mm/s)
4.62	3.79	3.50	3.98

The similarity in vertical profiles of mean longitudinal velocity and depth mean velocity between the three filtering techniques indicates that there is not a dramatic impact on the results and interpretation of velocity given any of the filter methods. Figure 4.11 also shows that, for the example time series used in this section, there is little difference in the filtered time series between the three methods. That considered; the phase space filtering technique was judged the more appropriate filtering method as it yields fewer spike events – thus retaining as much time series data as possible – and matches most accurately to the area mean velocity when the vertical velocity profiles are integrated. Note that the unusual profile behaviour for the 1.00 and 1.50 l/s cases – showing an increase in velocity towards the channel surface – has also been observed by other studies in low velocity emergent vegetation. Lui et al. (2008) also measured vertical velocity profiles in emergent, rigid cylinders and found that, for low velocity ($U < 0.1$ m/s), $U(z)$ exhibited distinct profile inflection towards the channel surface.

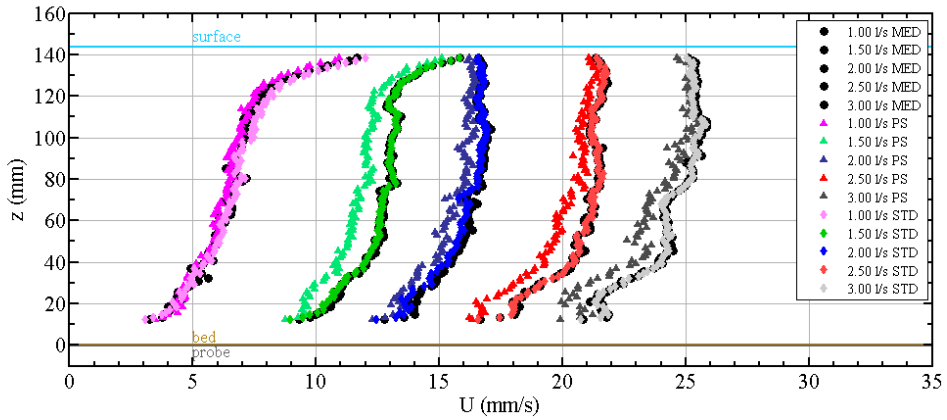

Figure 4.12: Vertical profiles of U are given for the Median (circles), Phase Space (triangles) and Standard Deviation (diamonds) filtering methods. The spatial mean is the average of 4 vertical profiles recorded at y = 0.135, 0.385, 0.660 and 0.880 m at the downstream measurement location, in the low density, artificial full vegetation.

4.4 Mean Velocity Profiles

This section presents the temporal mean vertical and horizontal profiles of longitudinal velocity, $U(z)$ and $U(y)$, for the two test scenarios (full and partial vegetation) and the four vegetation types. The results have been collated based on the test scenario, i.e. full and partial vegetation, for comparative reasons. The data has been filtered using the Phase Space filtering technique and temporally averaged for every velocity channel omitting zero velocity readings. The above sections describe the profile extraction (4.2) and filtering techniques (4.3) that were applied to the raw data.

Note that the differences in instrument and collection methods represent the development process of the experimental method over a sustained period (1-2 years). As such, the mean velocity profiles do not match in absolute range between types but have been collected such that general profile trends and bulk hydrodynamic characteristics may be compared. In all cases the specific sampling methods (i.e. surface, bed or transverse mounting of the probe) and ADV instrumentation (*Metflow UVP* or *Vectrino*) are detailed.

4.4.1 Full vegetation velocity profiles

The profiles of $U(z)$ and $U(y)$ recorded in all of the full vegetation tests are presented in this subsection. In the high-density artificial tests (N = 1394 stem/m^2) the *Vectrino II* probe was employed. Poor instrumentation calibration demanded that only the velocity at the mid-depth could be certified as reliable and data beyond the mid-depth was considered erroneous. Therefore, the transverse profiles of velocity in the low-density artificial vegetation tests were computed by calculating the temporal mean, mid-depth velocity at each transverse measurement location.

The *Metflow UVP* profiler was employed for the remaining vegetation types (high density artificial and winter and summer season *typha*). Only the vertical profiles of $U(z)$ are provided for the *typha* tests as the heterogeneity in stem distribution of the real vegetation stems prevented the un-attenuated transverse propagation of the ultrasound through the water column. However, the vertical profiles of longitudinal velocity were measured in sufficiently sparse locations that their recordings were considered valid. Note that an accurate estimate of mean longitudinal and transverse velocity was also calculated using tracer pulse injections – these findings are discussed in more depth in the following Analysis Chapter.

a) Artificial vegetation – high density

The transverse profiles of temporal mean, mid-depth velocity measured in the high density artificial vegetation are presented in Figure 4.13. Profiles were recorded using the *Vectrino II* device at 9 transverse locations across the flow at the upstream measurement site.

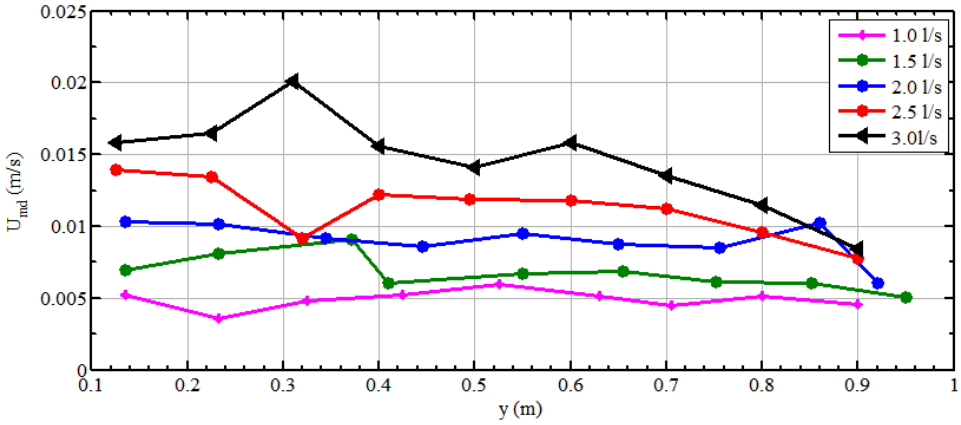

Figure 4.13: Mid-depth temporal mean longitudinal velocity, U_{md}, recorded in the high density artificial vegetation.

b) Artificial vegetation – low density

Longitudinal velocity was measured using *Metflow UVP* device and eight probes were employed – inserted into the channel walls and bed to minimize the local flow disturbance (Figure 4.14). To maintain velocity magnitude resolution – and to minimise error – the ultrasound beam length was reduced; where recording the full transverse profile of velocity, $U(y)$, using a single probe would have compromised on the measurement accuracy. Employing two transducers from either side of the channel allowed a complete transverse profile to be measured. Further, two profiles of the same transverse location were needed to construct a complete transverse velocity profile given the attenuation in ultrasound velocity power.

Vertical profiles of longitudinal velocity, $U(z)$, were recorded from the bed at four transverse locations between vegetation stems (Figure 4.14). The profiles of $U(y)$ recorded at the upstream and downstream locations are presented in Figure 4.15. Profiles recorded from either side of the channel are distinguished using the black and blue lines, respectively. Figure 4.17 provides the four profiles of $U(z)$ (feint lines) and the mean vertical profile, $\langle U \rangle(z)$, of the four locations (thick line) for the 5 cases. The brown and blue horizontal lines indicate the channel bed and water's surface, respectively. The location of the probe's head is indicted with the grey horizontal line. Note that the depth scale, z, is the distance in mm from the base

of the vegetation stems. The feint profiles lines for the four transverse locations have been included to provide an indication of the spread in data across the channel reach.

The transverse profiles of $U(y)$ are attenuated towards the limits of the measurement window; where approximately 300 mm of the transverse profiles is valid. Figure 4.16 compares the transverse velocity profiles for 3 discharges (1.00, 3.00 and 7.50 l/s) in the region $0 < y < 400$ mm. The close-up plot demonstrates the cyclic nature of the mean longitudinal velocity about the regular artificial stems. The following chapter provides a method for extracting meaningful values of temporal and spatial channel mean longitudinal velocity given both the cyclic nature and attenuation of $U(y)$.

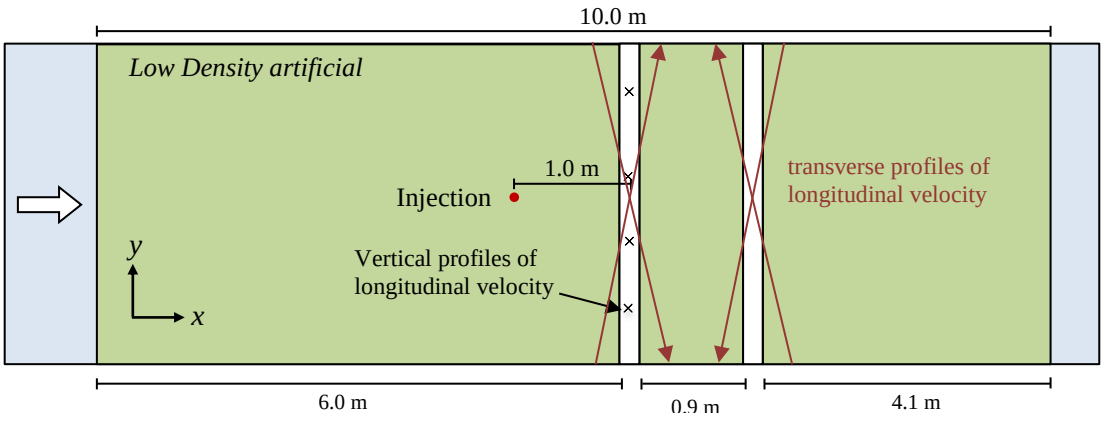

Figure 4.14: Plan view longitudinal velocity measurement method for the full vegetation, low density artificial scenario.

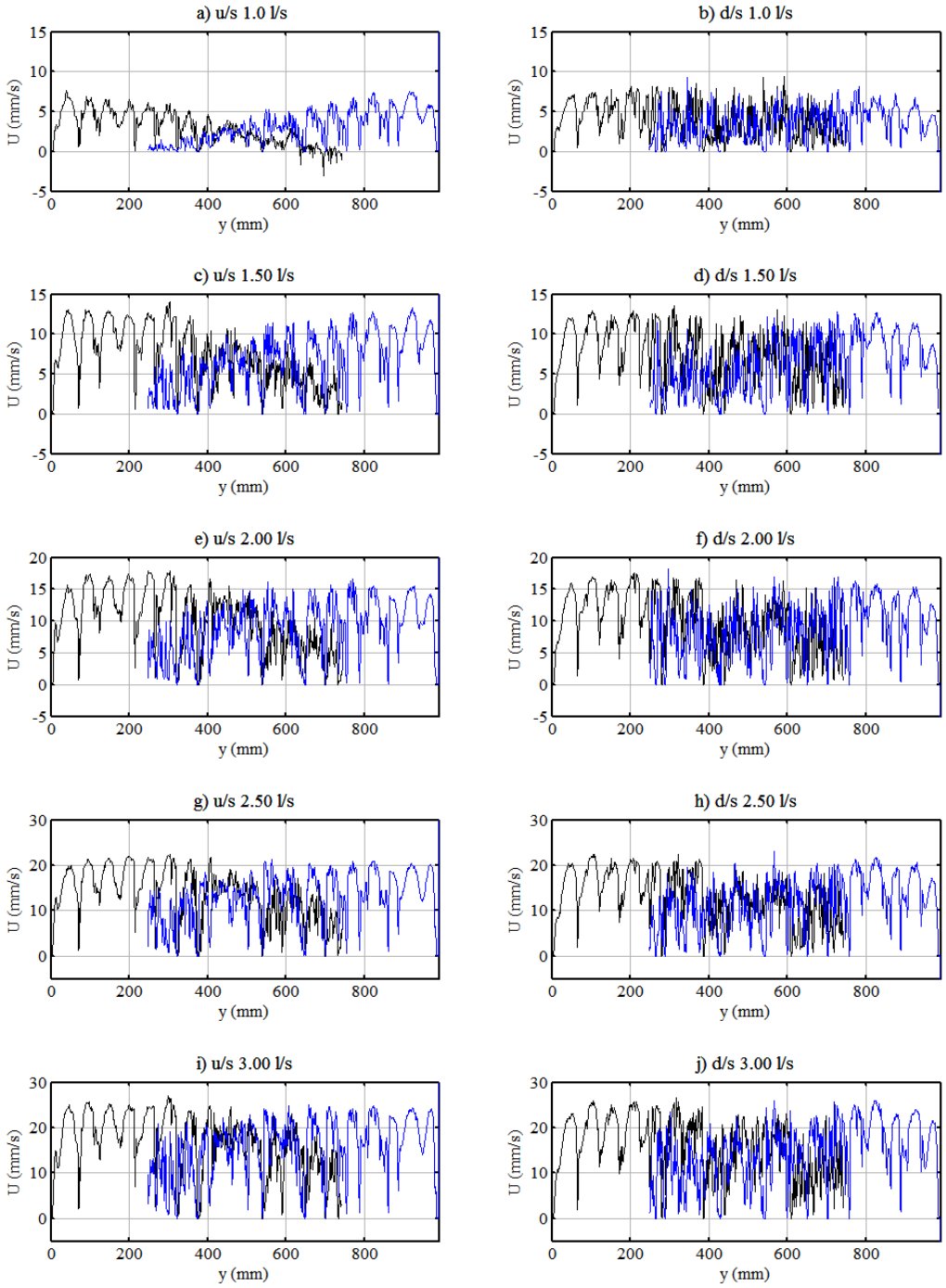

Figure 4.15: Transverse profiles of mid-depth, temporal mean longitudinal velocity recorded in the full, sparse artificial vegetation are plotted for the left (black) and right (blue) hand sides of the channel x = 1.0 (u/s) and 2.0 m (d/s) .

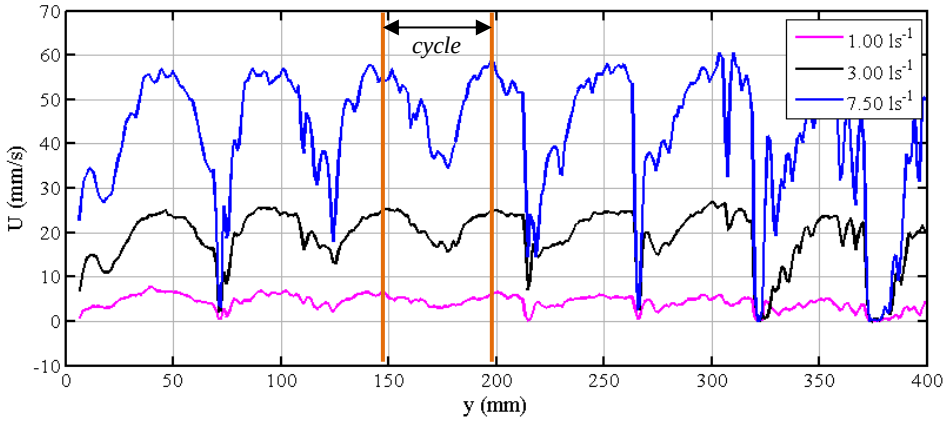

Figure 4.16: Close up transverse profiles of temporal mean longitudinal velocity, *U*, in the region of $0 < y < 400$ mm showing stem-cycle nature in the low density, full artificial vegetation.

c) Real vegetation – winter *typha*

The winter growth *typha* represents the first chronological experimentation using the *Metflow UVP* probes. The probes could not be mounted from the bed (in accordance with the sparse artificial case) due to the nature of the living bed that contained the *typha* rooting and other organic matter. Moreover, the thickness of the real vegetation bed (*O*~10 cm) (Figure 2.12) did not practically permit the bed mounting of the transducers. As such, vertical profiles of longitudinal velocity were measured from the channel surface at 8 locations within the test section. Four vertical profiles were measured at both the upstream and downstream windows where the surface mounted probes were located randomly to account for the heterogeneous distribution of vegetation; where Figure 4.2 shows the heterogeneity of the winter *typha* test section. Measurement locations were chosen such that the ultra-sound beam did not encounter any obstructions.

The temporal mean velocity profiles collected in the *typha* test cases are presented in Figure 4.18. The vertical profiles from the 8 measurement locations (feint lines) are included alongside the patch-mean vertical profile (thick line) for 5 discharges. Note that the spikes in the profiles are attributed to the obstruction of stem debris or significant signal echo from adjacent stems or leaves. Similar features were observed by Lightbody et al., (2008).

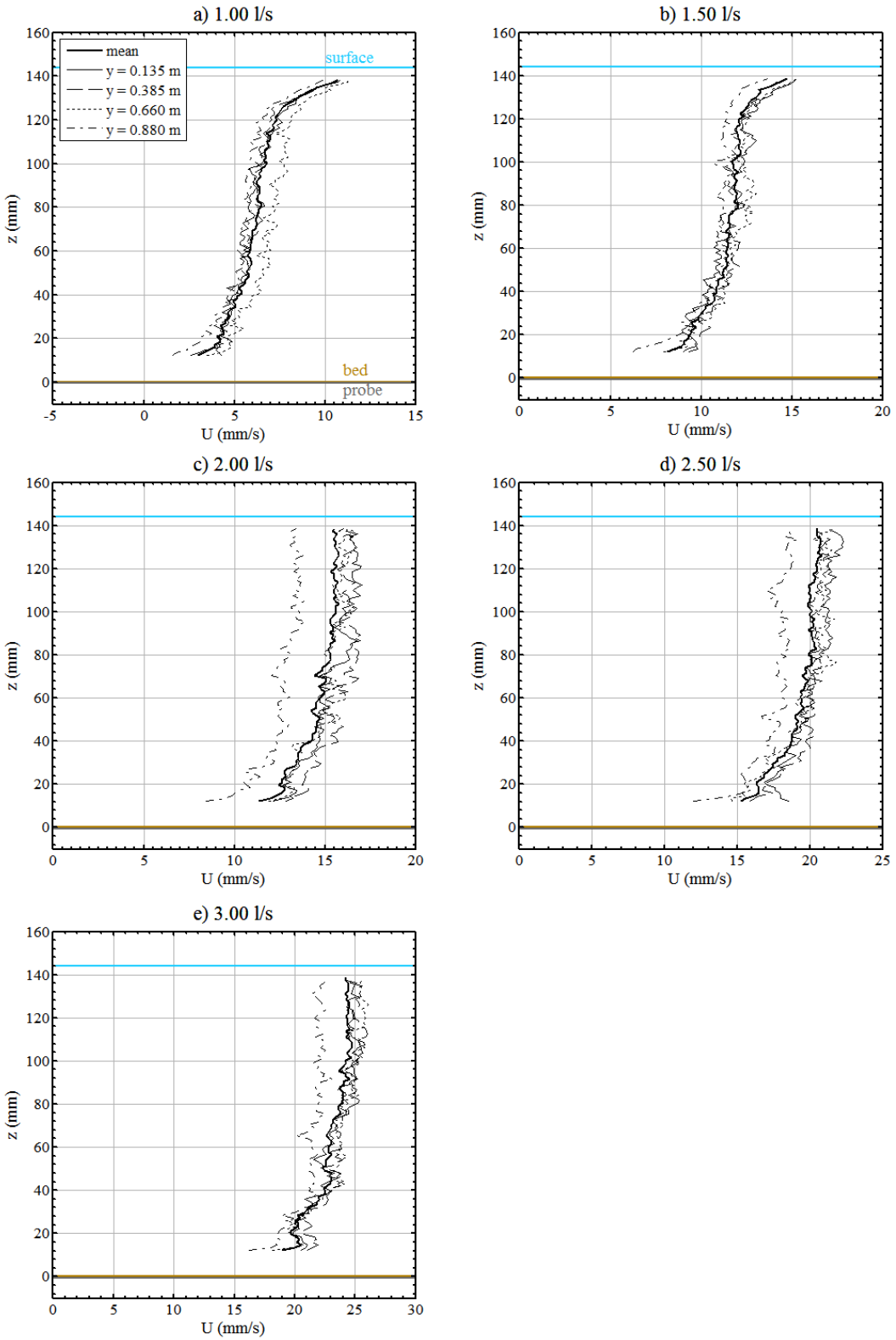

Figure 4.17: Vertical profiles of temporal mean longitudinal velocity measured at 4x transverse location and the spatial mean (black line) measured in the low density, full artificial vegetation.

d) Real vegetation– *summer typha*

Vertical profiles of longitudinal velocity recorded in the full vegetation summer *typha* cases were conducted using the same procedure and probe orientation as the low-density artificial test case. The summer *typha* vegetation was denser than the winter season and there was a large amount of dead stem matter on the bed of the channel. Therefore, care was taken to ensure that any dead matter was not transported downstream into the path of the bed mounted velocity probes. Further, an array of batons was installed across the channel; clear of the water's surface, to prevent the large *typha* stems from flexing into the path of the ultrasound beam. (Figure 4.2 provides an image of the denser, summer season *typha* in the full vegetation scenario). The mean vertical profiles measured in the full vegetation scenario and are presented in Figure 4.19.

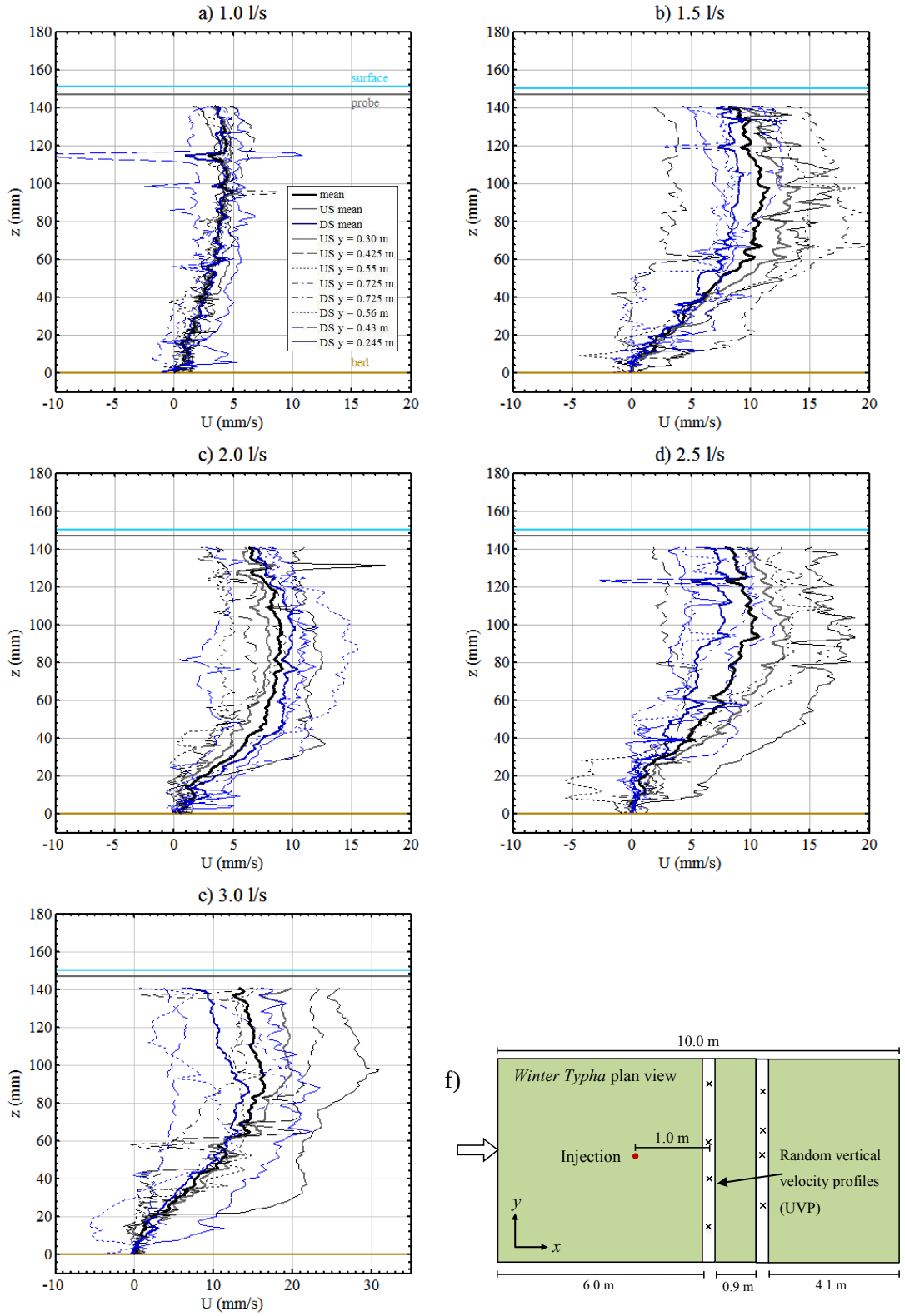

Figure 4.18: Temporal mean vertical profiles of longitudinal velocity, $U(z)$, and spatial mean (sold black line) measured in the winter *typha* full vegetation cases (a-e). Upstream and downstream is denoted with US and DS respectively. f) Plan view velocity measurement locations.

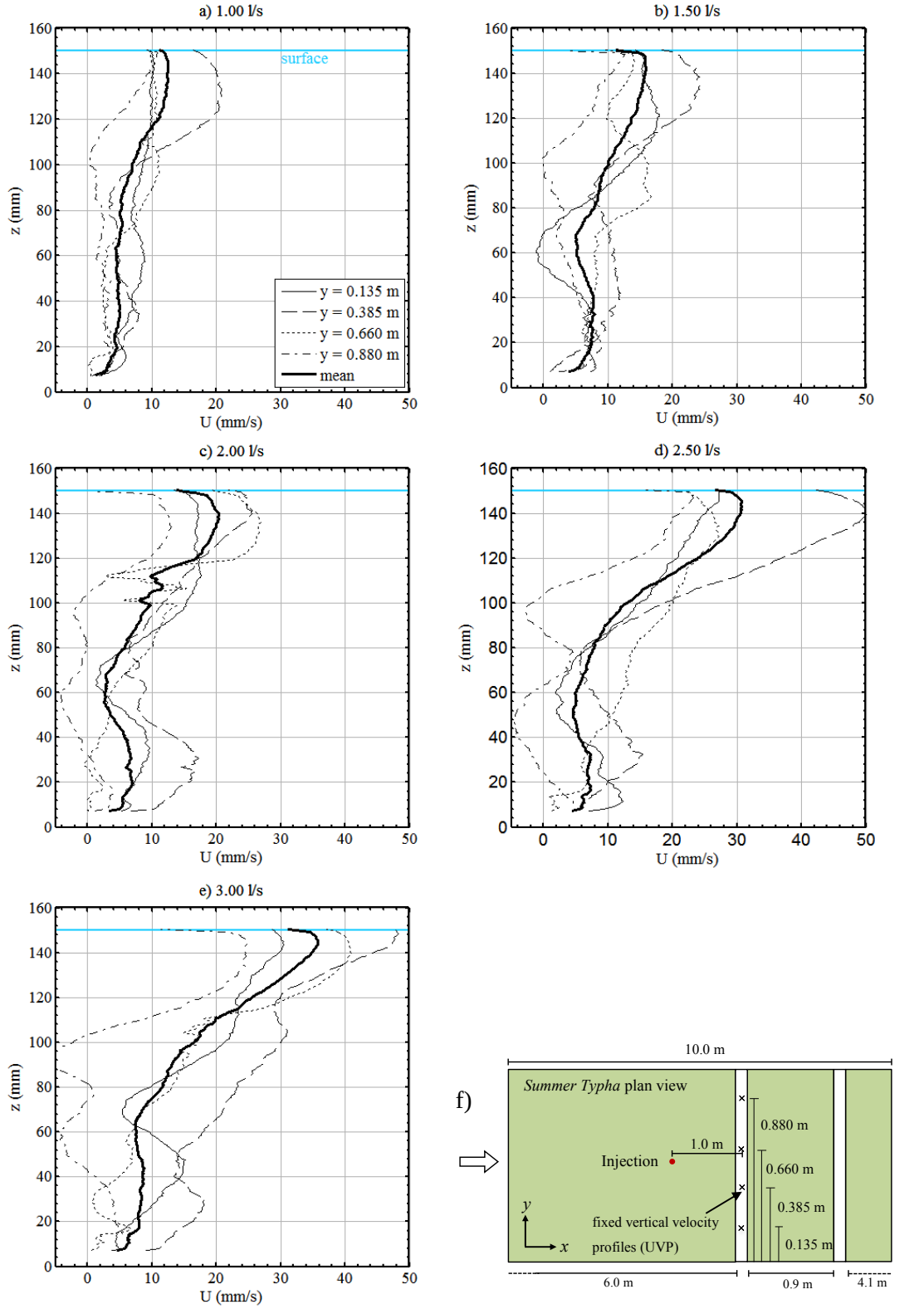

Figure 4.19: Temporal mean vertical profiles of longitudinal velocity, $U(z)$, and spatial mean (sold black line) measured in the summer *typha* full vegetation (a-e). The horizontal blue line indicates the location of the water's surface. f) Plan view of the velocity measurement locations.

4.4.2 Partial vegetation velocity profiles

a) Artificial vegetation – high density

The transverse profiles of mid-depth, temporal mean longitudinal velocity, $U_{md}(y)$, measured in the high density partial, artificial vegetation are presented in Figure 4.20. Profiles were measured using the *Vectrino II* device at 16 transverse locations at the upstream measurement window. The vegetation interface is indicated by the vertical green line at $y = 0.60$ m; where the vegetation and open channel occupied the regions $0 \text{ m} \leq y \leq 0.60$ m and $y > 0.60$ m, respectively.

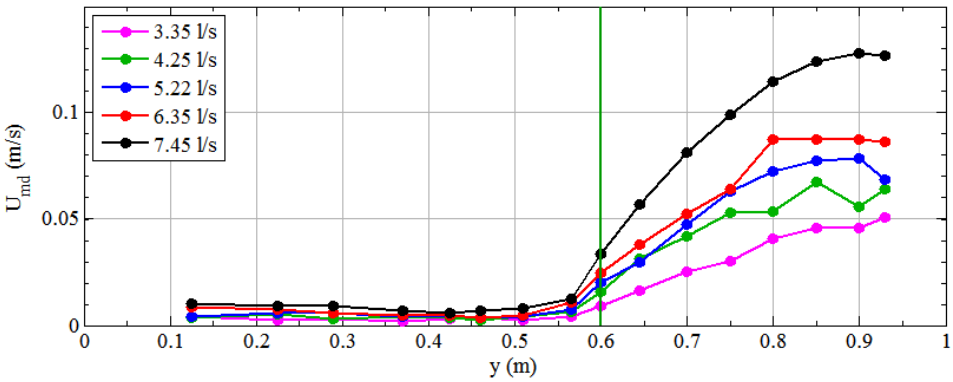

Figure 4.20: Mid-depth, temporal mean longitudinal velocity, $U_{md}(y)$, for the high density, partial, artificial vegetation cases.

b) Artificial vegetation – low density

The transverse profiles of temporal mean longitudinal velocity recorded in the low density partial, artificial vegetation are presented in Figure 4.21. Profiles were recorded using the *Metflow UVP* profiler. Two profilers were employed at both the upstream and downstream locations and were mounted within the channel walls at the flow mid-depth, such that longitudinal velocity was measured from either side of the of the vegetation interface. The black and blue lines give the velocity profiles recorded from the vegetated and open-channel sides of the channel, respectively. The persistence of ultrasound attenuation in the partial vegetation scenario is problematic and is discussed in the Analysis Chapter.

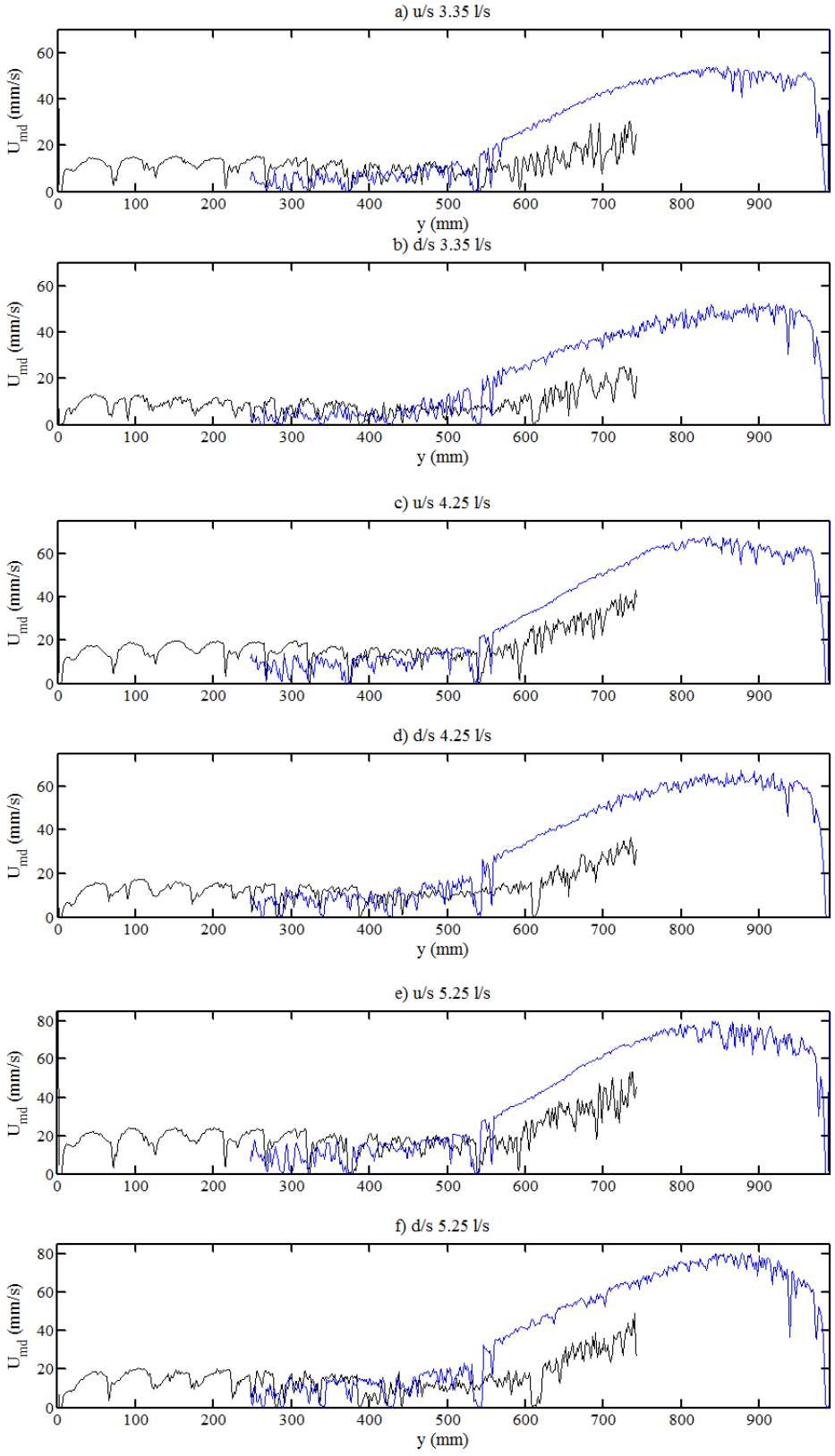
a) u/s 3.35 l/s
b) d/s 3.35 l/s
c) u/s 4.25 l/s
d) d/s 4.25 l/s
e) u/s 5.25 l/s
f) d/s 5.25 l/s
U_md (mm/s)
y (mm)

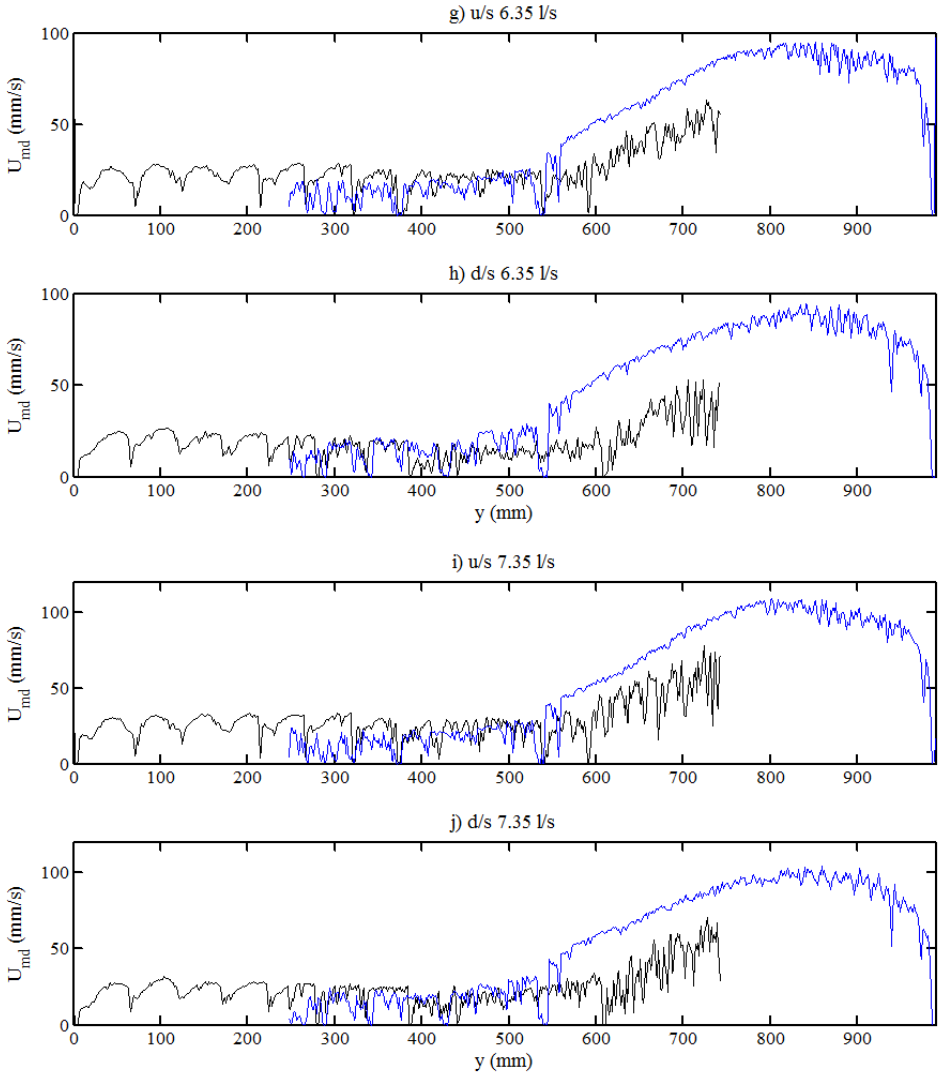

Figure 4.21: Transverse profiles of mid-depth, temporal mean longitudinal velocity, $U_{md}(y)$, measured in the partial, low density artificial vegetation for the upstream (u/s) and downstream (d/s); recorded from the left (black) and right (blue) hand sides of the channel at the flow mid-depth.

c) Partial real vegetation– winter typha

Transverse profiles of mid-depth, longitudinal velocity were measured in the partial winter *typha* cases using the *Metflow UVP* probes located at the upstream and downstream measurement windows. As previously stated, the winter *typha* cases were preliminary in the implementation of the *Metflow UVP* probes. As such, only one probe was employed at the channel mid-depth located at both measurement windows. Further, only a 750 mm profile was obtained at each longitudinal measurement location given the measurement accuracy constraints discussed above. The relative low density of the winter *typha* enabled

uninterrupted transverse profiles of velocity to be collected. Figure 4.22a gives an image of the partially vegetated winter *typha* test section (where the direction of primary flow is top to bottom in the image). The first measurement point was, therefore, translated to $y = 0.150$ m to ensure that the shear layer region of the flow was well described. The transverse profiles of velocity measured at the upstream and downstream measurement locations are presented in Figure 4.23a. The grey and green lines give the locations of the probe face and vegetation interface, respectively; where the vegetation occupied the region $y > 0.500$ m.

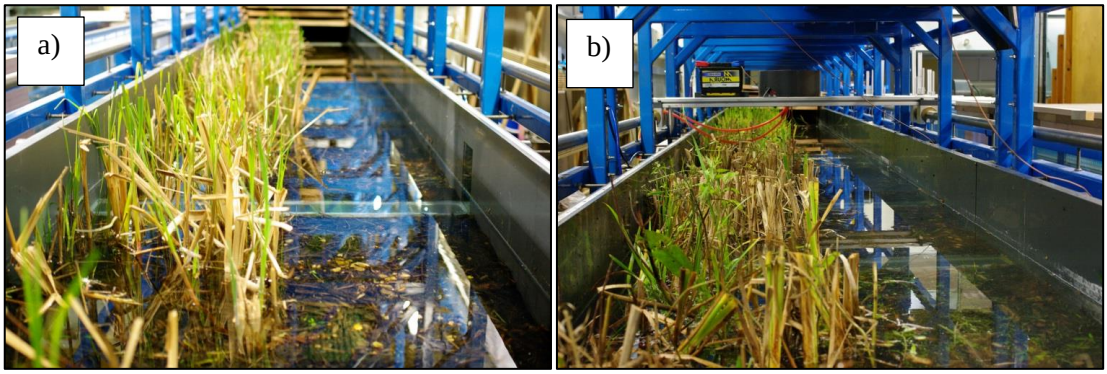

Figure 4.22: a) Winter and b) *typha* partial vegetation test scenario.

d) Partial real vegetation – summer typha

Figure 4.22b shows the partial summer *typha* vegetation test section (where the direction of primary flow is top to bottom in the image). The transverse profiles of mid-depth, temporal mean longitudinal velocity measured in the partial summer *typha* vegetation case are presented in Figure 4.23b. Two *Metflow UVP* probes were installed within the channel walls at both measurement locations enabling full transverse profiles to be collected simultaneously. Note that the open channel region was located in $y > 500$ mm. The summer *typha* tests were the final cases to be studied and represent the current best practice experimental method.

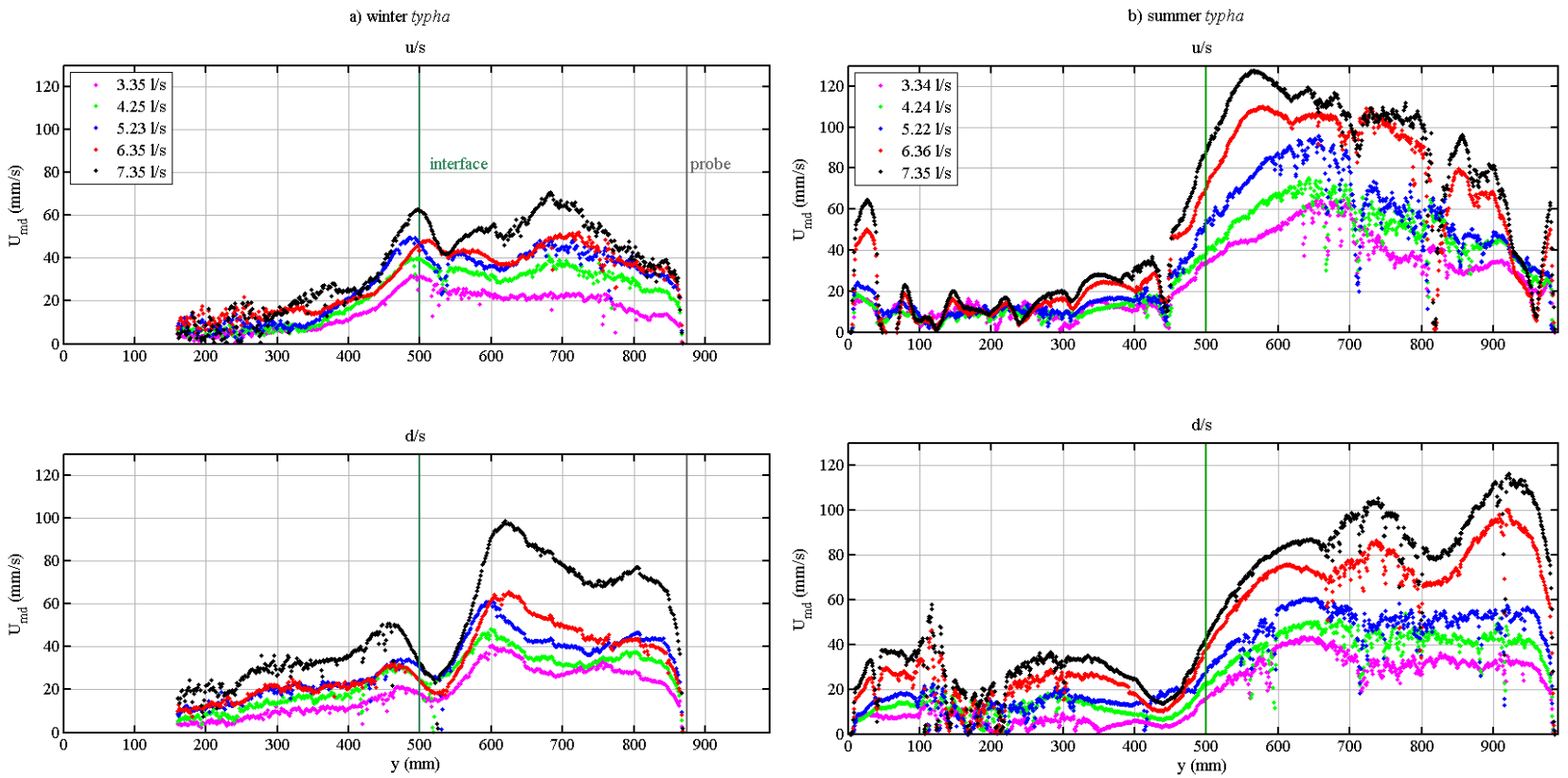

Figure 4.23: Upstream (u/s) and downstream (d/s) transverse profiles of mid-depth, temporal mean longitudinal velocity, $U_{md}(y)$, measured in the partial a) winter and b) summer *typha* types.

4.5 Fluorescent Tracing Results

This section presents the processed and calibrated results of the Rhodamine 6G tracer experiments. Two tracer injection methods were employed depending on the vegetation scenario: pulse injections were conducted in the full vegetation and bare channel scenarios; while a continuous injection was used for the partial vegetation cases[4]. Recall that the pulse injections permit the simultaneous calculation of longitudinal and transverse mixing coefficient while the constant injection allows only the transverse mixing coefficient to be calculated. Note that the pulse injection results for the full vegetation and bare channel scenarios are needed to parameterise a finite difference model detailed in the following chapter. The calibration of the raw intensity LIF images is detailed in full in Appendix II. Averaging of the continuous injection data – detailed in Appendix IV – to attain steady-state transverse concentration distributions is also discussed.

4.5.1 Full vegetation – pulse injection

The pulse injection results are presented as two-dimensional contour plots as a means of qualitatively viewing the changes in spatial and temporal concentration distributions. For every discharge case, 10 repeat pulse injections were made. Note that further statistical analysis to quantify transverse and longitudinal mixing as well as mean longitudinal and transverse velocity was conducted using the individual tests to eliminate the effects of data smoothing as a result of averaging (the results of which are discussed in the following chapter). All 10 repeat pulse injection tests for every case and vegetation type can be found in full in Appendix IV. The following figures provide the full vegetation tracer results for the

[4]Additional continuous injections were made in the full vegetation scenario for the low density artificial vegetation and the winter and summer *typha*.

high density (Figure 4.24) and low density (Figure 4.25) artificial vegetation and the winter (Figure 4.26) and summer (Figure 4.27) *typha*. Concentrations below 1% of the maximum value have been converted to white pixels to improve visualisation. The data provide a qualitative comparison between the effects of artificial and real vegetation where the significant alteration to the 2D distribution in the real vegetation is attributed to the heterogeneous stem morphology and distribution.

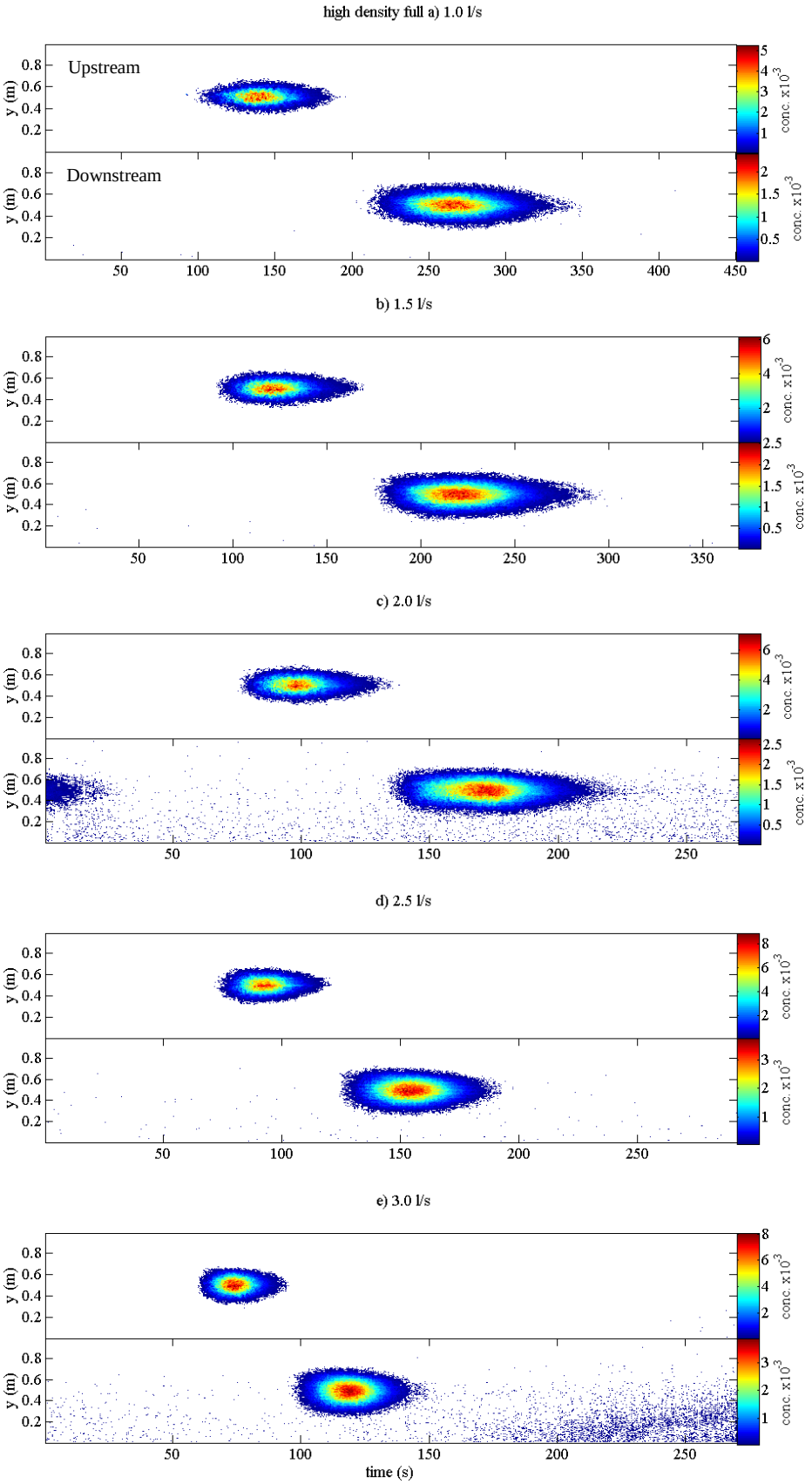

Figure 4.24: Temporal mean pulse tracer results in the high density, full artificial vegetation.

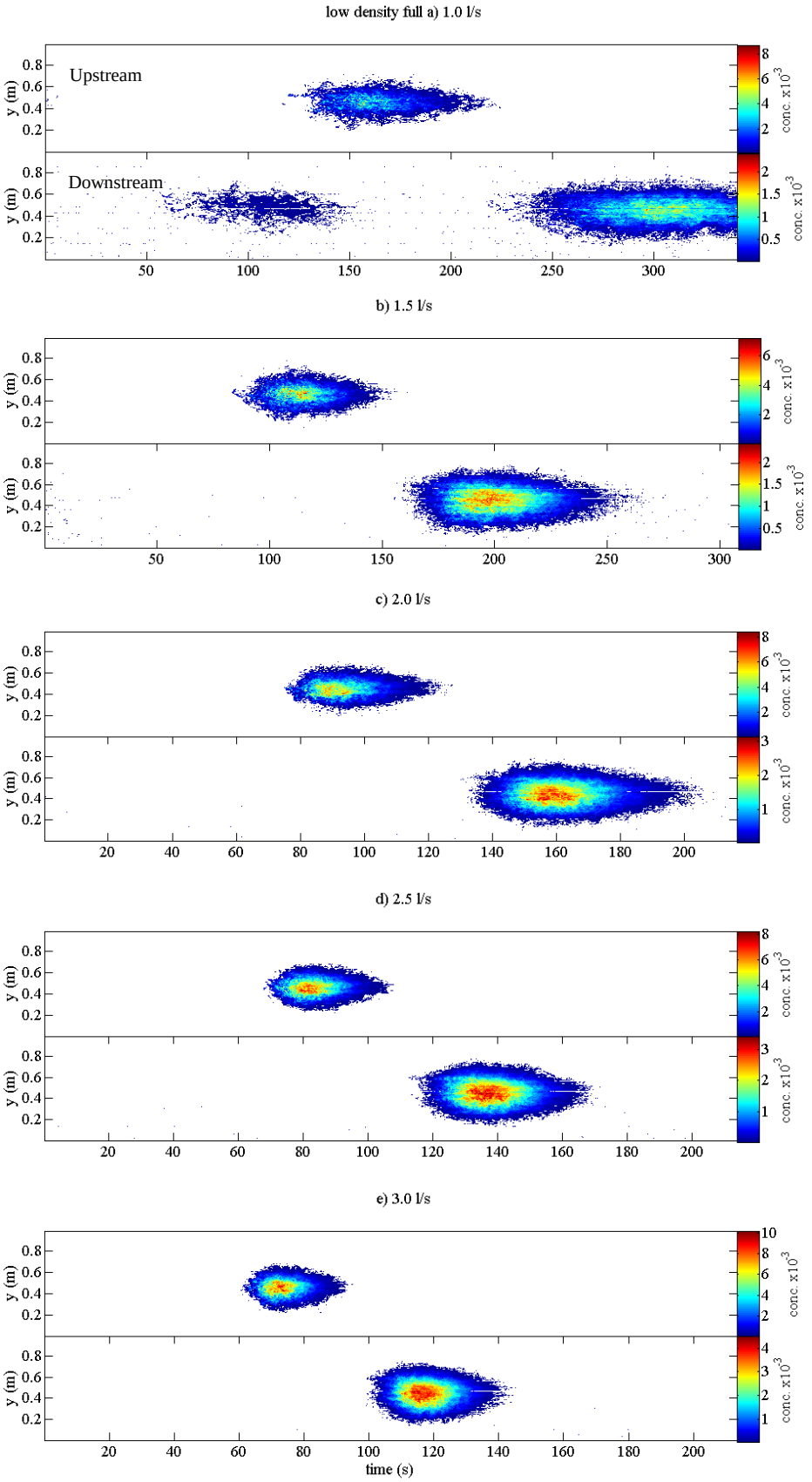

Figure 4.25: Temporal mean pulse tracer results in the low density, full artificial vegetation.

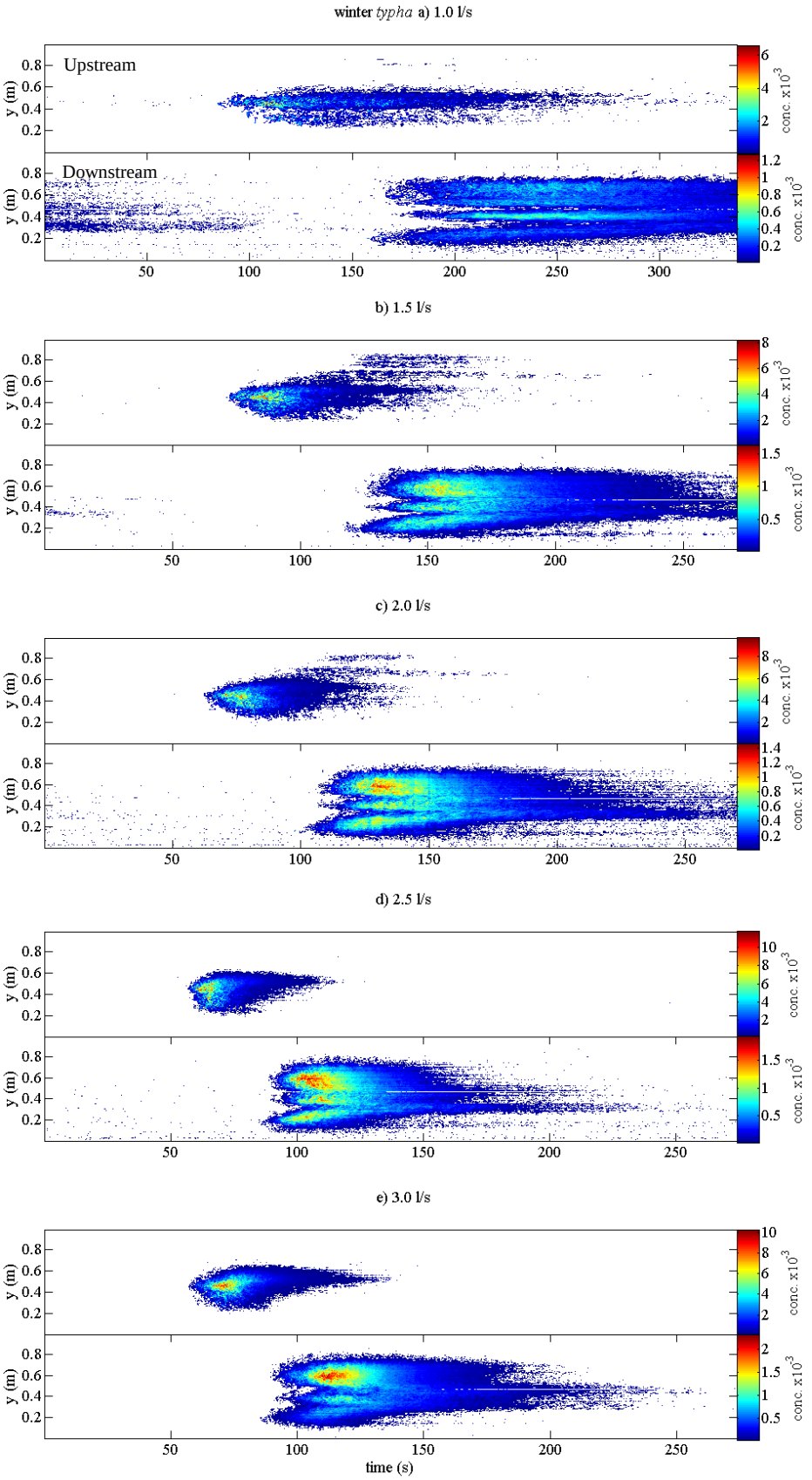

Figure 4.26: Temporal mean pulse tracer results in the winter *typha*, full vegetation.

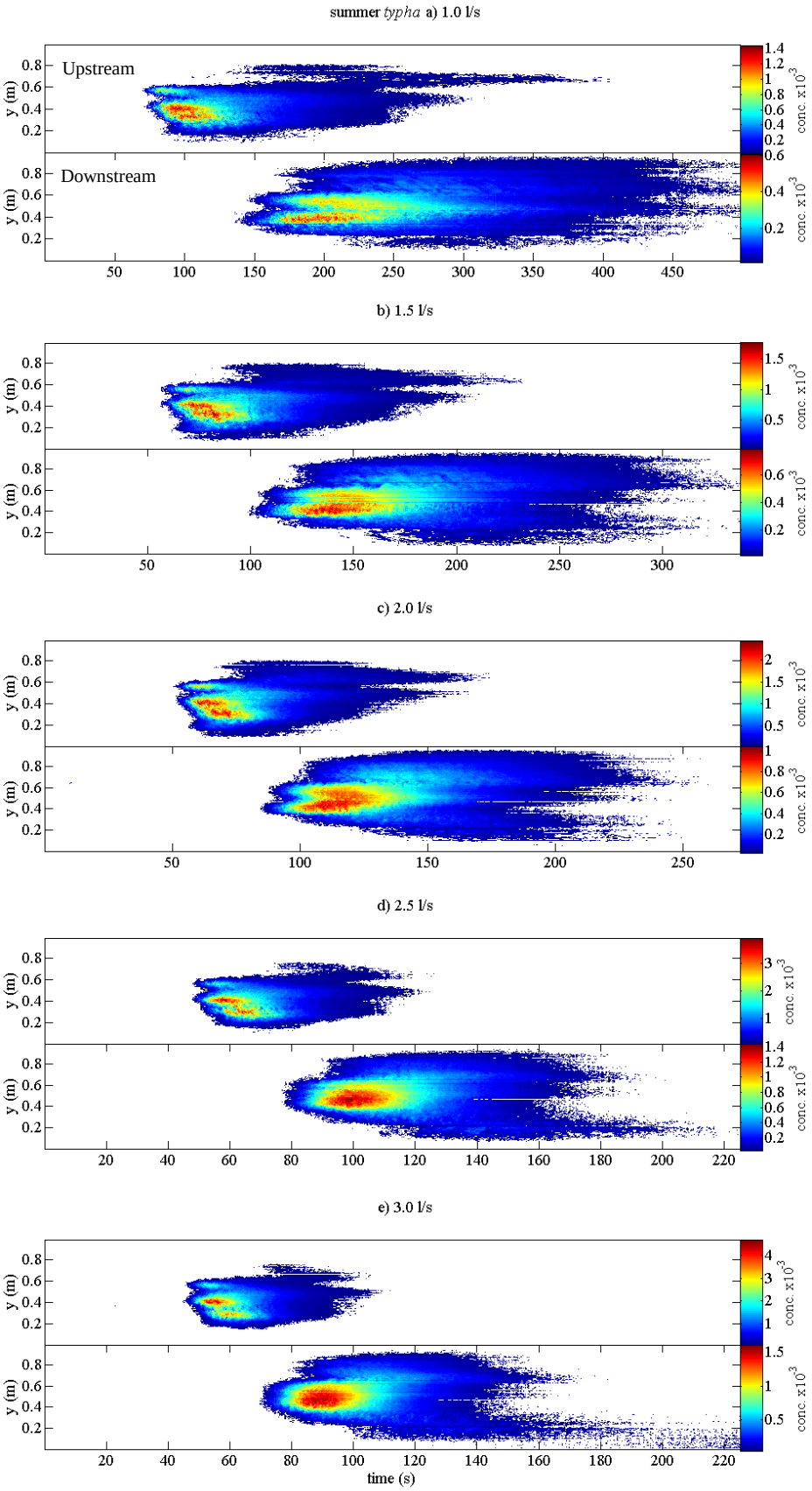

Figure 4.27: Temporal mean pulse tracer results in the summer *typha*, full vegetation.

4.5.2 Full vegetation – continuous injection

Figure 4.28 gives an example of the continuous injection results measured in the 3.00 l/s case in the summer *typha* full vegetation. Plot (a) and (b) show the temporal change in transverse concentration distribution at x = 1.0 and 2.0 m, respectively. The concentrations below 1% of the maximum value have been converted into white to improve visual resolution. Plot (c) shows the channel centreline concentration while plot (d) gives the mean transverse concentration distribution within the region of steady-state concentration. The region of steady state concentration was selected as the time interval between ± 80% of the maximum concentration (see Appendix IV). The stead-state profiles were mass-balanced such that the area under the downstream distribution was equal to that of the upstream distribution.

The contour results for the full vegetation continuous injection tests can be found in Appendix IV. The steady-state, transverse concentration distributions recorded in the full vegetation, high density artificial, winter and summer *typha* types are provided in Figure 4.29, Figure 4.30 and Figure 4.31, respectively.

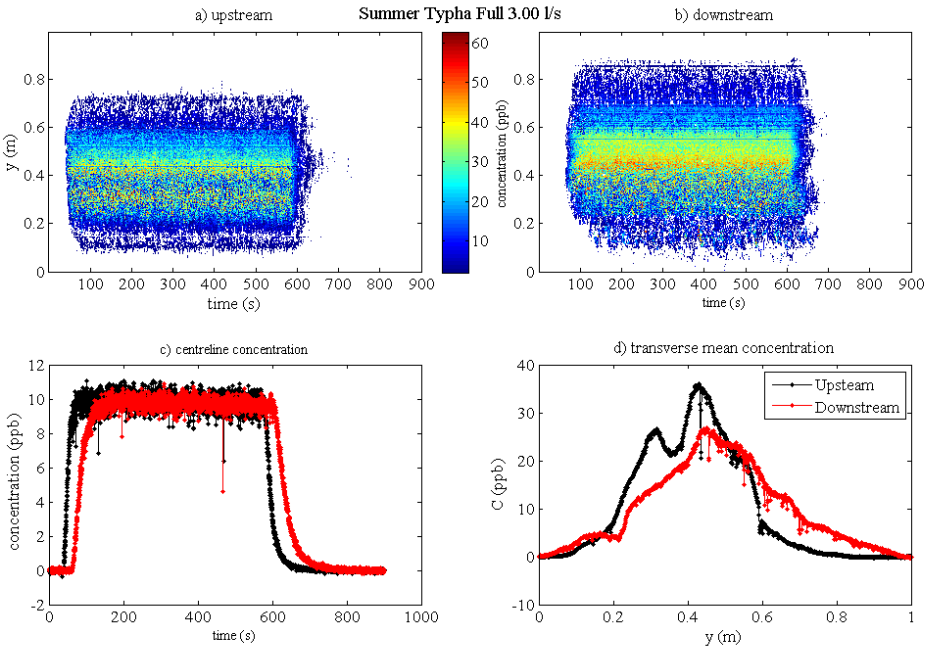

Figure 4.28: Example continuous injection results for a) upstream and b) downstream. c) centreline concentration with time and d) steady-state transverse concentration distribution in the full, summer *typha* at 3.00 l/s.

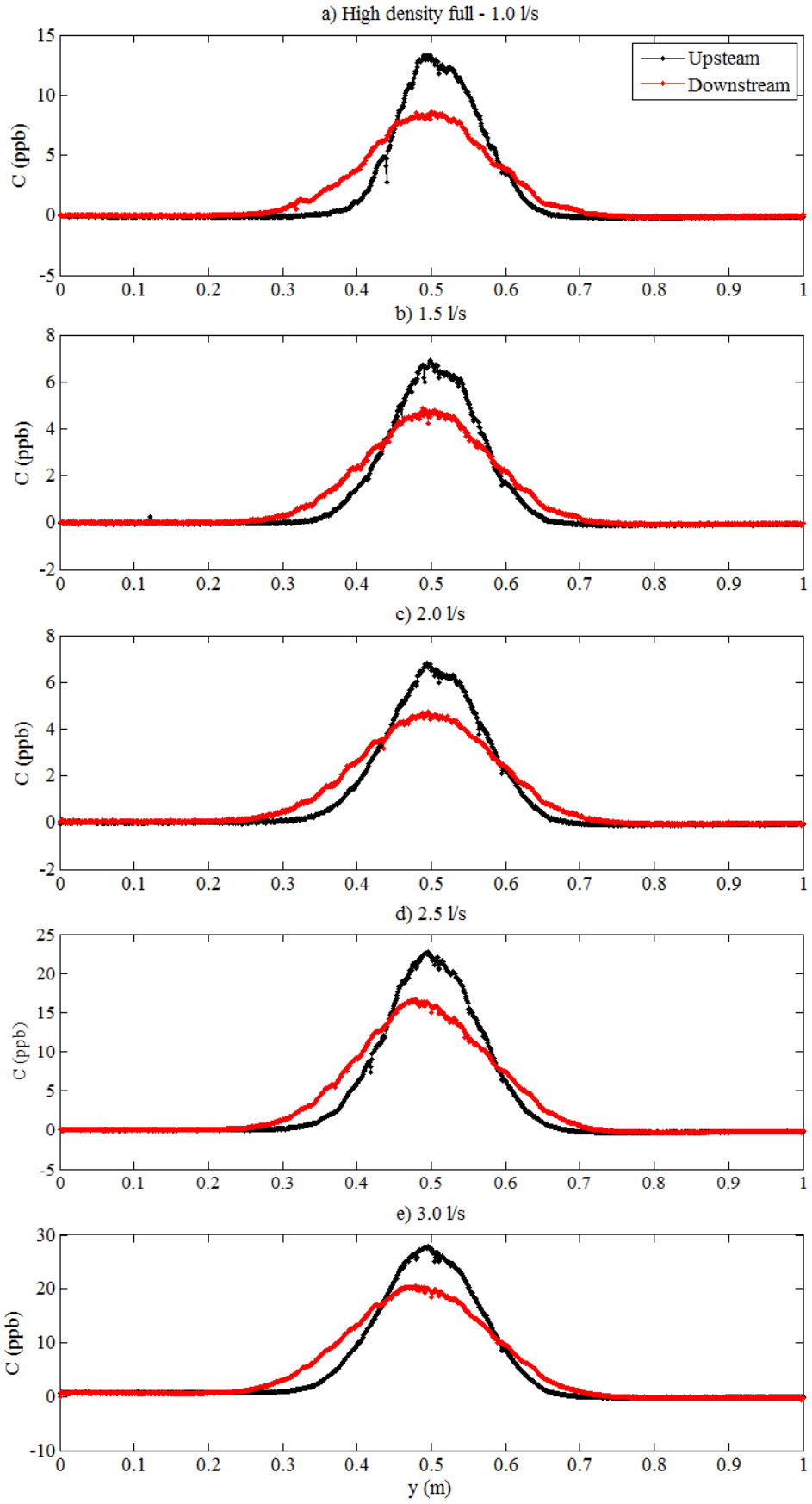

Figure 4.29: Steady-state profiles of $C(y)$ for the high density, full artificial vegetation.

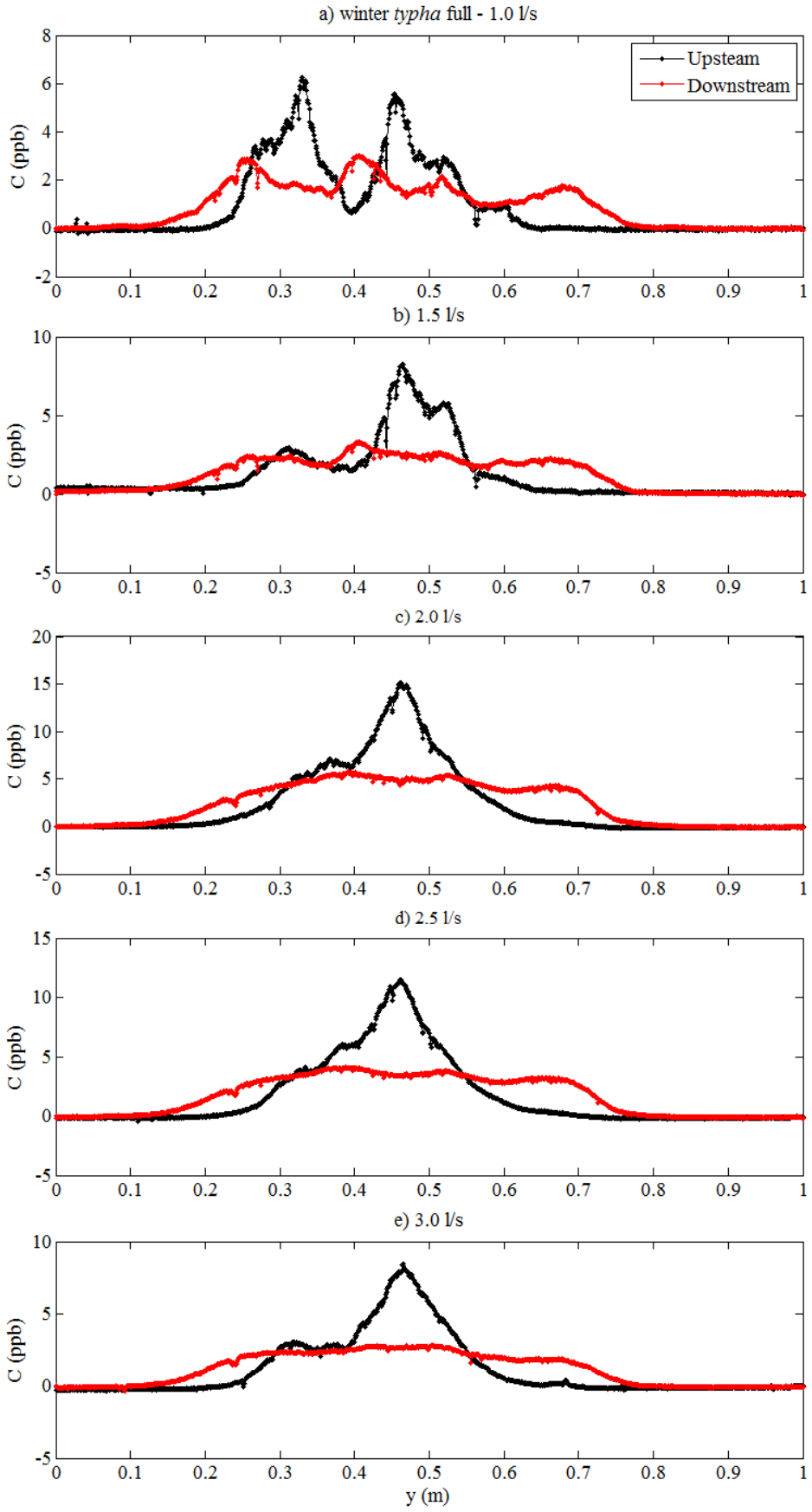

Figure 4.30: Steady-state profiles of $C(y)$ for the winter *typha*, full vegetation.

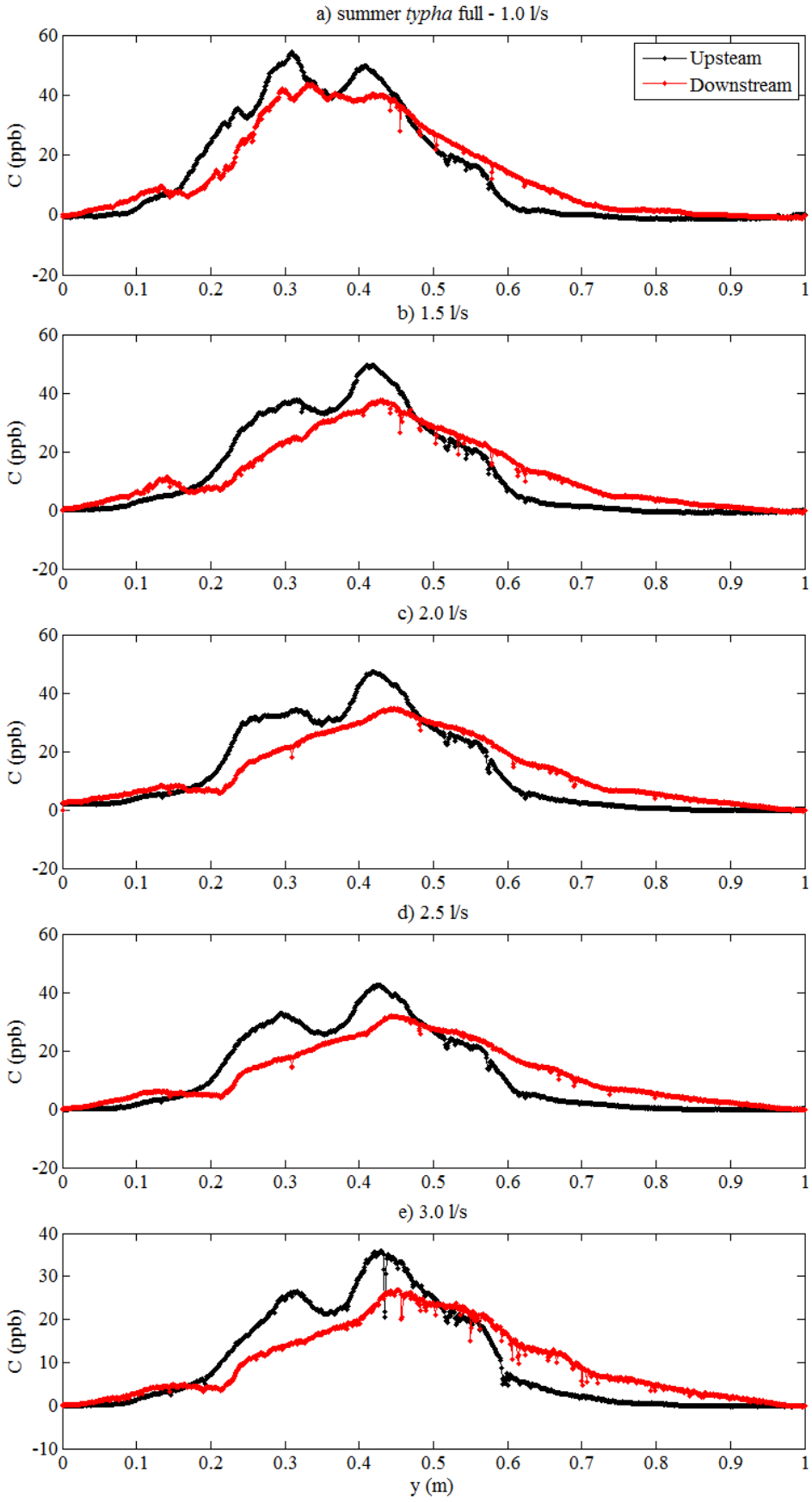

Figure 4.31: Steady-state profiles of $C(y)$ for the summer *typha*, full vegetation.

4.5.3 Partial vegetation – continuous injection

The mean transverse concentration distributions for the four vegetation types for the continuous injection in the partial vegetation scenario are presented below. Each contour distribution for the upstream and downstream measurement sites can be found in Appendix IV. An example constant injection in the partial vegetation scenario is given below in Figure 4.32 for the low density, artificial vegetation at 5.25 l/s.

Figure 4.32 gives an example of the upstream and downstream contour distributions and the centreline and steady-state concentration distributions where the vegetation occupied the region $y < 0.60$ m. The cyclic nature of the shear layer vortices can be seen in the contour distributions (plots a and b) – adding uncertainty to the definition of the steady-state region (plot c). The transverse mean profiles were flux-balanced to maintain conservation of mass from upstream to downstream (see Appendix IV).

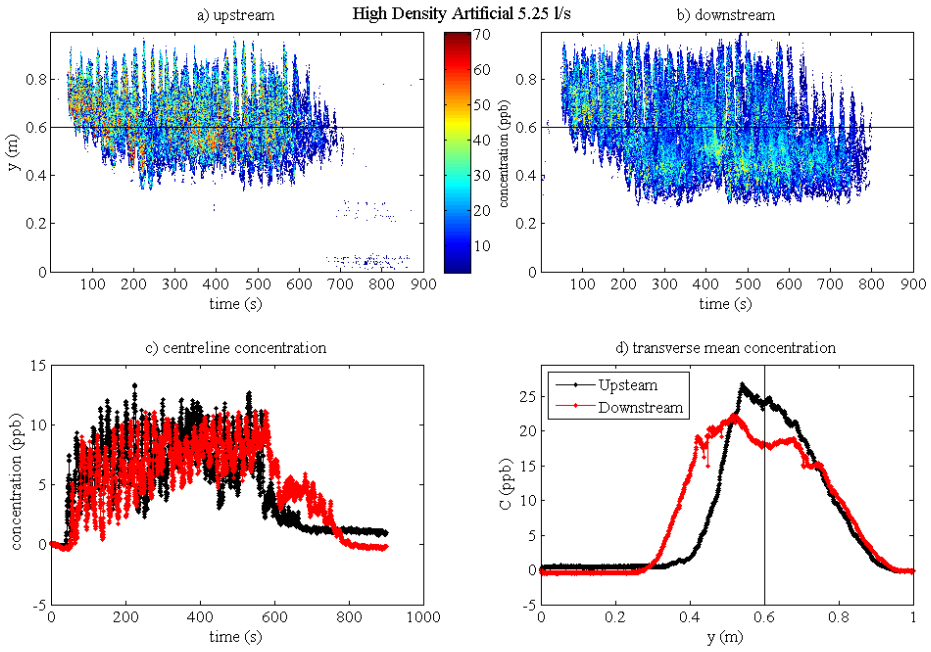

Figure 4.32: Example continuous injection trace results for the low density, artificial partial vegetation.

The steady-state, transverse concentration distributions recorded in the partial vegetation, high and low density artificial, winter and summer *typha* types are provided in Figure 4.33,

Figure 4.34, Figure 4.35 and Figure 4.36, respectively. The location of the vegetation interface is given by the vertical line where the vegetation occupies the region $y < 0.60$ m and $y < 0.50$ m for the artificial and *typha* types, respectively.

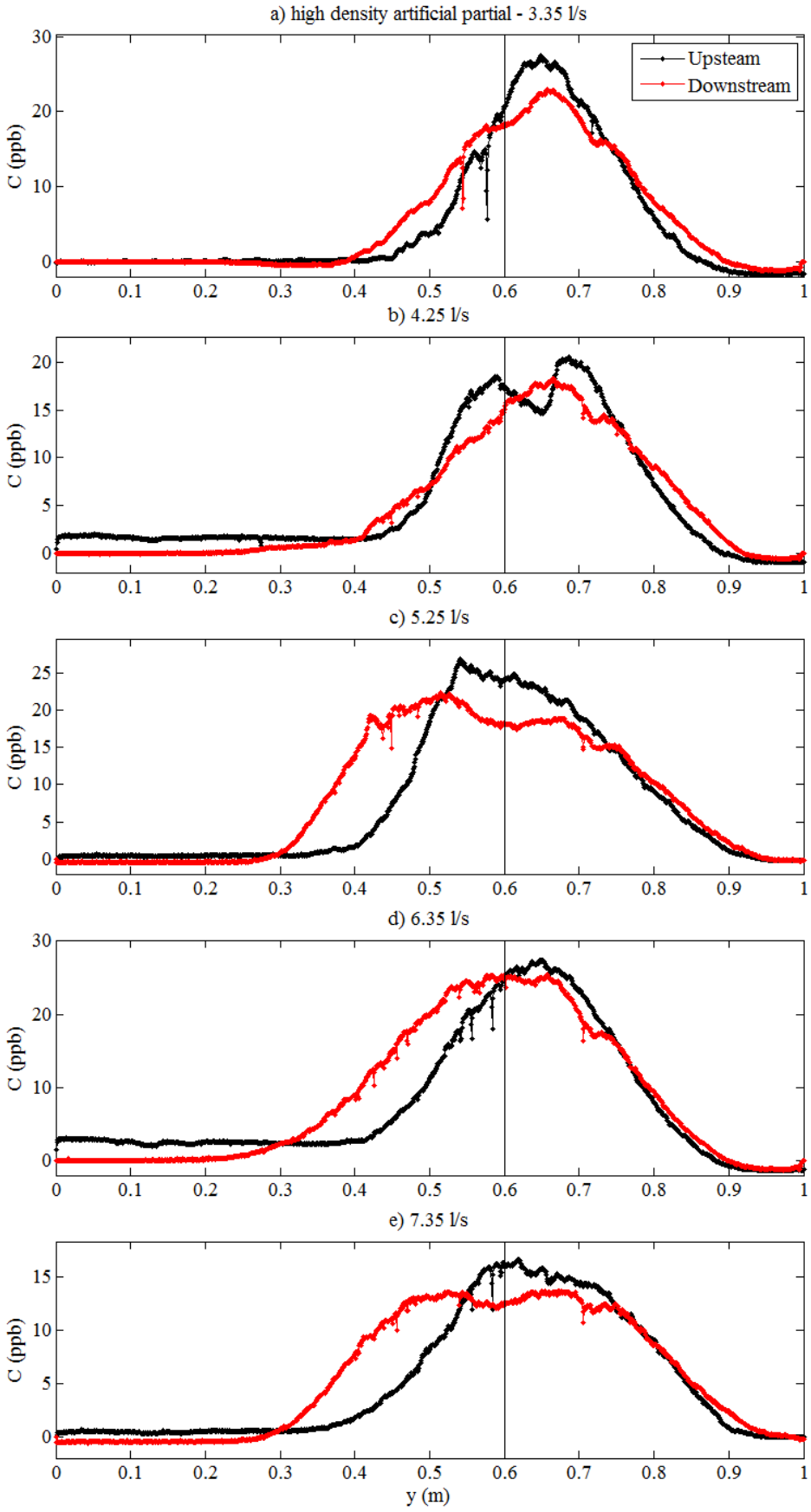

Figure 4.33: Steady-state profiles of $C(y)$ for the high density, partial artificial vegetation.

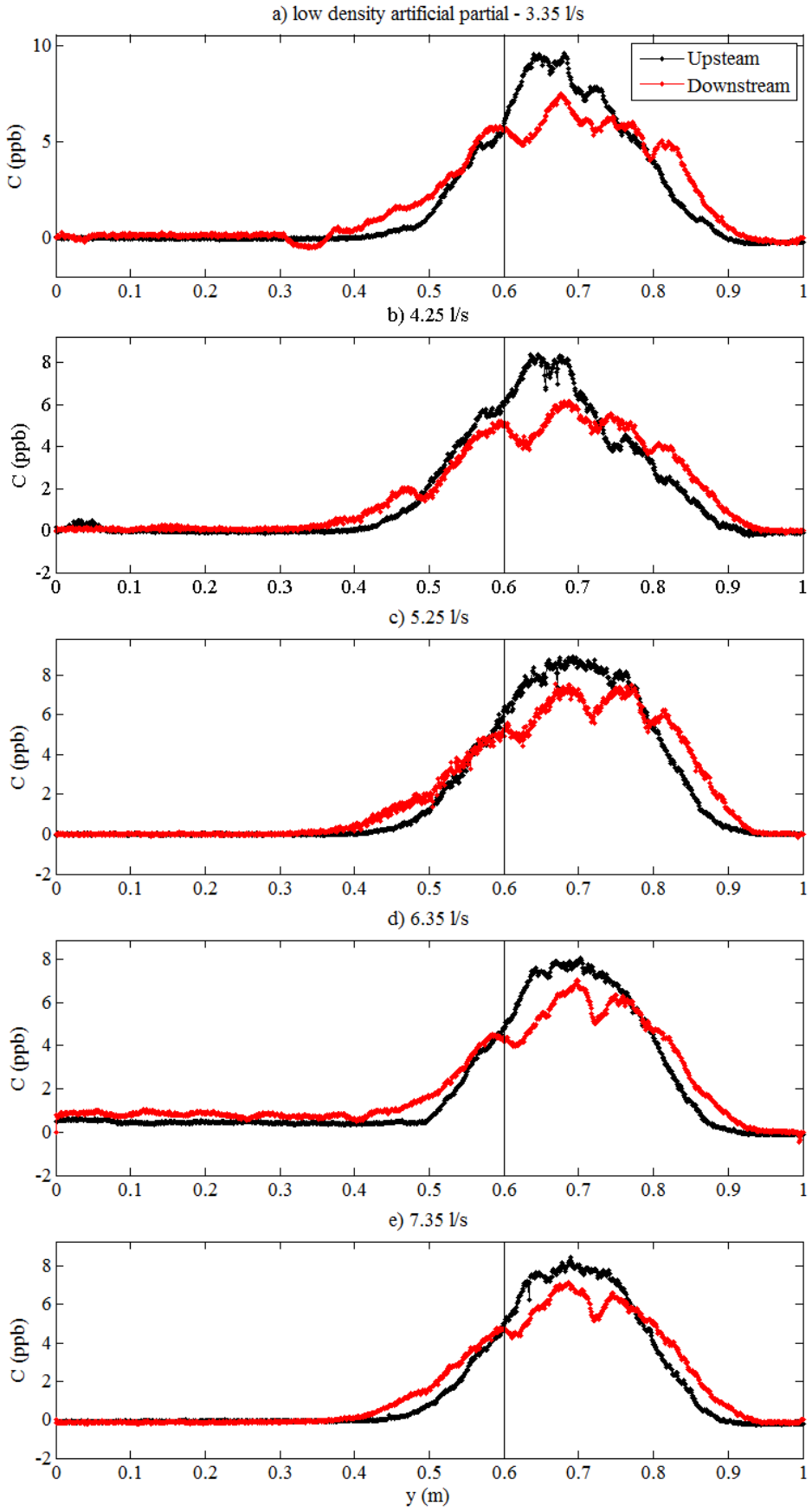

Figure 4.34: Steady-state profiles of $C(y)$ for the low density, partial artificial vegetation.

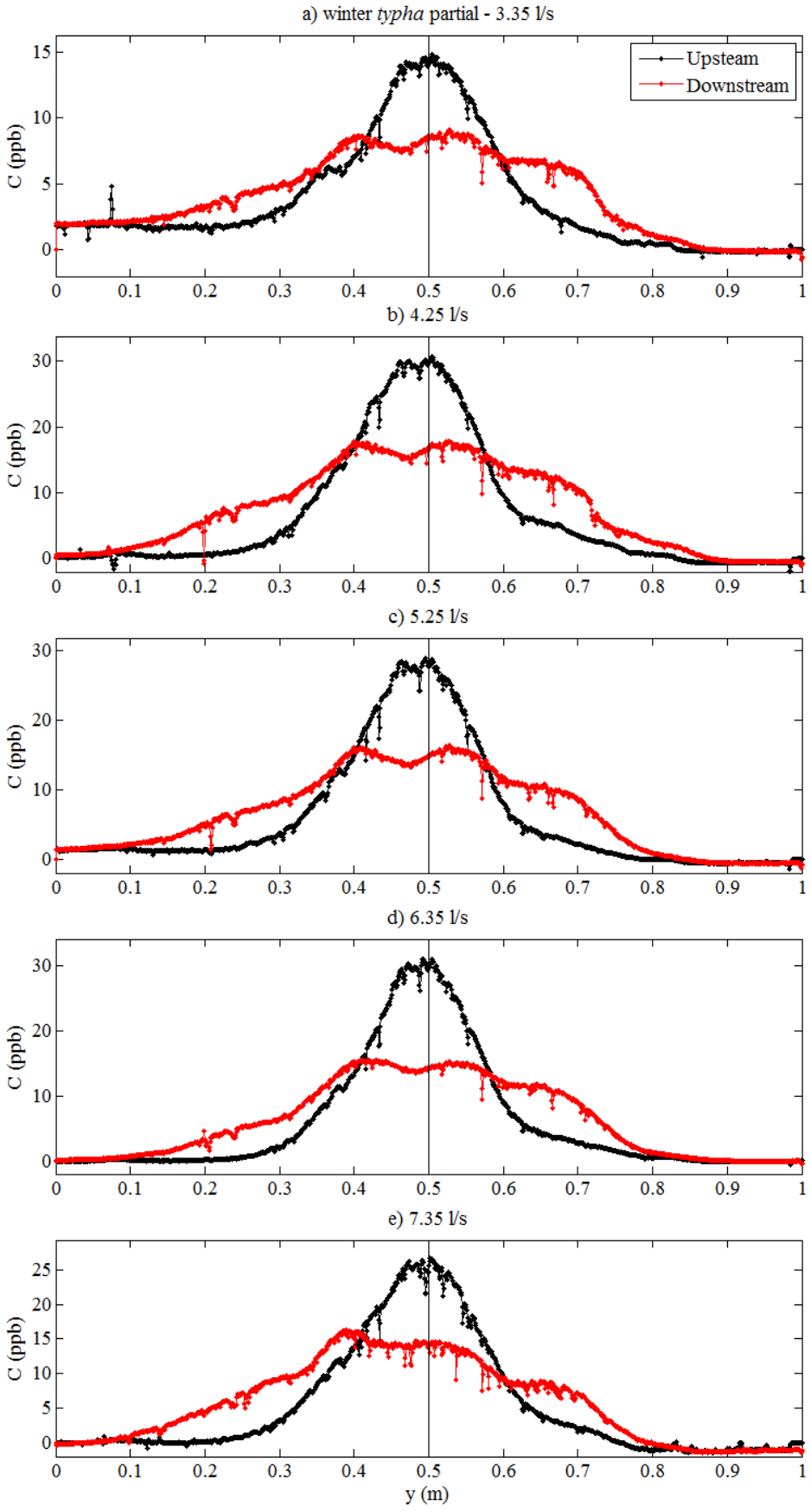

Figure 4.35: Steady-state profiles of $C(y)$ for the winter *typha*, partial vegetation.

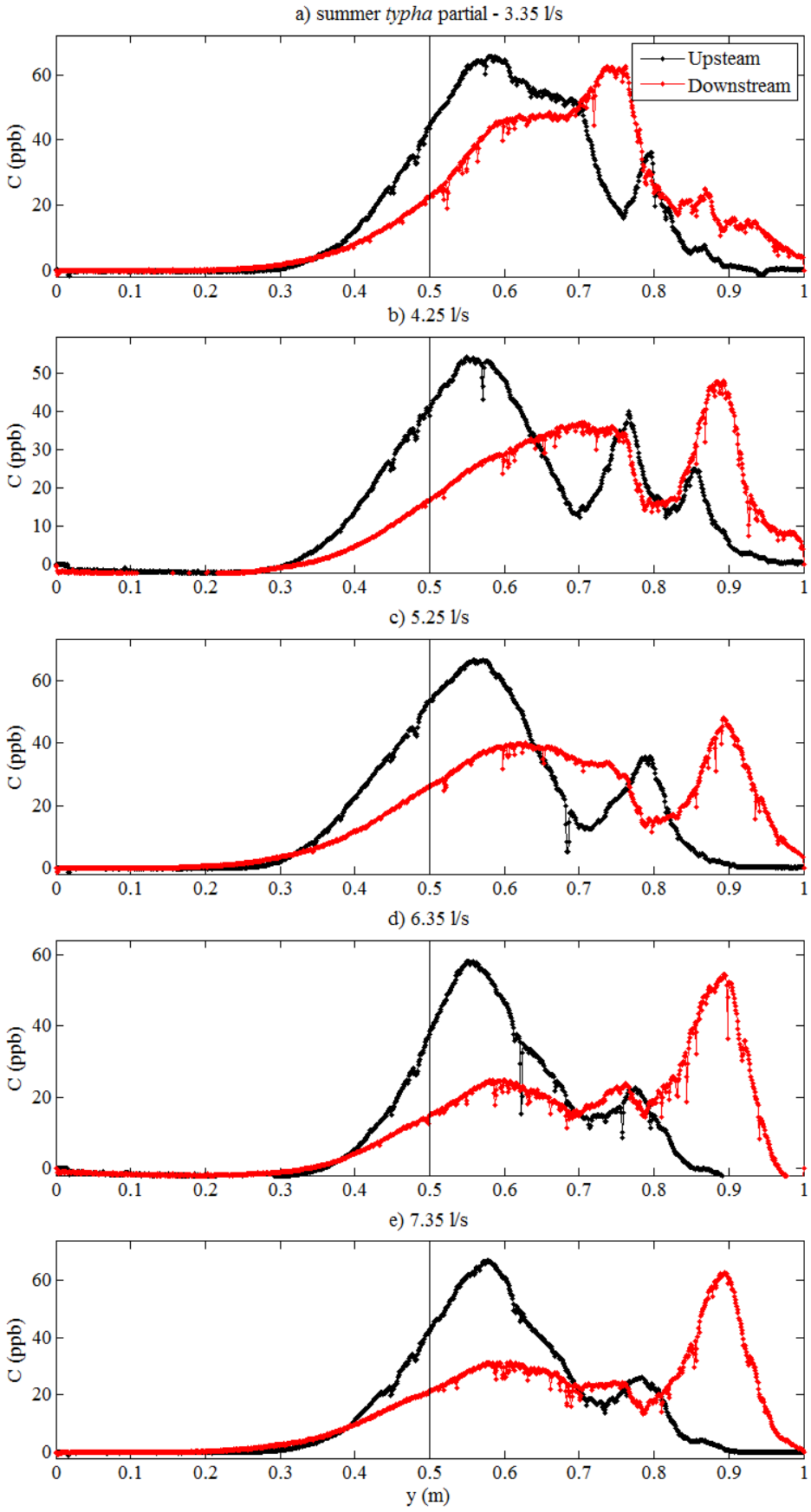

Figure 4.36: Steady-state profiles of $C(y)$ for the summer *typha*, partial vegetation.

5. Velocity and Solute Mixing Analysis

The first section of this analysis chapter presents the mean transverse and vertical profiles of longitudinal velocity used to accurately characterise the bulk hydrodynamic conditions and to provide functional descriptions of the mean velocity field for a finite element application. The second section further evaluates the flux-gradient analytical approached discussed in Chapter 3 and defines a finite difference model used to optimise the lateral variation in transverse mixing coefficient, $D_y(y)$.

5.1 Mean Velocity Analysis

This section describes the methods used to provide complete transverse and vertical profiles of temporal mean longitudinal velocity, $U(y)$ and $U(z)$, to quantify the characteristic features of shear layer vegetation. In the low density artificial cases the transverse profiles of velocity (Results Chapter section 4.4) are incomplete or exhibited undesirable attenuation and/or interference effects due to the proximate vegetation stems. Precise data needed to be extracted from the profiles to accurately characterize and compare the bulk hydrodynamic properties between the four vegetation types. Moreover, the quantification of mixing in the partial vegetation scenarios required the attainment of a complete transverse function for the temporal mean longitudinal velocity. As such, this section describes two methods of velocity characterization:

1) A means of providing a complete profile of U as a continuous function of transverse location, y;

2) A means of describing the bulk hydraulic characteristics e.g. depth-averaged, temporal mean vegetation velocity, $\langle U_1 \rangle$.

5.1.1 Fitting the transverse profile of velocity

In the partial vegetation scenario, the *Metflow UVP* probes enabled full transverse profiles of longitudinal velocity, $u(y)$, to be measured without the need for probe translation across the channel between readings. This approach was limited by to the attenuation of ultrasound signal power along the beam length; leading to erroneous and/or incomplete data towards the profiles limits and in the immediate vicinity of vegetation stems. A fitting method to obtain viable information from the incomplete transverse data records was sought. In developing the profile fitting it was assumed that $u(y)$ recorded from either side of the vegetation interface matches in the absence of attenuation effects. Such an assumption holds true if the temporal mean velocity field recorded over the test section did not vary significantly with downstream location i.e. if $U(y) \neq f(x)$. Recall that the transverse pointing UVP transducers were installed at 26° to the longitudinal direction and therefore recorded longitudinal velocity at different locations in x along the beam. Secondly, it was desirable to obtain profiles of $U(y)$ that contained few velocity inflection points and that were continuous. These profiles aided the analysis (detailed below) and allowed for better description of the characteristic flow regions. Finally, a description of $U(y)$ using a continuous mathematical function allow data point resolution matching with the steady-state concentration distributions, $C(y)$ – given above – required for a finite difference analysis.

The partial vegetation scenario is depicted in-profile in Figure 5.1 showing the vegetation interface located at $y_i = 600$ mm; where the emergent vegetation and open channel occupy $0 \leq y \leq 600$ mm and $990 > y > 600$ mm, respectively (e.g. Figure 4.21). The transverse profile of $U(y)$ depicted is typical of shear layer emergent vegetation. Recall that the horizontal interfacial shear vortices penetrate asymmetrically into the vegetation and open channel by δ_v

and δ_o, respectively. Beyond the penetration limits of the vortices, the velocity is considered constant. Within the vegetation, $0 \leq y \leq y_i - \delta_v$, the mean longitudinal velocity is denoted as U_1; while within the open channel, $y > y_i + \delta_o$, the mean longitudinal velocity is denoted as U_2. The slip velocity, U_s, is defined as the velocity difference between that at the interface and U_1 (e.g. White & Nepf, 2008 and Nikora et al., 2013).

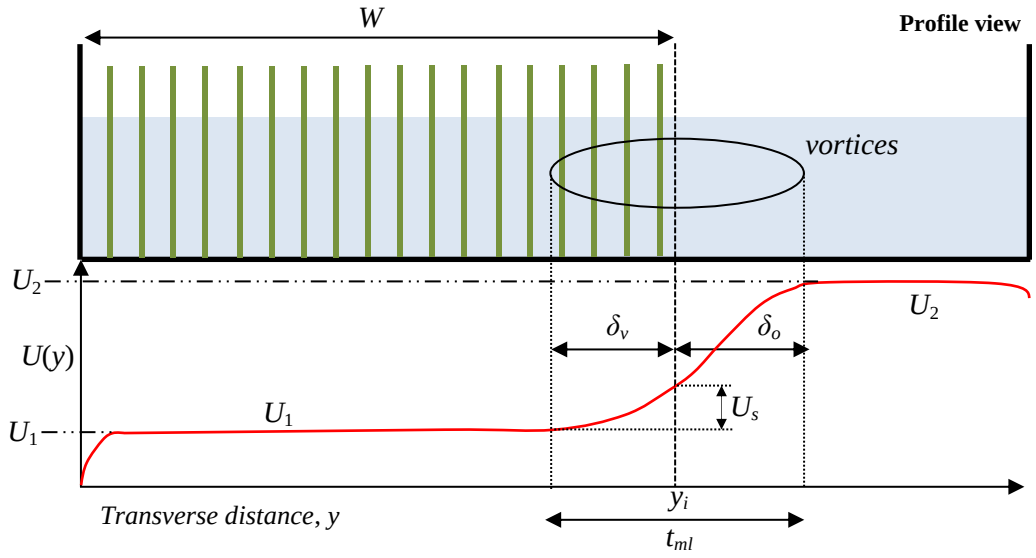

Figure 5.1: Idealised description of the velocity profile, $U(y)$ in shear layer, emergent vegetation.

a) Extracting viable data

Firstly, the viable data was defined as the data that did not exhibit significant ultrasound attenuation affects; however, the spatial limits containing the viable data needed to be defined. The measurement limitations of recording longitudinal velocity simultaneously from either side of the channel are exemplified in Figure 5.2 for the temporal mean profile, $U(y)$. The black line is the velocity measured from the channel wall at $y = 0$ mm. There is, qualitatively, a successful record of velocity within the first ~300 mm of the profile, after which the signal begins to decay towards the vegetation interface at $y \approx 600$ mm. The red line is the velocity measured from the open channel side of the channel at $y = 990$ mm. There is a general shear layer trend until the data becomes erroneous, shortly after the vegetation interface at $y \leq 550$ mm. Both profiles were measured at the same downstream location ($x = 11.31$ m) and

should, therefore, match in shape and magnitude in the region of the mixing layer ($300 \lesssim y \lesssim 850$ mm).

It was proposed that the data recorded using both transducers should be truncated from either side of the interface up to the spatial limits of accurate velocity measurements; and, since the data should match across the interface, a function could be fitted to this remaining data to provide a continuous profile of $U(y)$. Qualitatively, the acceptable data are seen in the regions $y \leq 250$ mm (vertical black line) and $y \geq 600$ mm (vertical red line) for the inner and outer regions of the profile, respectively.

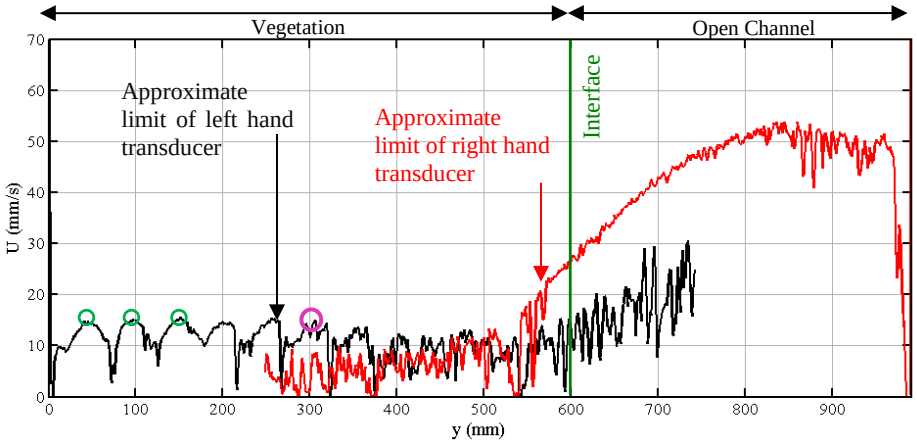

Figure 5.2: Temporal mean, mid-depth velocity, $U(y)$, measured in the low density, partial artificial vegetation from the left (black) and right (red) hand sides of the channel. Cyclical peaks in velocity are indicated using the green circles (U = 14.8, 14.8 and 15.1 mm/s). The pink circle indicates the point at which the local peak drops below the mean peak value minus the standard deviation.

b) Mean longitudinal velocity within the vegetation

The inner region of the profile ($y \lesssim 500$ mm) – within the vegetation – should theoretically exhibit a transversely constant mean longitudinal velocity (averaged over a distance greater than the stem spacing) and then increase towards the vegetation interface. The penetration distance of the shear layer vortices determines the location at which this increase begins. Figure 5.2 shows the region of approximately constant longitudinal velocity in the limits of $y \lesssim 250$ mm. Between $y \approx 50$ mm and $y \approx 150$ mm the local peak velocity, u_p, denoted by the green circles, remains at ($\pm \sigma_p$) 15 ± 0.2 mm/s. The peak velocity for the three green circles are 14.84, 14.83, 15.15 mm/s from left to right, respectively. An inner spatial limit was defined as

the penultimate location of u_p before $U(y)$, within one stem cycle, falls below one standard deviation of $\langle u_p \rangle$ for the first 3 cycles. The corresponding mean and standard deviation of the example peak data points are $\langle u_p \rangle$ = 14.94 mm/s and σ_p = 0.18 mm/s. Therefore, the cut-off in peak cycle velocity ($\langle u_p \rangle - \sigma_p$) is 14.76 mm/s. The acceptable data was defined as the data up to the point at which this peak cycle velocity drops below the value of 14.76 mm/s. In this example, this criterion was found at $y \approx 300$ mm. The point denoted with the pink circle is the location of the last peak-cycle velocity that is within the $\langle u_p \rangle - \sigma_p$ limit. Therefore, the data up to this point was considered acceptable and the inner region of the profile was truncated accordingly.

c) Mean longitudinal velocity in the open channel region

The spatial limit of accurate longitudinal velocity measured in the open channel by the open channel probe was defined as the vegetation interface (y = 600 mm in the case presented in Figure 5.2). This limit ensured that all of the contained data was not perturbed by stem obstructions or signal decay. Figure 5.3 presents the viable extracted data (black stars) when applying the defined spatial limits for the inner and outer regions to $U(y)$.

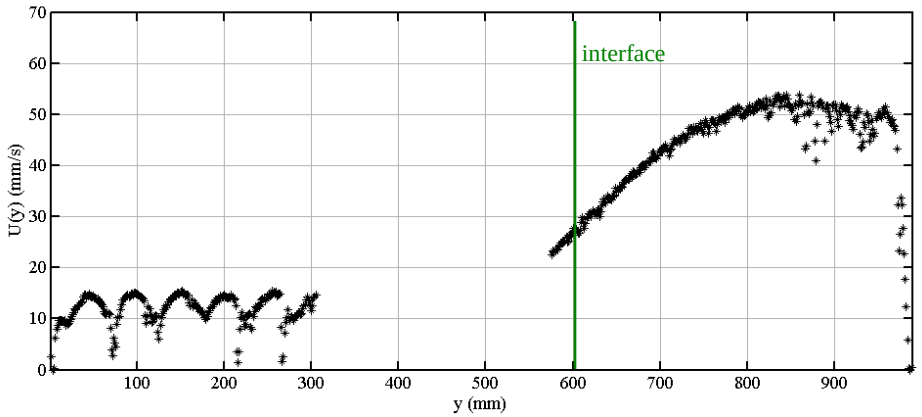

Figure 5.3: The extracted velocity data from $U(y)$ using the defined spatial limits of viable data.

d) Completing the mean transverse profile

The incomplete region of the extracted profile was fitted using the approach proposed by White and Nepf (2007) to create a continuous profile. The Authors used hyperbolic tangent

curves to predict $U(y)$ in emergent shear layer vegetation. The inner region was described using the following function:

$$U_i(y) = U_1 + U_s\left(1+\tanh\left(\frac{y-y_0}{\delta_v}\right)\right) \qquad \textbf{Equation 5.1}$$

where $U_i(y)$ is the inner region velocity profile, U_1 is the mean velocity within the vegetation beyond the mixing layer, U_s is the slip velocity defined as the velocity difference between that at the vegetation interface, U_{y0}, and U_1 (i.e. $U_s = U_{y0} - U_1$). In this case, U_1 was calculated as the mean of the acceptable data in the inner region (defined above). Note that a hyperbolic tangent function could not be employed to fit the full profile given the shear layer asymmetry ($\delta_v \neq \delta_o$).

The inner hyperbolic tangent profile (Equation 5.1) was evaluated for the channel conditions presented in Figure 5.3. The velocity measured within the vegetation recorded using the open channel mounted probe (y = 580-600 mm, red line in Figure 5.2) was retained to optimize the fit. This region was truncated at y = 580 mm as the following data points (in the region y < 580 mm) became erroneous. Figure 5.4 presents the implementation of the inner hyperbolic tangent fitting to the incomplete extracted profile of $U(y)$. The region of the curve within the vegetation (y < 300 mm) tends towards the vegetation mean velocity, U_1, of 12.3 mm/s.

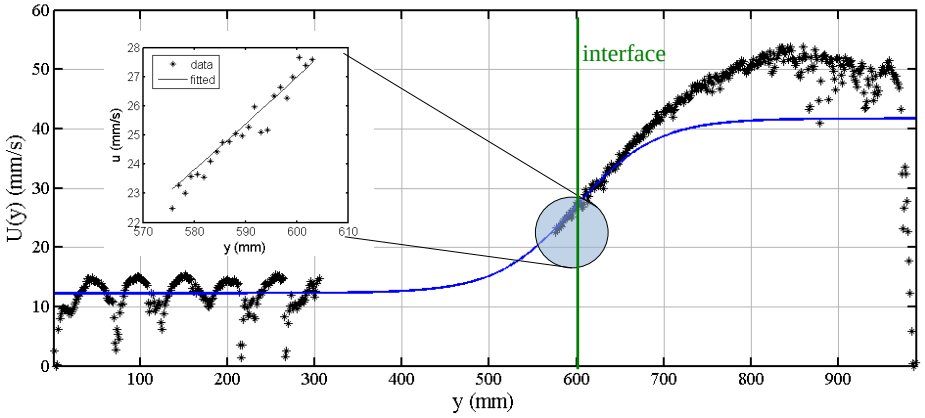

Figure 5.4: The region of erroneous data was bridged using a hyperbolic tangent profile (blue). Accuracy evaluation is shown in the subplot.

The accuracy of the fitting was evaluated by comparing the fitted curve with the velocity data in the vegetated region measured by the open channel probe (See circled area in Figure 5.4 and subplot). An R^2 regression quantified the fit between the hyperbolic tangent profile and the data in the blue-circled region $R^2 = 0.933$, in this instance; where varying the input value of δ_v was conducted to maximize the value of fit.

The fitted hyperbolic curve between the two regions was combined with the extracted velocity profile to create a complete, or *bridged*, transverse profile of velocity. The completed profile (Figure 5.5) was then used to evaluate the feasibility of other fitting and smoothing approaches to provide a continuous profile $U = f(y)$. The following section describes three approaches for achieving a continuous transverse profile of longitudinal velocity.

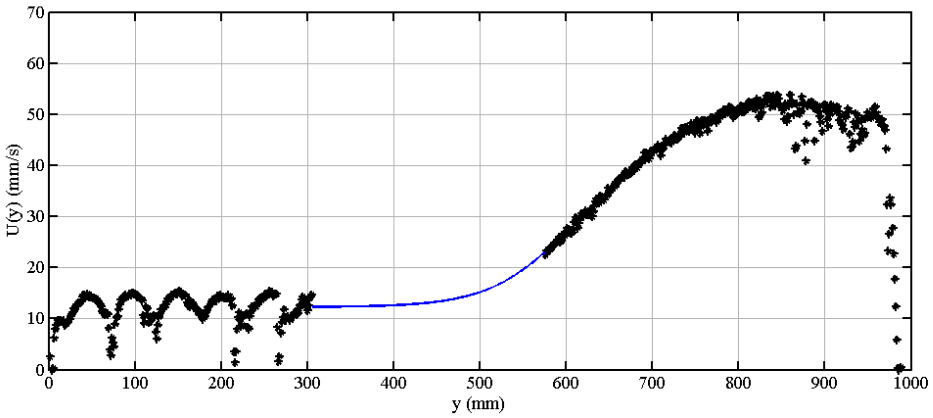

Figure 5.5: Bridge velocity profiles using inner hyperbolic tangent function (blue) superimposed onto the acceptable temporal mean longitudinal velocity data.

e) Velocity profile fitting approach 1 – running mean

The first proposed fitting approach was to implement a smoothing technique using a running-mean calculation. A running mean calculates the value of U at the location i along the profile as the arithmetic mean over a range k data points, e.g.

$$\overline{U_i} = \frac{\sum_{i=-\frac{k}{2}}^{i=\frac{k}{2}} U_i}{k}$$ **Equation 5.2**

This approach is favourable as it retains as much of the original raw data as possible. Equation 5.2 was applied to the bridged data shown in Figure 5.5. To reduce the effects of the cyclic

nature of the velocity profile between and behind the stems a value of $k = 40$ was applied (corresponding to a spacing of 50 mm). The running mean results are plotted in Figure 5.6. It can be seen that errors occur in the extreme limits of the profile (e.g. $y < 20$ mm and $y > 970$ mm) where the data to average is exhausted and therefore returns the same values.

The smoothing approach provides a continuous profile of velocity without losing any of the shear layer geometry; however, peak velocities are reduced due to local averaging effect. Despite the smoothing effects, the cyclic nature of $U(y)$ is still visible within the vegetation. These effects could be reduced further by increasing the value of k. However, the running-mean technique does not provide a mathematical description of $U(y)$ necessary to achieve mathcing of the data resolution required for the mixing analysis.

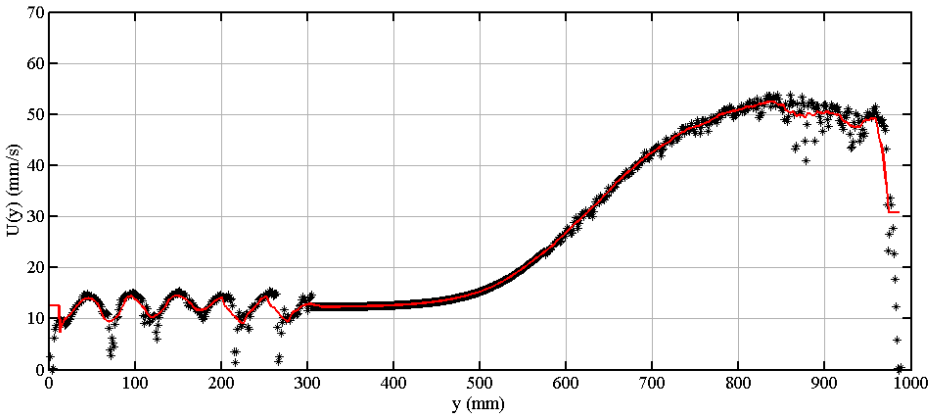

Figure 5.6: A 40 point running-mean smoothing of the bridged velocity data.

f) Velocity profile fitting approach 2 – full Hyperbolic profile

The second approach was to implement the full transverse hyperbolic fitting presented by White and Nepf (2007) – and later modified by Nikora et al. (2013) for submerged vegetation – with the inclusion of an outer-region hyperbolic tangent profile. The velocity profile in the outer region was given as function of the mean outer velocity, U_2, δ_o, and the location where the transverse velocity gradient of the two hyperbolic profiles match, y_m:

$$U_o = U_2 \tanh^2\left[\sqrt{\frac{3}{4(U_m/U_2+2)}}\left(y - y_m\right)\Big/\delta_o + A\right] - 2 \qquad \textbf{Equation 5.3}$$

where U_m is the matching velocity, $U(y_m)$, and A is given by,

$$A = \tanh^{-1}\sqrt{1+\frac{U_m/U_2\text{-}1}{3}} \qquad \textbf{Equation 5.4}$$

The outer profile equation was applied to the extracted data (Figure 5.3) in the outer region ($y > y_m$) and the fit was again evaluated using an R^2 regression. A complete fitted profile was created by combining the hyperbolic tangent profiles for the inner ($y < y_m$) and outer ($y > y_m$) regions. The hyperbolic fitting is shown in Figure 5.7 (red line) – where the subplot shows the fitting of the outer hyperbolic tangent profile using Equation 5.3.

The fitted hyperbolic tangent profile successfully captures the trend in velocity; where the vegetation velocity, U_1, and the open channel velocity, U_2, are matched well. However, the fitting fails to match the data in the extreme transverse limits ($y > 900$ mm, $R^2 = 0.221$) where the trend in raw velocity reduces towards 0 mm/s at the channel wall. A larger value of R^2 would have been attainable if the data was fitted up to the approximate location $y = 900$ mm; however, such a fit may omit valuable information regarding the profile shape towards the channel boundary. The ease of implementation of the hyperbolic fitting technique is advantageous and the parameterization of the governing equations – using U_1, U_2, δ_v and δ_O – also provides the required hydraulic parameters to characterize the mixing layer.

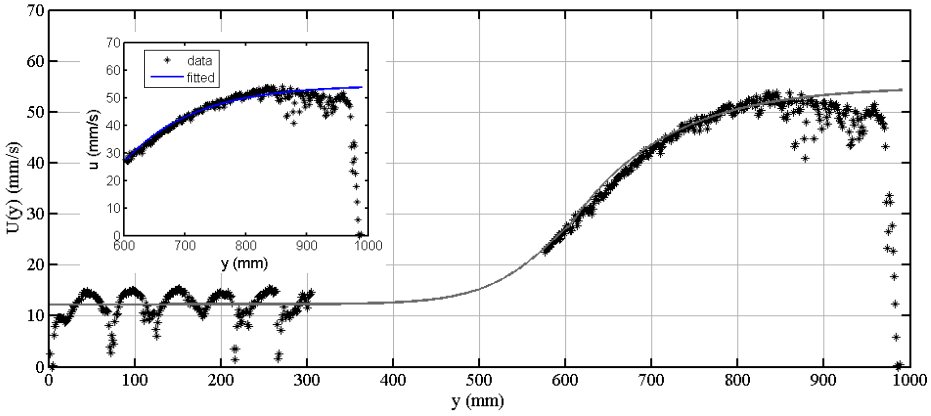

Figure 5.7: Tangential hyperbolic fitting for both the inner and outer regions using White and Nepf (2007).

g) Velocity profile fitting approach 3 – mathematical series

The final fitting approach was to fit the bridged data with a prescribed mathematical function. Fourier, Gaussian and Polynomial series were selected as the appropriate functions

capable of modelling the asymmetry in $U(y)$. The order of each function could be varied to describe the bridged velocity data depending on the complexity. The *Curve Fitting Toolbox* available with *Matlab 2012b* (Mathworks®) provides a range of functions that may be fitted to any data series and is advantageous as it provides a quantification of the fit (using R^2) and an explicit equation to describe the final trend $U = f(y)$.

The three function types were fitted to the bridge data – after smoothing using a 20-point running mean to minimize the effects of erroneous data points, such as the minima in the vegetated region ($y < 300$ mm) and the reduced velocity points in the open channel region ($850 \leq y \leq 920$ mm). A range of equation orders was also investigated to observe the impact on the quality of fit. The fitting series and the respective equations are:

Fourier $$U(y) = a_0 + a_1 \cos(y\varepsilon) + b_1 \sin(y\varepsilon) + \ldots a_i \cos(iy\varepsilon) + b_i \sin(iy\varepsilon)$$ **Equation 5.5**

where i is the series order, a_i, b_i and ε are constants.

Gaussian $$U(y) = a_1 \exp\left[-\left(\frac{y-b_1}{c_1}\right)^2\right] + \ldots a_i \exp\left[-\left(\frac{y-b_i}{c_i}\right)^2\right]$$ **Equation 5.6**

where a_i, b_i and c_i are constants.

Polynomial $$U(y) = P_0 + P_1 y + \ldots P_i y^{i-1}$$ **Equation 5.7**

where P_i is a constant.

The data fitting evaluation is provided in Table 5.1 for the three equation types and the 8 series orders. The best-fit values for each equation type are indicated by the shaded grey cells. The fits with the highest R^2-value do not necessarily yield the most desirable function shape for further analysis; as such, the best fits, from inspection, are given as bold text. The most desirable fits are plotted in Figure 5.8 for the a) Fourier, b) Gaussian and c) Polynomial series. All of the series fit strongly to the smoothed velocity profiles. The 5th-order Gaussian function provides the best fit; however, the precision of velocity within the open channel region may hinder further applications due to the changing sign in velocity gradient ($900 < y < 950$ mm). The 8th-order polynomial function is the worst of the fits ($R^2 = 0.9922$) and predicts the least constant velocity within the vegetated region. The Fourier 5th-order fit is the most desirable

result for further analytical application to shear layer mixing phenomena as it yields a near constant velocity within the vegetated region and a definitive plateau velocity within the open channel region. The profiles of $U(y)$ measured in 4 vegetation types for the 5 discharges were fitted using an appropriate order Fourier function. The profile order was varied between 3 and 5 for the individual cases to ensure that the results were the most suitable for the mixing analysis. The fitting results are detailed in the following sub-section.

Table 5.1: Goodness of fit values for three fitting methods over a range of series orders.

	Goodness of Fit (R^2)							
Eq. Order (i)	1	2	3	4	5	6	7	8
Fourier	0.9241	0.9841	0.9892	0.9923	**0.9949**	0.9952	0.9955	0.9960
Gaussian	0.8551	0.9860	0.9935	0.9637	**0.9969**	0.9939	0.9970	0.9970
Polynomial	0.7917	0.8466	0.9095	0.9841	0.9865	0.9888	0.9888	**0.9922**

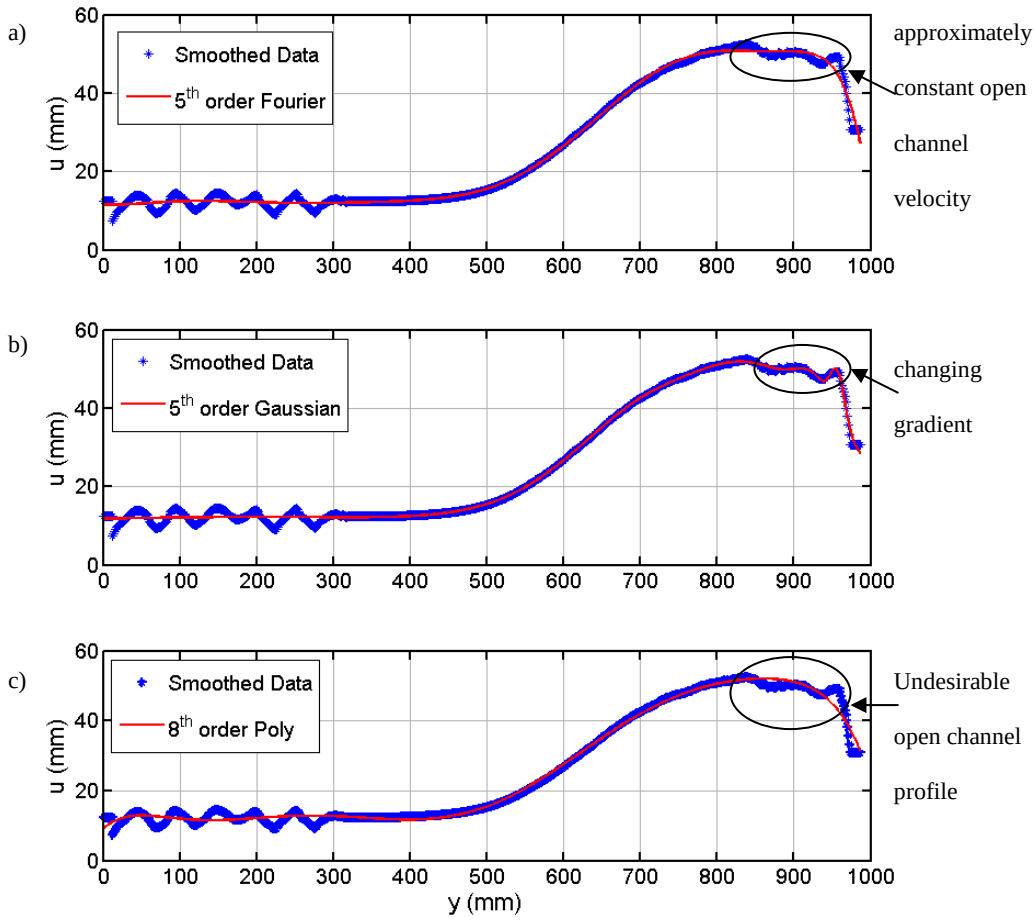

Figure 5.8: Example fitting functions used to fit the smoothed transverse profiles of longitudinal velocity using a) 5th order Fourier, b) 5th order Gaussian and c) 8th order polynomial series.

5.1.2 Mean transverse profiles of longitudinal velocity

a) Partially vegetated, high density artificial vegetation

The transverse profiles of mid-depth, temporal mean longitudinal velocity, $U_{md}(y)$, measured in the high density, partial artificial vegetation are plotted in Figure 5.9a (linear interpolation is made between the points) and are compared to the best-fit 5th order Fourier functions in Figure 5.9b (where the circles are the raw data).

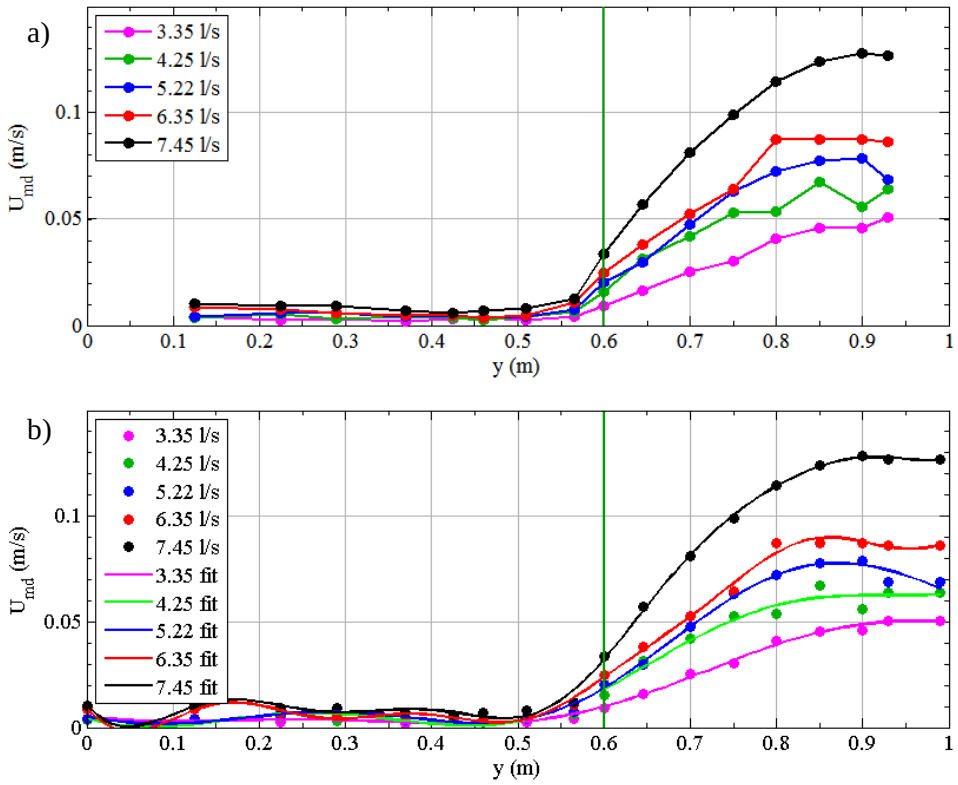

Figure 5.9: Transverse profiles of a) temporal mean, mid-depth longitudinal velocity, $U_{md}(y)$ are compared to b) the 5th order Fourier fitted profiles.

b) Partially vegetation, low density artificial vegetation

The best-fit 5th order Fourier functions were fitted to the bridged profiles of $U_{md}(y)$ measured in the low density artificial, partial vegetation. Figure 5.10 presents the results of this fitting for the a) upstream and b) downstream measurement locations and c) the mean fitted profiles. Note that the mean profile is the average of the upstream and downstream fittings.

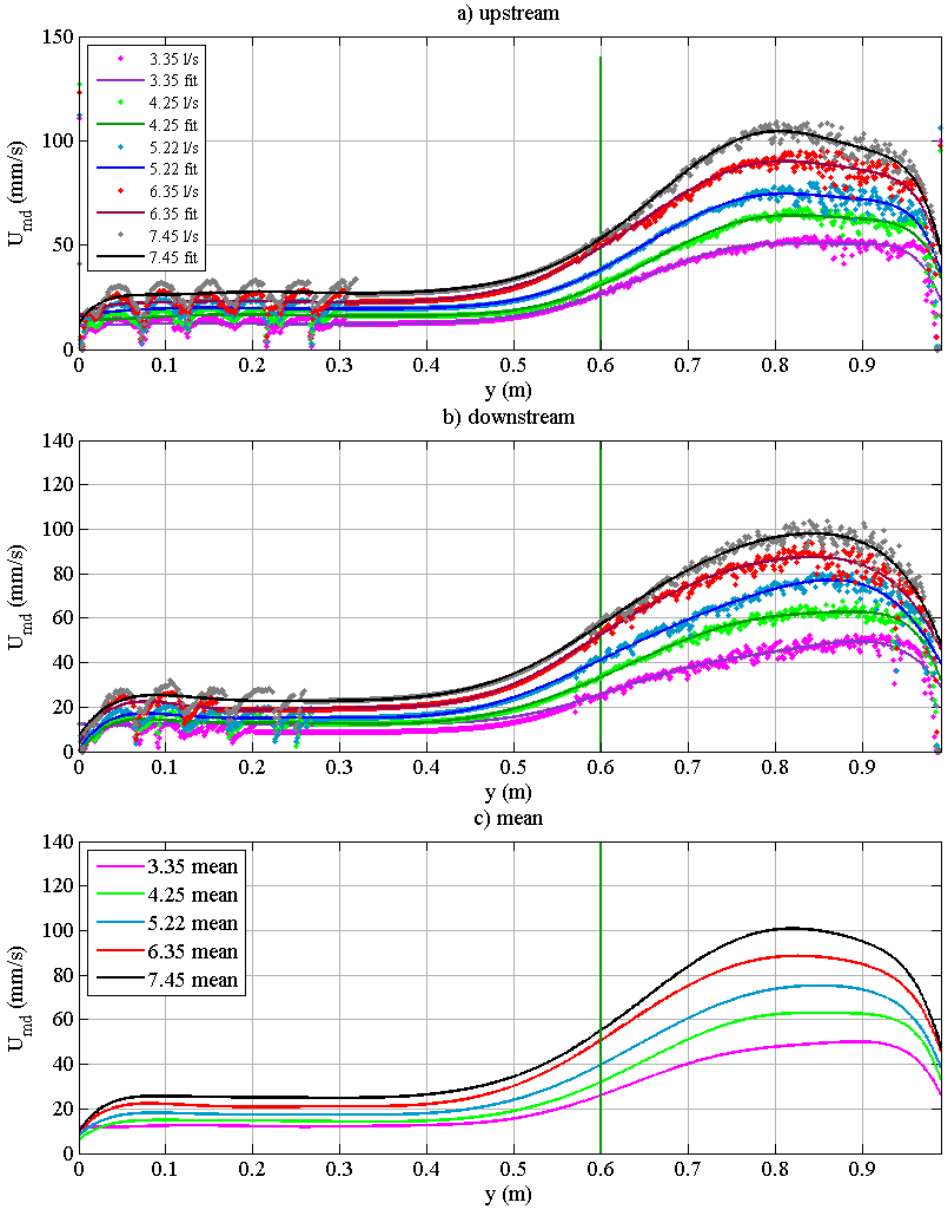

Figure 5.10: The best fit 5th order Fourier functions fitted to the a) upstream, b) downstream and c) the mean bridged profiles of $U_{md}(y)$ for the low density, partial artificial vegetation.

The best fit 5th order Fourier functions were also fitted for the 20-point smoothed bridged data and are presented in Figure 5.11 for a) upstream, b) downstream. The similarity between the functions fitted for the raw and smoothed data provide confidence for the use of the smoothed velocity profiles within the analysis and show that the Fourier function successfully describes the velocity shear.

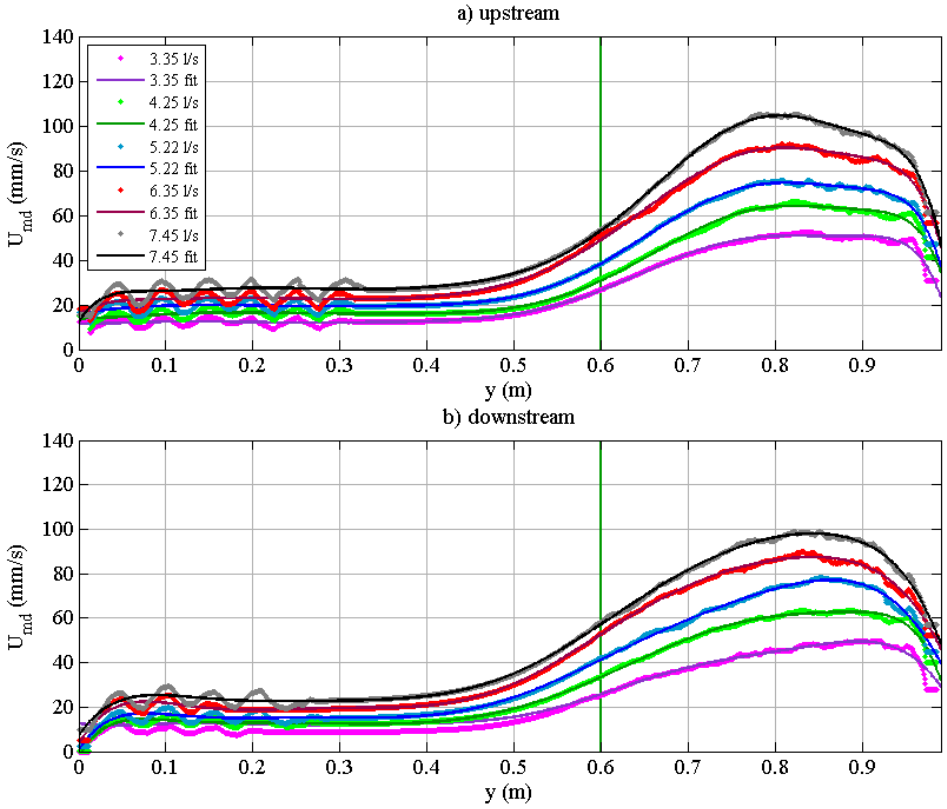

Figure 5.11: The best fit 5th order Fourier functions fitted to 40 point smoothed a) upstream and b) downstream bridged temporal mean, profiles of $U_{md}(y)$ measured in the low density, partial artificial vegetation.

c) Partially vegetated, winter typha

The 5th order Fourier function was fitted to the mean of the upstream and downstream transverse profiles of mid-depth, temporal mean longitudinal velocity measured in the partial winter *typha*. Figure 5.12 presents the results of the fitting; where the vegetation occupies the region $y < 0.500$ m. Recall that profiles of $U_{md}(y)$ recorded in the winter *typha* were not spatially complete. As such, the last data point of the raw velocity profiles at either extreme limit was populated along the remaining length of the profiles using the final data point to

complete the full 0.99 m channel profile. The Fourier function was then fitted to this extended profile.

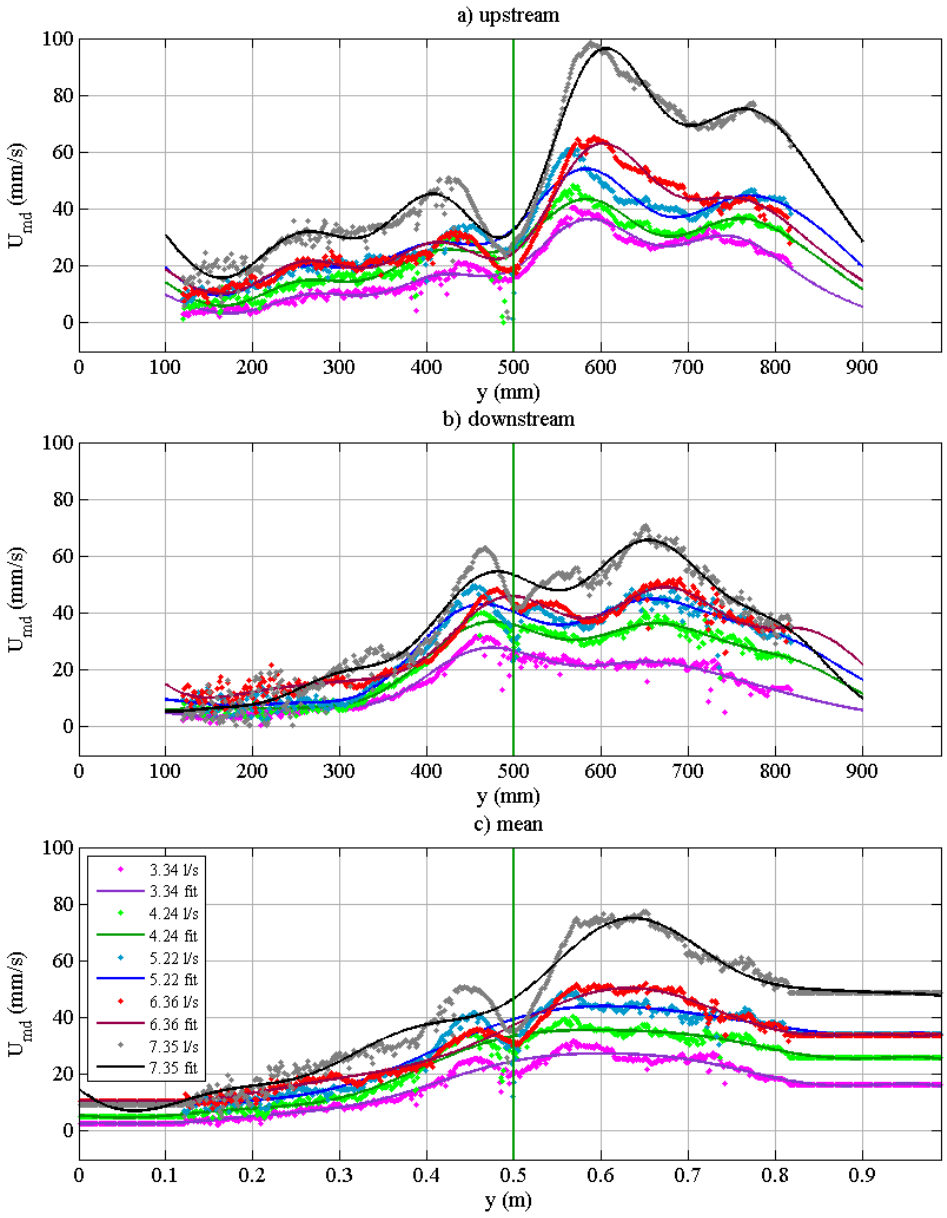

Figure 5.12: a) Upstream and b) downstream profiles of $U_{md}(y)$ measured in the winter *typha*, partial vegetation and c) the 5th order Fourier functions fitted to the mean profile of $U_{md}(y)$ with the inclusion of the extended data.

d) Partially vegetated, summer typha

Figure 5.13 presents the results of the 5th order Fourier fitting when applied to the partial summer *typha* vegetation. The vegetation occupies the region $y < 0.500$ m. Longitudinal velocity was measured at the channel mid-depth from either side of the channel. The complete profile was constructed by joining the profiles measured from either side at the vegetation

interface. The observation windows were larger for the real vegetation and therefore, attenuation affects did not occur. This was conducted for both the upstream and downstream locations and then averaged to produce the raw data shown in Figure 5.13.

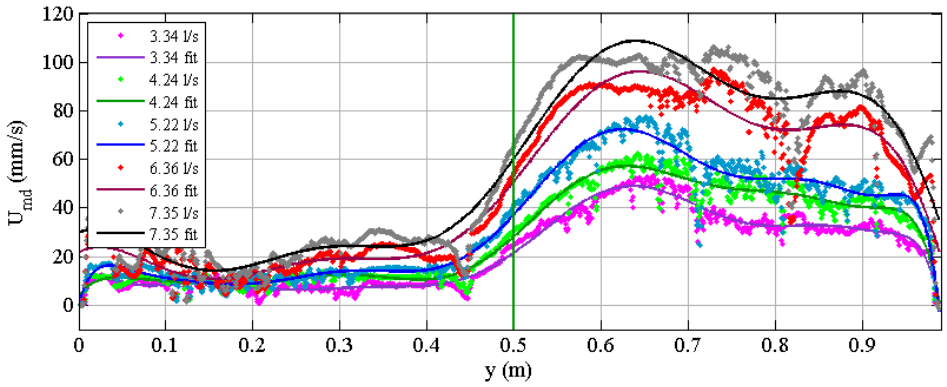

Figure 5.13: The best fit 5th order Fourier functions fitted to the mean of the upstream and downstream transverse profiles of mid-depth, temporal mean longitudinal velocity, $U_{md}(y)$, measured in the summer *typha*, partial vegetation.

5.1.3 Estimating the mixing layer width

The shear layer vortex penetration distances ($t_{ml} = \delta_v$ and δ_o) were required for the analysis of the transverse mixing. Mixing is considered spatially constant deep within the vegetation and into the open channel ($y < y_i - \delta_v$ and $y > y_i + \delta_o$); while the mixing in the velocity inflexion region is non-constant. It will be shown below that the quantification of a spatially variable transverse mixing coefficient relies on the spatial definition of the three mixing regions.

The Fourier fitted transverse profiles of longitudinal velocity were used to facilitate the definition of δ_v and δ_o. It can be seen that characteristic shear layer phenomena (Figure 5.9 & Figure 5.10) is well defined in the fitted profiles for both artificial vegetation types. Defining the mixing layer width is, therefore, potentially easier for the artificial cases. The distances δ_o and δ_v were determined using the regression to a hyperbolic fit proposed by White and Nepf (2007) (see above in Equation 1.32 and Equation 1.34). In contrast, the fitted profiles of $U(y)$ for both *typha* types deviated from the classical characterisation of shear layer vegetation and presented a difficulty when attempting to define the penetration distances. In the artificial cases, δ_v and δ_o were found at the location $U(y) \approx 0.2U_{max}$ and $U(y) \approx 0.98U_{max}$.

The hyperbolic tangent profiles could not be accurately fitted to the real vegetation profiles, $U(y)$, and therefore, the vortex limits were defined as fractions of the maximum open channel velocity. The in-vegetation penetration distance was defined using the relations seen in the artificial cases; where the maximum velocity within the open channel reduces by 80%, i.e. $\delta_v = y_i - y\,|_{U=0.2\max(U)}$. Secondly, the open-channel penetration distance was defined as the location where the velocity reduces by 2% of the maximum open-channel value, i.e. $\delta_o = y_i - y\,|_{U=0.98\max(U)}$.

5.1.4 Bulk-flow characteristics

This section details the methods used to categorize the bulk flow parameters for the test conditions. Characterising the flow cases and tests in terms of bulk flow parameters facilitates stronger comparisons between conditions and/or vegetation types. In the full vegetation, the flow was characterized using the depth-average, temporal mean longitudinal velocity from the vertical profiles. In the partial vegetation scenario the flow is characterized using U_1, U_2, ΔU and the mixing layer width (using t_{ml} to follow conventional notation).

a) Flow characterization – full vegetation

In the full vegetation cases, the channel mean longitudinal velocity was defined using the depth-averaged, temporal mean longitudinal velocity, $\langle U \rangle$. In the cases where full vertical profiles were measured, $\langle U \rangle$ was calculated as the mean, depth-average velocity of all of the available profiles, e.g. if 4x vertical profiles were collected then the mean vertical profile was calculated as the average of these four and then U was calculated as the mean of this average profile. However two exceptions were made. In the high density artificial case, profiles of velocity around the channel mid-depth were collected using the Vectrino II profiler; $\langle U \rangle$ was therefore calculated using the average of all the 10x mid-depth velocity values. This limits the validity of $\langle U \rangle$; however, the variation in mean longitudinal velocity with depth within the

vertically homogeneous full vegetation did not change significantly (see Results Chapter). Therefore the characterization of $\langle U \rangle$ using the reach-average, mid-depth velocity is a good approximation of the channel mean. Secondly, in the low density artificial case, transverse profiles of longitudinal velocity were collected in combination with the four vertical profiles. As such, three values of $\langle U \rangle$ are provided for the low density cases – representing the mean, depth-average from the vertical profiles; the mean of the mid-depth transverse profiles and the mean of one transverse "stem-cycle" (see below).

Figure 5.14 shows a close up of the mid-depth, transverse profile of temporal mean longitudinal velocity measured in the low density artificial case for 1.00, 3.00 and 7.50 l/s in the region $y < 0.400$ m. The transverse profiles are attenuated beyond $y = 0.400$ m. The "stem-cycle" velocity – i.e. the mean velocity over the length of the stem spacing – was calculated between the limits indicated by the vertical lines. The mean, mid-depth velocity was calculated as the average velocity over a number of complete "cycles" up to a "cut-off" point (the definition of the cycle "cut-off" point is described in the above section: *Transverse Profile Fitting*).

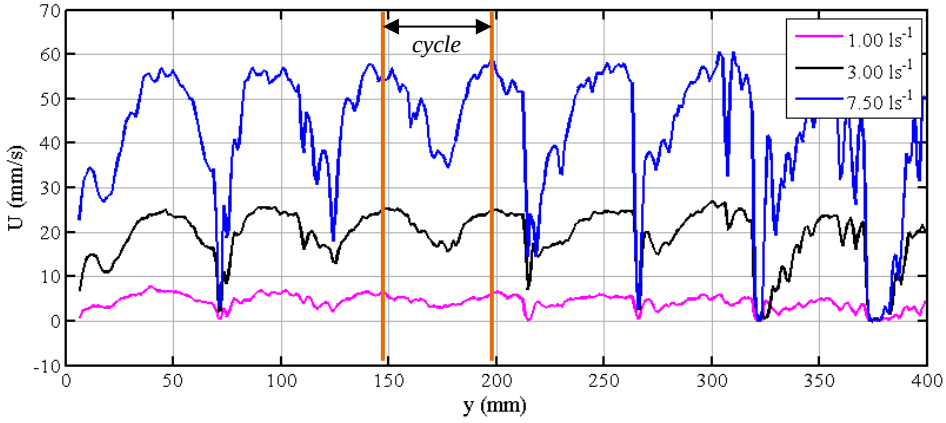

Figure 5.14: Close up mid-depth, transverse velocity profiles measured in the low density, artificial vegetation in the region $y < 0.400$ m. The cyclic nature of the velocity is observed between stems. The stem cycle velocity is the mean over one "stem-cycle".

Complete mid-depth, transverse profiles of longitudinal velocity could not be measured in both *typha* cases as the heterogeneous distribution of vegetation prevented the un-attenuated propagation of the ultra-sound beams. However, there was sufficient space between stems to

collect vertical velocity profiles. The vertical velocity profiles provided in the Results Chapter show that there was transverse variation in both the form and magnitude of $U(z)$. As such, describing the flow characteristics for the full *typha* vegetation using a single bulk parameter may fail to convey the heterogeneous nature of the velocity behaviour. Therefore, three values were calculated for each bulk parameter; the minimum, mean and maximum depth-average, temporal mean longitudinal velocity – where the minimum and maximum depth-average velocity is the smallest and largest depth-average velocity for a particular profile, respectively, and the mean, depth-average velocity is the mean of all of the combined vertical profiles.

Table 5.2 and Table 5.3 present the bulk flow characteristics for the full artificial and *typha* vegetation cases, respectively. The distinctions between mid-depth, depth-average or "stem-cycle" $\langle U \rangle$ are provided accordingly. The flow was characterised using a Stem Reynolds number, Re_d, based on the assumption that the major contributor to turbulence was the vegetation stems – where the stem diameter is therefore the appropriate length scale. Two values of Re_d are given for the low density artificial case calculated using the mean, mid-depth velocity and the depth-average velocity.

b) Flow characterization – partial vegetation

Estimates of U_1, U_2, δ_v and δ_o were made from the Fourier fitted profiles of $U(y)$ described above. The velocity shear and the mixing layer width were then determined from these estimates; where Table 5.4 and Table 5.5 show the results.

Figure 5.15a shows the increase in U_1 with channel discharge: where the highest velocity, for a given discharge, is observed for the low density artificial vegetation; while the lowest velocity is observed in the more dense, high density artificial vegetation. In contrast, the high density artificial vegetation shows the highest values of U_2 seen in Figure 5.15b. The winter and summer *typha* types show vegetation velocities that comparable and between those observed for the artificial cases. However U_2 is consistently lower than both artificial types for the winter and summer cases indicating that the enhanced resistance of the real vegetation bed

reduces the velocity. Finally, Figure 5.15c shows the change in ΔU with discharge. The high density artificial vegetation exhibits the strongest shear for a given flow rate. The differences in ΔU for the difference vegetation types confirms that the velocity shear is a function of vegetation characteristics – where the least dense types, winter *typha*, shows the lowest ΔU for a given discharge.

Table 5.2: Hydraulic parameters for the full artificial vegetation test cases. $\langle U \rangle$ is the depth-average temporal mean longitudinal velocity. The stem Reynolds number, Re_d, is scaled on the stem diameter, d.

Q (l/s)	N (stems/m^2)	$\langle U \rangle^{\#}$ (mm/s)	$\langle U \rangle^{\S}$ (mm/s)	$\langle U \rangle^{*}$ (mm/s)	$Re_d^{\#}$	$Re_d^{\S}$
1.00	1594	5.6	n/a	n/a	22.2	-
	398	6.6	6.25	4.9	24.9	24.8
1.50	1594	8.68	n/a	n/a	34.7	-
	398	9.3	11.6	9.5	46.2	45.8
2.00	1594	11.8	n/a	n/a	47.1	-
	398	12.1	14.9	12.9	59.3	58.7
2.50	1594	14.3	n/a	n/a	56.9	-
	398	15.3	19.7	17.2	78.8	77.1
3.00	1594	18.3	n/a	n/a	72.9	-
	398	18.8	23.2	20.8	92.6	92.1

$^{\#}$Depth average, temporal mean longitudinal velocity.
§Spatial average, mid-depth, temporal mean longitudinal velocity measured using the transverse *Metflow UVP* probes.
*Temporal mean longitudinal velocity calculated over one cycle between stem and wake.

Table 5.3: Hydraulic parameters full *typha* vegetation cases. $\langle U \rangle$ is the depth-average temporal mean longitudinal velocity.

Q (l/s)	*Vegetation*	$\langle U \rangle$ (mm/s)		Re_d
1.00	Winter	Min.	1.5	14
		Mean	3.1	28
		Max.	4.8	44
	Summer	Min.	3.5	67
		Mean	6.9	131
		Max.	9.4	179
1.50	Winter	Min.	2.0	18
		Mean	7.7	69
		Max.	13.5	121
	Summer	Min.	5.2	98
		Mean	9.4	179
		Max.	12.9	244
2.00	Winter	Min.	3.0	28
		Mean	6.6	60
		Max.	9.5	86
	Summer	Min.	2.4	46
		Mean	9.2	174
		Max.	13.8	262
2.50	Winter	Min.	2.9	26
		Mean	6.5	59
		Max.	10.2	119
	Summer	Min.	4.7	91
		Mean	13.1	249
		Max.	20.0	381
3.00	Winter	Min.	3.8	35
		Mean	10.9	98
		Max.	20.8	187
	Summer	Min.	5.9	112
		Mean	15.7	298
		Max.	24.8	473

Table 5.4: Hydraulic parameters for the partial artificial vegetation test cases. Stem Reynolds number, Re_d, was scaled on the stem diameter. Reynolds number, Re_H, was scaled on the flow depth, H (= 0.150 m in all cases).

Q (l/s)	N (stems/m^2)	U_1 (mm/s)	U_2 (mm/s)	ΔU (mm/s)	Re_d	Re_H	δ_v (mm)	δ_o (mm)	t_{ml} (mm)
3.35	1594	2.7	61.6	58.9	11	921	120	310	430
	398	10.6	49.6	39.0	42	7418	220	260	480
4.25	1594	4.0	72.6	69.0	16	10875	100	260	360
	398	14.0	63.5	49.5	56	9515	230	250	480
5.25	1594	5.5	81.0	75.5	22	12125	140	230	370
	398	16.8	74.9	58.1	67	11218	260	240	500
6.35	1594	7.8	103.5	95.7	31	15499	140	230	370
	398	20.7	88.7	68.0	82	13285	270	230	500
7.35	1594	9.4	140.6	131.2	37	21042	160	260	420
	398	24.2	100.9	76.8	97	15122	280	220	500

Table 5.5: Hydraulic parameters for the partial *typha* vegetation cases. Stem Reynolds number, Re_d, was scaled on the stem diameter. Reynolds number, Re_H, was scaled on the flow depth, H.

Q (l/s)	Season	U_1 (mm/s)	U_2 (mm/s)	ΔU (mm/s)	Re_d	Re_H	δ_v (mm)	δ_o (mm)	t_{ml} (mm)
3.35	Winter	3.9	26.6	22.7	35	3979	446	150	596
	Summer	8.5	37.9	29.4	163	5671	175	158	333
4.25	Winter	6.9	34.8	27.9	63	5203	447	168	615
	Summer	9.9	48.9	39.0	190	7549	212	125	337
5.25	Winter	9.5	42.8	33.3	86	6413	428	159	587
	Summer	11.4	56.5	45.1	220	8461	148	101	249
6.35	Winter	10.9	48.6	37.7	99	7135	490	186	676
	Summer	15.9	79.9	64.0	308	11973	214	91	332
7.35	Winter	11.9	70.8	58.9	107	10594	435	164	599
	Summer	20.4	92.1	71.7	394	13786	249	67	312

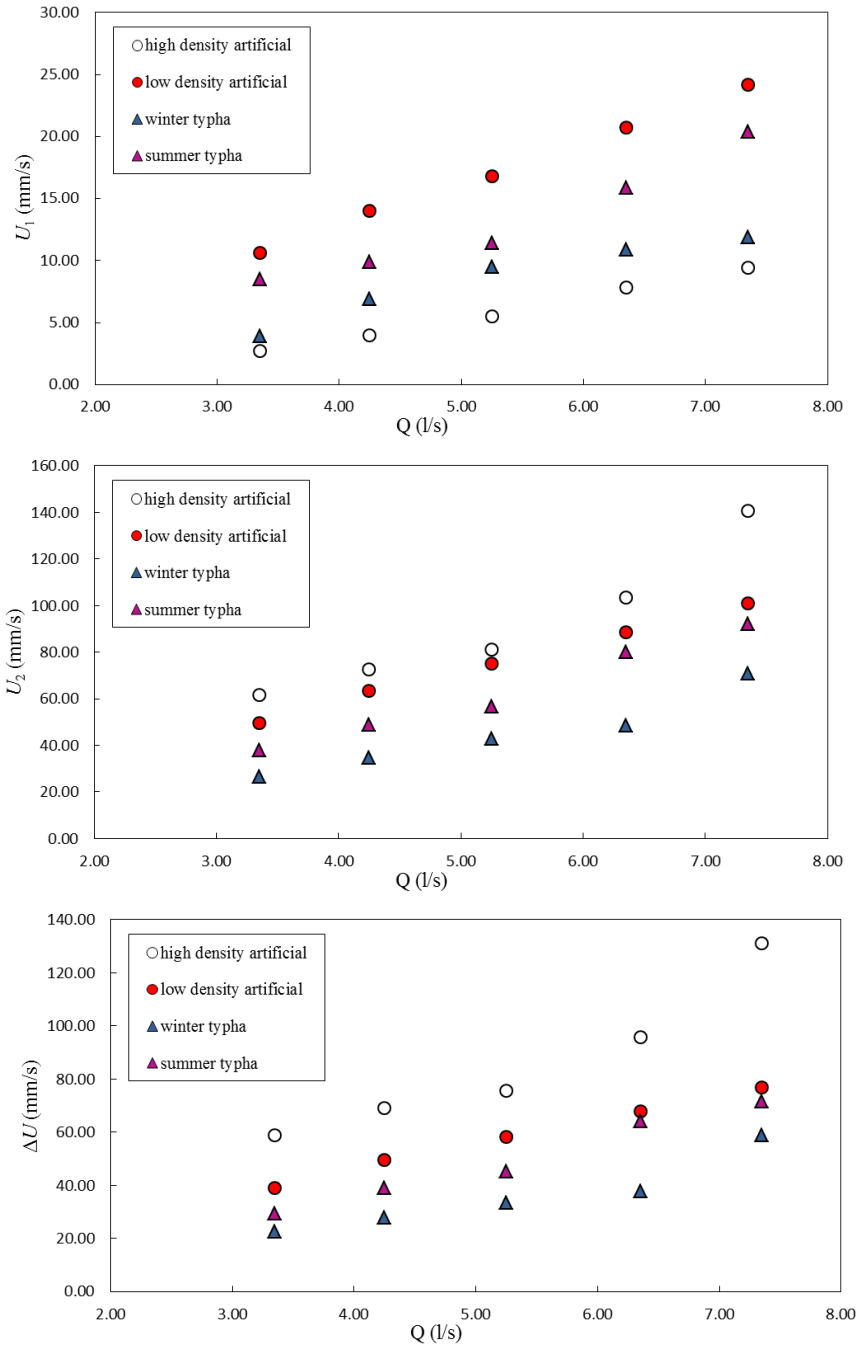

Figure 5.15: a) Vegetation velocity, U_1, b) open channel velocity, U_2, and c) velocity shear, ΔU, for the four vegetation types in measured in the partial scenario.

Figure 5.16 presents the Fourier fitted transverse profiles of mid-depth, temporal mean longitudinal velocity. The fitted profiles for the artificial types show a strong resemblance to the theoretical formulation described in the Review Chapter. The vortex penetration into the artificial vegetation was, as expected, greater for the more sparse, low density type. The large

frontal area per unit volume of the high density artificial acts as a greater sink of momentum and arrests the penetration of vortices. It is expect that – given the formulation between C_D, a and δ_v (White and Nepf, 2008) – a reduction in a from the high to low density ($a_{high}/a_{low} = 0.25$) would increase the vortex penetration by a factor of 4. The results do not confirm this relation but do suggest that the penetration increases by at least factor of 2 between the two types.

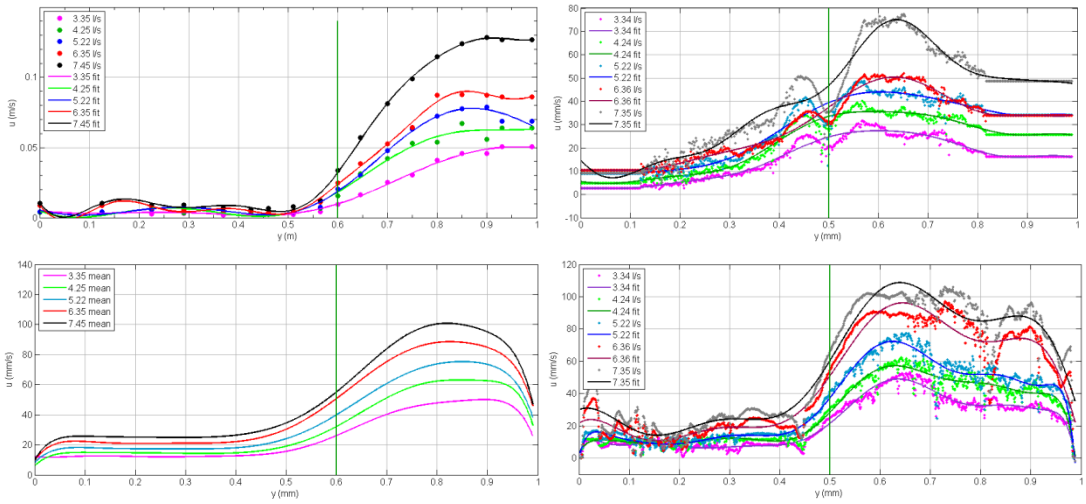

Figure 5.16: The fitted transverse profiles of mid-depth, temporal mean longitudinal velocity, $U_{md}(y)$, for the (clockwise), high density artificial, low winter *typha*, low density artificial and summer *typha* partial vegetation types.

The largest values of t_{ml} are observed for the winter *typha* supporting the hypothesis that the sparsely populated vegetation permits the penetration of shear layer vortices further into the region. When considering only the *typha* vegetation, the more dense and less porous summer vegetation generates a mixing layer that is approximately half that of the winter season. However, the non-classical nature of the transverse profiles of velocity recorded in the *typha* types meant that the characterization of t_{ml} was difficult; where the precision of the Fourier fitted velocity profile also limited[5] the accuracy in the prescription of t_{ml}. Note that the definition of the vortex penetration distance is based on the theoretical assumption that the velocity within the vegetation is constant. In making this assumption the complexity of the

[5]Recall that the vortex penetration limits were calculated using 20% and 98% of the maximum open channel velocity.

velocity field within the *typha* is reduced. The categorization of real vegetation velocity fields into theoretical shear layers is, therefore, a key limitation of this mixing layer analysis.

5.2 Solute Mixing Analysis

The solute mixing analysis is presented for a) assumed spatially constant transverse mixing in the full vegetation and bare channel scenarios and b) spatially variable transverse mixing in the partial vegetation scenario. Firstly, the spatially constant transverse mixing coefficients are calculated for the full vegetation and bare channel cases using a two-dimensional optimised Advection-Diffusion Model. Secondly, the application of a flux-gradient analysis (Equation 3.1) (e.g. Ghisalberti and Nepf, 2005) is evaluated for real transverse profiles of longitudinal velocity, $U(y)$, and steady-state concentration distributions, $C(y)$, measured in the partial artificial vegetation cases. Finally, a finite difference solution for the steady-state Advection Diffusion equation is evaluated and applied for a range of profile forms of the transverse mixing coefficient, $D_y(y)$.

5.2.1 Spatially constant mixing analysis – 2D ADE Model

The analysis of the pulse injection trace results measured in the full vegetation and bare channel scenarios is presented in this subsection. It will be shown that the spatial and temporal observations of concentration from an instantaneous trace injection permit simultaneous quantification of longitudinal and transverse mixing coefficients, D_x and D_y and the spatial mean longitudinal and transverse velocity, U_{ADE} and V_{ADE}. A two dimensional routing procedure was applied to calculate D_x and D_y as functions of U_{ADE} and V_{ADE}. It will be shown that estimates of D_y within the vegetated and open channel regions are required for the analysis of spatially variable transverse mixing coefficients.

a) Two-dimensional Advection-Diffusion Model

A two-dimensional advection-diffusion (2D ADE) routing analysis was applied to the pulse injection trace results to calculate average values of D_x, D_y, U_{ADE} and V_{ADE} (e.g. West et al., 2016). Note that, such a procedure relies on the assumption that the longitudinal and transverse mixing coefficients are spatially uniform, i.e. $\partial/\partial x$, $\partial/\partial y = 0$, when averaged over distances greater than the mean stem spacing.

Firstly, the measured upstream concentration distribution ($C_{x1}(y, t)$) was discretized. The ADE model was then employed to predict the advection-diffusion behaviour of every discretized component, or 'unit', of the 2D-concentration distribution – assuming that the spatial diffusion of every unit is Gaussian. The downstream distribution ($C_{x2}(y, t)$) was predicted by advecting and diffusing every unit of the upstream distribution using an initial set of guess input parameters; D_x and D_y, U_{ADE} and V_{ADE}. The quality of fit between the downstream measured and predicted distributions was quantified using an R^2 regression evaluation. Finally, the input parameters were optimised by interactively varying their magnitude to acquire the best-fit between downstream predictions and observations.

b) 2D ADE routing results

The 2D routing procedure was independently applied to the ten repeat instantaneous injections. The best fit input parameters (D_x, D_y, U_{ADE} and V_{ADE}) were then calculated using the average optimal values from all repeats – and not from the mean concentration distribution (i.e. the average of all 10 repeats) since averaging of the concentration field reduces resolution and smooths detailed trace features. Note that, the upstream and downstream concentration distributions were mass-balanced to facilitate a successful optimization.

Figure 5.17 shows the average optimised mean longitudinal velocity, U_{ADE}, for the four vegetation types;[6] where the solid line indicates the area mean velocity (Q/A). Longitudinal velocity in the summer *typha* is expected to be the highest as the large solid volume fraction

[6]The optimized travel time between upstream and downstream centroids of the respective concentration distributions was used to calculate U_{ADE}.

effectively reducing the total volume of water per unit channel volume. The mean optimized values if D_x and D_y are presented in Figure 5.18 and Figure 5.19, respectively, comparing a) the 10 repeat optimal values and b) the average values; where the error bars denote the range. A summary of the optimized parameters is provided in Table 5.6. Greater spread is given to the *typha* vegetation where the tests are less reproducible (compared to the artificial types). The winter *typha* exhibits the largest spread in mixing coefficient and is associated with strong geometric heterogeneities in the vegetation.

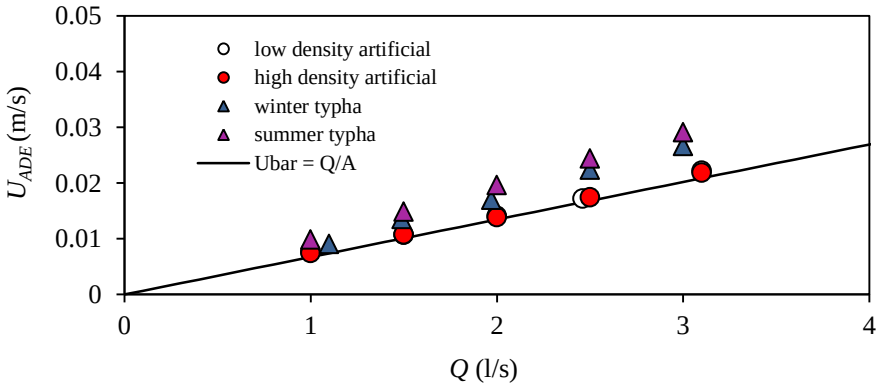

Figure 5.17: Mean longitudinal velocity, U_{ADE}, for the full vegetation types calculated using the optimized travel time from the 2D ADE optimised routing analysis.

Longitudinal and transverse mixing in the artificial vegetation is of comparable magnitude for both densities. The high density artificial exhibits greater longitudinal mixing, in general, while the rates of transverse mixing are approximately equal to those in the low density type, given the repeat test error. The winter *typha* exhibits lower rates of longitudinal mixing, when compared to the summer type, while the rates of transverse mixing show the opposite relation. Longitudinal and transverse mixing is greater in both real vegetation types compared to the artificial types for all discharges. In all the cases there is a general trend of increasing mixing with channel discharge; however, both *typha* cases show a stronger increase in mixing with discharge compared to the artificial vegetation. Longitudinal mixing is an order of magnitude larger than transverse mixing; although the difference is less noticeable for the *typha*.

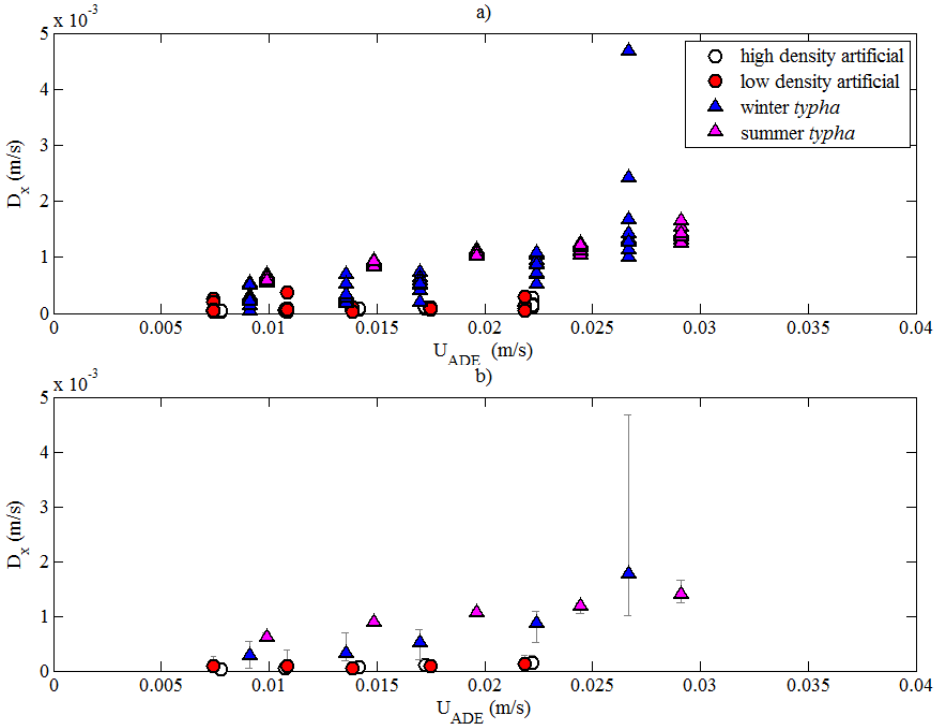

Figure 5.18: Optimized values of D_x using the 2D ADE routing analysis in the full vegetation scenario are compared to U_{ADE} for a) all 10x repeat pulse injections and b) the mean of the 10x repeats; where the error bars denote the range in D_x.

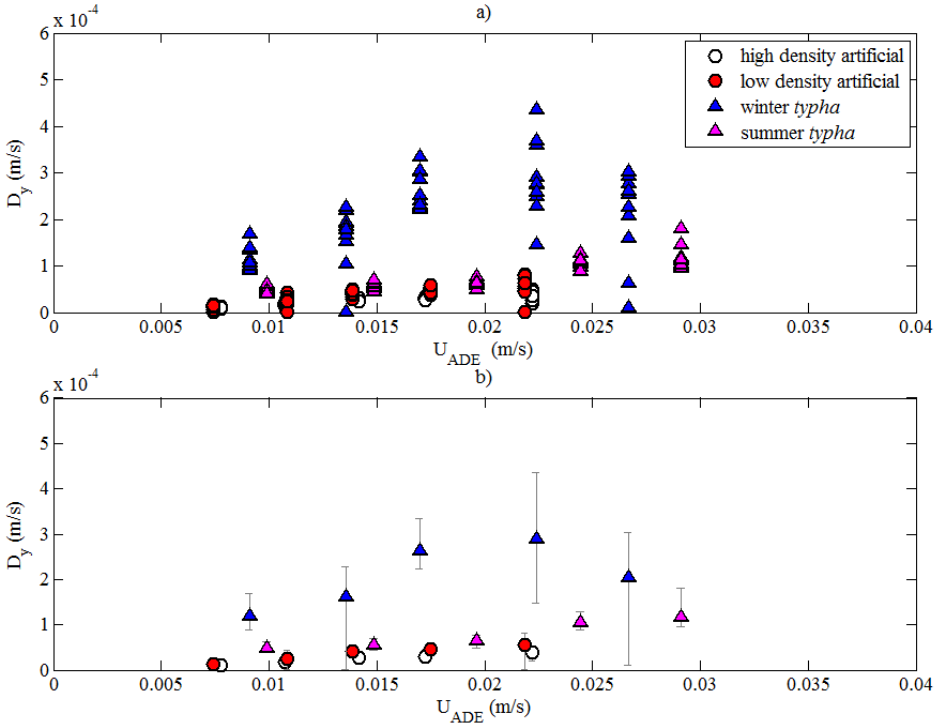

Figure 5.19: Optimized values of D_y using the 2D ADE routing analysis in the full vegetation scenario are compared to U_{ADE} for a) all 10x repeat pulse injections and b) the mean of the 10x repeats; where the error bars denote the range in D_y.

Table 5.6: The optimized values of D_x, D_y and mean U_{ADE} calculated using the 2D ADE routing procedure. Mixing coefficients and velocity are quoted in 10^{-5} m^2/s and mm/s, respectively.

	High density artificial			Low density artificial		
Q	D_x	D_y	U_{ADE}	D_x	D_y	U_{ADE}
1.0	3.51	1.04	7.7	4.98	1.70	7.5
1.5	5.36	1.79	10.7	5.15	2.93	9.0
2.0	7.47	3.03	14.1	5.53	3.12	9.5
2.5	10.15	3.07	17.2	8.42	4.05	13.0
3.0	11.60	4.35	22.2	7.95	4.74	16.1
	Winter *typha*			Summer *typha*		
Q	D_x	D_y	U_{ADE}	D_x	D_y	U_{ADE}
1.0	30.60	11.70	8.6	40.95	2.27	6.6
1.5	28.22	16.70	13.2	71.31	4.54	11.9
2.0	50.05	23.66	15.9	79.49	4.75	14.4
2.5	69.60	29.14	21.1	100	9.21	21.2
3.0	85.57	29.35	23.9	140	12.23	29.1

c) Concluding remarks on 2D ADE

The distinctive increase in longitudinal mixing with mean velocity for the *typha* vegetation is attributed to the heterogeneous stem morphologies and distribution; e.g. Figure 4.26 (winter *typha*) and Figure 4.27 (summer *typha*) show a distinct deviation from the Gaussian spreading when compared to Figure 4.24 (high density) and Figure 4.25 (low density). These heterogeneities cause local and regional variations in the flow field and, as such, increase turbulent and mechanical diffusion. Moreover, differential advection due to bed shear affects is promoted in the real vegetated given the increased bed roughness; where the vertical profiles of temporal mean longitudinal velocity, $U(z)$, for both *typha* seasons exhibit greater vertical shear when compared to artificial equivalents.

There is, however, a smaller difference in the transverse mixing between the *typha* and the artificial vegetation tests. The summer *typha* and low density artificial vegetation show more comparable transverse mixing than longitudinal mixing. Despite the solid volume fraction of the summer *typha* being 7 times larger than the low density artificial ($\Phi = 0.037$ compared to

0.005), the comparable frontal area per unit volume ($a = 0.035$ compared to $0.016\ cm^{-1}$) suggests that turbulent and mechanical diffusion are of similar magnitudes.

5.2.2 Evaluation of analytical Advection Diffusion solution

a) Application to real data

The efficacy of the flux-gradient analysis (Equation 3.1) proposed by Ghisalberti and Nepf (2005) was evaluated for the low density, artificial, partial vegetation (evaluated for three analytical cases in Chapter 3) in order to quantify the transverse mixing in vegetated shear layers. The case conducted at 5.25 l/s was chosen as a suitable test condition for the application as the steady-state concentration distributions and mean transverse profile of longitudinal velocity, $U(y)$, qualitatively match those required for the analysis (e.g. continuous profiles with minimal variation in the sign of the concentration gradient). Given the models sensitivity to the mean transverse concentration gradient, $\langle \partial C/\partial y \rangle$; the concentration profiles were firstly fitted with a 3rd order Gaussian distributions using a curve fitting application (Mathworks, 2012) (section 5.1.1). Figure 5.20a shows the raw transverse concentration profiles measured at 1 and 2 m downstream of the continuous injection point and the 3rd order Gaussian fit. Figure 5.20b provides the corresponding profiles of $U(y)$ measured at the flow mid-depth. The velocity profile was fitted using a 5th order Fourier series to provide a smooth, continuous distribution to facilitate the flux-gradient model's procedure (see section 5.1.1).

Recall that the constraining criteria, c_1 and c_2, are defined by the minimum and maximum changes in transverse concentration gradient between the upstream and downstream mean distributions. The constraining criteria were applied to real example profiles and are graphically visualized in Figure 5.21. The regions where the data exceeds the blue line in Figure 5.21a represents the locations where the model cannot be applied. Similarly, the region between the blue lines in Figure 5.21b represents violating locations. The presence of a secondary breach of the c_1 criteria (at $y \approx 0.7$ m in Figure 5.21a) is attributed to the region of

the concentration distributions where the upstream and downstream profiles simultaneously show negative and positive transverse concentration gradients, respectively (i.e. $\langle \partial C/\partial y \rangle_B >> \langle \partial C/\partial y \rangle_A$). The minimum change in gradient criteria, c_2, shows a definite extension in the negative y direction due to the absence of tracer deep within the vegetated region.

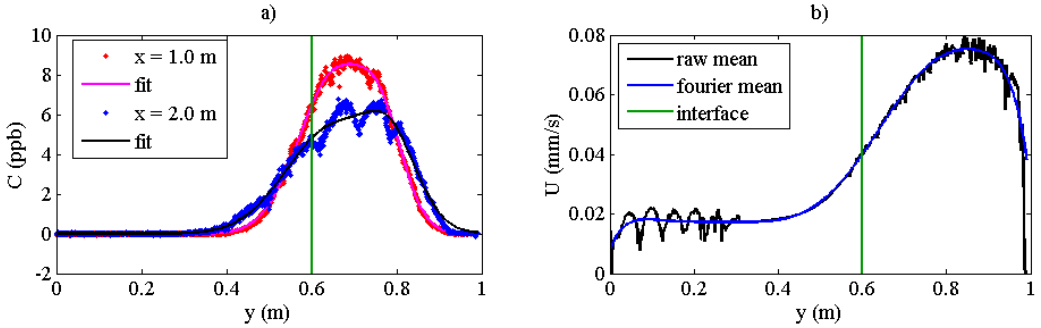

Figure 5.20: a) The raw and 3rd order Fourier fitted transverse concentration distributions measured in the in the low density artificial vegetation are provided with b) the corresponding profile of $U(y)$ (black) and the Fourier fitting (blue). The vegetation interface is given by the vertical green line where the region $y < 0.600$ m is vegetation.

The constraining criteria were then applied to the concentration distributions. The regions where the flux-gradient analysis cannot be applied are given by the grey shading in Figure 5.22a. The appearance of two small shaded regions in the vicinity of the concentration peaks (at $y \approx 0.7$ and $y \approx 0.75$ m) are attributed to the difference in sign of the concentration gradient and a small change in the fractional gradient, respectively.

The final evaluation of the Flux-Gradient analysis using the real measured data is shown in Figure 5.22b; where the violating regions are given by the grey shading. Equation 3.1 fails to produce a meaningful profile of $D_y(y)$; where the magnitude of D_y falls below 0 m^2/s at $0.75 \text{ m} > y > 0.6$ m. The prevalence of locations where the model cannot be applied causes a discontinuity between viable regions. The model fails to cope with the changes in concentration gradient in the vicinity of peak concentration ($0.65 < y < 0.8$ m) resulting in a profile of transverse mixing coefficient with little physical meaning. However, the peak value of D_y at $y \approx 0.5$ m is 4.56×10^{-5} m^2/s; similar in magnitude to the values of D_y measured in the full vegetation scenario.

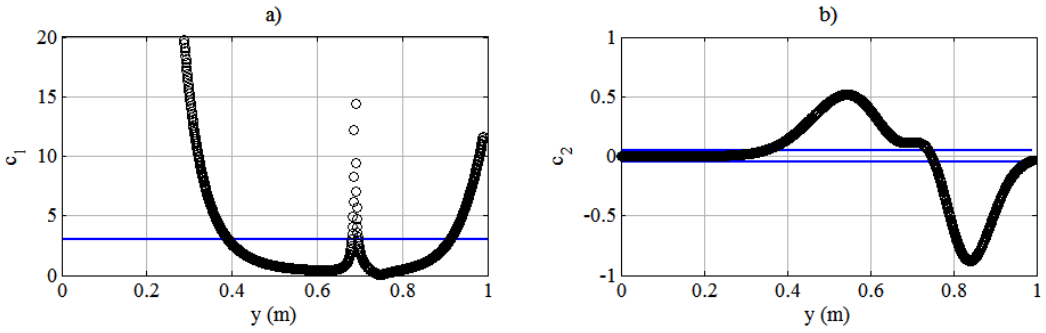

Figure 5.21: Constraining criteria a) c_1 and b) c_2 applied to the real concentration distributions.

b) Application to real data – concluding remarks

Equation 3.1 struggles to evaluate meaningful profiles of transverse mixing coefficient using the discontinuous, real velocity and concentration profiles. The model cannot be evaluated where there is a change in sign from upstream to downstream in the concentration gradient given the asymmetry in the upstream and downstream profiles of $C(y)$, i.e. regions where $\Delta(\partial C/\partial y)$ is large. In the case provided in Figure 5.22a, criteria c_1 is exceeded at $y \approx 0.7$ m as $(\mathrm{d}C/\mathrm{d}y)_{\text{downstream}} \approx (\partial C/\partial y)_{\text{upstream}}$; and criteria c_2 is violated at $y \approx 0.75$ m as $(\partial C/\partial y)_{\text{downstream}} << (\partial C/\partial y)_{\text{upstream}}$. There is also an undesirable influence on the values of $D_y(y)$ in non-violating regions from the violating regions. This has the effect of distorting the profile of $D_y(y)$ in apparent valid locations yielding unreliable results.

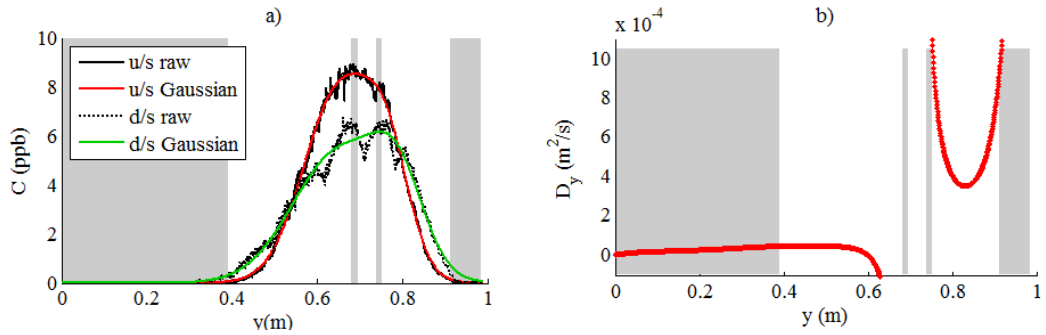

Figure 5.22: Constraining criteria visualized in grey shading for a) the fitted concentration distributions and b) the predicted profile of $D_y(y)$.

Finally, the model's failure to reliably evaluate $D_y(y)$ in the vicinity of the mixing layer renders it impractical for qualifying the mixing characteristics of shear layer vegetation. Moreover, the application to data measured using live, heterogeneous vegetation may prove to be undesirable given its inapplicability to less erroneous data shown here. As such, the

application of Equation 3.1 cannot be certified as an accurate method for quantifying mixing in spatially variable flow fields.

5.2.3 Finite Difference Model analysis

The limited applicability of Equation 3.1, discussed above and in Chapter 3, demanded another approach for quantifying $D_y(y)$. This section describes the evaluation and implementation of a Finite Difference Model (FDM) used to approximate the two-dimensional ADE equation for spatially variable temporal mean longitudinal velocity and transverse mixing coefficient, $U(y)$ and $D_y(y)$. The efficacy of the FDM was evaluated for analytical and real experimental scenarios and its customisation to vegetated shear layers is justified accordingly. Similarly to the evaluation of Equation 3.1, the evaluation of the FDM is conducted using increasingly complex input forms of $D_y(y)$.

a) Finite Difference Model

The FDM predicts the downstream concentration distribution given input transverse profiles of upstream concentration, channel depth, $h(y)$, $U(y)$ and $D_y(y)$, as follows:

- Input the measured upstream transverse concentration distribution, $C_1(y)$;
- Input a mean transverse profile of stream-wise velocity, $U(y)$ and depth, $h(y)$;
- Input a transverse profile of $D_y(y)$;
- Calculate the resultant downstream transverse concentration distribution for a chosen location in x, $C_2(y)$.

The governing equation for the FDM was the 2D steady-state Advection-Diffusion equation (Equation 1.17) solved for the scenario $\partial C/\partial t = 0$. Allowing for a transverse variation of depth, U and D_y and assuming depth-averaged quantities, the steady-state equation becomes (Heinrich et al., 1977);

$$\mathrm{h}(y)U(y)\frac{\partial C(x,y)}{\partial y} = \frac{\partial}{\partial y}\left[h(y)D_y(y)\frac{\partial C(x,y)}{\partial y}\right] \qquad \textbf{Equation 5.8}$$

Note that, in this formulation, D_y and U are not functions of x; however, in reality, for real vegetation, the transverse variation of longitudinal velocity, and therefore transverse mixing coefficient, will vary longitudinally due to the heterogeneous distribution of vegetation, e.g. N, a, $\Phi = f(x)$. To minimize this limitation the application of the FDM in real vegetation requires the mean transverse profile of longitudinal velocity between adjacent longitudinal measurement locations. Another assumption is that the rate of vertical mixing is insignificant compared to transverse mixing. Recall that a vertical line source of tracer was employed in the experimental stage to eliminate this effect; however, differential advection due to vertical shear would have been significantly greater in the real vegetation tests given the increased bed roughness.

A finite difference solution to Equation 5.8 was evaluated on a uniform rectangular grid, with i and j longitudinal and transverse computational nodes, assuming that values of h, U and D_y are available at all nodes. Such a solution creates N-2 simultaneous equations that were efficiently solved using the Thomas algorithm; where Appendix V provides the derivation of the model discretization. Further, the transverse mixing was treated with a "central" approximation while the longitudinal advection was treated with an "upwind" approximation.

Firstly, the FDM was evaluated for two analytical solutions: a spatially constant transverse mixing coefficient and a transverse discontinuity in $D_y(y)$ (i.e. Kay, 1987); where i and j were discretized into 1 mm spacing. Transverse concentration distributions from a continuous source were estimated for 1 and 2 m downstream using the steady-state solution (Equation 3.2) and the discontinuity solution provided by Kay (1987). The downstream distribution was then predicted using the FDM where Figure 5.23a & b show the strong recover of downstream concentration for the constant and discontinuity models respectively; where $R^2 = 1$ and 0.99 for both cases. The models sensitivity to discretized spacing in the longitudinal direction is also provided in Figure 5.23c & d – showing that the downstream concentration is well predicted even for large discretized longitudinal spacing.

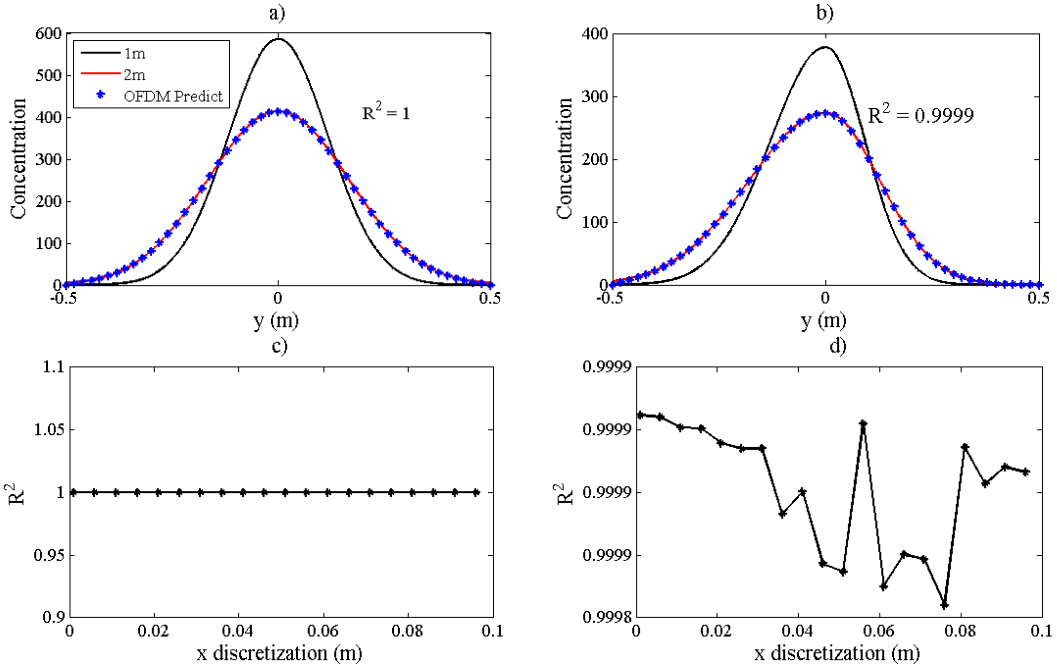

Figure 5.23: Upstream (black) and downstream (red) analytical concentration distributions and the predicted downstream distributions (blue stars) using the FDM for a a) spatially constant D_y and b) transverse discontinuity in $D_y(y)$. Sensitivity analysis comparing R^2 with longitudinal discretization shown for the c) constant and d) discontinuity D_y.

b) Proposed form for $D_y(y)$ in shear layer vegetation

The requirement of the FDM was to provide a profile of $D_y(y)$ for a specific hydrodynamic condition. However, a physically justified form of $D_y(y)$ and input function needed to be devised to produce a physically meaningful profile. In a rectangular channel with flow field uniformity and when average over a distance greater than the stem spacing, D_y is spatially constant, i.e. $dD_y/dy = 0$ and $D_y(y)$ = constant. In shear layer vegetation $D_y(y)$ is not constant due to the different scales of turbulence across the vegetation interface (Ghisalberti and Nepf, 2005 & 2007; Okamoto et al., 2012). Guymer and Spence (2009) investigated the functionality of transverse mixing and eddy viscosity in a trapezoidal compound channel. The analogy between compound channels and shear vegetation holds as $U(y)$ is not dissimilar between the two cases, i.e. both exhibit velocity shear and velocity inflexion points. Guymer and Spence (2009) suggest that the peak-mixing coefficient is located at the point of maximum shear, i.e. the velocity inflection point. Experimentally, Guymer and Spence (2009) found that the peak eddy viscosity, an indicator of total mixing, is found at the location of

peak Reynolds stress and maximum transverse velocity gradient, $\partial U/\partial y_{max}$. They found that, when the form of $D_y(y)$ is similar to that of the spatial distribution of Reynolds stress, the transverse concentration distributions were better predicted.

Ghisalberti and Nepf (2005) provide a form for $D_y(y)$ using the Equation 3.1. They also showed that peak $D_y(y)$ coincides with the location of peak Reynolds stress; approximately at the centre of the shear layer vortices; while Okamoto et al. (2012) provided an approximate Gaussian form of $D_y(y)$, peaking in the vicinity of the interface. It is suitably to assume, therefore, that – given the measurable extent of the shear layer vortices within the vegetation and open channel – the functionality of $D_y(y)$ will contain two constant regions, within the vegetated and open channel zones, and a near triangular or Gaussian form of $D_y(y)$ that connects the two constant zones, peaking in the region of the velocity inflection.

A physically meaningful form of the functionality for $D_y(y)$, given the current understanding of shear layer vegetated hydrodynamics in homogeneous, uniform vegetation (e.g. cylindrical artificial vegetation), was applied to real vegetation shear layer flows. Real vegetation shear layer flows are complex, three-dimensional systems that cannot be described perfectly using current understandings or basic computational techniques. However, the application of a physically justified theoretical functionality for $D_y(y)$ not only allows for the evaluation of its application to real vegetation but also facilitates the extension of current knowledge to complex systems.

The proposed functionality of $D_y(y)$ is presented in Figure 5.24. Within the mixing layer region a Gaussian functionality was assumed. The transverse mixing coefficients within the vegetated and open channel regions are modelled as constant (e.g. D_v and D_o, respectively); where D_y within the open channel is larger than that within the vegetation but does not exceed the peak value within the mixing layer, i.e. $\max(D_y) \geq D_o \geq D_v$. Further, the extents of the shear layer vortices within the vegetation and open channel were estimated from the measured, Fourier-fitted, average transverse profiles of mean longitudinal velocity. Further, the values D_v and D_o were prescribed given the relationships between D_y and channel mean

velocity, U, observed in the supplementary fully vegetated and bare channel tests[7]. The requirement of the FDM procedure was thus reduced to an optimization of the magnitude and skew of the Gaussian function describing D_y in the mixing layer region.

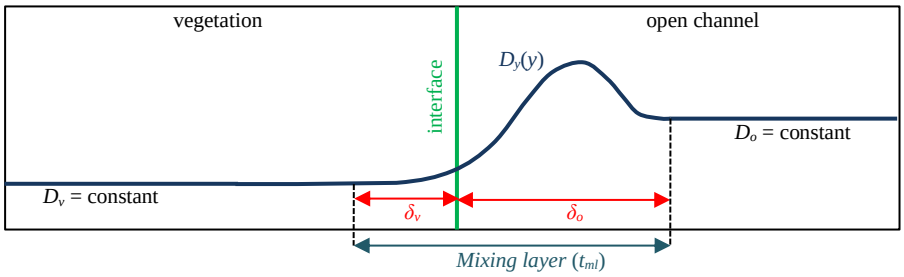

Figure 5.24: Proposed functionality of $D_y(y)$ associated with shear layer vegetation.

A routing procedure and subsequent optimization was applied to provide both the form and magnitude of $D_y(y)$. The optimization of $D_y(y)$ was executed by calculating the fit between the measured and predicted downstream transverse concentration distributions – in line with the method described for the 2D ADE model. Incremental iterations to the input profile of D_y were made until the fit (e.g. R^2 regression) between downstream measurements and predictions was maximized – with the capacity to retrieve an optimize profile for any given input form of $D_y(y)$.

The proposed functionality for $D_y(y)$ was constructed from four functions; where Figure 5.25 provides a flow through of the construction process. Firstly, the width of the mixing layer was approximated from the longitudinal average profiles of $U(y)$. The values of D_v and D_o were then input using their empirical relation to the mean velocity within their respective regions. The transverse mixing coefficient within the vegetated zone was assumed to be constant from $y = 0$ m to the limit of the penetration of mixing layer vortices within the vegetation i.e. $D_y(y) \neq f(y)$ for $y \leq y_i - \delta_v$. Figure 5.25a shows the construction of the constant transverse mixing coefficient for within the vegetated zone. Similarly, the transverse mixing

[7] D_v and D_o were calculated using the 2D trace data measured from the instantaneous injections in the full vegetation and bare channel scenarios. The 2D ADE routing optimization was then used to provide a best fit prediction of the mean transverse mixing coefficient, e.g. D_v, $D_o = f(U_1, U_2)$ for each vegetation type.

coefficient in the open channel zone was assumed to be constant and was constructed in the same manner, i.e. $D_y(y) \neq f(y)$ for $y \geq y_i + \delta_o$ (Figure 5.25b). A Gaussian function – e.g. ;

$$D_y(y) = A\exp\left[-\frac{(y-Y)^2}{2B^2}\right] \qquad \textbf{Equation 5.9}$$

where A is a constant, y is the transverse location, Y is an offset and B defines the spread – was then constructed within the mixing layer zone, $y_i - \delta_v < y < y_i + \delta_o$. Firstly, a straight line connecting the limits of the step functions (Figure 5.25c) was calculated using the D_v and D_o and the total with of the mixing layer ($t_{ml} = \delta_v + \delta_o$). Finally, the constructed Gaussian function was superimposed onto the sloping function such that $D_y(y)$ could be connected between D_v and D_o; where Figure 5.25d gives the final form of the proposed function. A Gaussian function was suitable for simulating the form of $D_y(y)$ as the peak value, location and spread (or variance) could be adjusted to optimise the FDM downstream predictions.

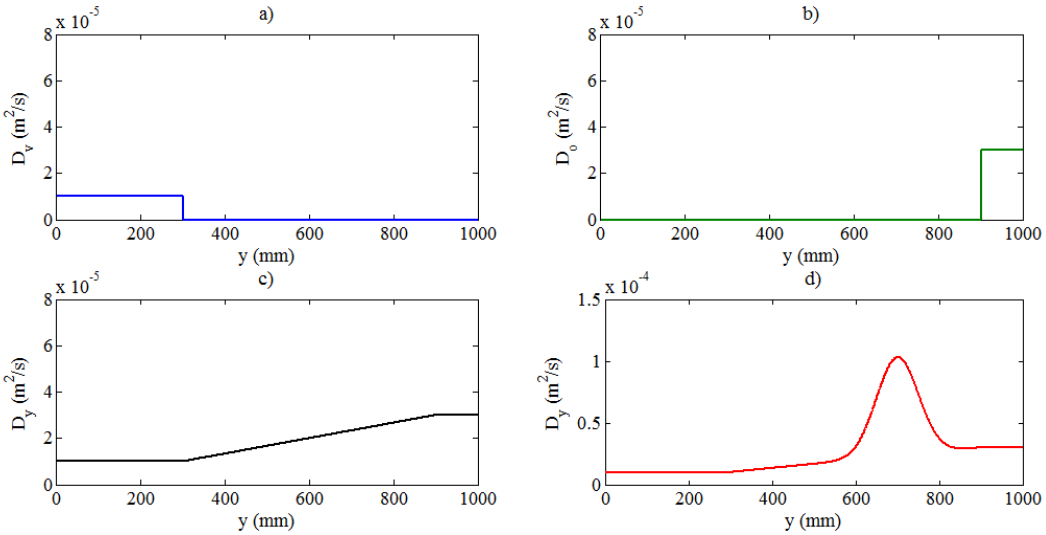

Figure 5.25: Construction of the transverse mixing coefficient in a) the vegetated and b) open channel zones. The 'scaffold' connecting the mixing coefficients of the vegetated and open channel zones is given in c). d) The final proposed form of the transverse mixing coefficient using a Gaussian function.

c) Finite Difference Model development

The development of the Optimized Finite Difference Model (OFDM) is presented to provide a clear understanding of the optimization process and highlight potential shortcomings when attempting to optimize multiple input parameters. The efficacy of the

optimized profiles of $D_y(y)$ was evaluated by comparing the predicted and measured downstream concentration distributions using an R^2 regression fit.

Firstly, the OFDM was evaluated using a spatially constant input of $D_y(y)$, i.e. optimized to give the best single value of D_y assuming spatially uniform mixing. The second approach was to model the vegetated and open channel zones as two distinct regions with constant mixing (e.g. Kay (1987) analytical solution for a depth-discontinuity). Thirdly, the functionality was also modelled using two constant zones with the inclusion of a triangular form of $D_y(y)$ to describe the mixing layer region and finally, a Gaussian function was optimised. The four optimisation functions are evaluated in the following sections.

5.2.4 OFDM analysis – spatially constant transverse mixing

The assumption of spatially constant transverse mixing, i.e. $D_y \neq f(y)$, is invalid for the spatially variable flow fields in question but provides the first clear step in the development of a multi-parameter optimization procedure. Continuous injections conducted in the high density artificial and winter and summer *typha* vegetation were measured and serve as a verification of the constant OFDM analysis.

a) Full vegetation evaluation

An appropriate evaluation of the constant D_y model was to compare the results to those calculated using a 2D ADE routing procedure in the full vegetation scenario where it can be assumed that D_y, $U \neq f(y)$.

The steady-state transverse concentration distributions measured in the full vegetation scenario were processed using the OFDM for the constant mixing function (Note that data was not collected for the low density artificial vegetation due to time constraints). A transverse profile of temporal mean longitudinal velocity, $U(y)$, was prescribed to each test using the velocity calculated from the optimized the ADE approach (Table 5.6). Figure 5.26 shows example the best fit downstream optimized predicted concentration distributions and

constant values of D_{OFDM} for the 1.00 l/s case in the high density artificial and winter and summer *typha* types, respectively. Sensitivity analysis showed that one solution provided the best-fit predicted concentration distribution. Appendix VI provides the optimized results for all experimental discharges. Table 5.7 compares the optimized values of D_y calculated using the 2D ADE, routing, D_{ADE} and D_{OFDM} where the R^2 values are given for the OFDM only. A third comparison was also made with values calculated using a one-dimensional method of moments procedure – i.e. from the spatial change in concentration variance – and is denoted by D_{MM}.

Table 5.7: Optimized constant value D_y (x10^{-5} m^2/s) for the full vegetation. The optimized fits for the ADE and OFDM were evaluated using R^2 correlating. D_{MM} indicates the values calculated using the method of moments. R^2 refers to the OFDM values only. The subplot compares the values for the three methods.

	D_y High Density Artificial				*D_y Winter typha*			
Q (l/s)	D_{MM}	D_{ADE}	D_{OFDM}	R^2	D_{MM}	D_{ADE}	D_{OFDM}	R^2
1.0	0.279	1.05	1.5489	0.9722	6.189	10.93	11.103	0.7654
1.5	1.205	1.76	1.9198	0.9919	6.950	15.51	16.136	0.8691
2.0	2.363	2.78	3.2084	0.9901	12.195	26.22	19.702	0.9237
2.5	2.641	2.99	3.2558	0.9855	14.090	28.86	28.156	0.9051
3.0	2.756	3.9	4.4375	0.9843	13.610	20.55	33.190	0.9352

	D_y Summer typha			
Q (l/s)	D_{MM}	D_{ADE}	D_{OFDM}	R^2
1.0	2.057	4.91	3.7813	0.9200
1.5	8.347	5.56	10.964	0.8766
2.0	14.007	6.38	17.753	0.8405
2.5	17.474	10.55	24.237	0.8036
3.0	20.022	11.17	27.349	0.8089

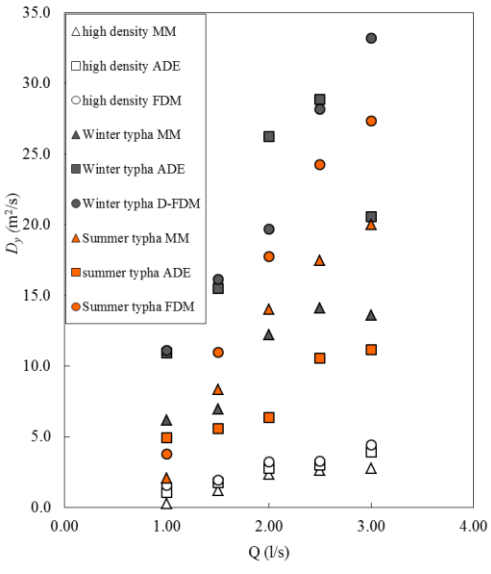

The 2D ADE routing procedure and the OFDM provide agreeable results for the value of D_y in the high-density artificial vegetation type. The optimized values of D_y are of the same

order of magnitude for both calculation methods; apart from the 1.00 l/s case, where D_{OFDM} is 3 times small than D_{ADE}. The similarities between D_{ADE} and D_{OFDM} for the high-density artificial vegetation indicate that the OFDM operates effectively in uniform conditions. The values provided by the method of moments are consistently smaller than the ADE and OFDM approaches for all of the high density artificial and winter *typha* cases.

The agreement between the OFDM and 2D ADE procedure deviates for the *typha* vegetation. The predicted values of D_{ADE} are consistently larger than D_{OFDM} in the winter *typha*, although both methods yield the same order of magnitude. The OFDM predictions in the summer *typha* are larger than those calculated using the 2D ADE procedure and are an order of magnitude larger in every case. This deviation may be attributed to the fact that the velocity field in the *typha* was less homogeneous than in the artificial case. The assumption of a mean longitudinal channel velocity using the optimized travel time may, therefore, not necessarily be sufficient to accurately predict trace advection.

The OFDM successfully fits the downstream measured concentration distribution. The coefficients of fit, R^2, in the artificial type indicate that a good fit was made in all cases – where the lowest and highest fitting coefficients are 0.9722 and 0.9919, respectively. Given the non-Gaussian nature of the transverse concentration distributions, the quality of fit for both *typha* types is agreeable – where the least successful fit has a R^2 value of 0.7654 and 9 out of the 10 *typha* cases produced a fit of $R^2 > 0.80$.

Figure 5.27 presents the transverse profiles of $U(y)$; the concentration distributions normalized by the upstream maximum concentration ($C_1(y)/C_{max}$ and $C_2(y)/C_{max}$) and the optimized best fit constant value profiles of $D_y(y)$ for the 3x full vegetation types (high density artificial, winter and summer *typha*). The profiles of show an increase in total mixing as the discharge increases. All three vegetation types show an increase in mixing of approximately 3 times from the lowest to the highest discharge.

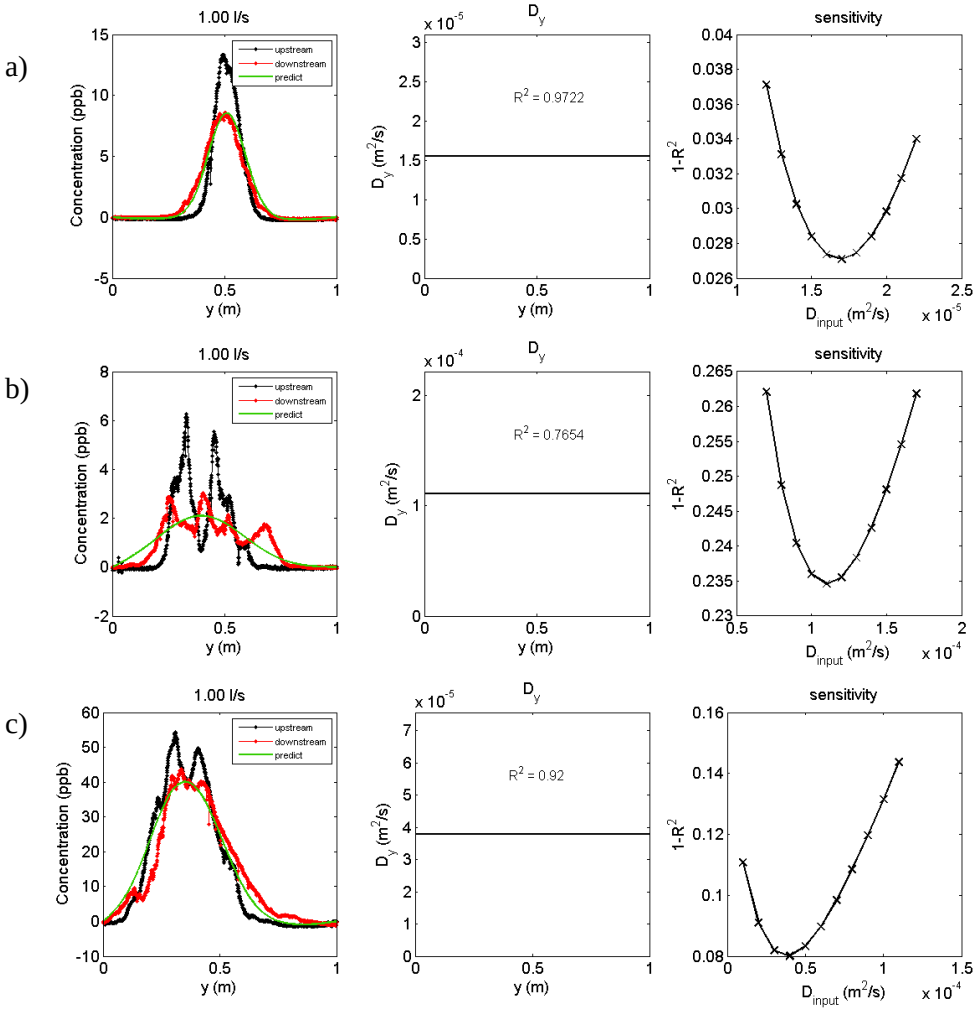

Figure 5.26: Best fit predicted downstream transverse concentration distributions are compared to the measured distribution and the optimized constant value of $D_y(y)$ for a) high density artificial, b) winter *typha* and c) summer *typha*. Sensitivity of the prediction to the input D_y is also provided.

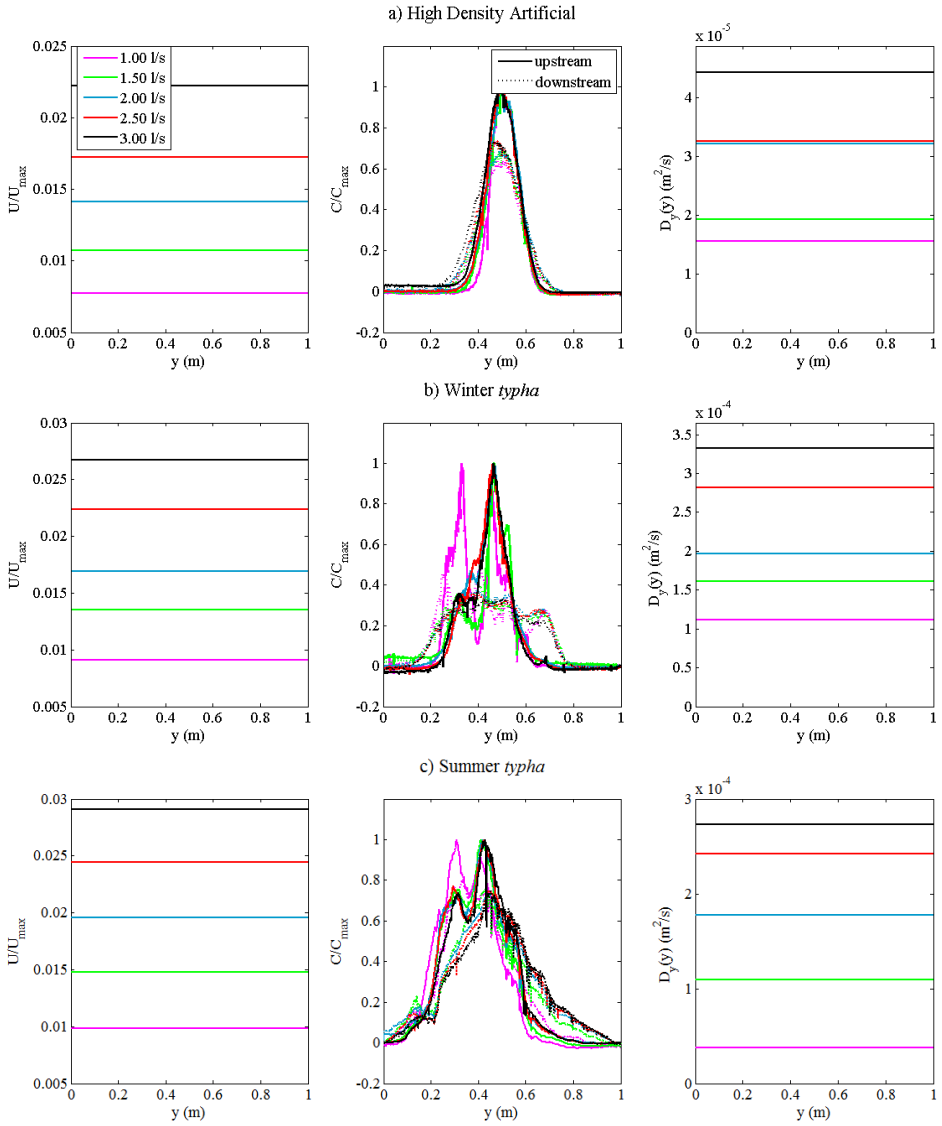

Figure 5.27: Full vegetation mean velocity, normalized concentration distributions and OFDM constant best fit values of $D_y(y)$ for the a) high density artificial and b) winter and c) summer *typha* vegetation types.

b) Partial vegetation evaluation

The constant value $D_y(y)$ OFDM was applied to the steady-state concentration distributions and velocity results for the partial vegetation cases. Figure 5.28 gives examples comparing the measured (red line) and optimized predicted (green line) downstream concentration distributions for the constant value D_y optimization for the 4.25 l/s case. (Appendix VI provides the complete best-fit concentration distributions for all discharges and vegetation types). The sensitivity analysis given in the right-hand plots shows that only one solution exists that maximizes the fit between predictions and observations.

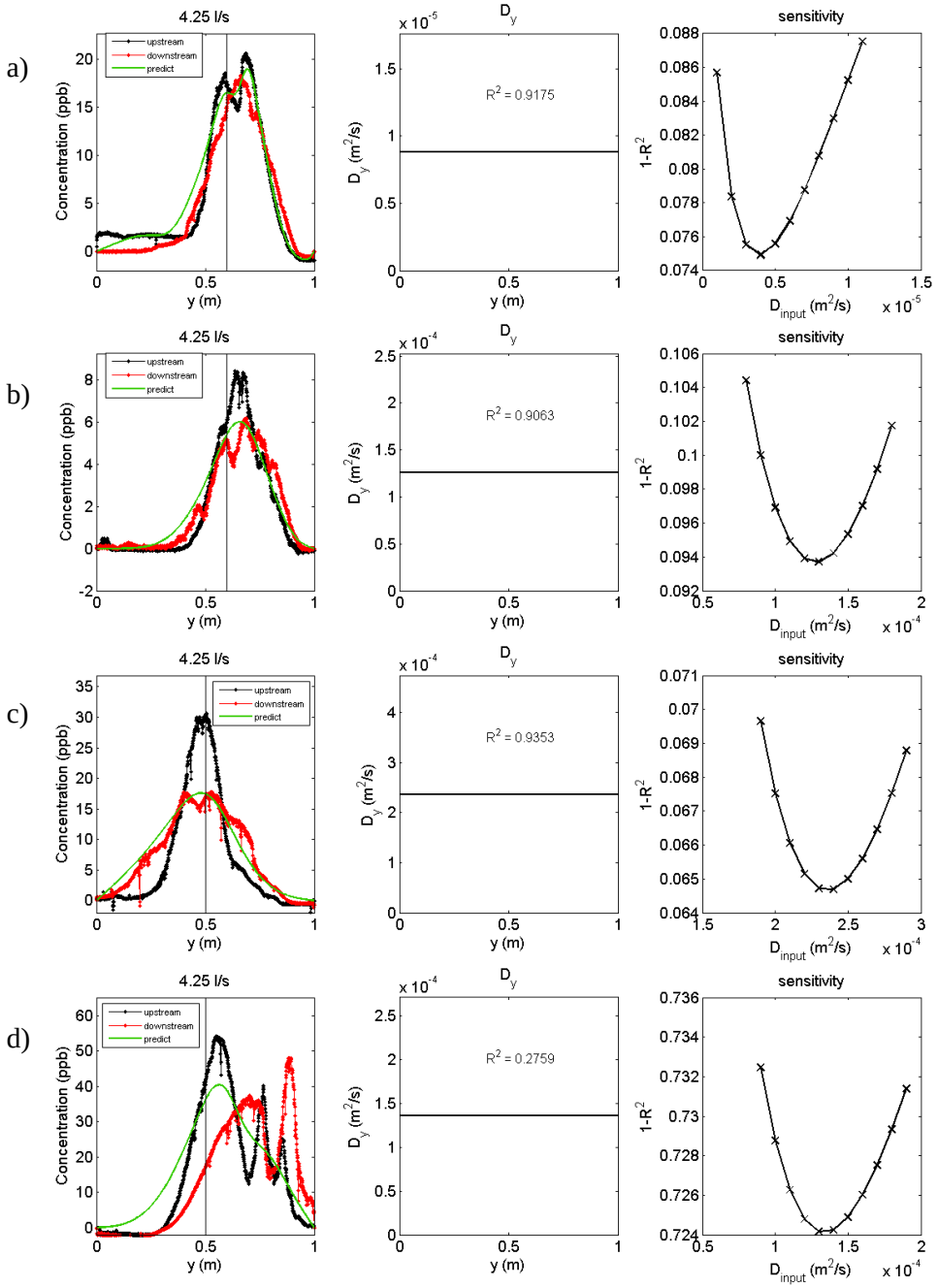

Figure 5.28: Optimized predicted downstream steady-state concentration profiles for the constant value D_y using the OFDM for a) high and b) low density partial artificial vegetation and c) winter and d) summer partial *typha*.

The spatially uniform function of $D_y(y)$ is a satisfactory predictor of the downstream concentration distribution even in the heterogeneous partial follow fields. The optimized profiles of D_y yield acceptable predicted concentration distributions for the high and low density artificial vegetation and for the winter *typha*; with minimum R^2 values of 0.8905, 0.9063 and 0.9218, respectively. The best-fit downstream concentration distribution for the

summer *typha* has a goodness of fit of only 0.2759. The large values of R^2 may, however, be perturbed by the inclusion of background data in the region $y < 0.2$ m. The optimized constant values of D_y for all of the 5x discharges for the 4x vegetation types are provided in Table 5.8 while the results are provided graphically in Figure 5.29.

Table 5.8: Optimized D_y (x10^{-4} m^2/s) and R^2 values for the constant value OFDM.

	High Density Artificial		*Low Density Artificial*		*Winter typha*		*Summer typha*	
Q (l/s)	D_y	R^2	D_y	R^2	D_y	R^2	D_y	R^2
3.35	0.123	0.9712	0.966	0.9409	1.933	0.9218	0.581	0.5936
4.25	0.088	0.9175	1.264	0.9063	2.373	0.9353	1.356	0.2759
5.25	0.536	0.8905	1.330	0.9502	2.902	0.9380	2.707	0.1408
6.35	1.784	0.8738	1.536	0.9341	2.668	0.9313	32.00	0.0895
7.35	1.125	0.9192	1.592	0.9751	3.344	0.9491	32.00	0.1139

Figure 5.30 presents the entire constant value OFDM results for all discharges and vegetation types; including the normalised profiles of $U(y)$ and sensitivity analysis. The optimized values of D_y for the high-density artificial vegetation (Figure 5.30a) are an order of magnitude greater than the measured values from the equivalent full vegetation scenario. This is to be expected, as the majority of the concentration distribution is located within the open flow – where the mixing is expected to be greater than in vegetation. Moreover, the optimized values are similar in magnitude to those measured in the bare channel scenario, indicating that the constant value OFDM yields physically sensible results. The low density artificial vegetation values (Figure 5.30b) are similar in magnitude to the high density values; although, greater mixing for the lower discharges is predicted for the low density type.

The optimized constant $D_y(y)$ profiles for the winter and summer *typha* vegetation are given in Figure 5.30c & d, respectively. The downstream concentration distributions are well predicted for the winter *typha* with an average goodness of fit of $\langle R^2 \rangle = 0.9351$. The relatively small skew in the concentration profiles resemble the constant injection results for the full vegetation and suggest an explanation for the quality of fit.

The quality of fit is significantly worse for summer *typha* type. The maximum value of R^2 is only 0.0.5936 (3.35 l/s) while the minimum is as low as 0.1139 (7.35 l/s), where $\langle R^2 \rangle = 0.2427$. It is clear from the predicted downstream concentration profiles that the 1D optimization model cannot predict the shift in profile peak from upstream to downstream. Further, the dissociation of the downstream concentration profile into two peaks cannot be described using a one-dimensional model. Therefore, the results provide a poor fit to both the location and magnitude of the peak concentration and to lateral shift in the distribution. The overall mixing, however, in general – in terms of profile spread – is acceptable.

The constant value OFDM fails to capture the skew of the concentration distributions for all the partial vegetation types. The one-dimensional approach may, therefore, be an appropriate tool for calculating an initial guess for the magnitude of the transverse mixing before further refinement.

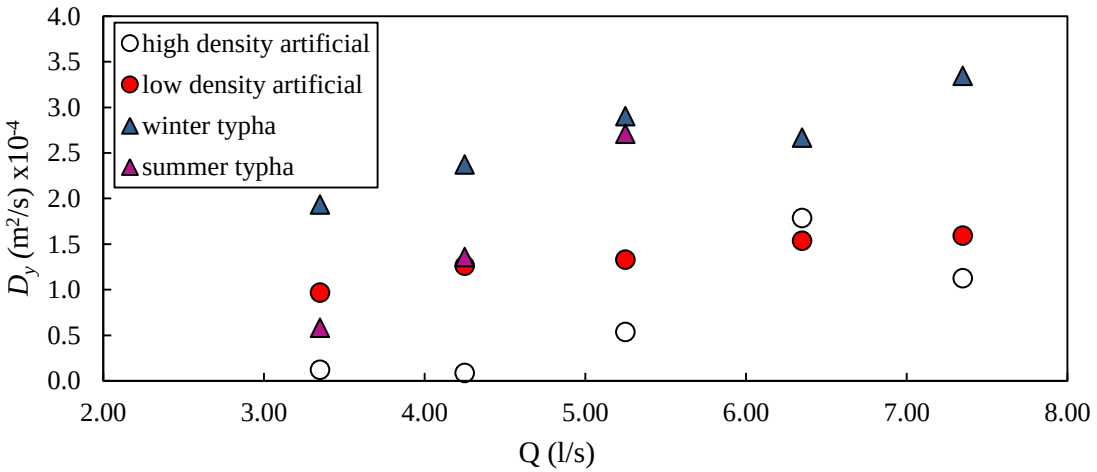

Figure 5.29: Constant value OFDM results for the partial vegetation scenario.

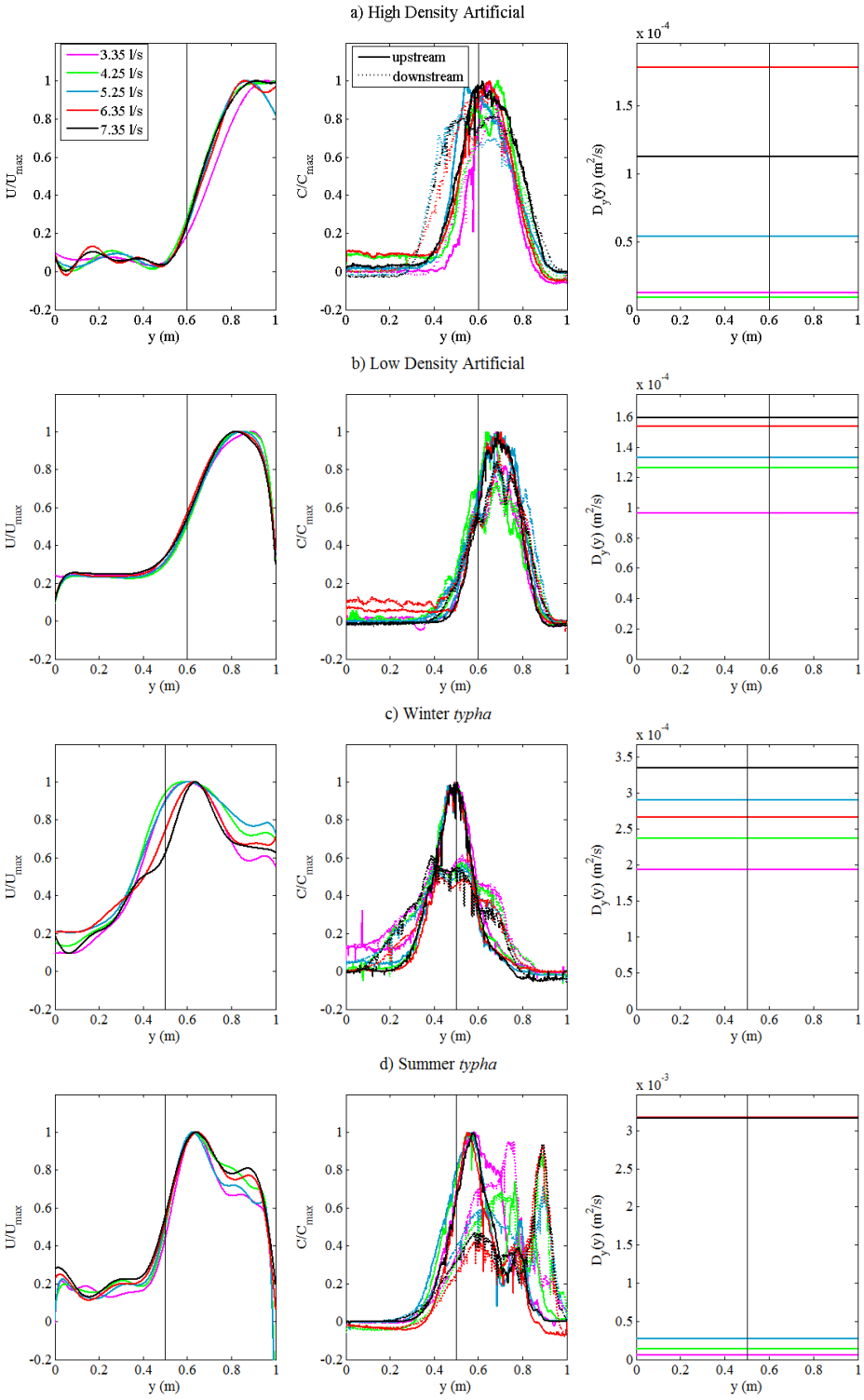

Figure 5.30: Normalized profiles of $U(y)$, $C_1(y)$ and $C_2(y)$ are compared to the constant OFDM values of $D_y(y)$ for a) high and b) low density artificial and c) winter and d) summer *typha*.

5.2.5 OFDM analysis – transverse discontinuity in transverse mixing

The second development of the OFDM was the evaluation of a discrete change in transverse mixing coefficient – located at the interface between the vegetation and open channel. Figure 5.31 shows how a constant value of D_y was prescribed for both the vegetation and open channel zones. The interface was the location of the discrete change in D_y such that $D_y(y) = D_1$ for $y < y_i$ and $D_y(y) = D_2$ for $y \geq y_i$.

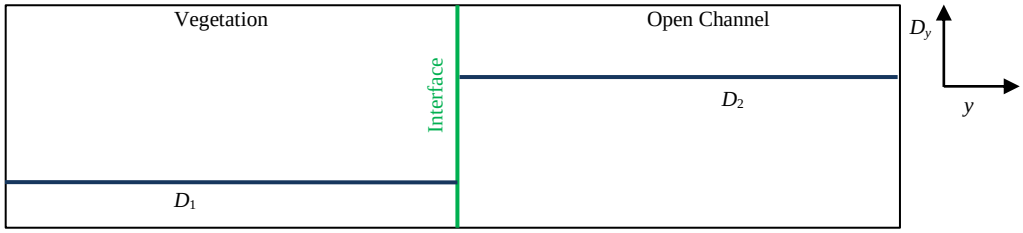

Figure 5.31: Approximate functionality of the transverse mixing coefficient, $D_y(y)$ across the shear layer vegetation interface for the depth-discontinuity scenario.

The increase complexity of the form of $D_y(y)$ (from a constant value to two-regions) required a more thorough investigation into the viability of the optimized solution. There was potential for multiple solutions to occur for different parameter combinations (i.e. multiple peak values of R^2) with an increase in the number of fitting parameters. The sensitivity of the goodness of fit to the input values of D_1 and D_2 was investigated by observing the dependence of R^2. Figure 5.32 (right hand plots) give examples of the goodness of fit for a range of values of D_1 and D_2; where the shading indicates the quality of fit for a given parameter combination (red indicating a better fit than blue). It can be seen that there is only one maximum value of R^2 for each case and therefore, only one solution to the two-step optimization.

The left hand plots in Figure 5.32 give examples of the best-fit downstream-predicted concentration distribution for the 4.25 l/s cases. The central plots give examples of the best-fit profiles of $D_y(y)$ while Table 5.9 provides the optimized values of D_1 and D_2 and the respective goodness of fit (R^2). The full results for the step optimization fitting can be found in Appendix VI.

The quality of fitting using the discontinuity optimization, when compared to the constant value optimization, improved for the artificial types – with an increase in R^2 of 0.9175 to 0.9498 and 0.9324 to 0.9603 for the high and low density types, respectively. The quality of fitting for the *typha* cases also increased using the step optimization; most noticeably for the summer *typha* type with an increase in $\langle R^2 \rangle$ of 0.2759 to 0.4231 showing greater sympathy for the severe skew in the concentration distributions between the vegetation and open channel. There was a minimal increase in the goodness of fit in the winter *typha* case (0.9353 to 0.9583) and is attributed to the relative symmetry in the transverse concentration across the interface.

The depth-discontinuity model predicts greater transverse mixing in the open-channel region than the vegetation (Table 5.9 and Figure 5.34). In all but two cases D_2 is greater than D_1. In the high density artificial cases, D_2 ranges from approximately 2 to 20 times greater than D_1. The disparity between D_1 and D_2 is less for the low density artificial vegetation where the velocity shear is smaller. There is a small disparity between D_1 and D_2 in the winter *typha* case – reflecting the relatively small velocity shear (see Table 5.5) – with a minimum and maximum value of D_2/D_1 of 2.97 and 1.79 and a mean value of 2.18.

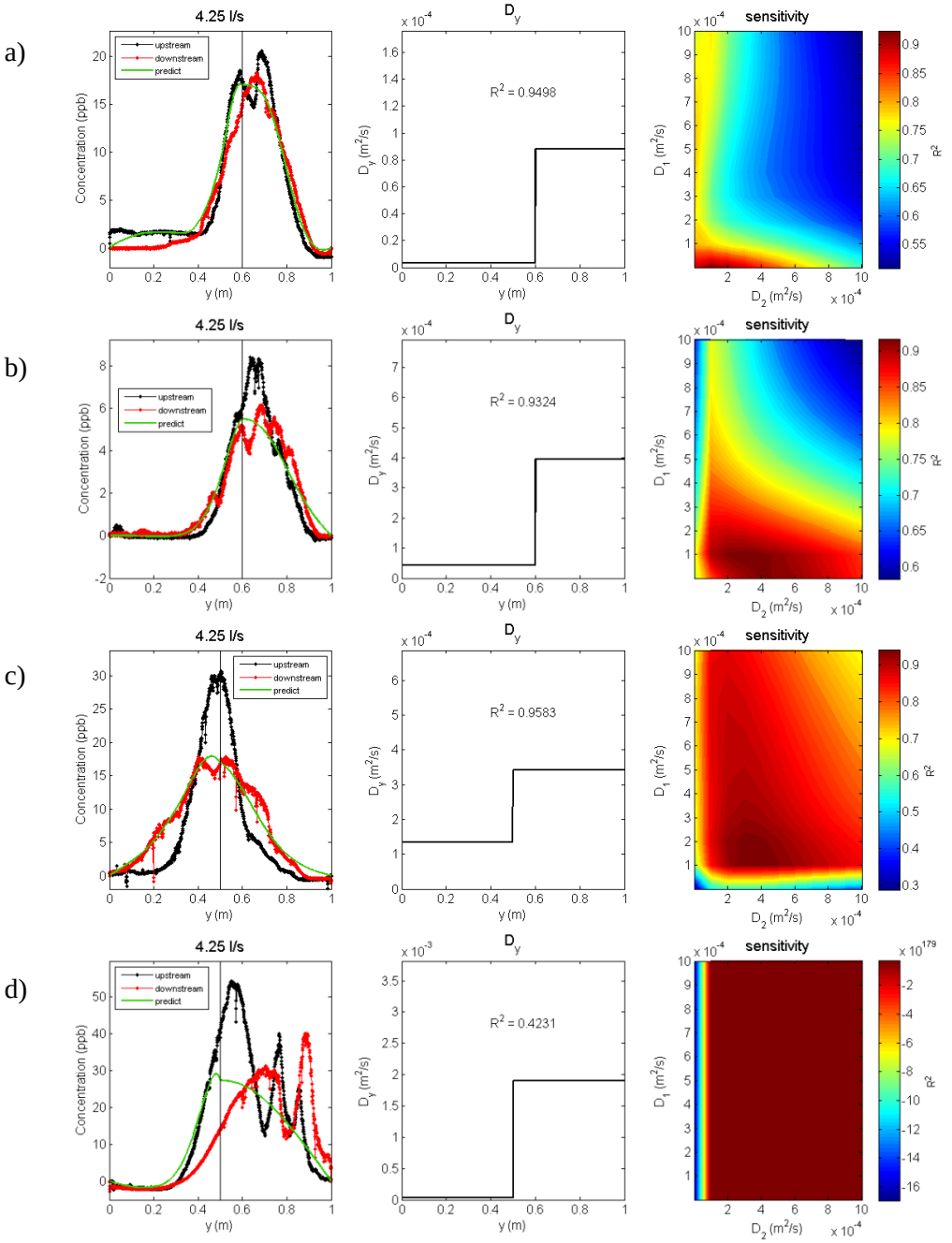

Figure 5.32: Example best-fit predicted downstream steady-state concentration distribution for the discontinuity OFDM for a) high and b) low density partial artificial and c) winter and d) summer partial *typha* vegetation.

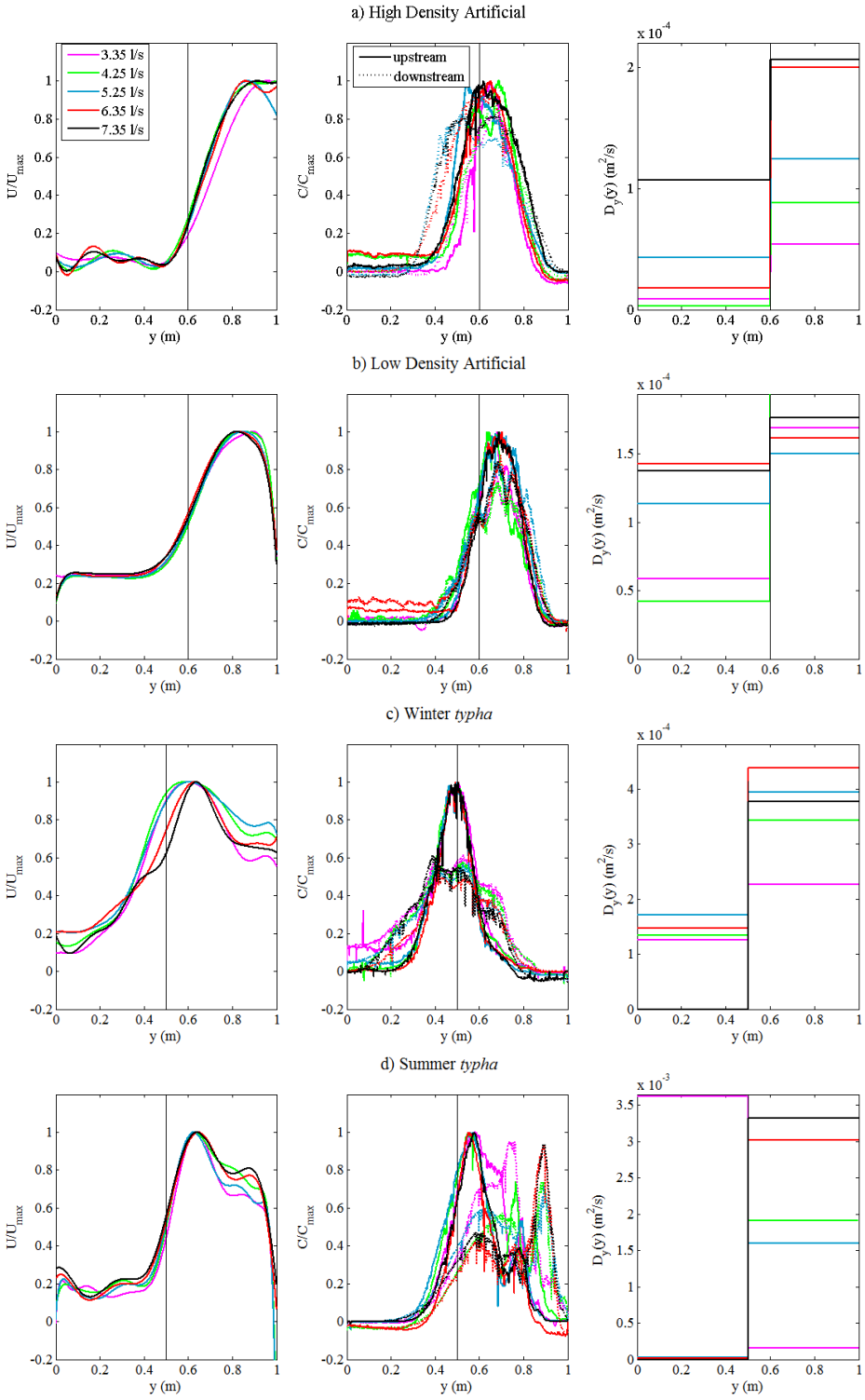

Figure 5.33: Normalized profiles of $U(y)$ and steady-state transverse concentration are compared to the optimized discontinuity profiles of $D_y(y)$ for the a) high and b) low density artificial and the c) winter and b) summer *typha* vegetation.

The discontinuity model optimization indicates that, in general, there is greater transverse mixing associated with the *typha* vegetation than the artificial types. Further, the discontinuity

optimization provides stronger predicted downstream concentration distributions and is, therefore, an improvement on the constant D_y case shown above. However, the simplicity of the model fails to successfully fit the downstream concentration distributions for the summer *typha* cases.

Table 5.9: Optimized values (x10^{-4} m^2/s) of D_1, D_2 and R^2 using the discontinuity approximation for the high and low density artificial vegetation and the winter and summer *typha*.

	High Density Artificial			Low Density Artificial		
Q (l/s)	D_1	D_2	R^2	D_1	D_2	R^2
3.35	0.0842	0.5379	0.9839	0.5856	1.6912	0.9492
4.25	0.0316	0.8808	0.9498	0.4211	3.9629	0.9324
5.25	0.4308	1.2395	0.8939	1.1358	1.4993	0.9510
6.35	0.3500	2.0000	2e40	1.4242	1.6165	0.9343
7.35	1.0703	2.0625	0.9219	1.3779	1.7627	0.9758
	Winter *typha*			Summer *typha*		
Q (l/s)	D_1	D_2	R^2	D_1	D_2	R^2
3.35	1.2626	2.2613	0.9265	54.000	2.395	0.8866
4.25	1.3397	3.450	0.9583	0.2533	19	0.4231
5.25	1.7153	3.9412	0.9551	0.4918	24	0.4609
6.35	1.4716	4.3775	0.9649	0.4033	57	0.2337
7.35	2.9075	3.7710	0.9503	100.00	17.000	0.3345

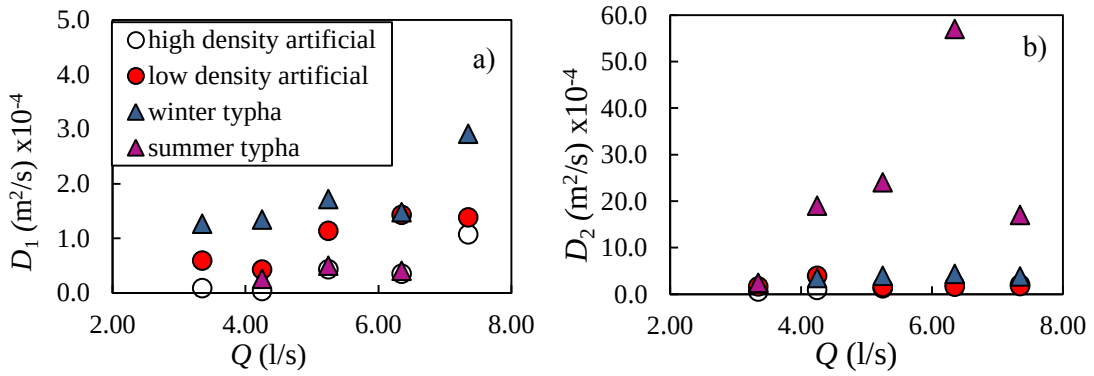

Figure 5.34: Comparisons of the optimized a) vegetation and b) open channel transverse mixing coefficients, D_1 and D_2, for the four vegetation types using the discontinuity OFDM.

5.2.6 OFDM analysis – triangular transverse mixing

A third development of the OFDM was to assume a triangular form of $D_y(y)$ within the mixing layer. The step function for $D_y(y)$ described above was modified to include a peak in the mixing coefficient exceeding the constant value of D_o, D_y in the open channel zone. The zones of constant mixing, D_v and D_o, were linearly connected to this peak.. Figure 5.35 gives an example of the estimated triangular functionality for $D_y(y)$ for the mixing layer zone. The definition of the mixing layer region requires two additional parameters to be inserted into the model – the penetration of the mixing layer into the vegetation, δ_v, and into the open channel, δ_o[8].

To reduce computation demand and minimize the potential for multiple solutions to occur, the mixing coefficients within the vegetation and the open channel were input into the model. The values of D_v and D_o were estimated from the relationship between the transverse mixing coefficient and the spatial mean longitudinal velocity within each region, i.e. U_1 and U_2, measured in the full vegetation and bare channel scenarios. Section 4.2.1 describes the implementation of a 2D ADE routing method to calculate the transverse mixing coefficients for the full vegetation and bare channel scenarios.

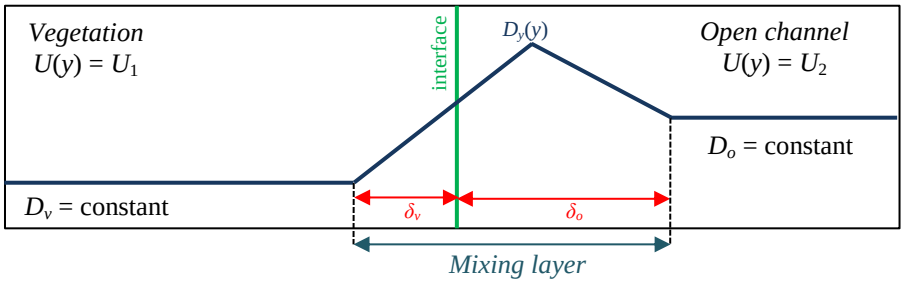

Figure 5.35: Estimated triangular functionality of $D_y(y)$ across the shear layer vegetation interface depicting the vortex penetration limits, δ_v and δ_o.

Since the values of U_1 and U_2 in the partial scenario may not concur with the exact mean longitudinal velocity in the full vegetation and bare channel scenarios, a regression of D_y against channel mean longitudinal velocity was determined for both the full vegetation and

[8] Estimates of shear layer penetration distances are made above in section 5.1.3.

bare channel cases, i.e. $D_v = f(U_1)$ and $D_o = f(U_2)$. Appropriate estimates of D_v and D_o could then be input into the triangular model to provide stronger physical foundations for the optimization. Figure 5.36a shows the regression fits used to characterize the relationship between D_v and the mean longitudinal velocity within the full vegetation. Similarly, the line of regression between D_y and U_2 for the bare artificial channel is shown in Figure 5.36b.

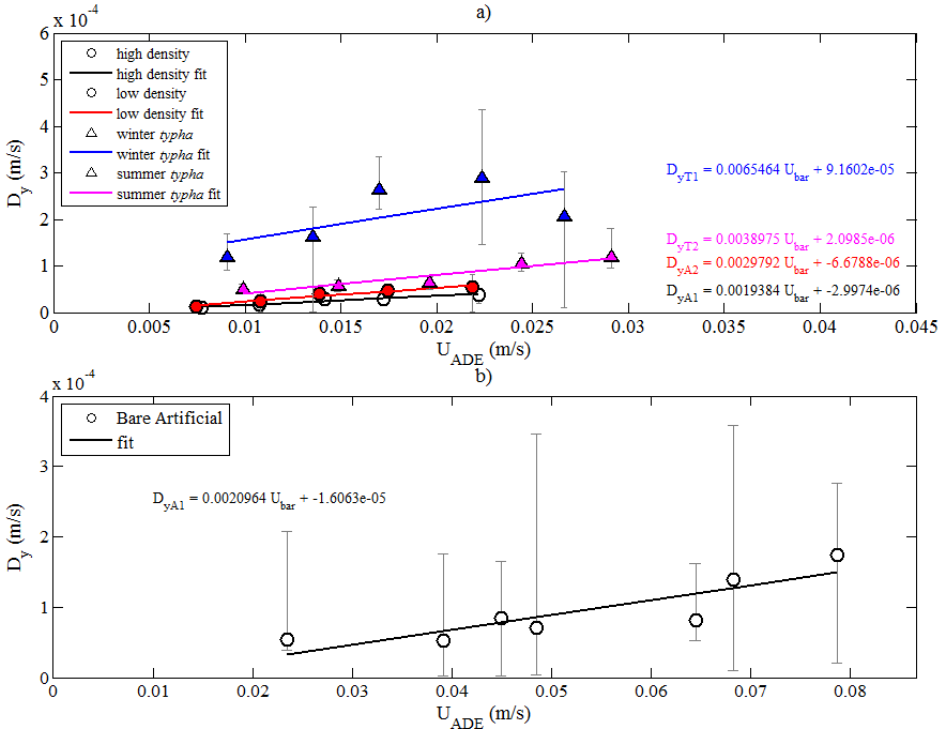

Figure 5.36: Regression fits for the optimized D_y measured in the a) full vegetation for the high (clear circles) and low (red circles) density artificial vegetation and winter (blue triangles) and summer (pink triangles) *typha* and b) the bare artificial channel against travel-time mean velocity, U_{ADE}, using the 2D ADE analysis.

The estimations of the shear layer penetration width and the constant mixing coefficients in the vegetated and open channels zones thus constrain the triangular formulation to a two-parameter optimization; where only the location and magnitude of the peak mixing needs to be determined. The physical form of the triangular fitting was finally constrained by:

- The peak value of D_y must be larger than D_o, the mixing coefficient in the open channel $D_y > D_o > D_v$;

- The transverse location of the peak, y_p, must be located between the vegetation interface and the penetration limit of the shear layer into the open channel – i.e. $y_i < y_p < y_o$.

The triangular OFDM was applied to the partial vegetation cases accordingly. Table 5.10 and Table 5.11 present the optimized values of D_{peak} and y_{peak}. Peak transverse mixing in the shear layer region is two orders of magnitude greater than within the vegetation for the high density artificial and one order greater for the low density. In contrast, peak mixing in both *typha* types is the same order of magnitude, but larger, than the vegetation mixing. In the high density artificial vegetation y_{peak} lies approximately 0.10 m from the vegetation interface; however, in the low density artificial vegetation, y_{peak} is 0.07 m from the interface. In the winter *typha*, y_{peak} is close to the interface at approximately 0.05 m while D_{peak} can be found approximately 0.07 m from the interface in the summer *typha*.

Figure 5.37 provides examples of the optimized triangular forms of $D_y(y)$ for the 7.35 l/s case; while Figure 5.38 provides the normalised optimal profiles (where Appendix VI provides the individual results and best-fit concentration distributions). All of the summer *typha* cases yield optimal profiles of $D_y(y)$ that are close in form to the step optimisation. The sensitivity analysis given in the right hand plots in Figure 5.37 indicates that triangular model is more sensitive to the magnitude of the triangle peak compared to its locations from the vegetation interface.

The goodness of fit for the triangular OFDM is similar to those given by the step OFDM analysis. In some cases there is an increase in R^2 – predominantly for the artificial cases, where the mean $R^2 = 0.9365$ – while a decrease was observed in all but one of the *typha* cases. This said, there is parity between the step and triangle goodness of fit when evaluated to 2 decimal places. The results for the winter *typha* are successful with minimum and maximum values of R^2 of 0.9009 and 0.9536, respectively ($\langle R^2 \rangle = 0.9305$). The triangular OFDM poorly predicts the downstream concentration distribution in the summer *typha* cases where the average value of R^2 for the summer *typha* is 0.0577.

Qualitatively, the triangular OFDM provides acceptable downstream concentration distributions (Appendix VI). The optimal profiles of $D_y(y)$ in the artificial vegetation are triangular. The optimal profiles in the winter *typha* are all triangular show a good recovery of the downstream concentration distributions.

Table 5.10: Optimized location (mm) and value of the peak transverse mixing coefficient, D_{peak}, (x10^{-5} m^2/s) from the triangular OFDM for the 2x partial artificial types. D_v and D_o refer to the transverse mixing coefficient in the vegetated and open channel zones, respectively.

	High Density Artificial					Low Density Artificial				
Q (l/s)	D_v	D_o	D_{peak}	y_{peak}	R^2	D_v	D_o	D_{peak}	y_{peak}	R^2
3.35	0.190	10.911	10.911	600	0.9155	3.669	6.803	10.225	600	0.9395
4.25	0.270	3.583	94.325	600	0.8666	4.292	9.004	11.374	600	0.8929
5.25	0.462	3.801	35.789	600	0.9791	5.216	10.383	13.046	600	0.9477
6.35	0.723	4.354	50.000	600	-	6.389	12.360	15.611	600	0.9340
7.35	1.194	7.177	87.218	600	0.9784	7.507	13.680	15.903	600	0.9752

Table 5.11: Optimized location (mm) and value of the peak transverse mixing coefficient, D_{peak}, (x10^{-4} m^2/s) using the triangular OFDM for the 2x partial *typha* types. D_v and D_o refer to the transverse mixing coefficient in the vegetated and open channel zones, respectively.

	Winter *typha*					Summer *typha*				
Q (l/s)	D_v	D_o	D_{peak}	y_{peak}	R^2	D_v	D_o	D_{peak}	y_{peak}	R^2
3.35	0.483	2.200	22.005	500	0.9009	0.303	2.388	23.885	500	0.460
4.25	0.772	2.321	23.218	500	0.9337	0.395	2.495	24.953	500	0.2195
5.25	1.284	2.432	27.558	500	0.9322	0.439	2.619	26.195	500	0.0980
6.35	1.462	2.441	26.728	500	0.9322	0.658	2.921	29.215	500	-0.288
7.35	1.269	2.665	39.401	500	0.9536	0.860	3.039	30.398	500	-0.204

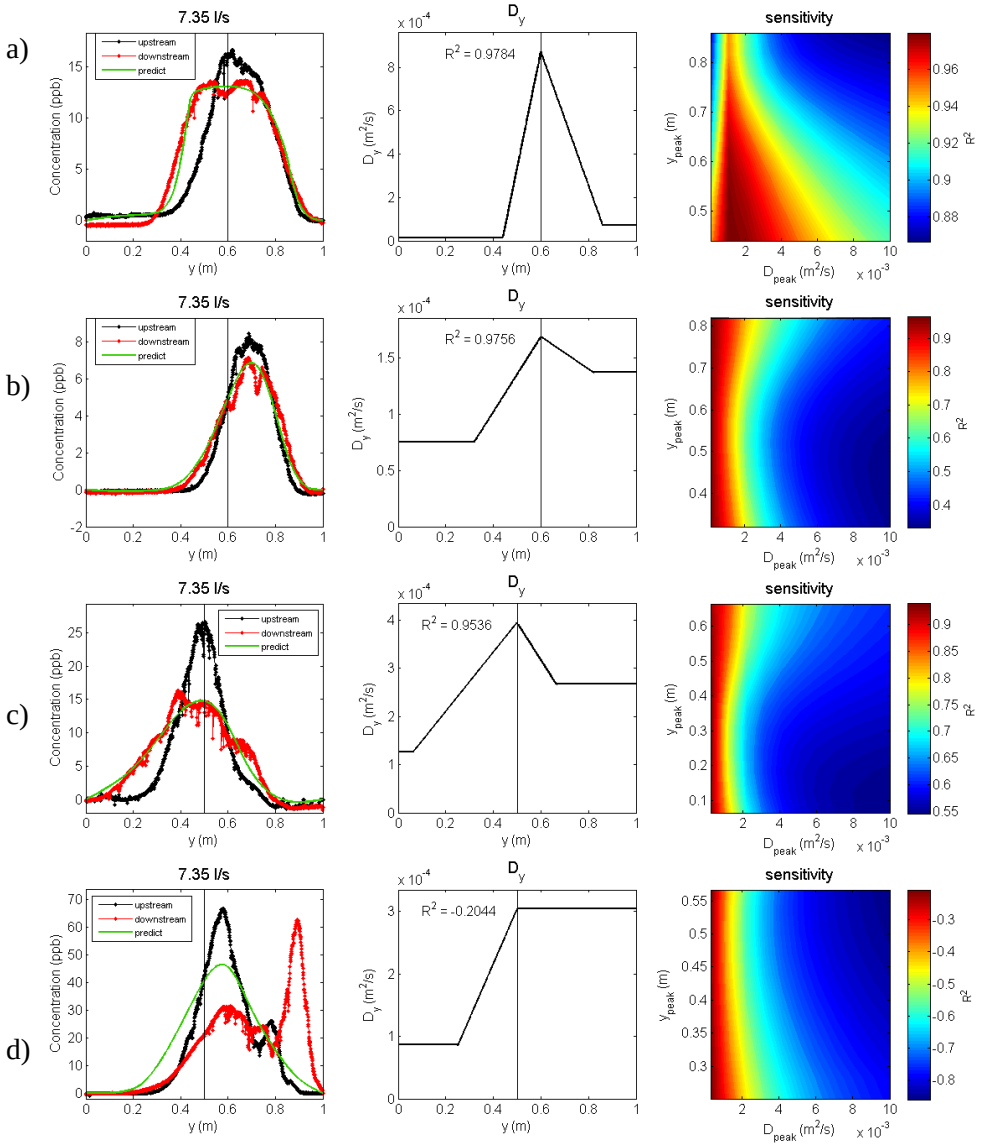

Figure 5.37: Best fit predicted downstream concentration distributions for the triangular OFDM are given for the 7.35 l/s case for the a) high and b) low density artificial vegetation and the c) winter and d) summer *typha*. The optimized profiles of $D_y(y)$ are also provided with the fitting sensitivity to D_{peak} and y_{peak}.

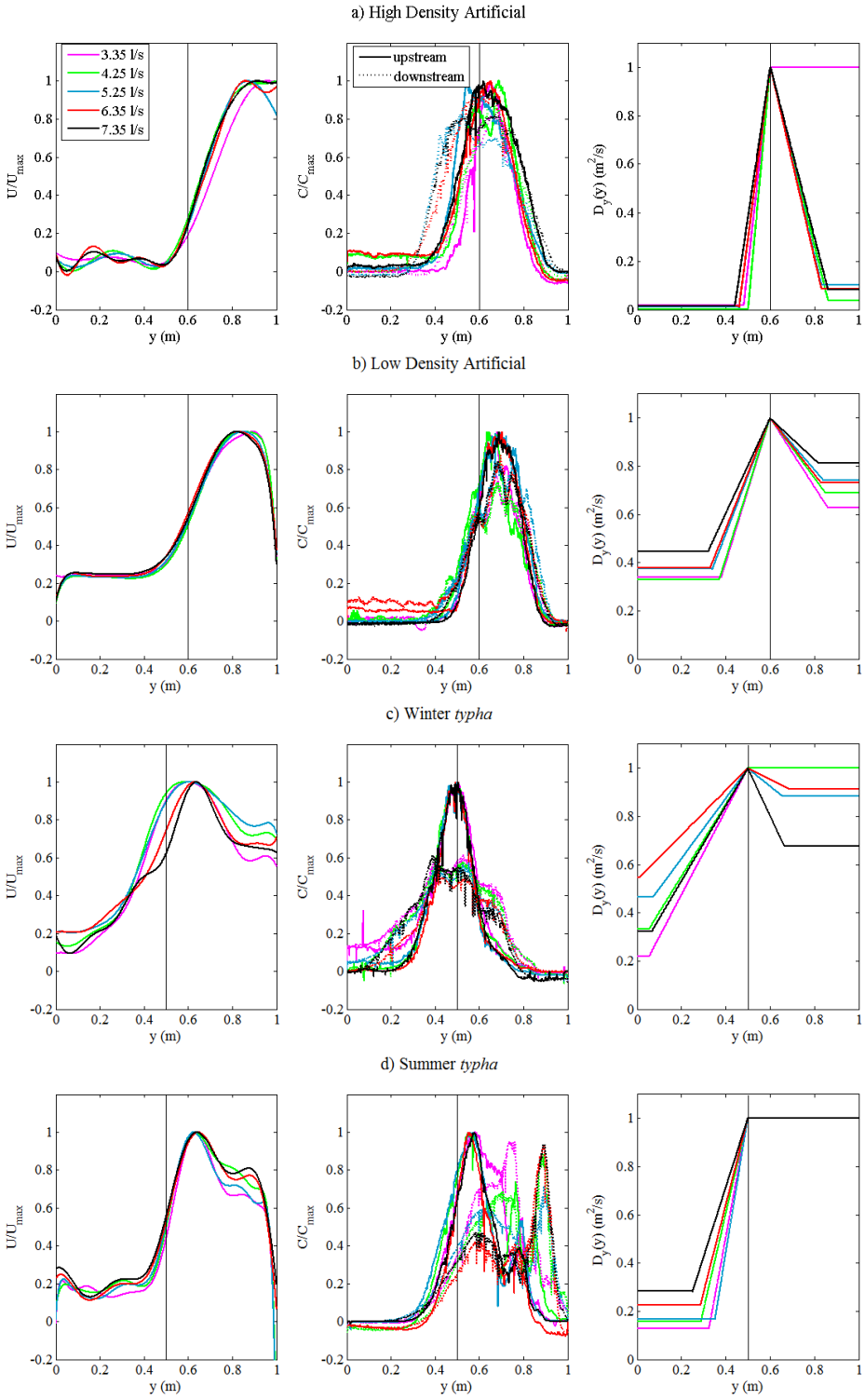

Figure 5.38: Profiles of $U(y)$ and $C(y)$ normalized by the max(U_2) and max(C_1), respectively, are compared to the best-fit normalised triangular profiles of $D_y(y)$.

5.2.7 OFDM analysis – Gaussian transverse mixing

The final development of the OFDM was to employ a Gaussian distribution to provide a continuous function for the transverse mixing coefficient in the mixing region. The functions construction was the same as that of the triangular form. The values of D_v and D_o were assigned to the vegetated and open channel regions with the same vortex penetration distances set as the spatial limits. The Gaussian function was then superimposed onto the linear function connecting the two regions of constant mixing (e.g. Figure 5.24). The analysis of the Gaussian functions suitability required the optimization of three parameters used to describe the function: the amplitude; spread and offset. Note that the Gaussian function was constrained in order to generate physically meaningful results. The location and magnitude of the peak transverse mixing coefficient was prevented from lying within the vegetated region and from falling below the open channel mixing value, D_o; i.e. $D_{peak} \geq D_o$ and $y_{peak} \geq y_i$.

Table 5.12 and Table 5.13 provide the location and magnitude of D_{peak} as well as the goodness of fit in prediction for the artificial and *typha* cases, respectively; while Figure 5.39 gives examples of the best fit downstream concentration predictions, the optimized profiles of $D_y(y)$ and sensitivity analysis for the 7.35 l/s cases. The Gaussian OFDM yields R^2 values that are similar to those given by the triangular function. A reduction in the average R^2 was observed for the high density artificial (0.9349 reduces to 0.9118); while an increased was observed for the low density from 0.9378 to 0.9702. The fit was improved for both *typha* seasons; where the Gaussian OFDM improved the fitting from $\langle R^2 \rangle$ = 0.9305 to 0.9603 and 0.0505 to 0.1011 for the winter and summer, respectively.

The example best-fit concentration profiles in Figure 5.39 show that the Gaussian OFDM provides successful predictions of downstream concentration. Moreover, the large values of R^2 for all but the summer *typha* indicate that the physical assumption of a Gaussian form of $D_y(y)$ can provide adequate predictions of mixing in shear layer vegetated flows. The optimal profiles in Figure 5.40 support the theory that peak mixing occurs in the vicinity of the

interface and that the shear layer vortices significantly contribute to the over mixing characteristics. However, the failure of the Gaussian OFDM to provide acceptable predictions for the summer *typha* suggests that the physical assumptions may not hold true in real vegetation. This is discussed in more depth in the following chapter.

There are noticeable discontinuities in the example profiles of $D_y(y)$ in Figure 5.39 highlighting the potential limitations of using a routing optimisation which retrieves the best-fit concentration distribution regardless of physical meaning. Further, the real vegetation results are more similar to the step function – particularly for the summer *typha* – where D_{peak} is close in magnitude to D_v and D_o.

Table 5.12: Optimized values of y_{peak} (mm) and D_{peak} (x10^{-5} m^2/s) from the Gaussian OFDM for the 2x partial artificial types. D_v and D_o refer to the transverse mixing coefficient in the vegetated and open channel zones, respectively.

	High Density Artificial					Low Density Artificial				
Q (l/s)	D_v	D_o	D_{peak}	y_{peak}	R^2	D_v	D_o	D_{peak}	y_{peak}	R^2
3.35	0.190	10.911	200.0	600.9	0.8639	3.669	6.803	55.89	721.7	0.977
4.25	0.270	3.583	530.0	600.0	0.873	4.292	9.004	110.0	714.9	0.9627
5.25	0.462	3.801	51.17	600.9	0.9281	5.216	10.383	82.88	744.7	0.9761
6.35	0.723	4.354	52.10	600.9	-	6.389	12.360	61.23	735.3	0.9502
7.35	1.194	7.177	150.0	600.9	0.9825	7.507	13.680	62.68	739.6	0.9852

Table 5.13: Optimized values of y_{peak} (mm) and D_{peak} (x10^{-5} m^2/s) from the Gaussian OFDM for the 2x partial *typha* types. D_v and D_o refer to the transverse mixing coefficient in the vegetated and open channel zones, respectively.

	Winter *typha*					Summer *typha*				
Q (l/s)	D_v	D_o	D_{peak}	y_{peak}	R^2	D_v	D_o	D_{peak}	y_{peak}	R^2
3.35	4.832	22.005	49.502	556.1	0.929	3.037	23.885	69.677	601.4	0.5532
4.25	7.723	23.218	72.562	552.7	0.9733	3.958	24.953	72.251	603.1	0.2845
5.25	12.846	24.329	73.571	559.6	0.9698	4.398	26.195	56.183	601.4	0.1596
6.35	14.629	24.417	67.902	581.4	0.9746	6.581	29.215	58.727	590.9	-0.273
7.35	12.693	26.654	60.793	601.4	0.9551	8.600	30.398	56.087	566.6	-0.217

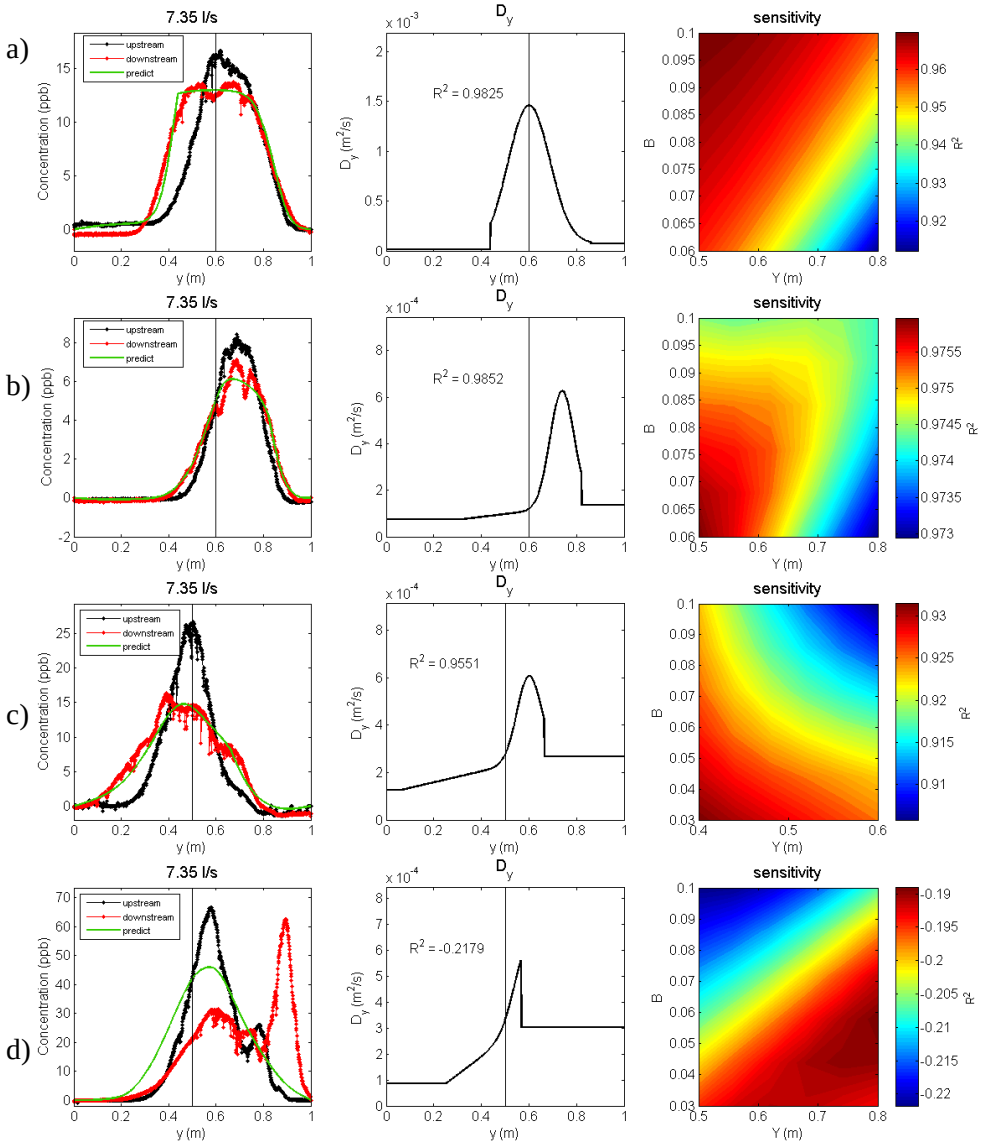

Figure 5.39: Best fit predicted downstream concentration distributions for the Gaussian OFDM are given for the 4.35 l/s case for the a) high and b) low density artificial vegetation and the c) winter and d) summer *typha*. The optimized profiles of $D_y(y)$ are also provided with the fitting sensitivity to the location of peak mixing, y_{peak} and spread parameter, B.

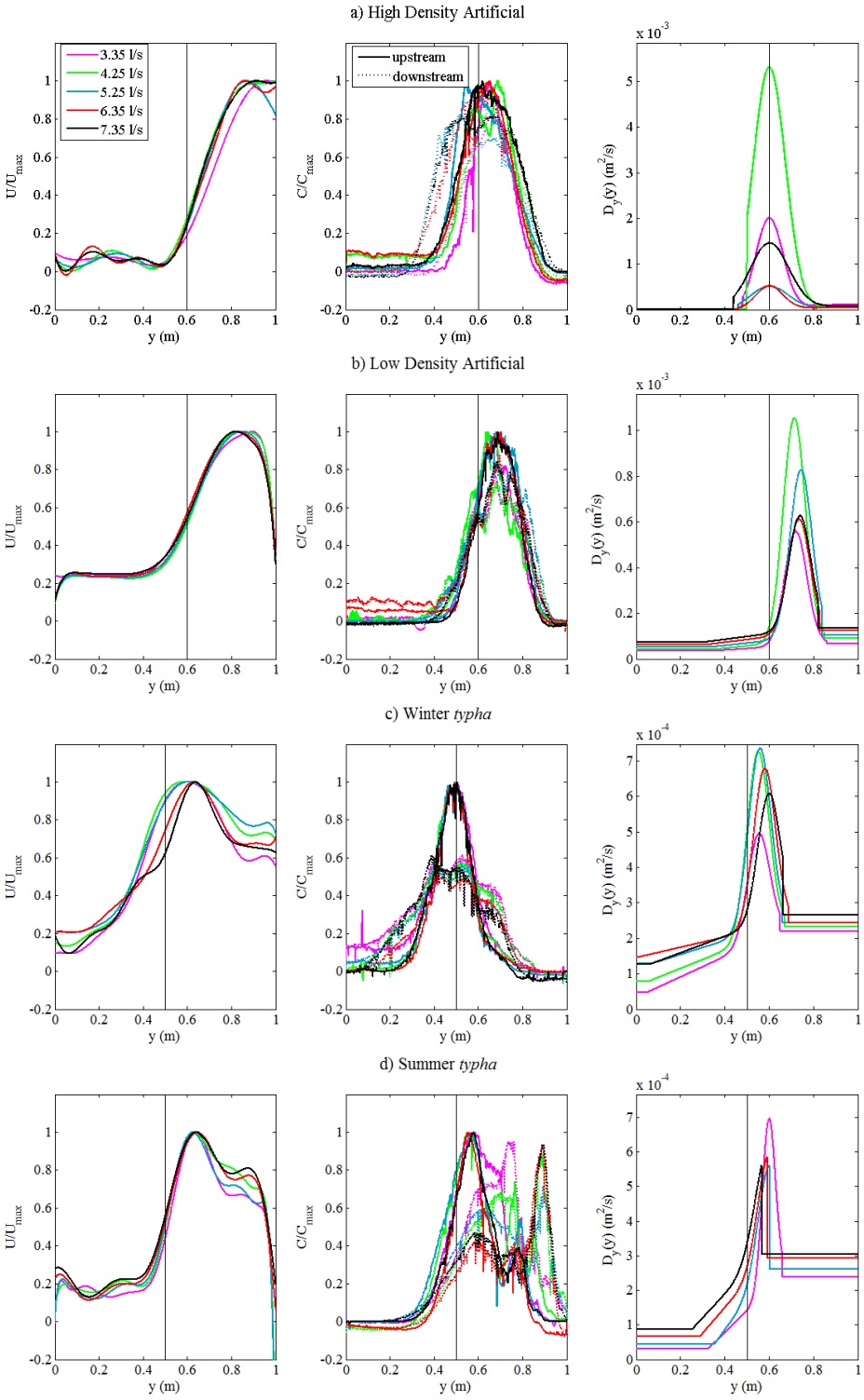

Figure 5.40: Profiles of $U(y)$ and $C(y)$ normalized by the max(U_2) and max(C_1), respectively, are compared to the best-fit profiles of $Dy(y)$ for the Gaussian OFDM analysis for a) high and b) low density artificial vegetation and the c) winter and d) summer *typha*.

6. Discussion

This chapter critically evaluates the application of shear layer analytical techniques developed in uniform, idealized artificial vegetation to characterise shear layers generated by real vegetation. It will show that the application of current shear layer hydrodynamic theory to real vegetation (winter and summer seasonal *typha* reeds) falls short of successfully predicting the observed concentration distributions – to the same degree as the idealized vegetation – when prescribing an input profile of the transverse mixing coefficient, $D_y(y)$. Further, lateral irregularities in the transverse profile of temporal mean longitudinal velocity, $U(y)$; vegetation morphology and distribution; and the 3D nature of the flow field limit the extension of the current understanding of shear layer vortices to non-idealized flows.

In addition, this chapter aims to reflect upon the processes used to quantify transverse mixing due to vegetated shear layers and evaluate the development of increasingly complex transverse mixing optimization functions. Firstly, the mean velocity fields in real *typha* reeds and the dependence on vegetation characteristics are explored in section 6.1. The optimisation of functions used to describe the lateral variation in transverse mixing coefficient is evaluated in section 6.2 – from a constant mixing assumption to a skewed Gaussian distribution within the mixing region. Finally, in section 6.3, the physically justified optimization constraints are lifted to further develop an understanding of mixing in real vegetation shear layers.

6.1 Velocity Shear, Vortex Penetration and Vegetation Characteristics

Recall that the shear layer system was characterised by three flow regions: a constant temporal mean longitudinal velocity, U_1, was prescribed for the vegetated region beyond the penetration of shear layer vortices (for $y < y_i - \delta_v$); the open channel region was prescribed a constant longitudinal velocity, U_2, beyond the penetration of the open channel vortices (for $y > y_i + \delta_o$); finally, the shear layer region was characterised by a transitional longitudinal velocity profile connecting U_1 and U_2 containing an inflection point. This study presents profiles of $U(y)$ for real *typha* vegetation that – while showing similarities – deviate in form from the classical description of shear layer mean velocity fields previously observed in uniformly distributed artificial vegetation (e.g. Nikora et al., 2013; White and Nepf, 2007 and Nepf and Vivoni, 2000).

Figure 6.1a & d compares the Fourier-fitted profiles of $U(y)$ measured in the high and low density artificial vegetation types, respectively. The profiles confirm expectations; exhibiting an approximate constant longitudinal velocity within the vegetation and open channel regions and an inflection point in the vicinity of the interface. Higher velocities persist in the low density type where the reduction in stem density acts as a weaker sink for momentum.

Normalisation[9] of $U(y)$ by U_2 (Figure 6.1b & e) confirms observations made by White and Nepf (2007) for partial, emergent cylinders. White and Nepf (2007) showed that the profiles $U(y)/U_2$ collapse in the open channel region and tended towards 0 – 0.1 within the vegetation for solid volume fractions, Φ, of 0.02 – 0.1. A similar trend is shown here for the artificial vegetation. In the high density ($\Phi = 0.02$), $U(y)/U_2$ tends towards 0.1 within the vegetation in agreement with the equivalent density reported by White and Nepf (see Figure 4a, page 5 of White and Nepf, 2008). In the low density vegetation ($\Phi = 0.005$), the profiles of $U(y)/U_2$ tend

[9] The open channel velocity, U_2, is the spatial-average velocity measured in the region $y > y_i + \delta_o$.

towards 0.22 (Figure 6.1e); providing results that have not been presented for relatively low vegetation densities. White and Nepf (2007) provided a nondimensionalization of $U(y)$ by the interfacial velocity, U_i, and the penetration into the vegetation, δ_v, to show that the profiles match in gradient and location up to the interface, y_i. Figure 6.1c shows that the profiles in the high density collapse together at the vegetation interface apart from the 4.25 l/s case – suggesting that δ_v may have been poorly defined in that case. However the successful collapse in Figure 6.1f for the low density type, and agreement with White and Nepf (2007), give reliability to the definition of δ_v for the low density cases.

Figure 6.2a & d show the fitted Fourier profiles of $U(y)$ measured in the winter and summer *typha* types, respectively. The same normalisation and non-dimensionalization methods were applied and are given in Figure 6.2b & e for $U(y)/U_2$ and c and f for $(U(y) - U_1)/(U_i-U_1)$. The normalised profiles (U/U_2) presented here for real vegetation provides a comparison between artificial and real studies. In the less dense winter season ($\Phi = 0.012$), U/U_2 tends towards ~0.2 within the vegetation (Figure 6.2b); but tends towards ~0.3 in the denser, summer season ($\Phi = 0.037$) (Figure 6.2e). This is in contrast to the artificial types shown here and by White and Nepf (2007), where U/U_2 tends towards 0 for the more dense vegetation. The normalisation for the summer season (Figure 6.2e) shows that the profiles collapse onto the same trend in the open channel region (like the artificial cases) – suggesting that the velocity field in the denser, summer *typha* is more similar to the idealised artificial types. This trend is less evident in the winter season (where U/U_2 exceeds unity); where the differences in the collapsed profiles are attributed to the difficulty in defining U_2 (Figure 6.2b).

Similarly, the non-dimensionalized profiles in the summer season (Figure 6.2f) exhibit a match in between profile gradients at the interface but is not shown for the winter season (Figure 6.2c) – further suggesting the non-classical nature of the flow field in the winter *typha*. The collapse of U/U_2 within the vegetation for the *typha* implies that, despite the relatively large solid volume fraction, comparatively large velocity occurs within the vegetated zone.

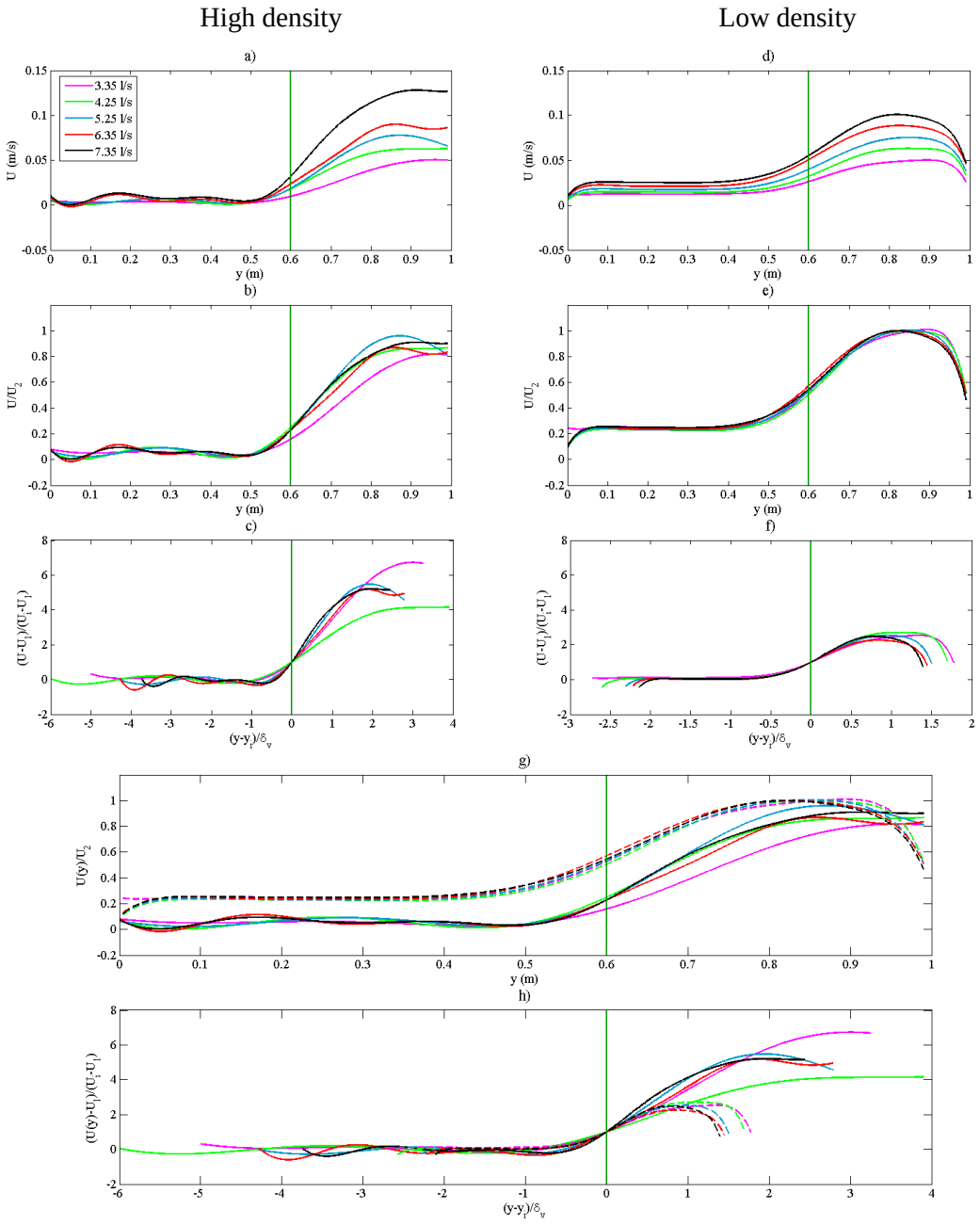

Figure 6.1: Fitted profiles of $U(y)$ for the a) low and d) high density artificial vegetation are normalised by U_2 in b) and e). The non-dimensionalization by the interface velocity, U_i, and the length scale δ_v are given in c) and f). The normalized and non-dimensionalized profiles are compared for both types in g) and h) (where the solid and dashed lines refer to the low and high density types, respectively).

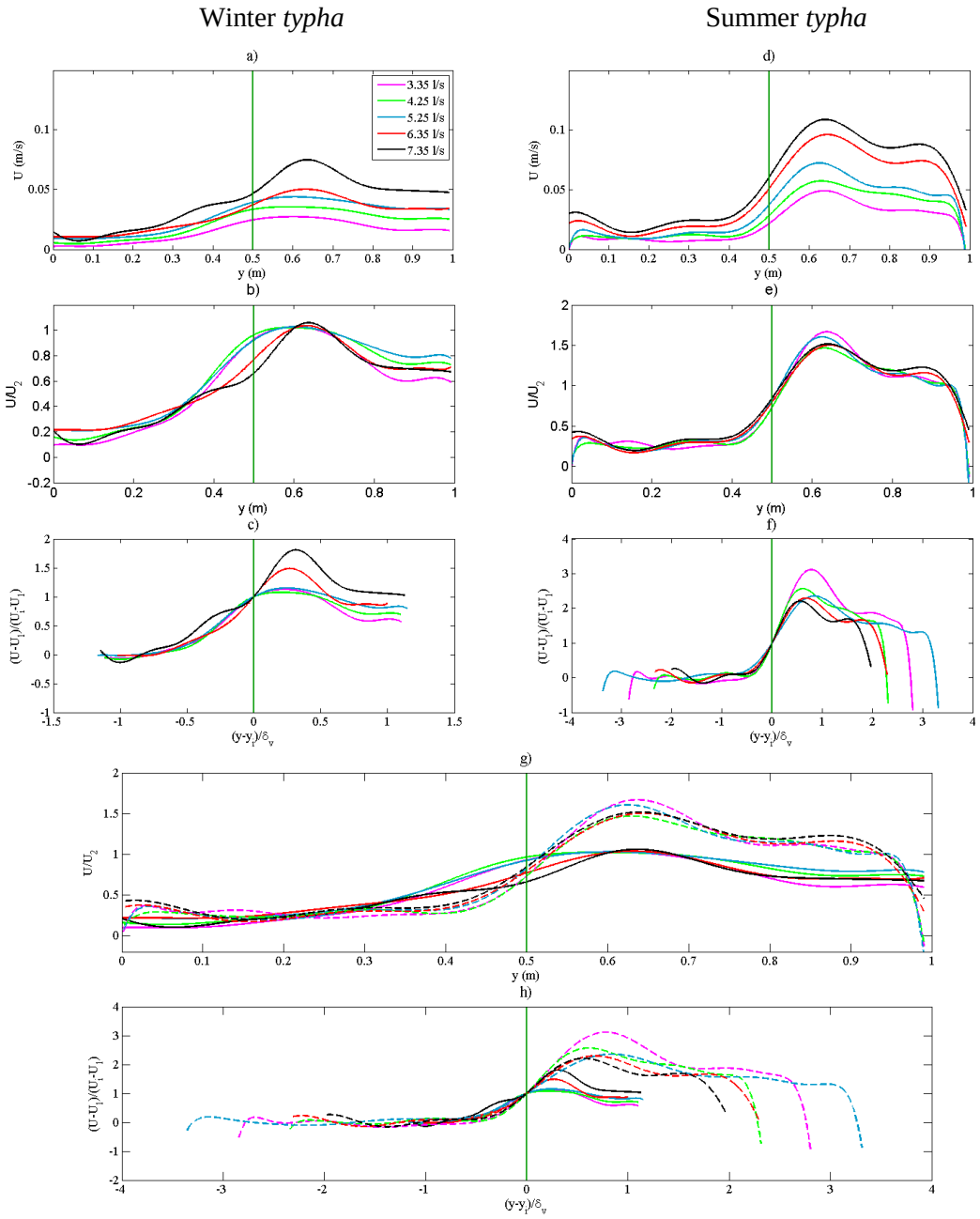

Figure 6.2: Fitted profiles of $U(y)$ for the a) winter and b) summer *typha* vegetation are normalised by U_2 in b) and e). The non-dimensionalization by the interface velocity, U_i, and the length scale δ_v are given in c) and f). The normalized and non-dimensionalized profiles are compared for both types in g) and h) (where the solid and dashed lines refer to the winter and summer seasons, respectively).

Despite the comparable solid volume fractions between the artificial and real types, the *typha* vegetation exhibits a weaker velocity shear. Figure 6.3a shows the velocity shear, ΔU, as a function of channel discharge, Q, for each vegetation type; confirming that ΔU increases with Q. The consistent difference in ΔU between each type ($d\Delta U/dQ$ = 17.04, 9.30, 8.15,

10.85respectively) indicates that the magnitude of the velocity shear is affected by the vegetation characteristics.

For the same discharge, ΔU is approximately 50% larger ($\langle \Delta U_{high}/\Delta U_{low} \rangle = 1.46$) in the high density artificial compared to the low density (Figure 6.3a). Similarly, ΔU is approximately 40% larger in the summer than the winter *typha* ($\langle \Delta U_{summer}/\Delta U_{winter} \rangle = 1.39$). These results suggest that the velocity shear is, primarily, affected by the total stem population density and frontal area per unit volume, rather than the solid volume fraction of the vegetated region. The assumption that the high stem density (1594 stems/m^2) and frontal area per unit volume (0.064 cm^{-1}) of the high density artificial vegetation leads to the greatest velocity shear would suggest that the summer *typha* – where $a = 0.035$ cm^{-1} and $\Phi = 0.037$ – exhibits the second largest velocity shear for any given discharge. The comparatively small ΔU in the summer *typha*, when compared to the low density artificial vegetation – with smaller Φ (= 0.005) and a (= 0.016 cm^{-1}) – does not support the hypothesis. The larger, but less densely populated, stems of the winter *typha* facilitate more flow paths through the vegetation compared to small diameter, densely populated artificial stems.

All but the low density artificial type collapse together when ΔU is normalised by a (Figure 6.3b). The displacement of the low density artificial type (red circles) suggests that the measured velocity shear is greater than expected for a relatively low value of a. Further, the similarity in the collapsed profiles between the winter (blue triangles) and summer (magenta triangles) *typha* suggests that difference in ΔU for real vegetation is determined by the frontal area per unit volume. This result can be used to provide a scaling[10] for ΔU (in mm/s) in shear layer vegetation given the discharge, Q [m^3/s], and the frontal area per unit volume, a for $0.027 \leq a \leq 0.064$ cm^{-1}:

$$\Delta U = a(29315Q - 18.8) \qquad \textbf{Equation 6.1}$$

[10]Note that Equation 6.1 was determined using only the grouped data from the high density artificial and the winter and summer *typha* cases.

where $R^2 = 0.91$. Ghisalberti and Nepf (2004) measured vertical profiles of longitudinal velocity, $U(z)$, in submerged cylindrical vegetation and empirically found that $\Delta U \sim a(11087Q+30.8)$ ($R^2 = 0.65$), for $0.025 \leq a \leq 0.080$ cm^{-1} (solid line Figure 6.3b).

White and Nepf (2007) also measured lateral mean longitudinal velocity profiles, $U(y)$, in shear layer emergent cylinders and found that $\Delta U \sim a(907Q+5.15)$ ($R^2 = 0.33$), for $0.004 \leq a \leq 0.02$ cm^{-1} (dashed line Figure 6.3b); while Zong and Nepf (2011) showed a poor correlation between ΔU and Q, with $\Delta U \sim a(151.03Q+145.7)$ ($R^2 = 5\text{x}10^{-5}$) (dotted line Figure 6.3b). There is agreement with Ghisalberti and Nepf (2004) and White and Nepf (2007); although the large values of ΔU for the low density artificial implies that the measured values of ΔU are greater than would be expected for the value of a. The prediction of velocity difference, presented here, given the vegetation characteristics (a) and the channel discharge for *typha* vegetation has not before been seen in any of the literature.

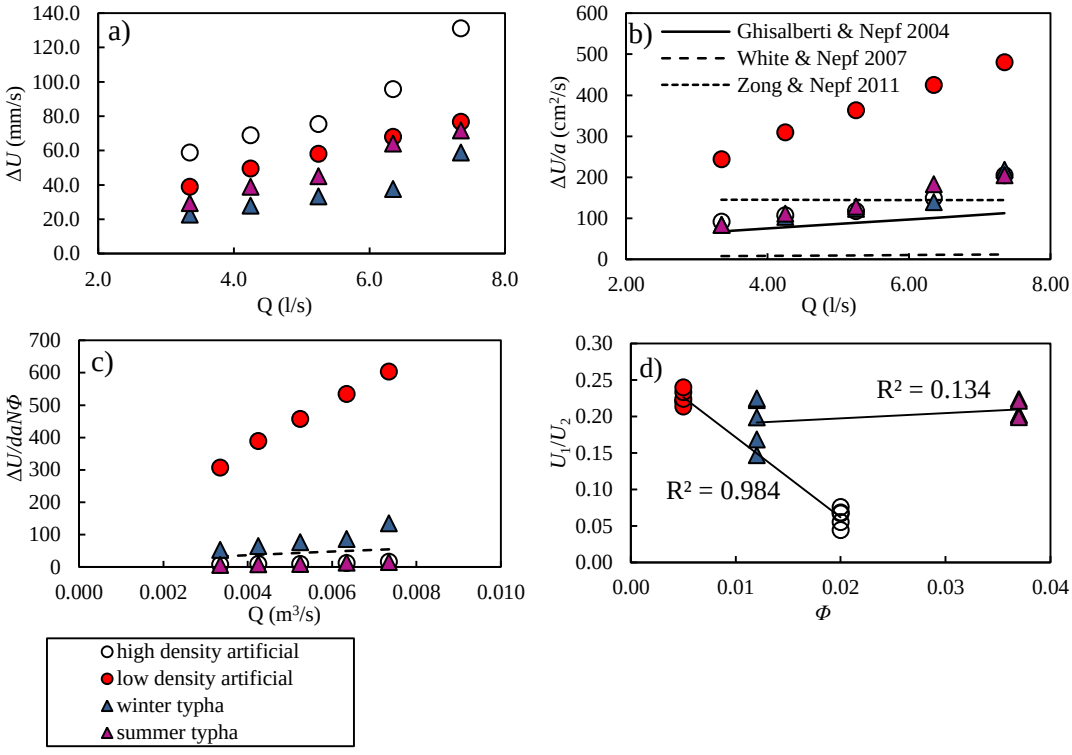

Figure 6.3: a) Velocity shear, ΔU, is compared to channel discharge, Q. b) Shear normalisation using a is compared previous studies; Ghisalberti and Nepf, 2004 (black line); White and Nepf, 2007 (dashed line); and Zong and Nepf, 2011 (dotted line). c) Normalisation by, a, N, d and Φ d) Ratio of U_1/U_2 compared to solid volume fraction, Φ.

Figure 6.3c attempts to elucidate the effect of vegetation characteristics on ΔU, using the nondimensionalization by the product of the diameter, solid volume fraction, frontal area per unit volume and stem density, $daN\Phi$. The figure shows a linear relation between $\Delta U/daN\Phi$ and Q in terms of R^2 (= 0.91, 0.99, 0.87 and 0.97 for the high and low density artificial and winter and summer *typha* types, respectively). The lack of a collapse in $\Delta U/daN\Phi$ against Q for the four vegetation types implies that the normalization using $daN\Phi$ does not take account of the changes in drag coefficient between the vegetation types and may explain the differences in the gradient of the lines of best-fit. The nondimensionalization for the *typha* types shows a similarity between the seasons; as such, velocity shear for the *typha* vegetation can be estimated as ($R^2 = 0.81$):

$$\Delta U_{typha} = daN\Phi(10460Q) - 9.1 \qquad \textbf{Equation 6.2}$$

White and Nepf (2007) found a weaker relation between ΔU and Q for shear layer emergent, artificial cylinders where $\Delta U/daN\Phi = 5553.7Q + 14.4$ (for $0.004 \leq a \leq 0.02$ cm^{-1}) (dashed line Figure 6.3c). This result is more similar to the high density artificial vegetation (Figure 6.3c, white circles) but is comparable to the summer *typha*. The empirical relation between velocity difference and vegetation characteristics presented here has, to date, not been experimentally investigated for real vegetation.

Finally, Figure 6.3d shows how the vegetation velocity, U_1, when normalised by U_2, groups together for each type and reduces with increasing Φ for the artificial vegetation (red and white circles); yielding $U_1/U_2 \sim 11/\Phi$ ($R^2 = 0.98$). The *typha* results presented here do not demonstrate the same trend with U_1/U_2, remaining approximately constant with increasing solid volume fraction – suggesting that Φ is not a reliable determinant of U_1 for real vegetation.

Recall that, despite the high population density, N, of the high density artificial vegetation, the type with the largest solid volume fraction was the summer *typha*. The porosity of the *typha* permits higher velocities within the vegetated region, thus reducing ΔU; however, the

increase in Φ from winter to summer does not increase the magnitude of ΔU to the same degree as from the low to high density artificial vegetation.

A Large mixing layer width, t_{ml}, implies that the vegetation is sparse, promoting the penetration of shear layer vortices and thus reducing the size of ΔU. Figure 6.4a shows that, when non-dimensionalized by the vegetation width, W, an increase in t_{ml} is associated with a reduction in ΔU for the artificial stems – where the large stem density of the high density artificial is expected to lead to the smallest mixing layer.

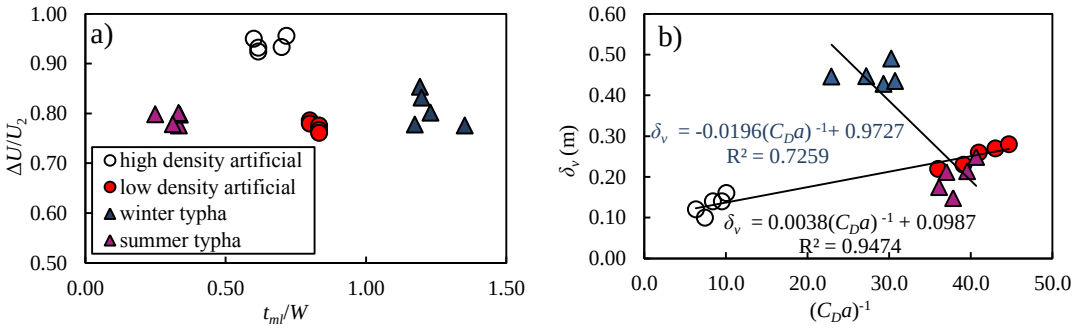

Figure 6.4:a) Mixing layer width, t_{ml}, is compared to velocity shear. b) Vegetation mixing penetration, δ_v, is compared to the vegetation drag using estimates of C_D from Nepf (1999) based on the stem Reynolds number.

Ghisalberti and Nepf (2007) found that t_{ml} in submerged vegetation scales with ΔU through $t_{ml} = \Delta U/40W$. Figure 6.4a shows that t_{ml} in this study is related to ΔU as $\Delta U/10W$ and $2\Delta U/5W$ for the high and low density artificial vegetation respectively; and $\Delta U/25W$ for the winter *typha*. The summer *typha* did not exhibited a correlation between t_{ml} and ΔU. It is also shown here that the t_{ml} scales with velocity shear $t_{ml}/W \sim 1.01\Delta U/U_2$ ($R^2 = 0.82$) for the artificial vegetation. However, a weak dependence was shown ($R^2 = -0.08$) for the *typha* vegetation indicating that the mixing layer width cannot be estimated from the velocity shear alone for real *typha* vegetation.

Nepf et al. (2007) empirically found that the vortex penetration into the vegetation is inversely proportional to the vegetation drag, $C_D a$, through $\delta_v = (0.23\pm 0.6)/C_D a$. Figure 6.4b compares δ_v for the four vegetation types against $(C_D a)^{-1}$. The drag coefficient, C_D, was not

recorded in this study due to equipment limitation[11]; however, Nepf (1999) provided estimates of C_D as a function of a and d for cylindrical vegetation given the stem Reynolds number. As such, C_D was estimated for the four types assuming perfect cylinders. The results in Figure 6.4b for the artificial vegetation support the increase in δ_v with reducing drag for the artificial types and the trend between δ_v and $C_D a$ is within the error reported by Nepf et al. (2007) ($\delta_v = 0.0038(C_D a)^{-1} + 0.098$). However, this study reports a positive correlation between δ_v and vegetation drag for the *typha* vegetation. A limiting factor in the characterisation of the real vegetation is, therefore, the definition of δ_v given the non-classical nature of the velocity profiles that exhibit multiple inflection points.

6.2 Optimized Finite Difference Model Evaluation

This section evaluates the application of the Optimised Finite Difference Model (OFDM) using constrained functions to describe the lateral profile in transverse mixing coefficient, $D_y(y)$. Recall that the FDM computes the concentration at each computation node given the input upstream concentration distribution, mean stream-wise velocity profile, $U(y)$, and $D_y(y)$. In this study, the FDM was optimised by performing a routing analysis in order to maximise the fit between the predicted and measured downstream concentration distributions. The Matlab (Mathworks, 2012b) minimization function *fmincon* was also employed to improve computation efficiency when optimizing the input parameters using the R^2 maximisation technique.

6.2.1 Spatially constant transverse mixing

Despite the simplified assumptions that $D_y \neq f(y)$, the constant mixing OFDM provides a useful technique for assessing the overall mixing for the different cases and vegetation types.

[11]The bed slope could not be varied and longitudinal surface elevation profiles could not be recorded in the *typha* cases due to the undulation of the natural bed.

The model predicts the downstream concentration distributions for the high and low density artificial and the winter *typha* vegetation types to a minimum accuracy of 91% (R^2_{min} = 0.91) and the mean goodness of fit, $\langle R^2 \rangle$, for the high and low artificial and winter and summer *typha* is 0.9144, 0.9413, 0.9351 and 0.2427, respectively. The poor fitting for the summer *typha* is attributed to the complex nature of the steady-state transverse concentration distributions (e.g. Figure 5.28d). This type exhibited a distinct transverse dissociation in concentration; where the peak concentration split into two local peaks and translated across the channel – deviating from a more classical profile shape (e.g. Figure 5.28a). This prevented the constant OFDM from successfully quantifying the mixing from upstream to downstream (see Appendix VI for all of the fitted profiles).

Figure 6.5 provides a comparison between the optimized constant D_y and bulk flow characteristic, ΔU, Q and an approximation of channel mean velocity, $U = (U_1+U_2)/2$. It can be seen in Figure 6.5a that the overall transverse mixing, D_y, increases with channel discharge, where the winter *typha* exhibits the greatest overall mixing with Q. Total mixing is expected to be greatest for the real vegetation types as the heterogeneities in the vegetation distribution, and thus the mean velocity field, enhance differential advection. The results also indicate that, despite the large shear in the artificial cases, overall channel mixing is dominated by vegetation type for a given discharge.

Figure 6.5b shows that transverse mixing normalised by stem diameter, d, increases with ΔU – where the straight lines are the linear best fit regressions – confirming findings by Ghisalberti and Nepf (2005) reporting that greater velocity shear is indicative of higher frequency shear layer vortices – thus increasing shear layer mixing. The rate of this increase is greatest for the *typha* vegetation while the trend for the high density artificial vegetation is less apparent. The summer *typha* shows the strongest increase in mixing with ΔU. The winter *typha* increases at the second highest rate but is similar to that of the low density artificial vegetation. Despite the largest velocity shear, the constant OFDM assigns the high density

artificial vegetation with relatively low overall mixing; where the correlation between D_y and ΔU is poor.

Transverse mixing is seen to scale similarly for the artificial and winter *typha* types but not the summer; where $D_y/d \sim 0.439\Delta U$, $0.408\Delta U$, $0.415\Delta U$ and $4.646\Delta U$ for the high and low density artificial and winter and summer *typha* types, respectively (Figure 6.5b). The similarity in scaling between the artificial and winter *typha* shows that, despite the increased geometric heterogeneity of the real vegetation, transverse mixing is of the same order of magnitude for a given velocity shear. The scaling presented for the summer *typha* is in agreement with Lightbody and Nepf (2006) who presented normalised longitudinal mixing coefficient, D_x/WU, for three emergent vegetation species, and found that $D_x/WU = 0.8$, 17 and 9 for *Atriplex portuloides*, *Alisma gramineum* and *Spartina Alterniflora*, respectively.

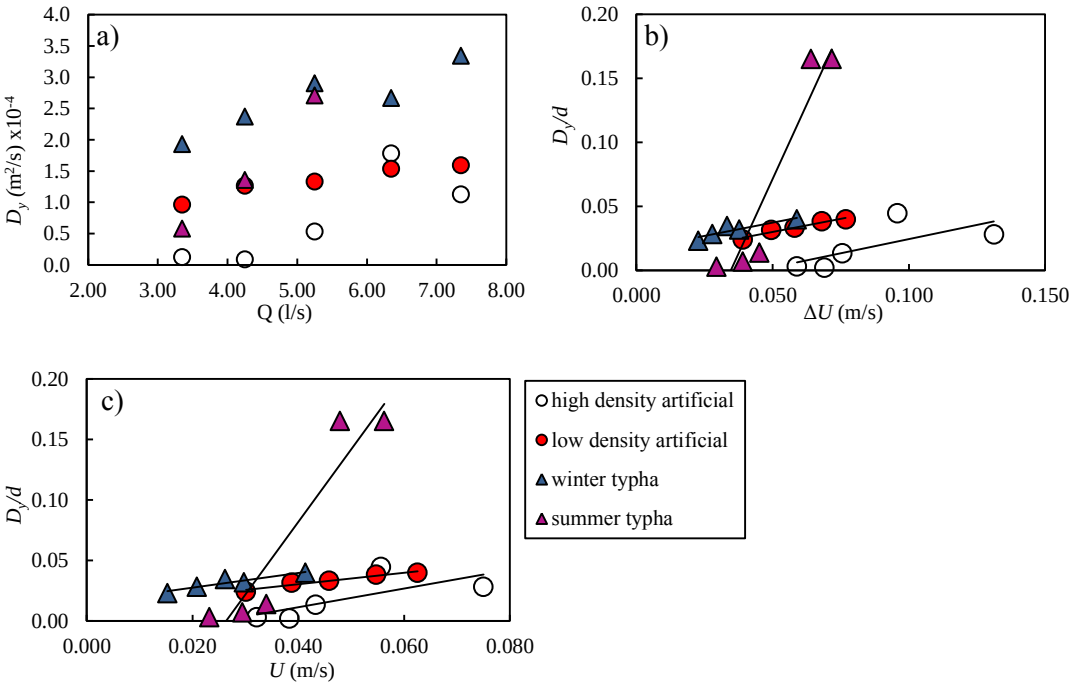

Figure 6.5: Comparisons between the best fit constant values of D_y and a) channel discharge, b) velocity shear, ΔU and c) channel mean velocity, $U = (U_1+U_2)/2$. The solid lines give the best fit linear regressions.

Additionally, Nepf (1999) showed that, for $Re_d < 100$, the normalised vertical diffusivity associated with emergent canopies is related to the mean longitudinal velocity and the stem diameter giving $D_z/Ud = 0.17$. Here $D_y/\Delta Ud$ scales to the same order as ΔU for all but the summer *typha*, giving 0.771, 0.473, and 0.610, for the high and low density artificial and

winter *typha*, respectively (Figure 6.5c). These values are in agreement with those reported by Nepf (1999) providing reliability over the OFDM technique and also indicate that transverse mixing in emergent vegetation is greater than vertical diffusivity. For ad = 0.01-0.09 and Re_d = 60-2000, Nepf (1999) also showed that D_y/Ud = 0.02-0.15. The equivalent values here for D_y are 0.47-0.77 for the artificial and 0.61-5.99 for the *typha*. The relatively large value of D_y/d for the summer *typha* demonstrates the potential limitation when employing constant mixing in the OFDM.

Further, the scaling relations between D_y and U or ΔU are, as expected, an order of magnitude lower than the scaling found by Lightbody and Nepf (2006) for longitudinal mixing in emergent, real vegetation. The scaling for the summer *typha* (D_y/Ud = 5.99) is close in magnitude to the value provided for a species of similar morphology, *Spartina Alterniflora*.

Despite the limited complexity in the constant value OFDM, the downstream concentration profiles are acceptable for the artificial types and the winter *typha*; predicting concentration distributions with average values of R^2 = 0.91, 0.94 and 0.94, respectively. Secondly, the agreement in normalised values of D_y with mixing coefficients reported by Nepf (1999) and Lightbody and Nepf (2006) suggests that the method is capable of quantifying mixing to the correct orders of magnitude for shear layer flows.

6.2.2 Transverse discontinuity in transverse mixing

The discontinuity OFDM provides better-predicted concentration distributions than the constant value optimization function. For the artificial vegetation, the average goodness of fit is $\langle R^2 \rangle$ = 0.937 and 0.948 for the high and low density types compared to 0.9144, 0.9413 for the constant OFDM. For the *typha* vegetation, the average goodness of fit improved from 0.9351 and 0.2427, for the winter and summer seasons, to 0.951 and 0.467, respectively.

The optimised transverse mixing coefficients for the two channel regions are compared in Figure 6.6. The optimized values of D_1 indicate that there is 1-2 orders of magnitude greater

transverse mixing in the real vegetation than artificial (Figure 6.6a). The model also predicts an order of magnitude greater transverse mixing within the low-density artificial vegetation compared to the high density. The low density facilitates stronger development of turbulent eddies associated with the stem diameter shedding (Figure 5.19b shows greater transverse mixing in the full vegetation scenario for the low density artificial). Weaker mixing in the high density type may be explained by the preferential flow paths associated with the dense linear array – where the longitudinal flow paths may inhibit mechanical diffusion around the stems. Greater open channel transverse mixing is predicted for the high density artificial as the greater solid volume fraction leads to stronger ΔU and therefore, enhances shear layer mixing (Figure 6.6b). The discontinuity OFDM compensates for this by increasing D_2.

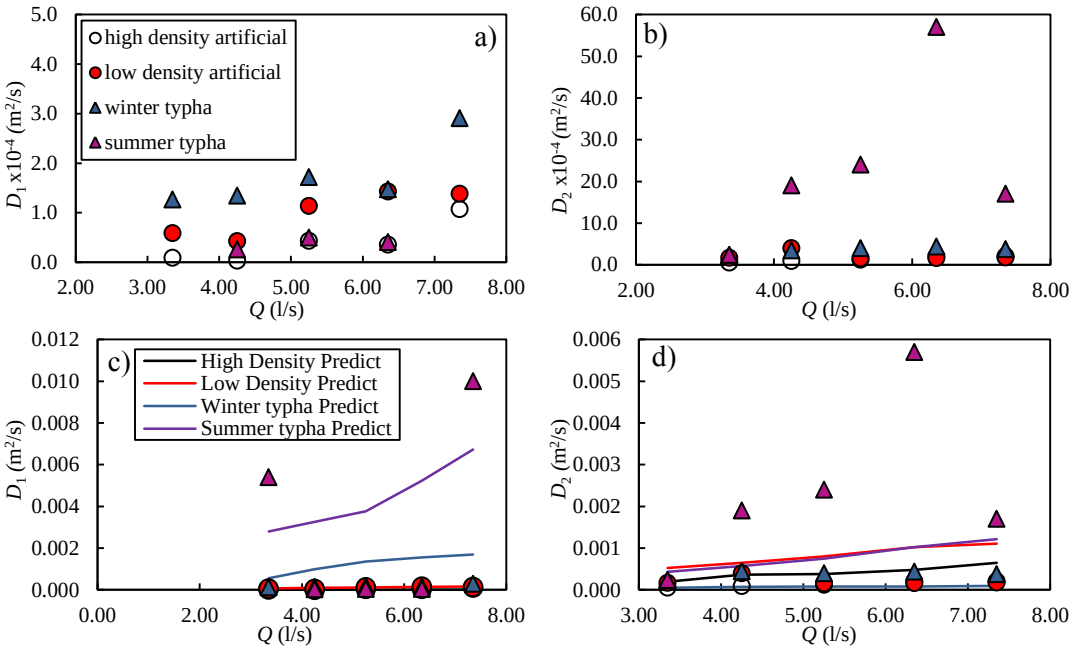

Figure 6.6: Step OFDM optimised values of $D_y(y)$ for the a) vegetation, D_1, and b) open channel, D_2. Predictions of D_1 and D_2 made using c) Nepf (1999) and d) Rutherford (1994).

The steady-state concentration distributions recorded in the winter *typha*, exhibiting small skew compared to the summer cases, resemble distributions more akin to the full vegetation scenario(e.g. Figure 4.30) (see Appendix VI for the concentration distributions measured in the full vegetation) – this is apparent in the relative similarity[12] between the optimized values

[12]On average, $D_2/D_1 = 2.3$ in the winter *typha* compared to 8.9, 3.2 and 53.0 for the high and low density artificial and summer *typha* types.

of D_1 and D_2 (see Figure 5.34). As such, the discontinuity OFDM provides good predictions of the downstream concentrations to within $R^2 = 0.95$ in the winter season. The step OFDM cannot take account of potential transverse advection through a positive transverse velocity apparent in the summer cases. The downstream concentration distributions in the summer *typha* exhibit dissociation in the peak concentration and may be symptomatic of major ejection events (e.g. see White and Nepf, 2008). The discontinuity OFDM cannot predict these distributions as it may only vary D_2 and not the mean velocity field. As a resultant, the R^2 values are low as the dissociated peak concentration downstream is at a transverse location where the equivalent upstream value is weaker. The discontinuity optimized profiles of $D_y(y)$ for the summer *typha* should, therefore, be appreciated with acknowledgement of the quality of fit and the nature of the steady-state concentration distributions.

Greater vegetation mixing, D_1, in the *typha* cases is attributed to the heterogeneity in stem morphology and distribution, maximizing mechanical diffusion and the development of turbulent eddies (see Figure 5.19). The presence of vegetation "clumps" (groups of multiple stems that, while maintaining the stem density, alter the frontal area per unit volume; Table 4.1) may also enhance local differential advection and generate similar shear layer vortices, enhancing transverse mixing. The large optimised values of D_2 are attributed to the increased drag of the real cropped bed compared to the smooth plastic artificial bed – generating greater turbulence and flow-field heterogeneity. Moreover, greater open channel mixing is expected for the summer season where the larger shear generates stronger shear layer mixing – apparent in the relative increase in D_2/D_1 (see footnote above).

The optimised values of D_1 and D_2 were compared to estimates made using empirical the relations presented by Nepf (1999) and Rutherford (1994). The relation between transverse mixing and velocity, $D_1 = 0.17U_1d$, provided by Nepf (1999) was used to estimate the expected values of D_1. Values of D_2 for the open channel were also estimated using $D_2 = 0.134u^*h$ Rutherford (1994), where u^* is the bed shear velocity. Here the bed shear

velocity is substituted for the velocity at the vegetation interface, U_i, as the vegetation interface dominates the form of the transverse velocity profiles.

The predicted values of D_1 are close to the discontinuity OFDM for the low density artificial vegetation (Figure 6.6c) – where the fit between the OFDM and the Nepf (1999) predictions is $R^2 = 0.77$. The error in predictions is given in Table 6.1 and shows that Nepf (1999) over predicts D_1 by 33% on average. The predicted values for the high density artificial vegetation are approximately an order of magnitude smaller than those optimized; but yield a similar fit, giving $R^2 = 0.76$ (Table 6.2) and are under predicted by 73% on average. Transverse mixing in the vegetation is over estimated for the *typha* by one order of magnitude in the winter and two orders in the summer (Table 6.3 and Table 6.4) – where the fit between the OFDM and predictions for the winter and summer seasons was $R^2 = 0.49$ and 0.28, respectively. Nepf (1999) over predicts D_1 by an average of 621% and 6630% for the winter and summer, respectively.

In the high density artificial vegetation, D_2 is over-estimated but is of the same order of magnitude as the discontinuity OFDM, giving $R^2 = 0.85$; while, in the low density, the values are over estimated by an order of magnitude, giving $R^2 = 0.14$ (Figure 6.6d). Rutherford (1994) over-predicts D_2 by an average of 227% and 353% in the high and low densities, respectively. Open channel mixing in the *typha* is under-predicted by 80%, on average, in winter ($R^2 = 0.34$) but is of the same magnitude in summer ($R^2 = 0.27$) and is under-predicted by 34% on average.

In the cases where the OFDM and predicted values deviate, the transverse mixing coefficient is: a) under-estimated in the vegetated region for the artificial but over-estimated for the *typha* and b) over-estimated in the open channel region for the artificial but under-estimated for the *typha* (see Table 6.1-4). The disparity in the OFDM values of D_1 and those predicted for the artificial cases is attributed to the limited complexity of the input profile $D_y(y)$. The step OFDM optimizes two discrete values, D_1 and D_2, and increases or decreases D_1 and/or D_2 to compensate for the nature of the steady-state concentration profiles. The

penetration of the mixing layer has the effect of increasing the average value of D_y within the vegetation thus increasing the optimized values of D_1 relative the full vegetation predictions given by Nepf (1999).

The over-prediction of D_2 for the artificial vegetation using Rutherford (1994) suggests that interfacial velocity, U_i, is not an appropriate quantity to parameterise the open-channel transverse mixing. The optimized values of D_2 using the discontinuity OFDM are expected to be larger than those predicted due to enhanced shear layer mixing; however, if the optimized values of D_1 are increased – relative to Nepf (1999) – then the step OFDM will compensate by reducing D_2 accordingly. Further, the over-prediction of D_1 and simultaneous under-prediction of D_2 in the *typha* cases is attributed to the same compensatory effect of the step OFDM; where large optimised values of D_2 will be compensated by reducing the relative size of D_1. This compensatory effect represents a limitation in the discontinuity OFDM for producing physically justified results. Despite the successful recovery (in terms of R^2) of downstream concentration for the artificial and winter *typha* types, the apparent compensatory effects limit the physical reliability of the best-fit profiles of $D_y(y)$ when using the discontinuity OFDM. The step OFDM is poor at predicting concentrations in the summer *typha*, yielding an average fit of $R^2 = 0.467$. These results imply that transverse mixing in shear layer vegetation cannot be accurately characterized as two distinct flow regimes using previously developed empirical relations (e.g. Nepf, 1999 and Rutherford, 1994).

Table 6.1: Optimized and predicted values of D_1 and D_2 for the high density artificial, partial vegetation. R^2 refers to the fit for the discontinuity OFDM where the error compares the OFDM results and theoretical predictions.

	Vegetated region				Open-channel region		
Q (l/s)	D_1 x10^{-6} Disc. OFDM	R^2	D_1 x10^{-6} Nepf (1999)	Error (%)	D_2 x10^{-6} Disc. OFDM	D_2 x10^{-6} Rutherford (1994)	Error (%)
3.35	8.42	0.9839	1.83	21	53.79	197	366
4.25	3.16	0.9498	2.72	86	88.08	366	415
5.25	43.08	0.8939	3.74	8	124.0	376	303
6.35	35.00	-	5.30	15	200.0	476	238
7.35	107.0	0.9219	6.39	6	206.3	645	312

Table 6.2: Optimized and predicted values of D_1 and D_2 for the low density artificial, partial vegetation. R^2 refers to the fit for the discontinuity OFDM.

Q (l/s)	D_1 x10^{-5} Disc. OFDM	R^2	D_1 x10^{-5} Nepf (1999)	Error (%)	D_2 x10^{-5} Disc. OFDM	D_2 x10^{-5} Rutherford (1994)	Error (%)
3.35	5.85	0.9492	7.20	123	16.91	52.7	311
4.25	4.21	0.9324	9.52	226	39.63	64.7	163
5.25	11.36	0.9510	11.42	100	14.99	80.2	535
6.35	14.24	0.9343	14.07	98	16.17	101.9	630
7.35	13.78	0.9758	16.45	119	17.63	110.8	628

Table 6.3: Optimized and predicted values of D_1 and D_2 for the winter *typha* artificial, partial vegetation. R^2 refers to the fit for the discontinuity OFDM.

Q (l/s)	D_1 x10^{-4} Disc. OFDM	R^2	D_1 x10^{-4} Nepf (1999)	Error (%)	D_2 x10^{-4} Disc. OFDM	D_2 x10^{-4} Rutherford (1994)	Error (%)
3.35	1.263	0.9265	5.569	440	2.261	0.497	22
4.25	1.340	0.9583	9.853	735	4.450	0.673	15
5.25	1.715	0.9551	13.57	791	3.941	0.794	20
6.35	1.472	0.9649	15.57	1057	4.378	0.752	17
7.35	2.908	0.9503	16.99	584	3.771	0.941	25

Table 6.4: Optimized and predicted values of D_1 and D_2 for the summer *typha* artificial, partial vegetation. R^2 refers to the fit for the discontinuity OFDM.

Q (l/s)	D_1 x10^{-4} Disc. OFDM	R^2	D_1 x10^{-4} Nepf (1999)	Error (%)	D_2 x10^{-4} Disc. OFDM	D_2 x10^{-4} Rutherford (1994)	Error (%)
3.35	54.00	0.8866	28.03	51.0	2.395	4.322	180
4.25	0.2533	0.4231	32.65	12889	19.00	5.688	29
5.25	0.4918	0.4609	37.59	7644	24.00	7.497	31
6.35	0.4033	0.2337	52.43	13002	57.00	10.23	17
7.35	100.0	0.3345	67.27	67	17.00	12.14	71

6.2.3 Triangular and Gaussian mixing functions

The demand for greater spatial resolution and versatility in $D_y(y)$ lead to the application of triangular and Gaussian optimisation functions – where section 5.2.3 of the Analysis Chapter provides a physical justification.

a) Defining the mixing region parameters

The Triangular and Gaussian optimisation functions demand definition of the mixing region parameters – channel transverse mixing coefficients, D_v and D_o for the constant mixing vegetation and open-channel regions, and the vortex penetration distances into the vegetation and the open channel, δ_v and δ_o (see Figure 5.24 and Figure 5.35). The triangular or Gaussian forms of $D_y(y)$ were then optimised within the defined constant mixing limits, in the region $y_i - \delta_v < y < y_i + \delta_o$. Reduction in the goodness of fit between the discontinuity and/or the triangular/Gaussian optimization functions is attributed to the physical constraints imposed on the model; as the physical distinction of three mixing zones (vegetated, shear layer and open channel) relies on the precise estimation of the penetration limits and the values of D_v and D_o – all of which have associated uncertainty and limitations.

The distances δ_v and δ_o are qualitatively visible in the artificial vegetation; where the fitted profiles of $U(y)$ conform to the expected shear layer forms (Figure 6.1a & d) meaning that δ_v and δ_o can be well defined (e.g. Figure 6.2a & f). The profiles of $U(y)$ in the *typha* exhibit a shear layer trend. However, the profiles (Figure 6.2a&d) are non-classical and do not permit accurate estimations of δ_v and δ_o; where the extent of the vortex penetration into the vegetation is poorly defined in the winter cases – due to multiple inflection points and local peaks. Further, both seasons fail to show an approximate constant longitudinal velocity in the open-channel region, U_2; where the definition of $0.98U_{max}$ is poorly visualised for the complex mean velocity field. The heterogeneous stem distribution (such as morphology and geometry, e.g. Figure 6.7) leads to a poorly defined vegetation interface location, where the presence or

absence of stems may strongly affect the profile shape. This can be seen in the mean fitted profiles of $U(y)$ – where, although the vegetated and open channel regions can be discerned, the effect of stem wakes causes local peaks and troughs. The vegetation was manually cropped and care was taken to ensure that the location of the interface did not vary longitudinally (i.e. $y_i \neq f(x)$) – although porous regions were present at some locations. Secondly, D_v and D_o were estimated using the regression between D_y and the area mean longitudinal velocity, U, investigated in the full vegetation and bare channel scenarios (Figure 5.36); where the spatial average velocity within the mixing regions defined the values of U_1 and U_2 ($U_1 = \langle U(y < y_i - \delta_v) \rangle$ and $U_2 = \langle U(y > y_i + \delta_o) \rangle$). However, the initial assumption that D_y scales linearly with U, is subject to greater uncertainty for non-uniform, real vegetation.

In the winter *typha*, $U(y)$ presents a peak velocity at $y \approx 0.6$ m, 0.1 m from the interface, and reduces again towards the open channel boundary (Figure 6.2a & d). The complementary trough in $U(y)$ at the interface ($y = 0.5$ m) indicates that there was a large stem (or groups of stems, e.g. Figure 6.7) causing an acceleration around the obstruction. The secondary peak in $U(y)$ at $y \approx 0.45$ m confirms this acceleration. The accelerated flow, and peak longitudinal velocity at a location closer than expected to the interface, meant that U_2 does not accurately describe the velocity in the open channel as reliably as for the artificial cases. Moreover, the extension of the incomplete raw velocity profiles contributes an additional source of uncertainty in the calculation of U_2. As such, defining U_1 and U_2 for the *typha* cases was limited by the deviation of $U(y)$ from the assumed classical shear layer form.

The profiles of $U(y)$ in the summer *typha* (Figure 6.2a & d) are more similar in form to those of the classical artificial cases; with an absence of lateral acceleration at the interface and clear distinction between the vegetated and open channel flow and profile inflection.

Figure 6.7: Image of winter *typha* vegetation shows groups of stems, or "clumps", with large porous zones.

It follows that, when assessing the predictive capabilities of the triangle and Gaussian models, one must reflect upon the relevance of drawing conclusions using an R^2 value – or other statistical techniques – as a qualitative indicator. Moreover, the assignment of a relatively large goodness of fit does not necessarily imply that the modelling techniques are a physically precise description of that system. Finally, the limitation in characterising the shear layer parameters discussed above must be considered when assessing the physical meaning of the results. As such, similarity in R^2 between the step and the constrained triangle or Gaussian OFDMs implies that models are equally successful in describing the mixing characteristics of the shear layer vegetation.

It should be emphasized that one aim of this thesis is to assess the applicability of theoretical understandings of shear layer mixing in idealized conditions to real vegetation. As such, the application of the triangle and Gaussian OFDMs should be assessed on its own merits, irrespective on other potential fitting functions that yield a better fit.

b) Triangle OFDM

In input of D_v, D_o, δ_v and δ_o into the triangle OFDM required the optimisation of the location, y_{peak}, and magnitude, D_{peak}, of the triangle superimposed in the region $y_i - \delta_v < y < y_i + \delta_o$. The predictions of the downstream concentration distributions are similar in fit to those predicted using the step mixing functions. In the artificial cases the mean goodness of fit for the high and low density is 0.9349 and 0.9379, respectively, compared to 0.937 and

0.948 for the step OFDM. However, the goodness of fit reduces for the *typha* types where the mean value for the winter and summer seasons is 0.9305 and 0.0577, respectively, compared to 0.951 and 0.467 for the step function.

Figure 6.8a show the relationship between D_{peak} and channel discharge (see Table 5.10 and Table 5.11 for values). The peak mixing coefficient increases with discharge most for the high density artificial vegetation. Although, there is an anomalous point at the 4.25 l/s case attributed to the high background concentration within the vegetation (Figure 8.75 in Appendix VI); where the OFDM compensates for the apparently high mixing in the vegetation by disproportionately increasing D_{peak}.

In the low density artificial, D_{peak} is of the same order of magnitude as the high density but smaller in every case, following a weaker relation with Q; confirming that the larger ΔU enhances transverse mixing within the shear layer region. In general, however, the triangle OFDM yields a better fit for the low density compared to the high density ($\langle R^2 \rangle = 0.938$ compared to 0.935); assigning greater reliability to that set of cases. On average the peak mixing in the high density is 416% larger than in the low density confirming that the greater solid volume fraction increases $D_y(y)$ within the mixing region. A similar increase was found by Okamoto et al. (2012), in a similar study using submerged cylinders, for a similar same increase in Φ (from 0.015 to 0.061), where the average D_{peak} increased by 310%.

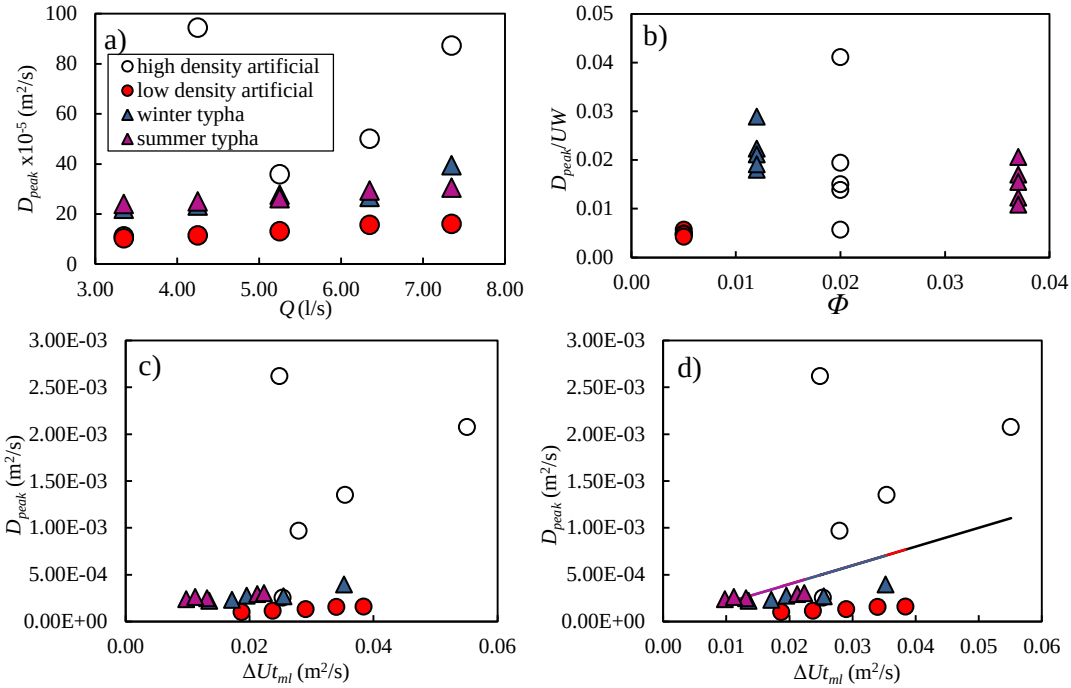

Figure 6.8: Triangle OFDM results for a) D_{peak} and Q b) D_{peak}/UW and Φ c) D_{peak} and ΔUt_{ml} and d) the predicted values of D_{peak} using Ghisalberti and Nepf (2005).

The peak mixing coefficient is similar for both *typha* seasons and lie between the low and high density artificial values; although there is an increase in D_{peak} from winter to summer of, on average, 95% for an approximate three-fold increase in Φ and contrasts with the artificial cases. The change in peak transverse mixing for an increase in the solid volume fraction has not been reported for real vegetation to date.

Recall that the artificial and real vegetation patches were not the same width (W = 0.60 and 0.50 m, respectively). A number of Authors report mixing coefficient values normalised by the mean velocity and W – since the vegetation width sets the maximum scale of turbulence (Ghisalberti and Nepf, 2005; Lightbody and Nepf, 2006b; Okamoto et al., 2012). When non-dimensionalized (Figure 6.8b), D_{peak} shows an increase with Φ for the artificial vegetation. Okamoto et al. (2012) reported D_{peak}/UW = 0.1 and D_{peak}/UW = 0.025 for Φ = 0.061 and 0.015. Similar results are found here where the average D_{peak}/UW = 0.018 (Φ = 0.02), 0.005 (Φ = 0.005), 0.022 (Φ = 0.012) and 0.015 (Φ = 0.037) for the high and low density artificial and winter and summer types, respectively.

An increase in D_{peak}/UW with Φ was not seen for the *typha* vegetation – where the summer season shows a reduction in D_{peak}/UW. The absence of trend in maximum shear layer mixing coefficient with solid volume fraction in real vegetation suggests that other characteristics control mixing in real vegetation. It should be noted that, for all but one case, the optimal profiles of $D_y(y)$ for the summer *typha* were step like in nature, i.e. $D_{peak} = D_o$, and as such, the trend in D_{peak}/UW with Φ for the real vegetation is not physically reliable for the triangle OFDM.

Ghisalberti and Nepf (2005) report that the transverse mixing at the vegetation interface, $D_y(y_i)$, is related to the velocity shear and mixing layer width through $D_y(y_i) = 0.032\Delta U t_{ml}$ for densities ad = 0.016-0.051; while Ghisalberti and Nepf (2009) showed that the maximum transverse mixing coefficient, $D_{peak} \approx 0.02\Delta U t_{ml}$. Figure 6.8d compares the predicted and optimized values of D_{peak} using Ghisalberti and Nepf (2009) and the triangle OFDM. Ghisalberti and Nepf (2009) over predict the expected values of D_{peak} for the low density artificial and *typha* types and under-predict them for the high density. In this study, only the high density artificial vegetation shows a similar trend to Ghisalberti and Nepf (2009); where $D_{peak} \sim 0.024\ \Delta U t_{ml}$. This study shows that, for real *typha* vegetation, using the triangular OFDM, the peak transverse mixing coefficient scales as $\max(D_{typha}) \sim 0.0056\ \Delta U t_{ml}$.

Figure 6.9a compares the non-dimensionalized profiles of $D_y(y)$ for the two artificial types showing that transverse mixing is increased in the mixing layer region. The distinction between shear layer mixing and that associated with the vegetation and open channel zones is less apparent for the *typha* types – where all of the summer *typha* cases provide non-triangular optimal profiles. The heighted bed-roughness of the summer *typha* may account for the relative magnitude in D_o leading to non-triangular $D_y(y)$.

In summary, peak transverse mixing for the artificial and winter *typha* types scales linearly with the vegetation solid volume fraction, confirming that an increase in the vegetation density enhances shear layer mixing. The deviation in the trend for the summer season suggests that the solid volume fraction is insufficient for characterising real vegetation; where

the relation with ΔUt_{ml} provides a clearer trend for the summer season. However, the maximum transverse mixing coefficient has a weaker scaling with ΔUt_{ml} than reported by Ghisalberti and Nepf (2005) for submerged, artificial vegetation. But, the optimisation of $D_{peak} = D_o$ in the summer seasons limits further conclusions.

The significant reduction in R^2 using the triangular OFDM when compared to the discontinuity optimization for the summer *typha* infers that the application of the mixing layer characteristics, while successfully describing artificial vegetation, is not appropriate for real vegetation. The results for the winter season, however, were relatively successful ($\langle R^2 \rangle = 0.9305$) suggesting that the model performs better with more classical transverse concentration distributions.

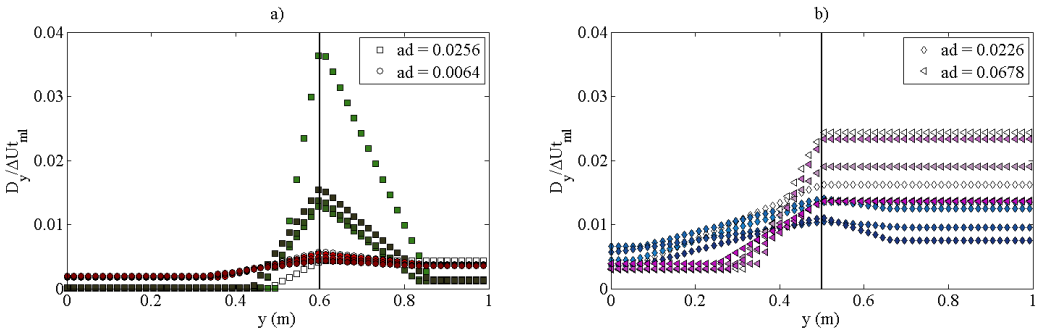

Figure 6.9: Non-dimensionalized profiles of $D_y(y)$ using the triangle OFDM for the a) high (squares) and low (circles) density artificial and b) winter (diamond) and summer (triangle) *typha*. The colour shading indicates increasing channel discharge.

c) Gaussian mixing function

The Gaussian OFDM was developed to provide a continuous profile of $D_y(y)$ that could adjusted to take the physical form of the lateral variation in mixing coefficient. Ghisalberti and Nepf (2004 & 2005) and Okamoto et al. (2012) presented profiles of $D_y(y)$ and eddy viscosity that were approximately Gaussian in shape. However, both studies employed a flux gradient and quadrant analysis, using artificial vegetation, that has been shown to be limited in real vegetation and other heterogeneous flow fields (e.g. section 5.2.2, Analysis Chapter).

The optimal profiles of $D_y(y)$ show qualitative similarities to the triangular results (Figure 5.40). The goodness of fit was improved upon when compared to the triangular function for the low density artificial cases; where the mean value of R^2 improved from 0.9379 to 0.9702.

However, for high density cases, the mean value of R^2 reduced from 0.9349 to 0.9118; although, there was an increase in R^2 for 2 of the 5 cases. For both the *typha* types (winter and summer), R^2 increased from 0.9305 and 0.0577 to 0.9603 and 0.1012, respectively, compared to the triangular function. The results do not provide a clear indication of a positive correlation between D_{peak} and flow rate (Figure 6.10a); however, when normalised by UW, there is an approximate negative trend between D_{peak}/UW and Q for the *typha* vegetation (Figure 6.10b). As stated above, Okamoto et al. (2012) report that, for $\Phi = 0.061$ and 0.015, $D_{peak}/UW = 0.1$ and 0.025. Figure 6.10c shows similarities to Okamoto et al., where the average $D_{peak}/UW = 0.081$ ($\Phi = 0.02$), 0.009 ($\Phi = 0.005$), 0.053 ($\Phi = 0.012$) and 0.037 ($\Phi = 0.037$), for the high and low density and *typha* types, respectively. The absence of trend when employing the Gaussian function between D_{peak}/UW and Φ for the *typha* concurs with the results for the triangular form.

On average, the peak mixing is 34% larger in the high density artificial vegetation compared to the low density – a smaller difference than the triangle OFDM but confirming that the greater solid volume fraction increases mixing. However, Okamoto et al. (2012) found an increase in D_{peak} of 310% for a similar change in solid volume fraction. Peak mixing in the summer *typha*, in contrast to the triangle OFDM, is smaller than the winter season at 99.1%. Figure 6.11 shows that, when non-dimensionalized by ΔUt_{ml}, peak mixing is larger in the summer season.

Figure 6.10c compares predicted D_{peak} using Ghisalberti and Nepf (2005) ($D_{peak} \approx 0.02\Delta Ut_{ml}$, for $ad = 0.016$-0.051) and those using the Gaussian OFDM. The optimised values are closer to the prediction than the triangular function results; although, the trends for the individual types do not support the scaling $D_{peak} \approx 0.02\Delta Ut_{ml}$. However, Figure 6.10d shows that the best fit line for D_{peak} against ΔUt_{ml} for all vegetation types provides a scaling of 0.0121. Taking the *typha* alone, there is no correlation between peak mixing coefficient and the product of the velocity shear and mixing layer width – indicating that the conclusions of Ghisalberti and Nepf (2005) break down for real vegetation.

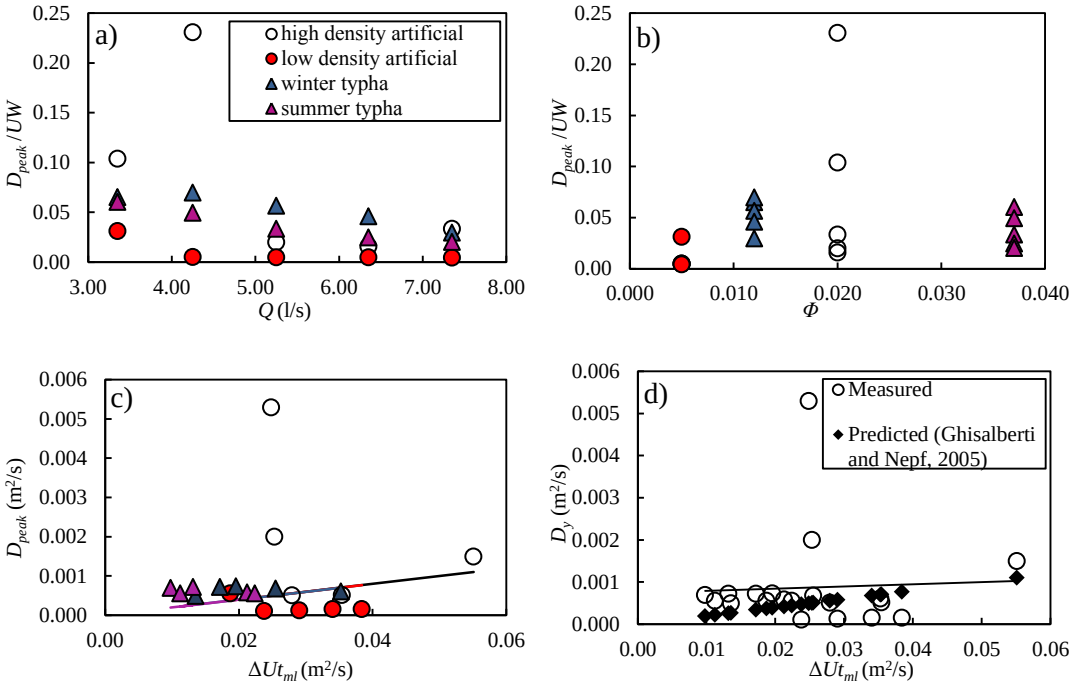

Figure 6.10: Gaussian OFDM results for a) D_{peak} and Q b) D_{peak} and Φ c) D_{peak} and ΔUt_{ml}. d) Predicted values of D_{peak} using Ghisalberti and Nepf (2005) where the straight line in the linear regression.

The normalised profiles of $D_y(y)$ in Figure 6.11 support the theory that transverse mixing is dominated by the shear layer vortices – where the profile shapes in Figure 6.11a are similar in form to those presented by Ghisalberti and Nepf (2005) and Okamoto et al. (2012) for artificial vegetation. However, the profiles in this study have been calculated using a finite difference solution that reduces the error of the output profile by performing a routing optimisation. As such the profiles are considered more reliable where the minimum goodness of fit for the artificial cases is 0.86. New results for *typha* vegetation are provided in Figure 6.11b and confirm the extension of shear layer theory to real vegetated shear layers. It is shown here that the dominance of the shear layer vortices in the overall transverse mixing is less for real vegetation where the mixing in the vegetation and open channel regions is comparable to D_{peak}.

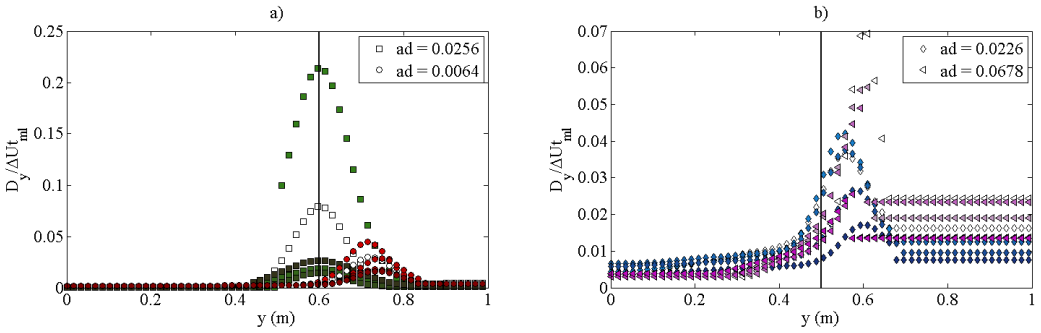

Figure 6.11: Non-dimensionalised profiles of $D_y(y)$ using the Gaussian OFDM for the a) high (squares) and low (circles) density artificial and b) winter (diamond) and summer (triangle) *typha*. The colour shading refers to the channel discharge where the darker shades indicate higher discharges.

Figure 6.12 provides profiles of the mean a) longitudinal and b) transverse velocity fluctuations as an indication of turbulence, u'^2 and v'^2 and c) the Reynolds stress, $\langle u'v' \rangle$, for the high density artificial vegetation measured using the *Vectrino II* ADV. It can be seen that turbulence is greater in the open channel region compared to the vegetation. The peak transverse mixing coefficient is expected to coincide with the location of peak turbulence; however, for the examples given, the location of peak turbulence is up to 0.10 m further into the open channel than the optimal location of D_{peak}. The difference between these two results may be attributed to the low spatial resolution velocity measurements in the vicinity of the interface (note that the *Vectrino II* probe was employed in this case and was manually translated across the channel). Despite this, Figure 6.12 demonstrates the increase in turbulence caused by the vegetation shear layer when compared to the vegetated region and supports the optimised results in Figure 6.11. The transverse fluctuations peak in the interfacial region. Reynolds stress is maximised at approximately $y = 0.55$ m although the 7.35 l/s case peaks deep in to the open-channel region.

The success in the prediction of the downstream concentration, in terms of goodness of fit, when employing the Gaussian function indicates that the continuous description of $D_y(y)$ within the mixing region improves the predictive capabilities of the OFDM.

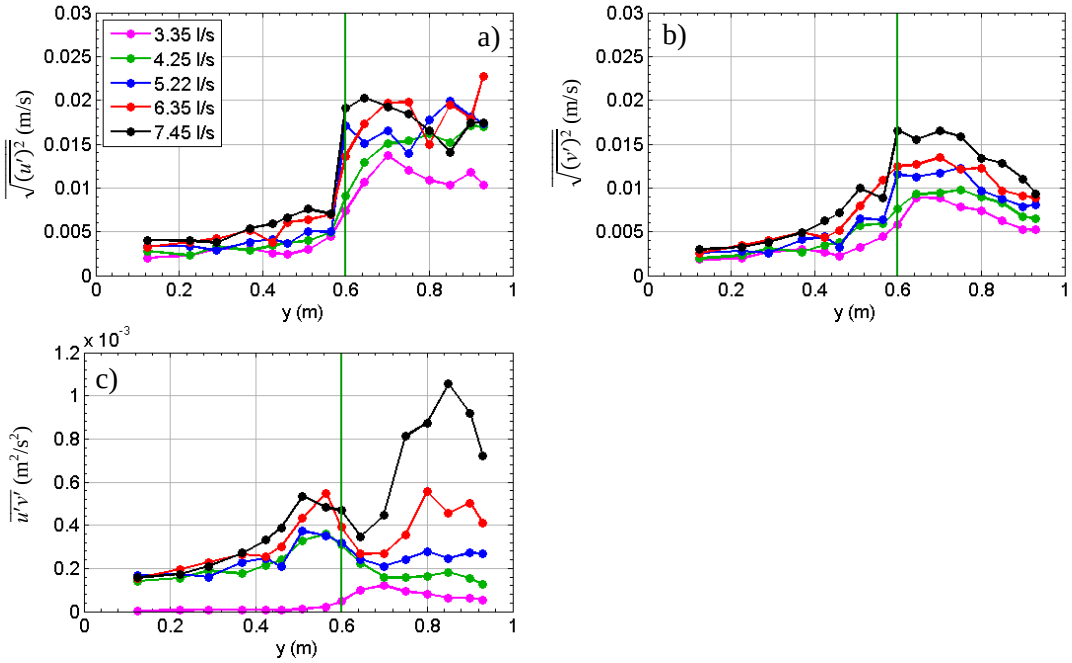

Figure 6.12: Profiles of mean turbulence fluctuation in a) $u(t)$ and b) $v(t)$ and c) Reynolds stress for the high density, partial artificial vegetation.

6.3 Comparison of Optimization Functions

In practical terms, there was minimal difference in predictability between the triangular and Gaussian optimization functions; where the mean R^2 was 0.9349, 0.9379, 0.9305 and 0.0577, for the triangular function and 0.9702, 0.9118, 0.9603 and 0.1012 for the Gaussian function for the four types, respectively. However, the description of the mixing properties in real vegetation is limited by the extension of shear layer theory developed in idealized conditions – e.g. uniform vegetation with spatially constant stem spacing and diameter. It is predicted that the definition of three mixing zones is a simplification of the hydrodynamic complexity for the *typha* vegetation. This is most apparent in the failure of the triangle and Gaussian functions to successfully predict concentrations for the summer *typha* cases. There was, therefore, a need to investigate other potential functions that could possibly, better predict concentration distributions in real vegetation.

6.3.1 Unconstrained triangular mixing function

The triangle OFDM was re-evaluated with the freedom to optimize the locations δ_v and δ_o and the values of D_v and D_o. However, the model was constrained such that the vegetation penetration distance could not exceed the vegetation interface and the open channel penetration distance could not fall below the interface location.

Figure 6.13 provides examples of the best fit concentration distributions predicted for the 7.35 l/s cases. The goodness of fit for the unconstrained triangle function is an improvement on the constrained triangle OFDM. In the high and low density artificial vegetation the mean goodness of fit, in terms of R^2 is 0.9777 and 0.9698 (compared to 0.9349 and 0.9378 for the constrained), respectively, suggesting that the unconstrained triangle is appropriate for predicting the downstream concentration distributions of ideal vegetation. In the winter *typha*, the average goodness of fit improved from the constrained to unconstrained functions from R^2 = 0.9305 to 0.9664. There was significant improvement in the downstream predictions in the summer *typha* where the mean R^2 was 0.4733 – compared to 0.0569 in the constrained optimization.

The unconstrained triangle OFDM predicts peak transverse mixing to occur at the vegetation interface for both artificial vegetation types (Figure 6.14a & b). The model does not, however, provide solutions to the best fit profile $D_y(y)$ that support the mixing penetration distances estimated from the transverse velocity profiles. For the high density type, the 3.35 l/s case provides a step best-fit profile of D_y; and in the 5.25 l/s cases the profile predicts δ_v = 0 m. However, in the 6.35 and 7.35 l/s case, $D_y(y)$ resembles the profiles optimized using the constrained triangle where t_{ml} is 0.37 and 0.44 m, respectively.

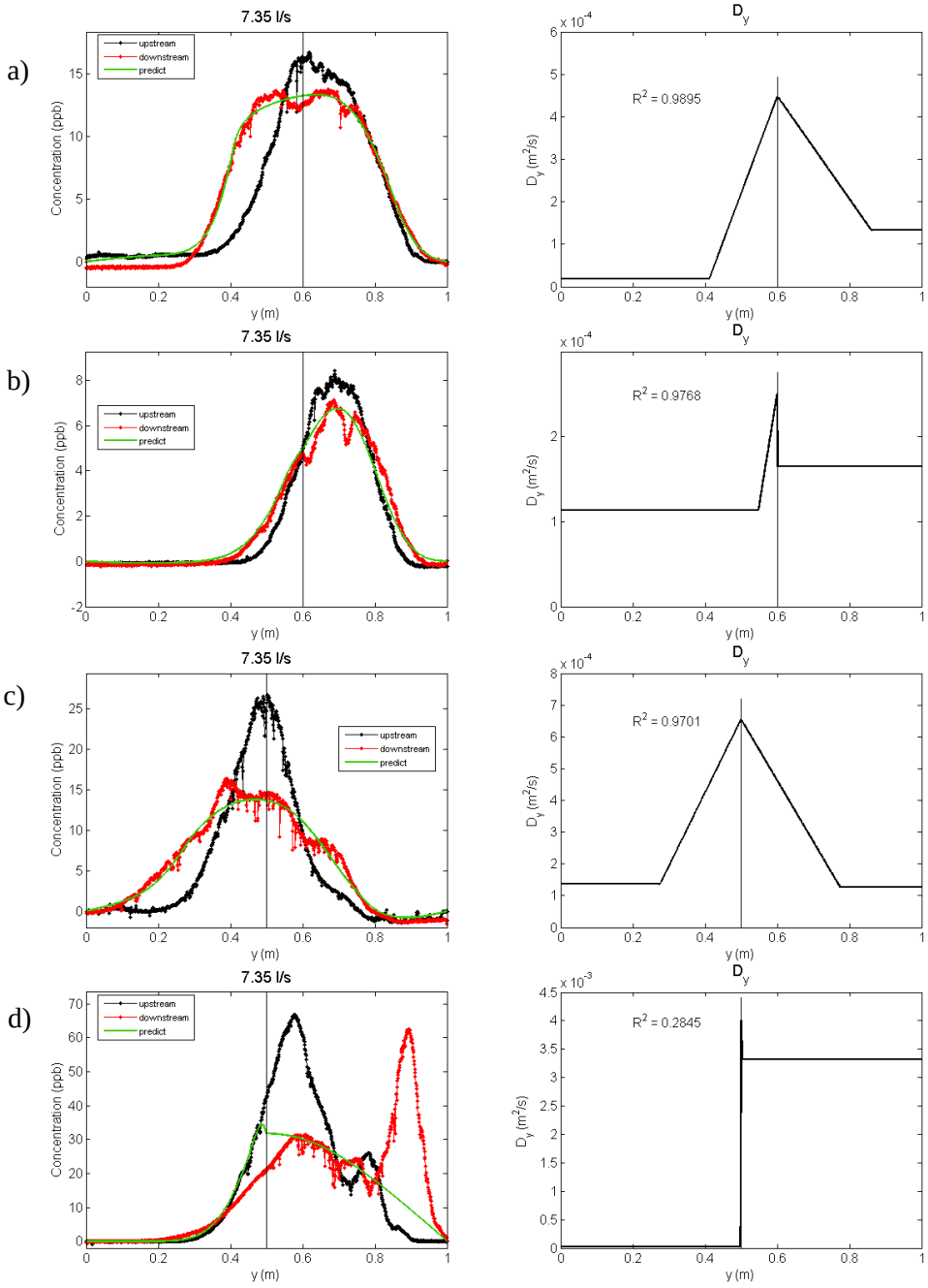

Figure 6.13: Best fit concentration predictions and the optimal profiles of $D_y(y)$ using the unconstrained triangular OFDM for the a) high and b) low density artificial and c) winter and d) summer *typha* vegetation for the 7.35 l/s case.

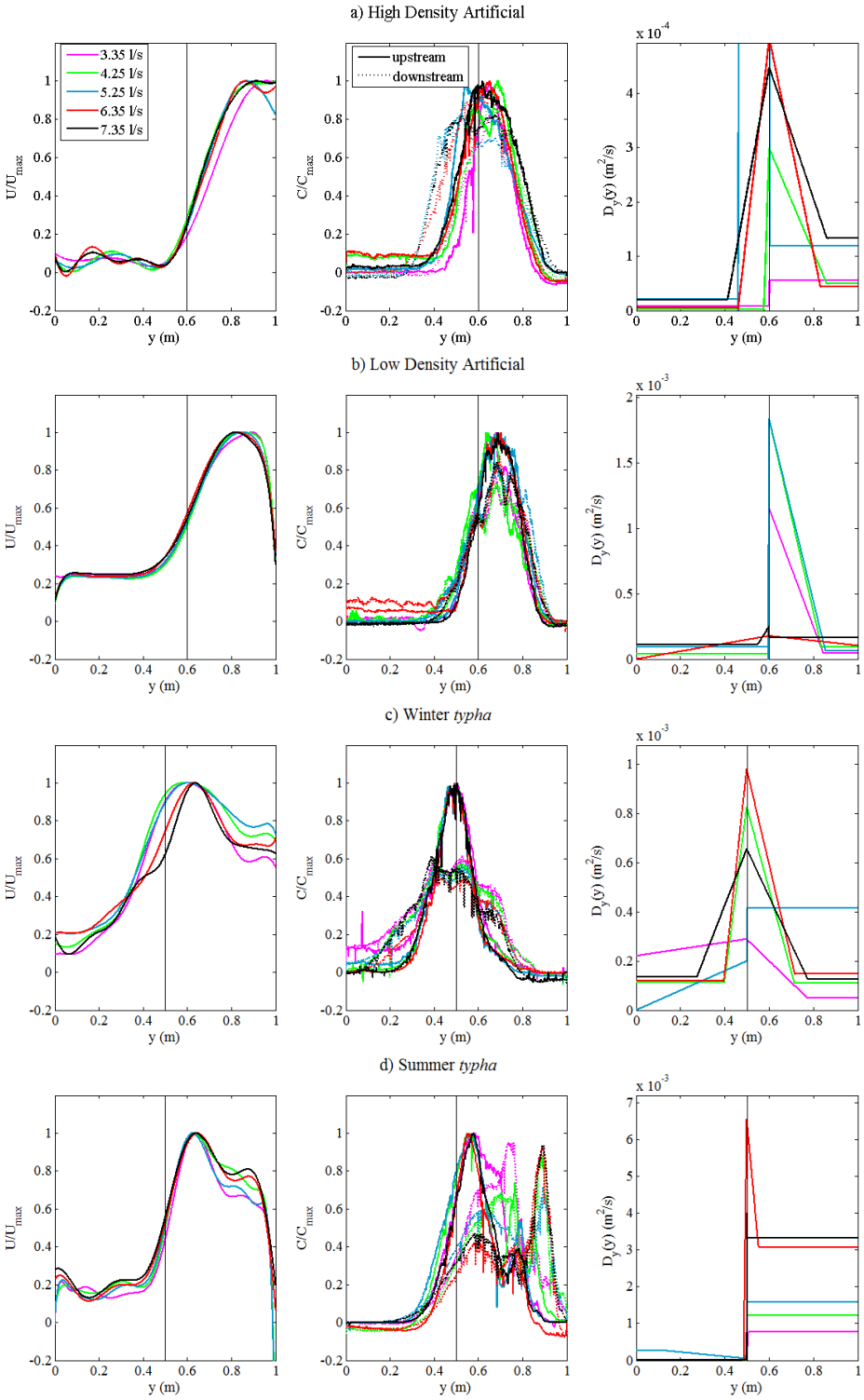

Figure 6.14: Unconstrained triangle OFDM best fit profiles of $D_y(y)$ are plotted with normalized $U(y)/U_2$ and $C(y)/\max C(y)_{upstream}$ for the a) high and b) low density artificial vegetation and c) winter and d) summer *typha* types.

Figure 6.14 compares the optimized profiles of $D_y(y)$ with the normalised longitudinal velocity profiles and the measured concentration distributions. In the low density cases, the

model optimizes the vegetation penetration distances at approximately the interface – and for the 6.35 l/s case δ_v is predicted at the vegetation boundary $y = 0$. The model optimizes three profiles that resemble the unconstrained triangle OFDM for the winter *typha* (4.25, 6.35 and 7.35 l/s); predicting the mixing layer width of 0.215, 0.216 and 0.273 m. The 3.35 l/s case predicts there to be greater mixing within the vegetation than the open channel while the 5.25 l/s case optimizes an approximate step profile.

The trend in peak mixing coefficient does not concur with Ghisalberti and Nepf (2005) (Figure 6.15a), where D_{peak} fails to match the trend $D_{peak} = 0.02\Delta U t_{ml}$ for a given vegetation type. Note that the value of t_{ml} was calculated given the optimised locations δ_v and δ_o ($t_{ml} = \delta_v + \delta_o$). Secondly, the function does not provides normalised results in the artificial vegetation that agree with Okamoto et al. (2012) (Figure 6.15b) who confirmed that D_{peak}/UW increases with solid volume fraction. Here $D_{peak}/UW = 0.018$ and 0.027 for $\Phi = 0.02$ and 0.005 for the high and low density artificial. However, an agreement is made for the *typha* vegetation where $D_{peak}/UW = 0.045$ and 0.065 for $\Phi = 0.012$ and 0.037.

It should be stressed that the best fit profiles for the summer *typha*, although an improvement on the constrained function, predominantly resemble the profiles for the discontinuity optimization. However, the concentration profiles within the open channel are better predicted using the unconstrained triangle approach. This approach yields the best prediction of the downstream concentration distribution compared to any method used, so far, giving large values of R^2 for the high and low density artificial and winter *typha* vegetation. The profiles of $D_y(y)$ using the unconstrained triangle are not as physically reliable as the constrained equivalent; where the relations between D_{peak} and $\Delta U t_{ml}$ do not conform with published findings.

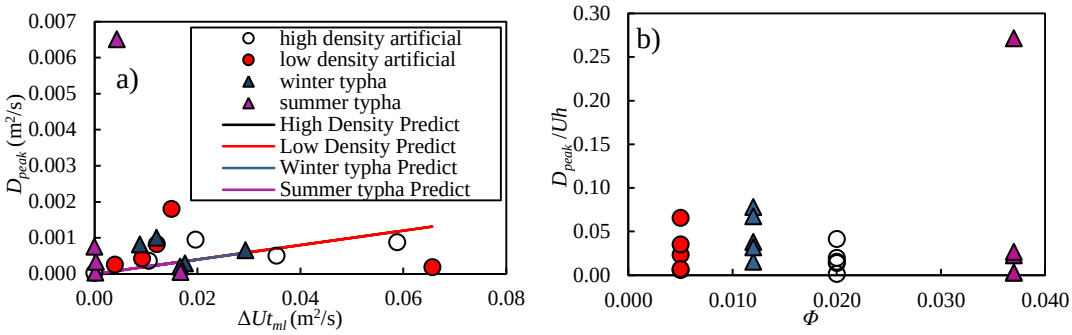

Figure 6.15: Peak transverse mixing coefficient using the unconstrained triangle OFDM are compared to a) predictions using Ghisalberti and Nepf (2005) and b) solid volume fraction, Φ.

6.3.2 Unconstrained Gaussian mixing function

The values of D_v, D_o, δ_v and δ_o were unconstrained for the Gaussian function demanding a 7 parameter optimization with the inclusion of the spread, magnitude and displacement of the Gaussian component. For the high density artificial cases, there was, on average, an improvement in the goodness of fit, compared to the constrained function, from 0.9702 to 0.9747; however, a reduction was observed for the low density of 0.9702 to 0.9618. In the winter and summer *typha* cases the fit increased compared to the constrained function from 0.9603 and 0.1012 to 0.9762 and 0.1500.

The predicted values of D_{peak} using Ghisalberti and Nepf (2005) are of the same order of magnitude as the optimal values (Figure 6.16a); however, the trend for the artificial vegetation does not confirm the predictions. The unconstrained Gaussian OFDM does provide a scaling between D_{peak} and ΔUt_{ml} of 0.0043 and is similar to that provided by the constrained triangular function (0.0056). Figure 6.16b shows agreement with Okamoto et al. (2012) for the high density artificial and the *typha* vegetation where the normalised transverse mixing coefficient scales with the solid volume fraction with $D_{peak}/UW = 0.018$ ($\Phi = 0.02$), 0.048 ($\Phi = 0.012$) and 0.092 ($\Phi = 0.037$); however, D_{peak}/UW increased in the low density to 0.021 (for $\Phi = 0.005$). The increase in normalised peak transverse mixing coefficient from winter to summer for an increase in solid volume fraction of the *typha* vegetation confirms that mixing in the shear layer region is enhanced by increased vegetation density.

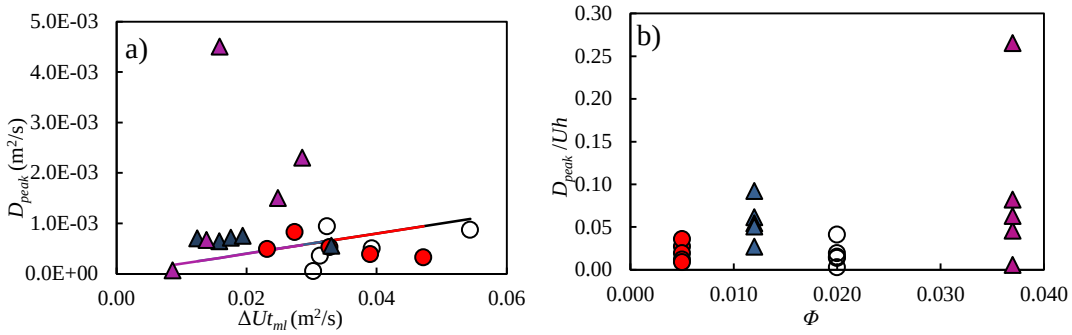

Figure 6.16: Unconstrained Gaussian OFDM normalisation results. a) The measured and predicted, using Ghisalberti and Nepf (2005), values of D_{peak} are compared. b) D_{peak}/Uh is compared to solid volume fraction, Φ.

Figure 6.17 gives examples of the best fit predicted concentration distributions showing the improved predictive capabilities of the unconstrained Gaussian function for the 4.25 l/s cases. The unconstrained Gaussian OFDM is better at predicting downstream concentration than the unconstrained triangular function for all types except for the summer *typha* (Figure 6.17d). The Models freedom to find the optimal locations of the mixing penetration distances allows for a comparison to the constrained Gaussian OFDM. Figure 6.18 provides the normalized velocity profiles and concentration distributions and the optimal profiles of $D_y(y)$ for the 4x vegetation types.

In general, the model provides best fit profiles that resemble the expected of $D_y(y)$ described in the Analysis Chapter (Figure 5.24); where the similarity in mixing coefficients and vortex penetration distances confirm that mixing in artificial vegetation can be characterised using a three-zone description. There is a clear constant value of D_y within the vegetation and open channel and distinct peak in the region of the interface. The strong fitting supports these conclusions.

In the winter *typha* the model provides optimal functions that justify shear layer theory. The optimal solutions for the summer *typha* also show a tendency for the model to produce step-like functions. However, the discontinuity seen between the vegetation and open channel regions demonstrates the model's propensity to provide not physical solutions – most apparent in the summer *typha* cases.

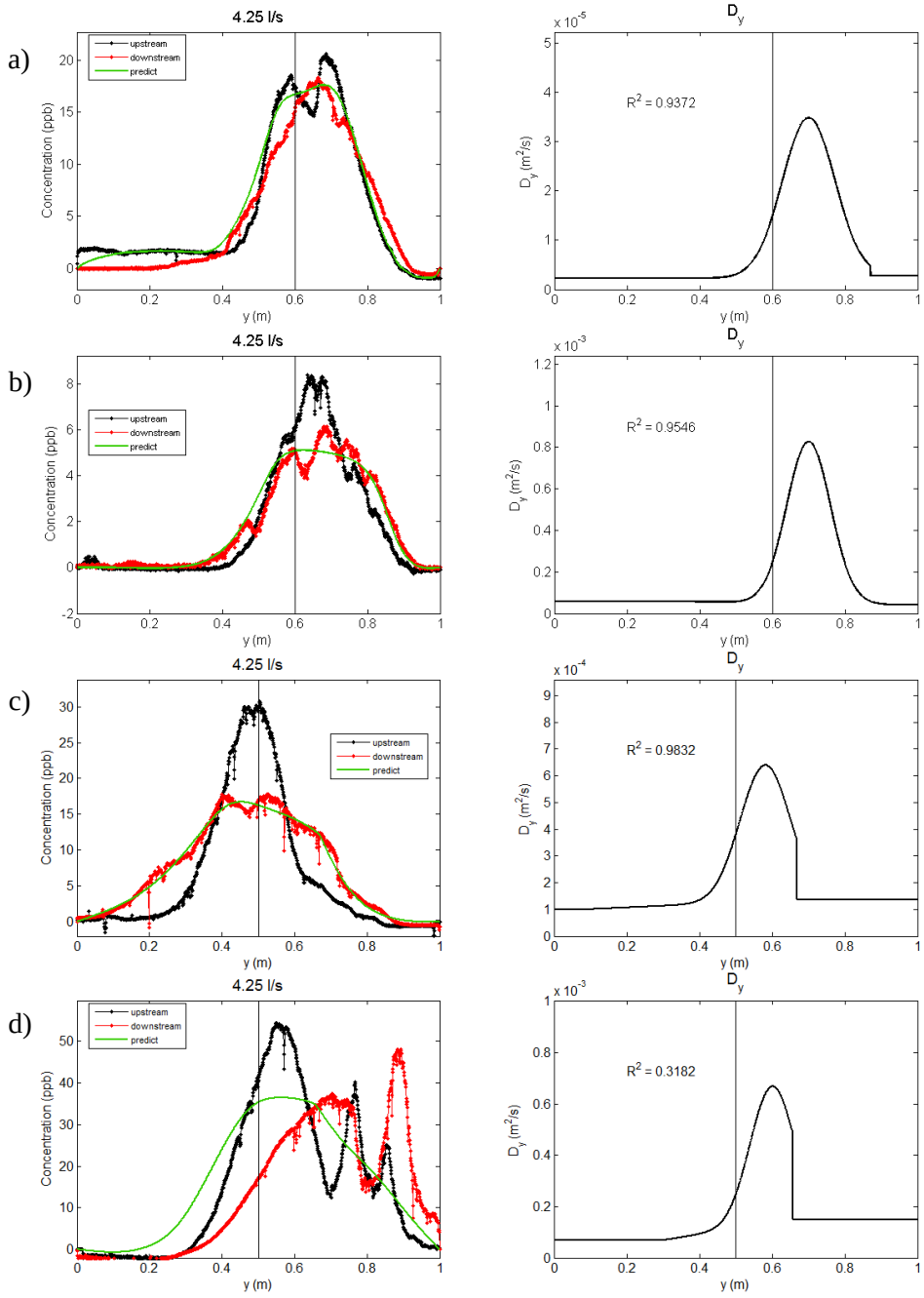

Figure 6.17: Best fit concentration predictions and the optimal profiles of $D_y(y)$ using the unconstrained Gaussian OFDM for the a) high and b) low density artificial and c) winter and d) summer *typha* vegetation for the 4.25 l/s case.

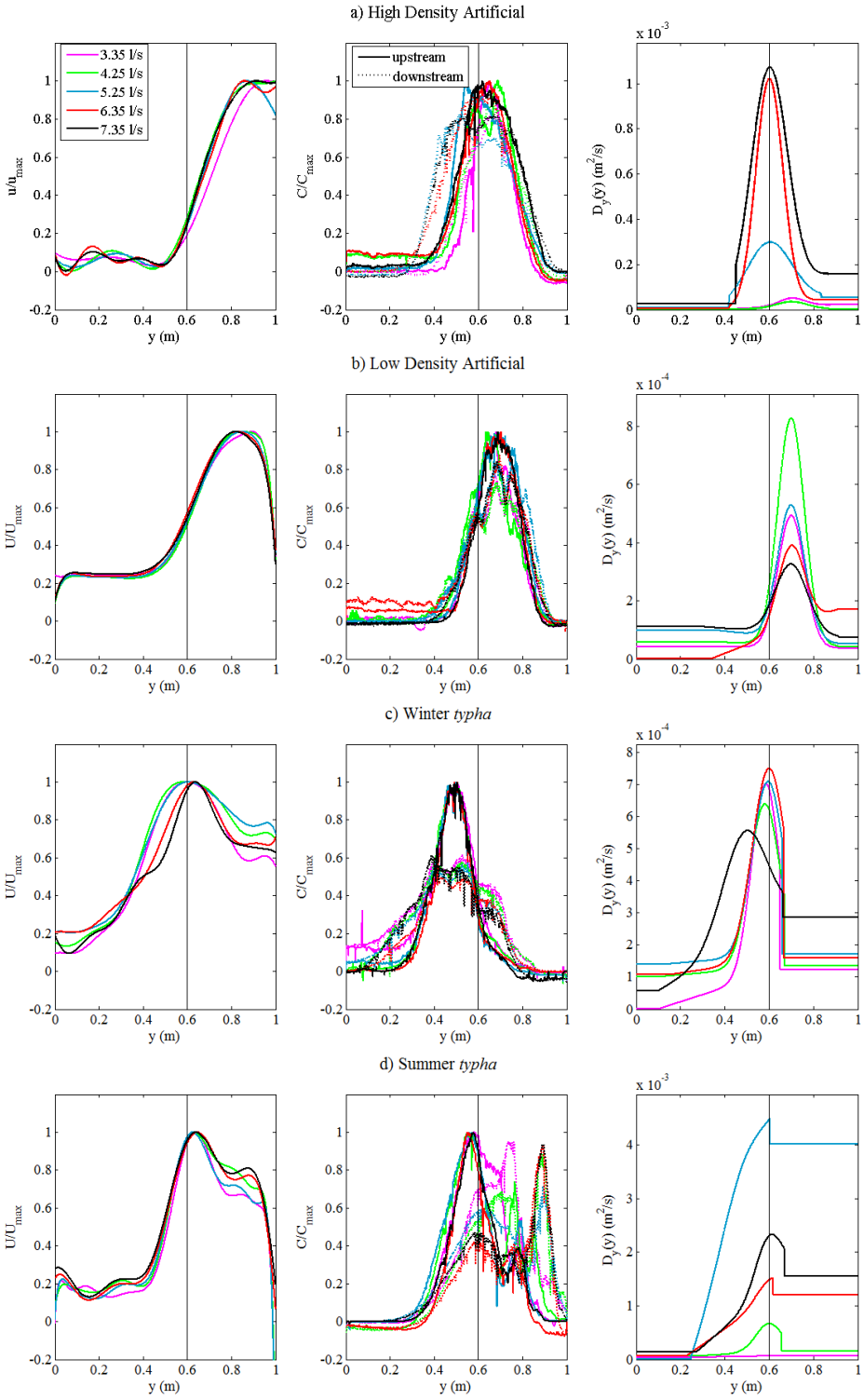

Figure 6.18: Unconstrained Gaussian OFDM best fit profiles of $D_y(y)$ are plotted with normalized $U(y)$ and $C(y)$ for the a) high and b) low density artificial vegetation and c) winter and d) summer *typha*.

Vegetation shear layer theory is, qualitatively, confirmed in Figure 6.19 comparing the unconstrained triangle and Gaussian functions; where peak mixing is located within the defined mixing region – indicating that the unconstrained OFDM provides physically

meaningful results. The optimal peak locations for the high density artificial vegetation agrees with the locations of maximum turbulence shown above in Figure 6.12 and are closer to the interface than the low density cases. Peak transverse mixing is also located in the mixing layer region for the *typha* vegetation although the Gaussian function predicts the location of peak mixing further into the open channel than the triangular function. The application of an unconstrained function has not before been used to describe the lateral variation in transverse mixing coefficient.

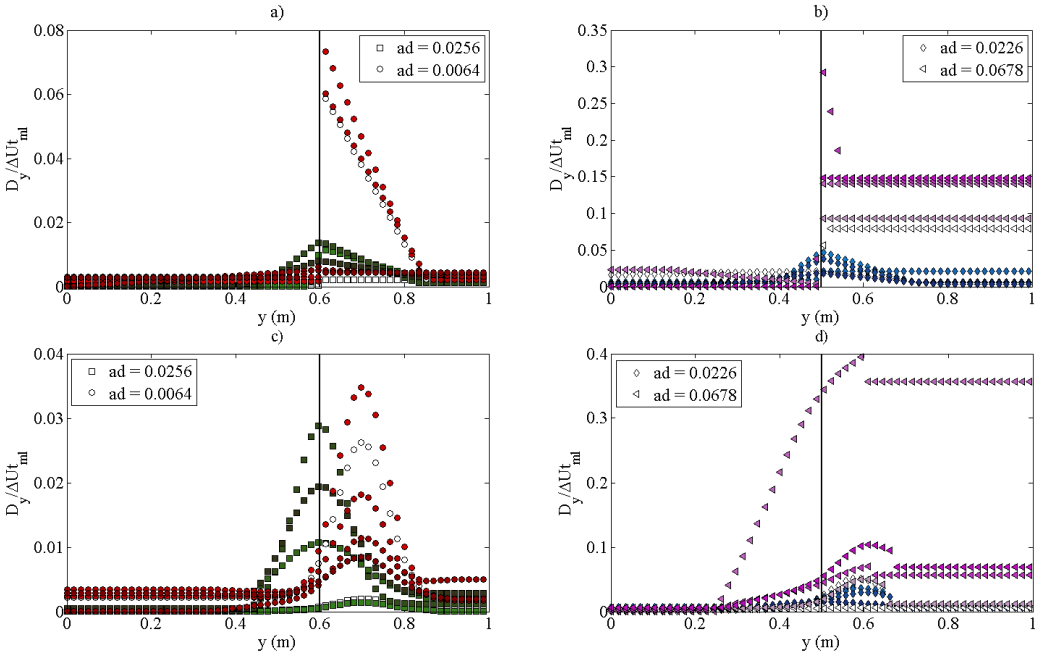

Figure 6.19: Optimal, non-dimensionalised profiles of $D_y(y)$ using the unconstrained triangle function for the a) artificial and b) *typha* vegetation and the unconstrained Gaussian functions for c) artificial and d) *typha* vegetation. The high and low density artificial and winter and summer *typha* are given by the squares, circles, diamonds and triangles, respectively.

6.3.3 Multi-zonal mixing function

The final mixing function evaluation was to discretize the channel into ten mixing zones, each with a prescribed value of D_y and represents a novel approach to the quantification of spatially variable transverse. The Finite Difference Model was employed such that the value of D_y in

each zone, D_n where n is the zone number, could be optimized to find the best fit downstream concentration distribution and appropriate form of $D_y(y)$[13].

Figure 6.20 shows the best fit concentration distributions and corresponding optimal profiles $D_y(y)$ for the 3.35 l/s case for the 4x vegetation types. The downstream profiles are well predicted in the examples given, showing a good match between peak concentration and the profile gradients. The ten zone OFDM provides the best predictions of the downstream concentration distributions for of all the optimization functions with an average goodness of fit for the high density, low density, winter and summer *typha* of R^2 = 0.9860, 0.9795, 0.9859 and 0.6669. Figure 6.21 provides the optimal profiles of $D_y(y)$ calculated for all cases in the 4x vegetation types (where Appendix VI provides the best-fit downstream concentration distributions). The model confirms that D_{peak} occurs in the vicinity of the interface and is significantly greater than the mixing within the vegetation and open channel.

The form of the optimal profiles shows similarities to those given by the unconstrained triangular and Gaussian functions. There is a distinct peak mixing in the vicinity of the interface; while D_y is smaller in the open channel and insignificant within the vegetation. However, the model does not confirm the expectation that D_{peak} increases with channel discharge suggesting that the optimal profiles of $D_y(y)$ may be non-physical.

In the high density artificial vegetation, the model predicts that y_{peak} is located closer to the interface than the low density; where $y_{peak} \approx 0.62$ m and 0.7 m, respectively for the two types. This shows agreement with the constrained Triangle and Gaussian OFDMs providing reliability to the new model. The relative magnitude of D_{peak} compared to the vegetation and open channel regions is larger for the new model than the triangular or Gaussian; implying further that the unconstrained nature of the optimization may permit non-physical solutions to be found.

[13]Note that the discretization of the channel was non-linear such that the interface region could be described with a higher resolution than the transverse limits of the distribution.

Successful predictions of concentrations in the winter *typha* where the goodness of fit ranged from 0.9807 to 0.9914 for the 7.35 and 6.35 l/s cases, respectively. The optimal profiles of $D_y(y)$ show that peak mixing is located at the vegetation interface and agree well with the results given by both the unconstrained functions. The model is more successful at predicting concentrations in the summer *typha* cases where the goodness of fit ranged from 0.4511 to 0.8819. The freedom to optimize D_y at a number of locations results in more accurate predictions of the non-classical downstream concentration distributions. The optimal profiles of $D_y(y)$ indicate that mixing associated with the shear layer is not as dominant as the other vegetation types, where the peak mixing in the 3.35, 4.25 and 5.25 l/s cases is less well defined than the other types. Similarly to the unconstrained functions, the optimal profiles in the 6.35 and 7.35 l/s cases resemble step profiles.

As stated above, one must always consider the physical meaning of evaluating a model using a goodness of fit parameter. While the ten zones OFDM provides strong predictions of the downstream concentrations, it does not necessarily allow the user to give precise conclusion about the nature of the hydrodynamics within the mixing zone. That said, qualitatively, the ten zone OFDM does provide sound support for the conventional wisdom that mixing is most significant in the region of the shear layer vortices and in the vicinity of the interface. There is also potential for evaluation or confirmation of analytical or computation fluid-dynamic models using this multi-zonal FDM analysis.

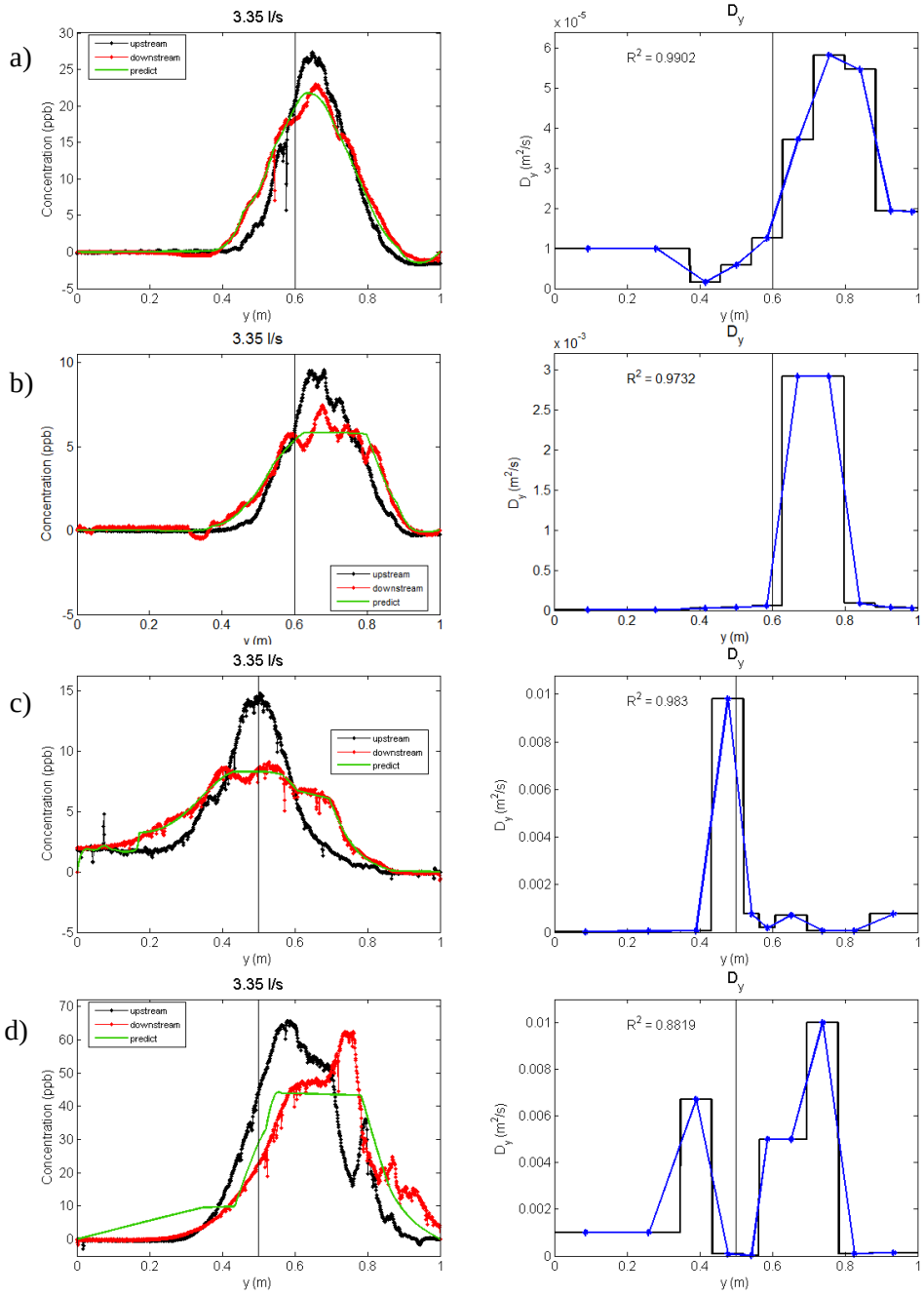

Figure 6.20: Best-fit downstream concentration distributions and optimal profiles of $D_y(y)$ for the 3.35 l/s case for the four vegetation type using the ten zone OFDM for the a) high and b) low density artificial and c) winter and d) summer *typha* types.

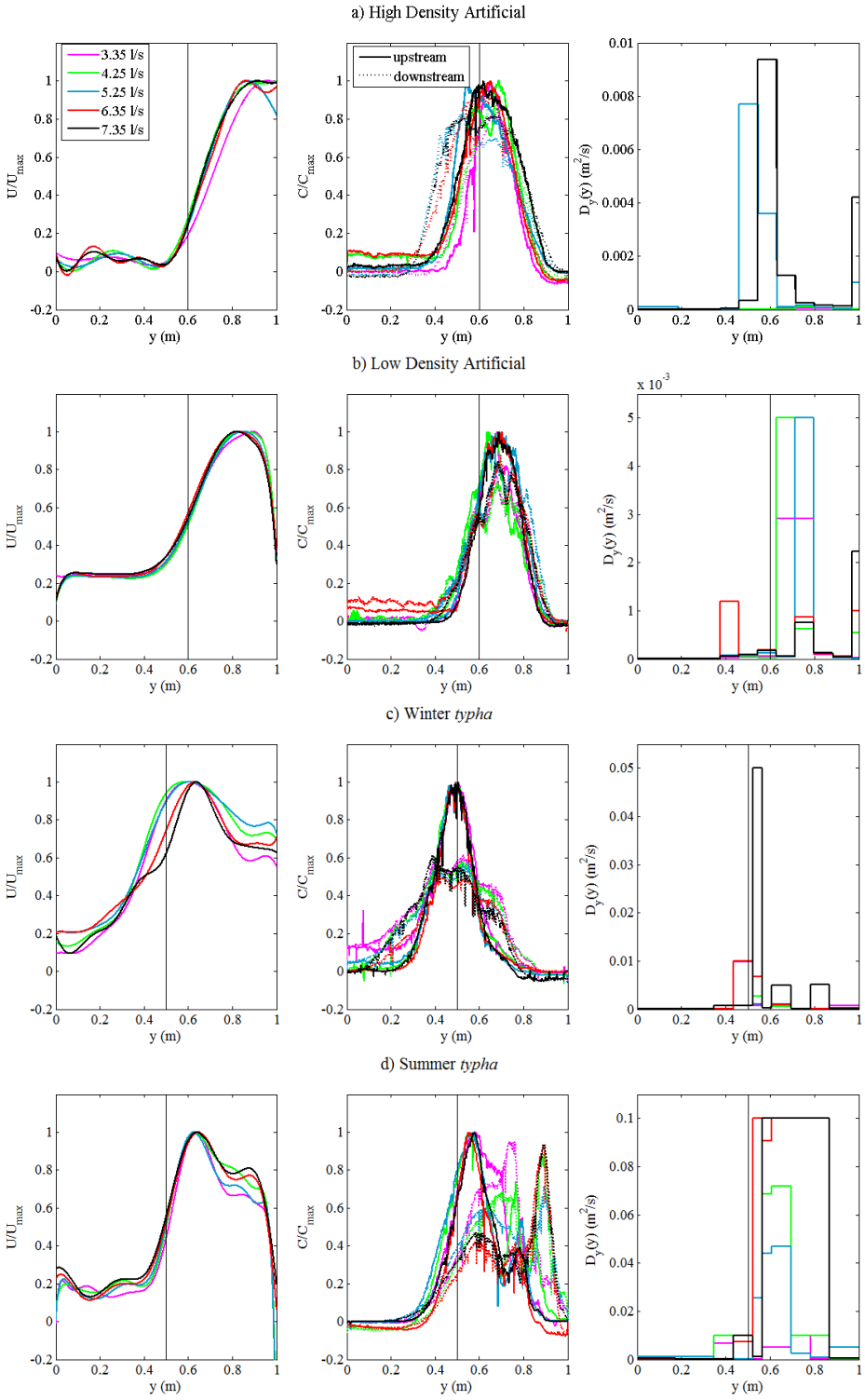

Figure 6.21: Best fit profiles of $D_y(y)$ for the 10 zone OFDM for the a) high and b) low density artificial vegetation and c) winter and d) summer *typha*.

6.4 Finite Difference Model – Conclusion

Figure 6.22 compares the goodness of fit values calculated for all optimization functions applied using the FDM – where Tables 6.5-6.8 provide the corresponding information. In general, as expected, the ten zone OFDM (cross) provides the best predictions of downstream concentration. The function's versatility allows it to create non-physical forms ensuring that R^2 is maximized. The unconstrained triangle (star) and Gaussian functions (circle) also yield good predictions – the results of which have a stronger physical bearing, in the artificial cases, than the ten zones. The constrained triangular (triangle) and Gaussian (diamond) OFDM also yield good predictions where the goodness of fit is comparable to the 10 zones and unconstrained functions for all but the summer *typha* types. The mean goodness of fit, R^2, for all artificial vegetation cases for the various functions is:

- Constant: 0.9278;
- Step: 0.9429;
- Triangle: 0.9581;
- Gaussian: 0.94106;
- Unconstrained Triangle: 0.96832;
- Unconstrained Gaussian: 0.9737;
- Ten zone: 0.9791.

The predictive success of the triangular model and, to an extent, the Gaussian function confirm the functional nature of $D_y(y)$ in the homogeneous, artificial vegetation – with near constant mixing within the vegetation and in the extreme limits of the open channel region, and heightened mixing in the vicinity of or at the interface where shear layer turbulence dominates (Figure 6.12). The general form of $D_y(y)$ was confirmed when applying the unconstrained functions – where the subsequent increase in R^2 for both the triangular and Gaussian models supports the three mixing region hypothesis in the artificial vegetation.

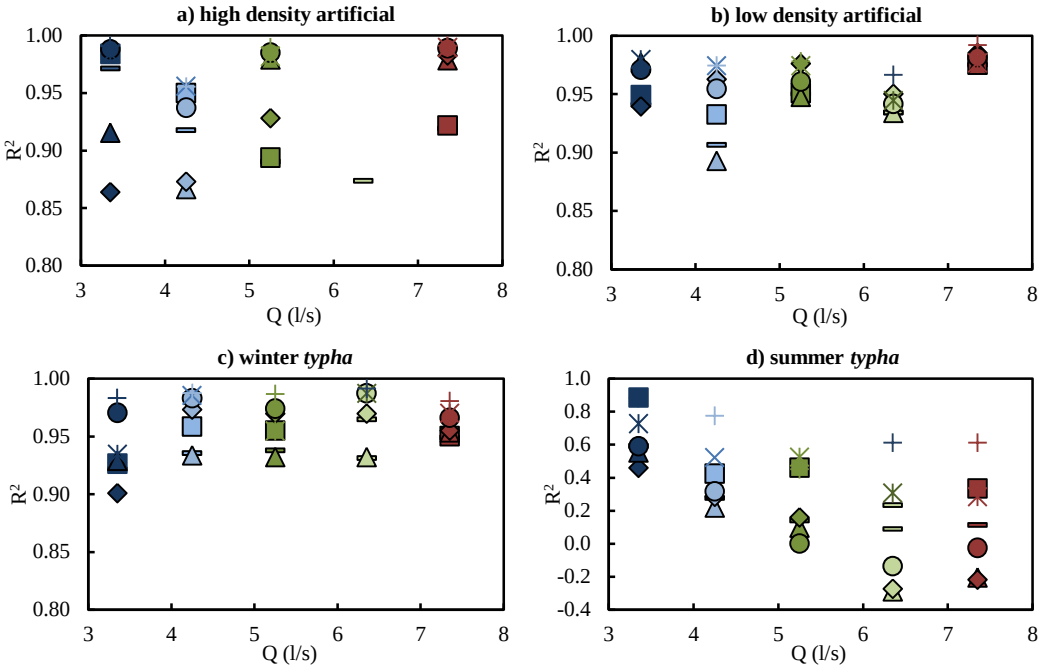

Figure 6.22: Goodness of fit, given as an R^2 value, for the line (bar), step (square), triangular (triangle), Gaussian (diamond), unconstrained Gaussian (circle), unconstrained triangle (star) and 10 zone (cross) Finite Difference Model optimization functions for the 5x experimental discharges recorded for each vegetation type.

However, the model's limited success for the *typha* cases –when compared to the artificial cases – suggests that the application of idealized functions to real vegetation is less reliable when characterizing mixing. The mean goodness of fit, R^2, for all *typha* cases for the various functions is:

- Constant: 0.5889;
- Step: 0.7093;
- Triangle: 0.4937;
- Gaussian: 0.5307;
- Unconstrained Triangle: 0.7198;
- Unconstrained Gaussian: 0.5631;
- Ten Zone: 0.8264.

All of the optimization models managed to provide acceptable predictions for the winter *typha*; where the near-classical concentration profiles facilitated effective optimizations and yield a minimum R^2 value of 0.9009. However, the skewed and dissociated concentration

profiles measured in the summer *typha* did not allow the physically constrained models to successfully predict downstream concentrations.

The relative success of the line and step functions over the triangular and Gaussian and their comparable predictability to the unconstrained functions suggests that mixing associated in real shear layer *typha* can be predicted using step, or near-step, approximations of $D_y(y)$. This conclusion is most noticeable in the summer *typha* where the step OFDM yields the second largest average value of R^2 after the unconstrained triangle. Furthermore, the step OFDM also provides successful predictions in the summer *typha* cases (mean $R^2 = 0.9510$) that are comparable to those predicted using the unconstrained Gaussian model (mean $R^2 = 0.9603$).

The success of the step OFDM for the *typha* cases is potentially attributed to the increased bed shear from the real bed – contributing a comparable amount to overall mixing when compared to the shear layer. As such, characteristic heightened mixing in the whole open channel region – as a combination of interfacial and bed shear – is potential more practical as a tool for prediction retention times and concentration distributions in real vegetation.

Finite difference model limitations

The finite difference model is a numerical approach that predicts the concentration distribution at every specific node from the upstream to downstream measured distributions. As such, it is limited in firstly, the resolution in the number of computational nodes and in the transfer functions between nodes – in this analysis the distributions were transferred in a Gaussian fashion from one node to the next – this approach may be an approximation for the real vegetation; and secondly, the model cannot account for lateral advection phenomena whereby any dye is distributed according to lateral velocity events – such as sweeps and ejections. However, the resolution analysis in Section 5.2.3 showed that the model was quite

insensitive to the longitudinal discretization – where, for the analysis of an analytical solution, the coefficient of fit, R^2, remained above 0.98 for 0.1 m longitudinal spacing.

The OFDM also relies on the accurate and representative input of a mean profile of stream-wise velocity. In this analysis, $U(y)$ was input with a Fourier fitted profile that reduces the local fluctuations due to stems wakes. The fitted profile, although successful at describing the raw velocity distribution, is not an exact representation of the velocity field and may limit the accuracy of the FDM.

Finally, the real vegetation was assumed to exhibit the same hydrodynamic features as the homogeneous, artificial vegetation. The *typha* was characterised by numerous clumps of stems and, while similar in terms of stem population density per unit area, had more noticeable sparse regions void of any stems. The interaction between the unpopulated regions and the clumps may have induced local, small scale shear mixing. The non-classical nature of the transverse velocity profiles supports this suggestion where locations of heightened velocity within the vegetation may generate large scale turbulence.

Table 6.5: High Density artificial vegetation R^2 values for the various optimization functions in the partial vegetation scenario.

Goodness of fit (R^2) High Density Artificial							
Q (l/s)	*Line*	*Step*	*triangle*	*Gaussian*	*Free Gaussian*	*Free triangle*	*10 parameter*
3.35	0.9712	0.9839	0.9155	0.8639	0.9879	0.9839	0.9902
4.25	0.9175	0.9498	0.8666	0.873	0.9372	9557	0.9555
5.25	0.8905	0.8939	0.9791	0.9281	0.9850	0.9817	0.9895
6.35	0.8738	-	-	-	-	-	-
7.35	0.9192	0.9219	0.9784	0.9825	0.9889	0.9895	0.991
mean	**0.9144**	**0.9373**	**0.9349**	**0.9118**	**0.9747**	**0.9777**	**0.9815**

Table 6.6: Low Density artificial vegetation R^2 values for the various optimization functions in the partial vegetation scenario.

Goodness of fit (R^2) Low Density Artificial							
Q (l/s)	*Line*	*Step*	*triangle*	*Gaussian*	*Free Gaussian*	*Free triangle*	*10 parameter*
3.35	0.9409	0.9492	0.9395	0.977	0.971	0.9797	0.9732
4.25	0.9063	0.9324	0.8929	0.9627	0.9546	0.974	0.9744
5.25	0.9502	0.9510	0.9477	0.9761	0.9608	0.9743	0.978
6.35	0.9341	0.9343	0.9340	0.9502	0.9415	0.9446	0.9664
7.35	0.9751	0.9758	0.9752	0.9852	0.9815	0.9768	0.992
mean	**0.9413**	**0.9485**	**0.9378**	**0.9702**	**0.9618**	**0.9698**	**0.9768**

Table 6.7: Winter *typha* vegetation R^2 values for the various optimization functions in the partial vegetation scenario.

Goodness of fit (R^2) Winter *typha*							
Q (l/s)	*Line*	*Step*	*triangle*	*Gaussian*	*Free Gaussian*	*Free triangle*	*10 parameter*
3.35	0.9218	0.9265	0.9009	0.929	0.9706	0.9347	0.983
4.25	0.9353	0.9583	0.9337	0.9733	0.9832	0.9853	0.9877
5.25	0.9380	0.9551	0.9322	0.9698	0.9742	0.9548	0.9867
6.35	0.9313	0.9649	0.9322	0.9746	0.9872	0.9874	0.9914
7.35	0.9491	0.9503	0.9536	0.9551	0.9662	0.9701	0.9807
mean	**0.9351**	**0.9510**	**0.9305**	**0.9603**	**0.9762**	**0.9664**	**0.9859**

Table 6.8: Summer *typha* vegetation R^2 values for the various optimization functions in the partial vegetation scenario.

Goodness of fit (R^2) Summer *typha*							
Q (l/s)	*Line*	*Step*	*triangle*	*Gaussian*	*Free Gaussian*	*Free triangle*	*10 parameter*
3.35	0.5936	0.8866	0.460	0.5532	0.5917	0.7279	0.8819
4.25	0.2759	0.4231	0.2195	0.2845	0.3182	0.5205	0.776
5.25	0.1408	0.4609	0.0980	0.1596	0.0017	0.5254	0.4511
6.35	0.0894	0.2337	-0.2885	-0.2733	-0.1365	0.3083	0.613
7.35	0.1139	0.3345	-0.2044	-0.2179	-0.0247	0.2845	0.6128
mean	**0.2427**	**0.4677**	**0.0569**	**0.1012**	**0.1500**	**0.4733**	**0.6669**

7. Conclusion

The aim of this research was to characterize the lateral variation in transverse mixing associated with shear layer real, seasonal vegetation in a manner that could be accessibly utilised by practitioners. Fundamental to this approach was the necessity to assess the application of shear layer hydrodynamic theory – developed in homogeneous, idealized vegetation – to real vegetated shear flows.

Homogeneous artificial and heterogeneous real vegetation were compared using detailed velocity and steady-state tracer concentration profiles. Controlled experimentation using naturally cultivated Cattail reeds (*Typha latifolia*) in an emergent partially vegetated scenario was conducted to allow for a comparison between four vegetation types – high and low density artificial stems and summer and winter season *typha*. Firstly, tracer experiments in artificial vegetation verified current theoretical understandings of mixing in vegetated shear layers and provided validation for the use of a finite difference model (FDM) to analyse the spatially variable transverse mixing coefficient, $D_y(y)$.

Secondly, a range of physically justified and constrained input functional forms of $D_y(y)$ were optimised using the FDM. Predictions of concentration were successfully made using constrained triangular and Gaussian forms in the artificial and winter *typha* types; confirming that peak transverse mixing is enhanced by the shear layer vortices. Poor predictions were made, however, for the summer *typha* where the dissociation in the concentration profiles could not be predicted with the current understandings of shear layer.

The goodness of fit (R^2) of the predicted concentrations using the constrained triangle and Gaussian forms is 0.9349 and 0.9702 for the high and low density artificial types, respectively. The application to winter season *typha* is successful (mean $R^2 = 0.9501$) and is

attributed to the similarity in stem density and morphology to the artificial vegetation. The model is not successful in the summer season where the goodness of fit for the constrained triangular and Gaussian functions is 0.0569 and 0.1012, respectively.

The lateral variation in transverse mixing is reported for real *typha* vegetation. A new relation between the peak transverse mixing coefficient, D_{peak}, and the product of velocity shear, ΔU and the width of the mixing layer, t_{ml}, is $D_{peak} = 0.0056\Delta U t_{ml}$. The relative magnitude of peak transverse mixing is reduced in real vegetation as the increased bed shear and local shear layer phenomena increase mixing in the open channel and vegetation regions, respectively.

A novel application of the optimised FDM was made to extend physical understandings by unconstraining the physical restraints imposed on the transverse mixing optimisation function. Unconstraining the vortex penetration limits and the magnitude of the transverse mixing in the vegetated and open channel zones for the artificial vegetation gives similar profiles of transverse mixing coefficient to the constrained functions; where peak mixing occurs in the vicinity of the vegetation interface and mixing can be characterised into three regions. The similarity in goodness of fit provides justification for the process where the mean $R^2 = 0.9777$ and 0.9698 for the high and low density types, respectively. The profile forms optimized using the unconstrained triangular, Gaussian and 10 zone functions support previous studies conducted in vegetated shear layers (e.g. Ghisalberti and Nepf, 2005; Okamoto et al., 2012; Zeng et al., 2008).

Here the application of unconstrained optimisation functions to real *typha* vegetation provides a small increase in the FDM's predictive capabilities. In the winter season the unconstrained Gaussian function increases the goodness of fit from 0.9603, for the constrained function, to 0.9762. While, in the summer season, the average value of R^2 increases from 0.1012 to only 0.1500 – although the unconstrained triangular functions yields $R^2 = 0.4733$. It is shown that, through comparisons with other functions, the unconstrained optimisations functions are not significantly more effective than a simple two-zone model of

transverse mixing. The goodness of fit for the winter and summer seasons using the two-zone function is 0.9510 and 0.4677, respectively and is comparable to value provided by the unconstrained functions.

The optimization of the FDM using 10 independent, discrete zones to describe $D_y(y)$ provides the best predictions of concentration, where R^2 = 0.9815, 0.9768, 0.9859 and 0.6669 for the high and low density artificial and winter and summer *typha* types, respectively. The 10 zones model also confirms that transverse mixing in shear layer vegetation is dominated by interfacial shear layer vortices and exhibits peak mixing in the vicinity of the interface. However, from inspection, the potentially non-physical solutions that the 10 zone model provided lead to the conclusion that such a model is applicable for qualitative comparisons only.

In conclusion, the success in the prediction of concentrations using both the constrained and unconstrained triangular and Gaussian optimization functions in the artificial vegetation confirms current shear layer hydrodynamic understandings that transverse mixing is dominated by shear layer vortices. Mixing far into the vegetation and the open channel is approximately spatially constant and is set by mechanical mixing at the stem scale and bed shear, respectively. In the shear layer region, vortices created by a velocity inflection, increase the degree of mixing relative to the constant zones. It has been shown that, while shear layer mixing is dominant in the artificial vegetation, the shear layer's contribution to overall mixing in the real *typha* vegetation is comparable, in magnitude, to the mixing associated with the vegetation and open channel regions.

The results show that, using a goodness of fit quantification, the simple two-zone model of $D_y(y)$ for the vegetated and open channel regions predicts downstream concentrations in real vegetation to a degree comparable to the more complex optimization functions. In the winter season, the step model yields an average goodness of fit of 0.9510 (where the 10 zone model yields R^2 = 0.9859) and in the summer season concentrations are predicted with R^2 = 0.4677 (where the 10 zone OFDM yields R^2 = 0.6669). In the summer season the step model yields

the 3rd largest goodness of fit behind the ten zone and the unconstrained triangular function (R^2 = 0.4733). The predictive capabilities and simplicity of the step OFDM make it more suitable over complex hydrodynamic models for use by practitioners and can readily be implemented on a spreadsheet format – increasing accessibility and potential for quantifying mixing in a wider range of real vegetation species.

Bibliography

ARNELL, N. W. 1999. The effect of climate change on hydrological regimes in Europe: a continental perspective. Global environmental change, Vol. 9, issue 1, pp. 5-23.

ARNELL, N. W. 2004. Climate change and global water resources: SRES emission and socioeconomic scenarios. Global Environmental Change, Vol. 14, pp. 31-52.

ARNELL, N. W. & DELANEY, E. K. 2006. Adapting to climate change: public water supply in England and Wales. Climate Change, Vol. 78(2), pp. 227-255.

BEER, T. & P. C. YOUNG. 1983. Longitudinal dispersion in natural streams. J. Environ. Eng., Vol. 109(5), pp. 1049-1067.

BELCHER, S. E., JERRAM, N. & HUNT, J. C. R. 2003. Adjustment of a turbulent boundary layer to a canopy of roughness elements. Journal of Fluid Mechanics. Vol. 488, pp. 369-398.

BOXALL, J. B. & GUYMER, I. 2003. Analysis and prediction of transverse mixing coefficients in natural channels. Journal of Hydraulic Engineering-Asce, 129.

BOXALL, J. B. & GUYMER, I. 2007. Longitudinal mixing in meandering channels: New experimental data set and verification of a predictive technique. Water Research, 41, 341-354.

BOXALL, J. B., GUYMER, I. & Marion, A. 2003. Transverse mixing in sinuous natural open channel flows. Journal of hydraulic research. Vol. 41(2), pp. 758-768.

CAMPBELL, L. J., MC EWAN, I. K., NIKORA, V., POKRAJAC, D. & GALLAGHER, M. 2005. Bed loading effects on hydrodynamics of rough-bed open-channel flows. J. of Hydr. Eng. Vol. 131, no. 7, pp. 576-585.

CAROLLO, F. G., FERRO, V. & TERMINI, D. 2002. Flow velocity measurements in vegetated channels. Journal of hydraulic engineering, Vol. 128, pp. 664-673.

CHIKWENDU, S. C. 1986. APPLICATION OF A SLOW-ZONE MODEL TO CONTAMINANT DISPERSION IN LAMINAR SHEAR FLOWS. International Journal of Engineering Science, 24, 1031-1044.

DENG, Z. Q., SINGH, V. P. & BENGTSSON, L. 2001. Longitudinal dispersion coefficient in straight rivers. Journal of Hydraulic Engineering-Asce, 127.

DE SMEDT, F. 2007. Analytical solution and analysis of solute transport in rivers affected by diffusive transfer in the hyporheic zone. Journal of Hydrology, 339, 29– 38

DIEBERG, F. E., JUSTON, J. J., DE BUSK, K. P. & GU, B. 2005. Relationship between hydraulic efficiency and phosphorus removal in a submerged aquatic vegetation-dominated treatment wetland. Ecolog. Eng., Vol. 25, pp. 9-23.

ELDER, J. W. 1959. The dispersion of marked fluid in turbulent shear flow. Journal of Fluid Mechanics, Vol. 5(4), pp. 544-560. DOI: http://dx.doi.org/10.1017/S0022112059000374

ERCIN, A. E. & HOEKSTRA, A. Y. 2012. Water footprint scenarios for 2050: a global analysis and case study for Europe. UNESCO-IHE Institute for Water Education.

FERRIER, A. J., FUNK, D. R. & ROBERTS, P. J. W. 1993. Applications of optical techniques to the study of plumes in stratified fluids. Dynam. Of. Atmos. And Oce, Vol. 20, pp. 155-183.

FOOD AND AGRICULTURAL ORGANISATION OF THE UNITED NATIONS (FAO). 2009. *The State of Food and Agriculture.* ISBN 978-92-5-106215-9

FICK, A. 1855. *Ueber Diffusion*, Pogg. Ann. Phys. Chem. 170 (4. Reihe 94), 59-86.

FISCHER, H. B. 1979. Mixing processes on the Atlantic continental shelf, Cape Cod to Cape Hatteras. Limnol. Oceanogr., 25(1), pp. 114-125.

GHISALBERTI, M. & NEPF, H. M. 2004. The limited growth of vegetated shear layers. Water Resources Research, 40, 12.

GHISALBERTI, M. & NEPF, H. M. 2005. Mass transport in vegetated shear flows. Environmental Fluid Mechanics, Vol. 5, pp. 527-551. DOI 10.1007/s10652-005-0419-1

GHISALBERTI, M. & NEPF, H. M. 2007. Retention time and dispersion associated with submerged aquatic canopies. Water. Res. Research, Vol. 43(4).

GHISALBERTI, M. & NEPF, H. M. 2009. Shallow flows over a permeable medium: the hydrodynamics of submerged aquatic canopies. Trans. in Porous Med. Vol. 78(2), pp. 309-326.

GORING, D. G. AND NIKORA, V. I., 2002. Despiking Acoustic Doppler Velocimeter Data. Journal of Hydraulic Engineering, DOI: 10.1061/(ASCE)0733-9429(2002)128:1

GUYMER, I. & STOVIN, V. R. 2011. One-Dimensional Mixing Model for Surcharged Manholes. Journal of Hydraulic Engineering-Asce, 137, 1160-1172.

HEINRICH, J. C., HUYAKORN, P. S. & ZIENKIEWICZ, O. C. 1977. An 'upwind' finite element scheme for two-dimensional convective transport equation. Int. Jour. for Num. Met. In Eng. Vol. 11, pp. 131-143.

HOLLAND, J. F., MARTIN, J. F., GRANATA, T., BOUCHARD, V., QUIGLEYD, M. & BROWN, L. 2004. Effects of wetland depth and flow rate on residence time distribution characteristics. Ecological Engineering 23.

HUANG, Y. H., SAIERS, J. E., HARVEY, J. W., NOE, G. B. & MYLON, S. 2008. Advection, dispersion, and filtration of fine particles within emergent vegetation of the Florida Everglades. Water Resources Research, 44, 13.

JEPPESEN, K., KRONVANG, B., MEERHOFF, M., SØNDERGAARD, M., HANSEN, K. M., ANDERSEN, H. E., LAURIDSEN, T. L., LIBORIUSSEN, L., BEKLIOGLU, M., ÖZEN, A. & OLESEN, J. E. 2009. Climate change effects on runoff, catchment phosphorus loading and lake ecological state, and potential adaptations. Journal of Environmental Quality. Vol. 38, no. 5.

JUSTUSSON, B. I., 1981. Median Filtering: Statistical Properties. Topics in Applied Physics, vol. 43, pp. 161 – 196.

KADLEC, R. H. 1990. Overland-flow in wetlands – vegetation resistance. J. Hydr. Eng. Vol. 119(5), pp. 691-706.

KADLEC, R. & KNIGHT, R. 1996. *Treatment Wetlands*. CRC press, Lewis Publishers.

KASHEFIPOUR, S. M. & FALCONER, R. A. 2002. Longitudinal dispersion coefficients in natural channels. Water Research, 36.

KAY, A. 1987. The effects of cross-stream depth variation upon contaminant dispersion in a vertically well-mixed current. Est. Coas. and Shelf. Sci., VOl. 24, pp. 177-204.

KING, A. T., RUEDA, F. J., TINOCO, R. O. & COWEN, E. A. 2009. Modeling flow and transport through aquatic vegetation in natural water bodies. In Proceedings of the 33rd IAHR Congress, Vancouver, BC, Canada, August 9–14, 2009.

KING, A. T., TINOCO, R. O. & COWEN, E. A. 2012. A k-epsilon turbulence model based on the scales of vertical shear and stem wakes valid for emergent and submerged vegetated flows. Journal of Fluid Mechanics, 701, 1-39.

KOCH, D. & LADD, A. 1997. Moderate Reynolds number flows through periodic and random arrays with heterogeneous morphology. Environ. Fluid. Mech., Vol. 6, pp. 477-488.

KOLMOGOVOR, A. N. 1931. Uber die analytischen Methoden in der Wahrscheinlichkeitscrechnung. *Math. Ann.*, Vol. 104, pp. 415-458.

KOLMOGOVOR, A. N. 1933. Zur Theorie der stetigen zufalligen Prozesse. *Math. Ann.*, Vol. 108, pp. 149-160.

KOSKIAHO, J. 2003. Flow velocity retardation and sediment retention in two constructed wetland-ponds. Ecol. Eng. Vol. 19(5), pp. 3250-337.

KOWEN, N., UNNY, T. E. & HILL, H. M. 1969. Flow retardance in vegetated channels. J. Irr. Drain. Div., Am. Soc. Civ. Eng., Vol. 120(3), pp. 406-412.

LIGHTBODY, A. F. & NEPF, H. M. 2006a. Prediction of near-field shear dispersion in an emergent canopy with heterogeneous morphology. Environmental Fluid Mechanics, 6, 477-488.

LIGHTBODY, A. F. & NEPF, H. M. 2006b. Prediction of velocity profiles and longitudinal dispersion in emergent salt marsh vegetation. Limnology and Oceanography, 51, 218-228.

LIGHTBODY, A. F., AVENER, M. E. & NEPF, H. M. 2008. Observations of short-circuiting flow paths within a free-surface wetland in Augusta, Georgia, USA. Limnol. Oceanogr., Vol. 53(3), pp. 1040-1053.

LUHAR, M., ROMINGER, J. & NEPF, H. 2008. Interaction between flow, transport and vegetation spatial structure. Environmental Fluid Mechanics, 8, 423-439.

LUI, D., DIPLAS, P., FAIRBANKS, J. D. & HODGES, C. C. 2008. An experimental study of flow through rigid vegetation. Journal of Geophysical Research, Vol. 113, doi:10.1029/2008JF001042.

MIDDELKOOP, H, DAAMEN, K., GELLENS, D., GRABS, W. KWADIJK, J. C. J., LANG, H., PARMET, B. W. A. H., SCHÄDLER, B., SCHULLA, J. & WILKE, K. 2001. Impact of climate change on hydrological regimes and water resources management in the Rhine basin. Climate Change, Vol. 49, issue 1, pp. 105-128.

MITSCH, W.J. 1992. Landscape design and the role of created, restored and natural riparian wetlands in controlling non-point source pollution. Ecol. Eng., Vol. 1, 27-47.

MURPHY, E., GHISALBERTI, M. & NEPF, H. 2007. Model and laboratory study of dispersion in flows with submerged vegetation. Water Resources Research, 43, 12.

MURPHY, J. M., SEXTON, D. M. H., JENKINS, G. J., BOORMAN, P. M., BOOTH, B. B. B., BROWN, C. C., CLARK, R. T., COLLINS, M., HARRIS, G. R., KENDON, E. J., BETTS, R. A., BROWN, S. J., HOWARD, T. P., HUMPHREY, K. A., MCCARTHY, M. P., MCDONALD, R. E., STEPHENS, A., WALLACE, C., WARREN, R., WILBY, R., WOOD, R. A. 2009. *UK Climate Projections Science Report: Climate change projections*. Met Office Hadley Centre, Exeter.

NEPF, H. M., SULLIVAN, J. A. & ZAVISTOSKI, R. A. 1997. A model for diffusion within emergent vegetation. Limnol. Oceanogr., VOl. 42(8), pp. 1735-1745.

NEPF, H. M. 1999. Drag, turbulence, and diffusion in flow through emergent vegetation. Water Resources Research, 35.

NEPF, H. M. & VIVONI, E. R. 2000. Flow structure in depth-limited, vegetated flow. Journal of Geophysical Research-Oceans, 105, 28547-28557.

NEPF, H. M. 2004. Vegetated flow dynamics. The ecogeomorphology of Tidal marshes, Coastal and Estuarine Studies. Am. Geo. Phys. Uni. Vol. 59.

NEPF, H., GHISALBERTI, M., WHITE, B. & MURPHY, E. 2007. Retention time and dispersion associated with submerged aquatic canopies. Water Resources Research, 43, 10.

NEPF, H. & GHISALBERTI, M. 2008. Flow and transport in channels with submerged vegetation. Acta Geophysica, 56.

NEPF, H. M. 2012. Flow and transport in regions with aquatic vegetation. Annual Review of Fluid Mechanics. Vol. 44, pp. 123-142.

NIKORA, V. 2007. Hydrodynamics of aquatic ecosystems: spatial averaging perspective. *Acta Geophysica*, vol. 55, no.1, pp. 3-10.

NIKORA, N., NIKORA, V. & O'DONOGHUE, T. 2013. Velocity profiles in vegetated open-channel flows: combined effects of multiple mechanisms. J. Hyra. Eng. Vol. 139(10), pp. 1021-1032.

OKAMOTO, T., NEZU, I. & IKEDA, H. 2012. Vertical mass transport in open-channel flows with submerged vegetation. J. Hydro-Env. Res., Vol. 6, pp. 287-297.

PATIL, S. & SINGH, V. P. 2011. Dispersion Model for Varying Vertical Shear in Vegetated Channels. Journal of Hydraulic Engineering-Asce, 137.

PERSSON, J., SOMES, N. L. G. & WONG, T. H. F. 1999. Hydraulic efficiency of constructed wetlands and ponds. Wat. Sci. Tech. Vol. 40(3), pp. 291-300.

POGGI, D., KRUG, C. & KATUL, G. G. 2009. Hydraulic resistance of submerged rigid vegetation derived from first order closure model. Water Resource Research, Vol. 45, doi:10.1029/2008WR007373

RAUPACH, M. R., FINNIGAN, J. J. & BRUNET, Y. 1996. Coherent eddies and turbulence in vegetation canopies: the mixing layer analogy. Boun. Lay. Met., Vol. 78, pp. 351-382.

RAUPACH, M. R. & SHAW, R. H. 1981. Averaging procedure for flow within vegetation canopies. Boundary Layer Meteorology, Vol. 22, pp. 79-90.

RAUPACH, M. R., COPPIN, P. A. & LEGG, B. J. 1985. Experiments on scalar dispersion within a model plant canopy Part 1: the turbulent structure. Boundary Layer Meteorology, Vol. 35, pp. 21-52.

ROMINGER, J. T. & NEPF, H. M. 2011. Flow adjustment and interior flow associated with a rectangular porous obstruction. Journal of Fluid Mechanics, Vol. 680. Pp. 636-659. doi:10.1017/jfm.2011.199

RUTHERFORD, J. C. 1994. River Mixing. Wiley, Chichester, U.K.

SEO, I. W., BAEK, K. O. & JEON, T. M. 2006. Analysis of transverse mixing in natural streams under slug tests. Journal of Hydraulic Research, 44(3), pp. 350-362.

SEO, I. W. & CHEONG, T. S. 1998. Predicting longitudinal dispersion coefficient in natural streams. Journal of Hydraulic Engineering. , Vol. 124(1), pp. 25-32.

SERRA, T., FERNANDO, H. J. S. & RODRIGUEZ, R. V. 2004. Effects of emergent vegetation on lateral diffusion in wetlands. Water. Res. Vol. 38, pp. 139-147.

SEXTON, D. M. H. & HARRIS, G. R. 2015. The importance of including variability in climate change projections used for adaptation. Nature Climate Change, Vol. 5, pp. 931-936.

SHAW, R. H. & SEGINER, I. 1985. The dissipation of turbulence in plant canopies. In Proceedings of the 7th Symposium of the American Meteorological Society on Turbulence and Diffusion, pp. 200–203. American Meteorological Society.

SHUCKSMITH, J. D., BOXALL, J. B. & GUYMER, I. 2010. Effects of emergent and submerged natural vegetation on longitudinal mixing in open channel flow. Water Resources Research, 46.

SHUCKSMITH, J. D., BOXALL, J. B. & GUYMER, I. 2011a. Determining longitudinal dispersion coefficients for submerged vegetated flow. Water Resources Research, 47.

SHUCKSMITH, J. D., BOXALL, J. B. & GUYMER, I. 2011b. Bulk flow resistance in vegetated channels: analysis of momentum balance approaches based on data obtained in aging live vegetation. J. Hydr. Eng. Vol. 137(12), pp. 1624-1635.

STOVIN, V. R., GRIMM, J. P. & LAU, S. T. D. 2008. Solute transport modeling for urban drainage structures. Journal of Environmental Engineering-Asce, 134, 640-650.

TANINO, Y. & NEPF, H. M. 2008a. Laboratory investigation of mean drag in a random array of rigid, emergent cylinders. Journal of Hydraulic Engineering, Vol. 134, pp. 34-41.

TANINO, Y. & NEPF, H. M. 2008b. Lateral dispersion in random cylinder arrays at high Reynolds number. J. Fluid Mech., Vol. 600, pp. 339-371.

TAYLOR, G. 1953. Dispersion of soluble matter in solvent flowing slowly through a tube. The Royal Society. Vol. 219(1137), DOI: 10.1098/rspa.1953.0139

WAGNER, W. 1961. Bouger-Beer Lambert Law. In MONISMITH, J. R., KOSEFF, J.K. THOMPSON, C. A. O'RIORDAN & H. M. NEPF (Editors), Encyclopedic Dictionary of Physics, pp. 481.

WAHL, M. D., BROWN, L. C., SOBOYEJO, A. O., MARTIN, J. & DONG, B. 2010. Quantifying the hydraulic performance of treatment wetlands using the moment index. Ecological Engineering, 36, 1691-1699.

WHITE, B. L. & NEPF, H. M. 2003. Scalar transport in random cylinder arrays at moderate Reynolds number. Journal of Fluid Mechanics, 487.

WHITE, B. L. & NEPF, H. M. 2007. Shear instability and coherent structures in shallow flow adjacent to porous layers. J. Fluid Mech., Vol. 593, pp. 1-32.

WHITE, B. L. & NEPF, H. M. 2008. A vortex based model of velocity and shear stress in a partially vegetated shallow channel. Water Resources Research, Vol. 44. doi:10.1029/2006WR005651

WILSON, N. R. & SHAW, R. H. 1977. A higher order closure model for canopy flow. Journal of Applied Meteorology, Vol. 16, pp. 1197-1205.

WONG, T. H. F., BREEN, P. F., SOMES, N. L. G. & LLOYD, S. D. 1998. *Managing Urban Stormwater using Constructed Wetlands,* Industry Report 98/7. Cooperative Research Centre for Catchment Hydrology.

WOOD, M. G., HOWES, T., KELLER, J. & JOHNS, M. R. 1998. Two dimensional computational fluid dynamic models for waste stabilisation ponds. Water Research, 32.

ZENG, U-H., HUAI, W-X. & GUYMER, I. 2008. Transverse mixing in a trapezoidal compound channel. J. Hydrodynamics. Vol. 20(5), pp. 645-649.

ZONG, L. & NEPF, H. 2010. Flow and deposition in and around a finite patch of vegetation. Geomorphology, 116, 363-372.

ZONG, L. & NEPF, H. 2011. Spatial distribution of deposition within a patch of vegetation. Water Resources Research, 47.

8. Appendices

8.1 Appendix I: Types of Vegetation

This appendix provides images and, where available, morphological characteristics of a number of plant species apparent in relevant literature. Their presence in associated publications is provided to supplement further reading. Morphological characteristics are the following; stem diameter, d [m], stem density, N [m^{-2}], frontal area per unit volume, a [m^{-1}] and drag coefficient, C_D.

Species Name	**Image**	***d*** **(cm)**	***N*** **(m^{-2})**	***a*** **(cm^{-1})**	**Authors**
Elocharis elongate		0.1	2200	0.016-0.022	Huang et al., 2008; Sand-Jensen & Pedersen, 1999.
Cladium jamaicense		0.76-1.04	92	8.5-33x10^{-4}	Huang et al., 2008

Carex		6	150-333	-	Shucksmith et al., 2010&2011
Typha latifolia		3	100	-	Dierberg et al., 2005; Lightbody et al., 2008; Koskiaho, 2003.
Sagittaria lancifolia		0.41	16	8.5-33x10^{-4}	Huang et al., 2008
Bacopa carolinia		0.36	12	4.13-14x10^{-4}	Huang et al., 2008
Panicum hemitomon		0.02	8	7.1-86x10^{-5}	Lightbody & Nepf 2006
Spartina alterniflora		0.5-1.5	90-370	0.01-0.07	Nepf & Vivoni 2000; Lightbody & Nepf 2006; Nepf, 1999;

8.2 Appendix II: Laser Induced Fluorometry (LIF)

8.2.1 Assembly and calibration

Brief

This appendix provides a description of the development and calibration of the one-dimensional Laser Induced Fluorometry (LIF) system.

Introduction

The decay in laser (or light) power through a medium is dependent upon the mediums absorbance or ability to absorb light. Through water, and other fluids, the decay in power can be modelled as an exponential one; where the power, P, at a given location, y, from the source can be described using the Beer-Lambert Law (Wagner, 1961); $P(y) = P_0 e^{-\alpha y}$ – where α [m^{-1}] is the linear attenuation coefficient in the direction of the beam and P_0 is the power at $y = 0$. Measurements of power as a function of distance from the source can then be used to calculate the attenuation coefficient.

When a fluorescent tracer is introduced, such as Rhodamine, light is absorbed and subsequently re-emitted at another wavelength after a short time interval. The intensity of the emitted light, $I(y)$, at a given location is directly proportional to tracer concentration – until the incident power exceeds a saturation limit (Ferrier et al., 1993). A portion of laser power is consumed in this process – by converting the incident light into another wavelength (absorption) and by altering the path of some of the beam (scattering). As such, laser attenuation through a medium with increasing concentration of fluorescent tracer will increase relative to a medium of lower concentration. The calibration of a LIF system cannot, therefore, be conducted using conventional observations of the attenuation in detected intensity with distance – since the attenuation coefficient is a function of tracer concentration.

An example laboratory system is depicted in Figure 8.1. The laser beam is pointed perpendicularly through the water column. A photo-detector (CCD camera) is mounted directly below the beam and is set such that the full beam length is in view. A parcel of fluorescent dye passing through the laser beam will fluoresce and emit light that is detected as pixel intensity at the camera. In the example, the camera may detect a lower intensity at a location, *B*, further along the route of the laser beam than that detected at the centre of the dye plume at *A*.

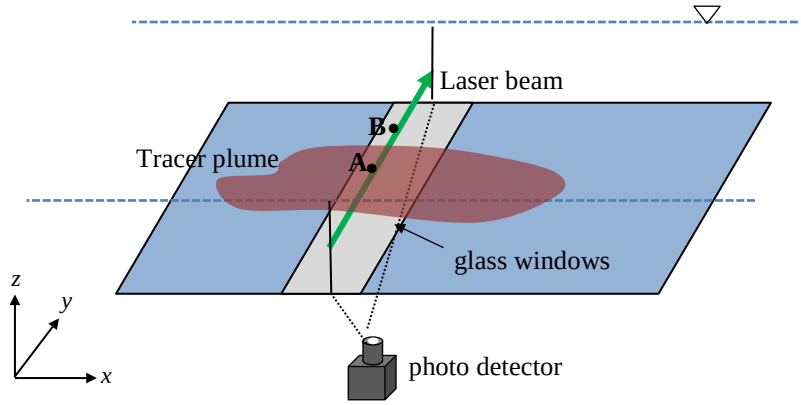

Figure 8.1: Laser Induced Fluorometry system showing the passage of fluorescent trace through the laser beam.

The lower intensity recorded at *B* may be as a result of two processes: firstly, that there is a weaker concentration of tracer at this location and the fluorescent intensity is, therefore, lower; or secondly, the path of the laser beam *en route* to *B* propagates through a region of relatively high tracer concentration and the laser power arriving at *B* is, therefore, weaker than without the intercepting plume. These two phenomena make it impossible to distinguish between a detected low intensity as a result of low concentration and low intensity as a result of a high laser-path concentration. Strong laser attenuation has been observed in un-published data even for generally weak Rhodamine concentrations (O < 200ppb) using a 1 W laser.

Theory

Ferrier et al. (1993, pp. 159-166) provided a solution for calibration when the light attenuation is a function of local concentration. The laser power, P_i, at a particular point or *cell* can be determined by the laser power that enters the previous cell, P_{i-1}, and the given attenuation

within that cell, $\alpha_w + \epsilon_0 C$. For example, the adjacent cell to the laser origin experiences an incident laser power P_0. The concentration in this cell, for continuity, can be called C_1 and the detected intensity at the camera shall be called I_1. The attenuation of laser power in this cell is dependent on the magnitude of C_1 such that the transmitted power is a function of P_0 and I_0. Figure 8.2 displays this process schematically.

The total attenuation coefficient, α, is the sum of both attenuation due to clear water and attenuation due to the tracer e.g.

$$\alpha = \alpha_w + \epsilon_0 C \qquad \textbf{Equation 8.1}$$

where ϵ_0 is the extinction coefficient resulting from the tracer, α_w is the attenuation due to clear water and C is the concentration. Note that, in this instance, C may be a function of y e.g. $C = C(y)$. The power leaving the cell, P_1, can be expressed as

$$P_1 = P_0 e^{-(\alpha_w + \epsilon_0 C(y))\Delta y} \qquad \textbf{Equation 8.2}$$

When the concentration of tracer is non-uniform with distance from the laser source, the cumulative effects of all previous cells and attenuation are integrated along the length of the interrogation path, giving:

$$P_{n+1} = P_0 e^{-\sum_{i=0}^{n} (\alpha_w + \epsilon_0 C_i)\Delta y_i} \qquad \textbf{Equation 8.3}$$

The functionality of ϵ_0 on C must be determined to apply Equation 8.2 to for the attenuation correction.

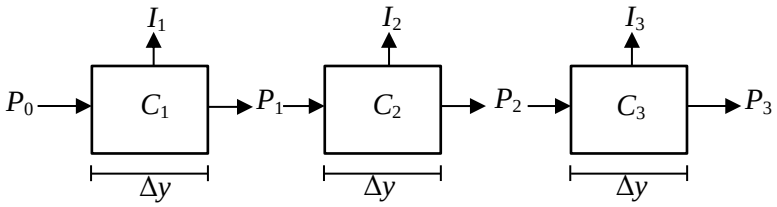

Figure 8.2: Schematic representation of the incremental correction for laser attenuation as a function of cell concentration. Ferrier et al., 1993.

Methodology

A desired concentration range was chosen as 0 – 50ppb as the maximum concentration does not lead to unwanted density disparity effects (e.g. sinking) between the tracer and surrounding water and represents a concentration safely within the linear limit of dye

fluorescence. Further, a suitable camera shutter speed (5 ms) was permitted at 50ppb retaining acceptable light intensity and maintaining image resolution. The attenuation coefficient for a range of tracer concentrations was determined by recording the decay in pixel intensity along the beam path for each concentration (Figure 8.3a). A section of the LIF measurement sites was isolated to form a known volume using baffles. The cameras were position pointing upwards and the wide-angle lens allowed for full capture of the laser beam. Rhodamine 6G was added to the isolated section and mixed until equal concentration was achieved at multiple sampling locations within the section. The concentration of the isolated volume was then checked against a laboratory fluorometer (Turner Designs 10AU). Images of fluorescence were taken at a frequency of 5Hz for 200s under blacked-out conditions. This process was then repeated incrementally at 5ppb up to 50ppb. The mean pixel intensity of 1000 recorded frames was calculated for each calibration concentration and for a range in laser powers.

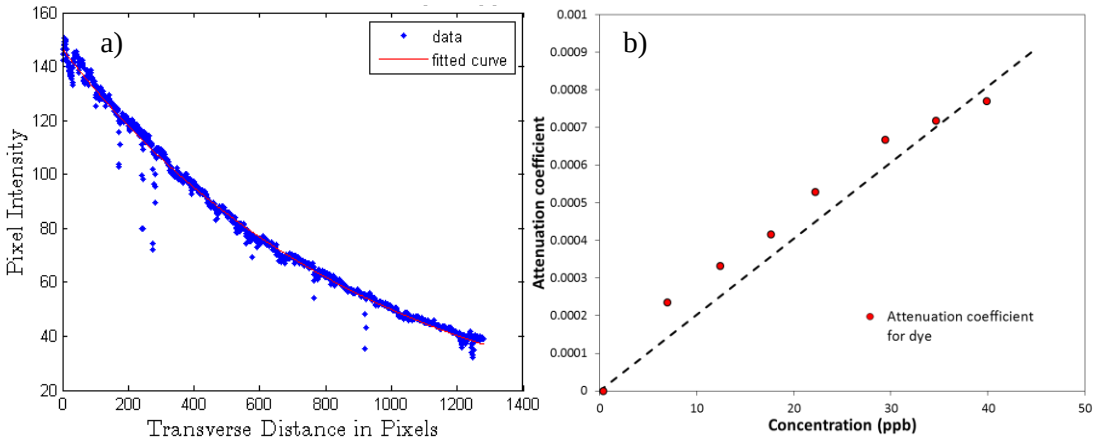

Figure 8.3: a) The laser beam attenuates considerably through the dye solution up to 70% in 0.5m. b) The attenuation coefficient [pixels^{-1}] is a function of the local Rhodamine concentration.

Laser power could not be directly altered at the laser source as the lasers were set at fixed powers. Therefore, neutral density filters (supplied by Thor Labs™) were employed to reduce the laser power post-emission at fraction of 90%, 80%, 60%, 40% and 10% of the total power. Discrete power was simultaneously recorded at the laser source to provide a value of P_0. This was done with the use of a laser power meter and allowed the relationship between power and

intensity to be determined and physically verified. A total of 60 fluorescent intensity tests were conducted for the ten desired calibration concentrations (0: 5: 50ppb) and the 6 possible laser powers (100, 90, 80, 60, 40 and 10%).

An exponential fit was made in accordance with the Beer-lambert Law for the decay curves in intensity with distance (Figure 8.3a). The resultant relationship between, laser power and detected intensity is assumed to be linear within the small concentration range given

$$I = \beta P \qquad \textbf{Equation 8.4}$$

where β is the fluorescent efficiency and is a linear function of concentration and

$$\beta = aC + b \qquad \textbf{Equation 8.5}$$

where a is a factor relating fluorescent intensity to concentration and b is a constant. It follows that

$$\mathrm{C}(y) = \frac{\left(\frac{I}{P} - b\right)}{a} \qquad \textbf{Equation 8.6}$$

The fluorescent efficiency β was calculated from the gradient of pixel intensity against laser power. The trend of β against concentration then allowed a to be calculated for each individual pixel along the beam given that the relationship between power and intensity is known. However, the mean calibration trend was employed to mitigate for accidental movements in the optical equipment or distortions to the lens or glass windows.

Measurements of detected intensity and power decay with distance for each concentration provided sufficient data to analyse the functionality of the attenuation. Key to this evaluation was the measurement of the initial concentration, power and intensity, C_0, P_0 and I_0. The attenuation of P_0 could be calculated given the concentration, cell width and ϵ_0. Thus the incident power at the next cell, say P_1, was calculated and the process could be repeated.

Results

Figure 8.3a gives an example plot of laser power attenuation. Note that the spikes on the plot are attributed to scratches on the optical equipment, e.g. the glass windows. Further, Figure

8.3b gives the attenuation coefficient as a function of tracer concentration for the full power case – only the full power case is required as it is the same power condition used for the trace studies. Remember that measurements of intensity with laser power were carried out to determine the relationship between power and intensity only.

Measurements of $I(y)$ as a function of laser power $P(y)$ are plotted for all eight calibration concentrations in Figure 8.4a and the gradient of each plot, β, is plotted with concentration in Figure 8.4b; where the data are given for the location at $y = 0$. Remember that each pixel across the beam length has its own relationship between β and concentration. The process depicted in Figure 8.2 was repeated for each pixel across the length of the laser beam.

The gradient of the line presented in Figure 8.4b is used in conjunction with Equation 8.6 and the correction function in Equation 8.3 to calibrate pixel intensity along the laser beam for scenarios where $C = f(y)$. Uncalibrated and calibrated transverse intensity and concentration distributions of the same steady state source are presented in Figure 8.5a and b, respectively.

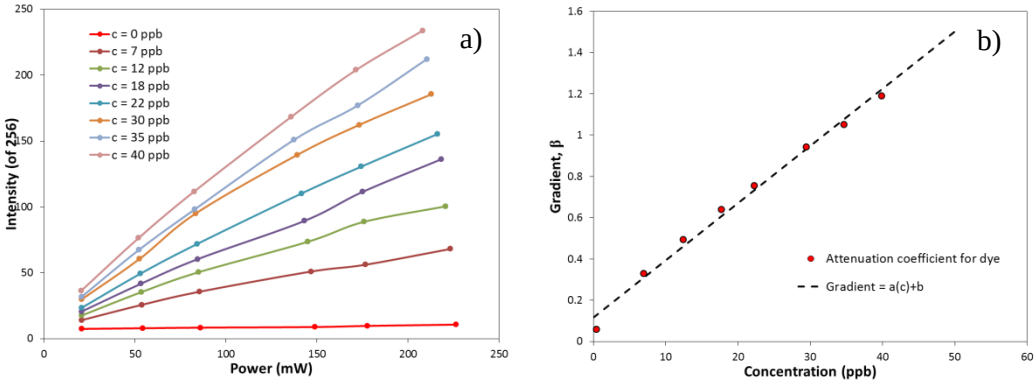

Figure 8.4: a) CCD measured intensity at a given pixel is plotted against laser power at that location. b) The gradient β is plotted against absolute concentration to calculate the factor a.

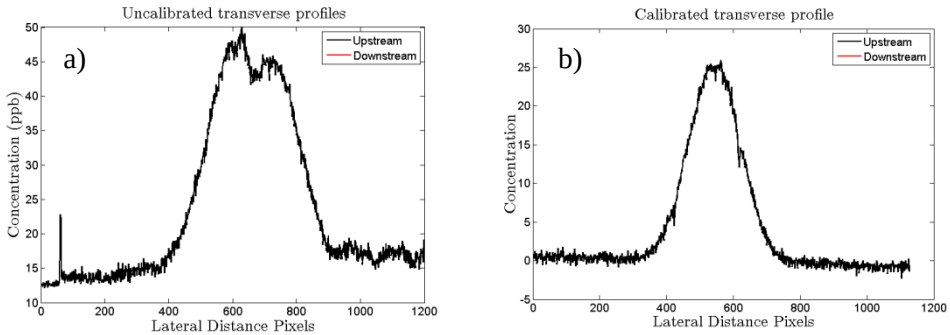

Figure 8.5: a) Uncalibrated pixel intensity. b) Calibrated pixel intensity as concentration in ppb post calibration procedure.

8.3 Appendix III: Characterizing Real Vegetation

8.3.1 Brief

This appendix describes the methods used to characterize real vegetation samples. The heterogeneity in stem diameter, geometry and morphology of the real vegetation made characterization difficult when compared to the homogeneous artificial examples. A range of parameters needed to be characterised: mean stem diameter, *d*, population density per unit area, *N* and an estimate of the stem frontal area per unit volume, *a*.

8.3.2 Mean stem diameter

The mean stem diameter was calculated from the average diameter of 130 samples taken from multiple locations using digital Vernier callipers with a precision of 0.01 mm. This method also allowed for an estimation of the range of diameters to be quantified. Figure 8.6a shows a sampling area within the measurement section of the winter *typha* vegetation.

Figure 8.6: a) sampling area to record stem diameter of the real *typha* vegetation. b) cylindrical nature of winter *typha* stem and leaf litter at the channel bed.

The *typha* stems were approximately cylindrical in shape and the diameter varied by up to 4 mm depending on the axis that was measured. However, diameter was measured in the

transverse direction – perpendicular to the direction of primary flow – providing appropriate scaling for the stem Reynolds number. It can be seen in Figure 8.6b that dead leaf litter was present in the bottom ~5 cm of the channel. The leaf litter was aligned randomly and could not be considered vertically uniform and not emergent. As much leaf litter was removed prior to testing to ensure that the hydrodynamics were associated with the living stems.

8.3.3 Stem population density

The vegetation density was calculated by counting the number of vegetation stems within a known cross-sectional area. This was conducted at a number of locations within the test section to provide an average density and standard deviation. The *typha* was similar in morphology to the artificial vegetation; where the stems were rigid and stood vertically from the channel bed. This allowed the number of stems to be easily counted within the isolated sections e.g. Figure 8.6a.

8.3.4 Stem frontal area per unit volume

The stem frontal area per unit volume, a, was estimated using cross-sectional image analysis. Figure 8.7 provides an example of the imaging process. Images of the frontal edge of the sample vegetation were taken against a white background. A scale was drawn on this background to calibrate image pixels into meters. Images were taken at the end of the experimental testing at 10 cm longitudinal intervals along the installation. The preceding section was cropped to the bed to prevent the stems obscuring the following image. The plan area of each image was known given the channel width and the distance between images (e.g. 0.99 m x 0.10 m).

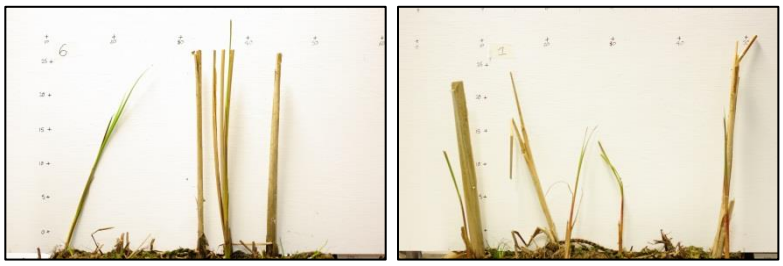

Figure 8.7: Example images of vegetation used for frontal area per unit volume analysis.

The fractional area of the vegetation to water was estimated by converting the cross-sectional images into black and white plots and the counting the number of pixels that correspond to vegetation. The stem frontal area per unit volume could then be estimated using the fractional occupancy of vegetation stems per unit plan area. Firstly, the images were cropped between the bed and the water depth. The colour images were then converted into grey-scale data files based on the pixel intensity; where 0 and 256 corresponded to absolute black and respectively. Figure 8.8a&b compares the black and white image converted from the greyscale sample. The white background was not perfectly white (intensity = 256). As such, an intensity threshold was used to select the pixels that would be converted into pure white and pixels below this threshold were converted into black. The threshold was determined from the histogram of intensities for a chosen image (Figure 8.8c). There was a distinct distribution of intensity in the histogram; a high frequency of large intensity pixels for the light background and a spectrum of darker intensities for the vegetation stems. The threshold was determined by systematically increasing the value as a percentage of saturation until shadows and parts of the image that were not the vegetation were included and turned into black points (e.g. Figure 8.8a). The final ratio of black and white pixels was then calculated and converted into meters to provide the frontal area of vegetation per unit volume.

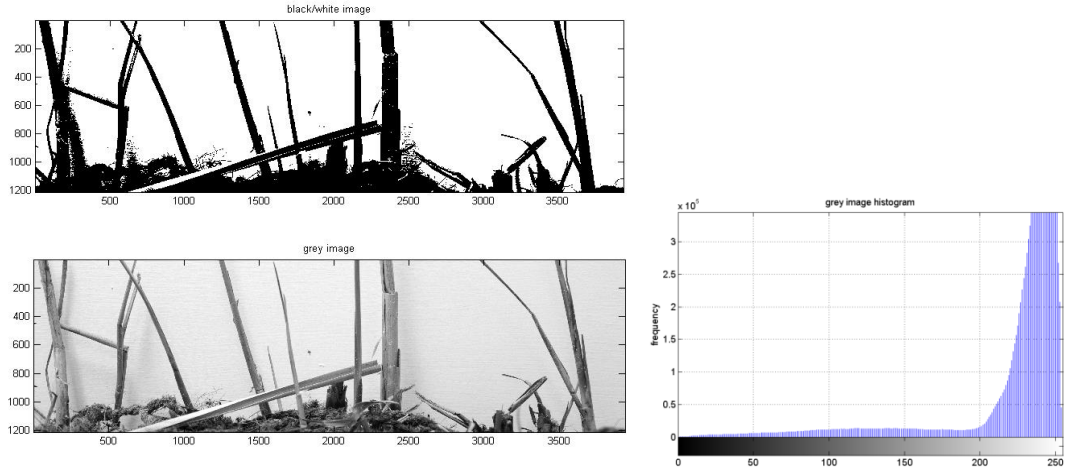

Figure 8.8: a) black and white image converted from the b) grey-scale image where the intensity threshold was determined for the c) intensity histogram of the grey-scale image.

8.4 Appendix IV: Trace Results

8.4.1 Introduction

The results for the continuous and pulse injection trace tests can be found on the accompanying disc entitled *Appendices Additions*. The appendix is divided into two parts: firstly, the 2-dimensional trace results for the 10x repeat pulse injection tests are presented for the 5x experimental discharges for every full vegetation type; and secondly, the 2-dimensional trace results and mean transverse concentration distributions are presented for the continuous injection tests for the 5x experimental discharges for the three full vegetation types (high density artificial and winter and summer *typha*) and the four partial vegetation types (high and low density artificial and winter and summer *typha*).

The steady-state, transverse concentration distribution, $C(y)$, was calculated as the temporal average concentration at each location in y for the region of constant concentration shown in the plots of $C(y, t)$ (see below). The centreline concentration distribution exhibits a rise and fall where the plateau concentration indicates steady-state conditions. The injections were made for a sufficient duration such that at least 5 minutes of steady-state concentration was

observed at the downstream measurement site. Mean transverse distributions of $C(y)$ were then calculated between 20% of the maximum concentration, e.g.:

$$\langle C \rangle (y) = \left[\sum_{C_{max} - 0.8C_{max}}^{C_{max} + 0.8C_{max}} C(y) \right] / n \qquad \textbf{Equation 8.7}$$

In the partial vegetation scenario the centreline concentration did not exhibit a constant value in the plateau region. As such, the mean transverse concentration distribution was calculated in the time interval well within the rise and fall in concentration; ensuring that $C(y)$ was representative of steady state conditions.

Despite the vertical injection method, the calibrated steady-state concentration distributions were not mass balanced between the upstream and downstream measurement sites. Mass and flux-balancing was performed on the final distributions, prior to analysis. In the full vegetation scenario, mass balancing was conducted by adjusting the area under the curve of the downstream distribution to match that upstream. In the partial scenario, the flow field was non-uniform and a flux-balance was conducted. The product of concentration and velocity was matched at every transverse interval across the channel such that the flux of the downstream interval matched that of the upstream. In this instance the mean velocity profile, $U(y)$, was employed.

8.4.2 Trace results – full vegetation pulse injection

Figures 1.1 to 1.5, 1.6 to 1.10, 1.11 to 1.15 and 1.16 to 1.20 on the accompanying disc provide the 2-dimensional concentration distributions for the mean 10x repeat tests measured at x = 1.0 and 2.0 m downstream of the vertical injection point for the 5x experimental discharges in the low and high density artificial and winter and summer *typha* full vegetation, respectively. The discharge is provided in the chart title.

8.4.3 Trace results – full vegetation continuous injection

Figures 1.21 to 1.25, 1.26 to 1.30 and 1.31 to 1.35 on the accompanying disc provide the 2-dimensional concentration distributions, the centreline concentration and the mean transverse concentration distributions measured at x = 1.0 and 2.0 m downstream of the continuous vertical injection for the 5x experimental discharges in the high density artificial, and winter and summer *typha* full vegetation, respectively.

8.4.5 Trace results – partial vegetation continuous injection

Figures 1.36 to 1.40, 1.41 to 1.45, 1.46 to 1.50 and 1.51 to 1.55 on the accompanying disc provide the 2-dimensional concentration distributions, the centreline concentration and the mean transverse concentration distributions measured at x = 1.0 and 2.0 m downstream of the continuous vertical injection for the 5x experimental discharges in the high and low density artificial and winter and summer *typha* partial vegetation, respectively.

8.5 Appendix V: Finite Difference Model Derivation

A finite difference solution was sought to describe the steady-state solute transport characteristics in laterally heterogeneous flow fields. The two-dimensional advection diffusion equation was employed; assuming a straight, prismatic channel where the depth, h, velocity, U, and transverse mixing coefficient, D_y, are functions of y but not x, e.g.:

$$\mathrm{h}(y)U(y)\frac{\partial C(x,y)}{\partial x} = \frac{\partial}{\partial y}\left[h(y)D_y(y)\frac{\partial C(x,y)}{\partial y}\right] \qquad \textbf{Equation 8.8}$$

Where $C(x, y)$ is the steady-state concentration and y and x are the transverse and longitudinal co-ordinate directions, respectively.

8.5.1 Model discretization

A finite difference solution was sought on a uniform, rectangular grid, assuming that the values of h, U, and D_y are available at each computational node. The transverse mixing is then treated with a "central" approximation; while the longitudinal advection is treated with an "upwind" approximation. The central approximation creates a symmetric stencil array for each computation node of the scheme. The upwind solution uses an adaptive scheme that alters the finite difference stencil to numerically simulate the direction of propagation of information in the flow field. The solution will, therefore, contain more computational nodes upwind of the scheme and will be "up-wind biased". Equation 8.8 is then discretized for each computation node where i and j denote the N^{th} location in the x and y directions, respectively; where the left-hand side becomes:

$$\frac{h^j U^j \left[C_i^j - C_{i-1}^j\right]}{\Delta x} \qquad \textbf{Equation 8.9}$$

and the right-hand side becomes;

$$\frac{1}{\Delta y}\left\{\frac{\left(h^{j+1}D^{j+1}+h^jD^j\right)}{2}\frac{\left[C_i^{j+1}-C_i^j\right]}{\Delta y} - \frac{\left(h^jD^j+h^{j-1}D^{j-1}\right)}{2}\frac{\left[C_i^j-C_i^{j-1}\right]}{\Delta y}\right\} \qquad \textbf{Equation 8.10}$$

After the grouping of terms, Equation 8.10 yields:

$$\alpha^{j-1}C_i^{j-1}+\beta^jC_j^j+\gamma^{j+1}C_j^{j+1}=\delta^j \qquad \textbf{Equation 8.11}$$

where;

$$\alpha^{j-1}=\frac{-\left(h^{j-1}D^{j-1}+h^jD^j\right)}{2\Delta y^2} \qquad \textbf{Equation 8.12}$$

$$\beta^j=\frac{h^jU^j}{\Delta x}+\frac{\left(h^{j+1}D^{j+1}+2h^jD^j+h^{j-1}D^{j-1}\right)}{2\Delta y^2} \qquad \textbf{Equation 8.13}$$

$$\gamma^{j+1}=\frac{-\left(h^{j+1}D^{j+1}+h^{j}D^{j}\right)}{2\Delta y^{2}} \qquad \textbf{Equation 8.14}$$

$$\delta^{j}=\frac{h^{j}U^{j}}{\Delta x}C^{j}_{i-1} \qquad \textbf{Equation 8.15}$$

Assuming that there are N nodes in the transverse direction, and the transverse boundary conditions will provide the concentrations for j = 0 and j = N - 1. The application of Equation 8.11 at $N-2$ interior nodes will provide N-2 simultaneous equations for N-2 unknown concentrations, C^{i}_{i} for j = 1 to N-2. The simultaneous equations form a tri-diagonal matrix, which is solved using the "Thomas algorithm" approach or the "double sweep" (Madsen and Larsen, 1987) method. Equation 8.11 for j = 1 is:

$$\alpha^{0}C^{0}+\beta^{1}C^{1}+\gamma^{2}C^{2}=\delta^{1} \qquad \textbf{Equation 8.16}$$

Since C^0 comes from the lower transverse boundary, it moves to the right hand side to join the other known terms, thus:

$$\beta^{1}C^{1}+\gamma^{2}C^{2}=\delta^{1}-\alpha^{0}C^{0} \qquad \textbf{Equation 8.17}$$

which is re-written as;

$$p^{1}C^{1}+q^{2}C^{2}=r^{0} \qquad \textbf{Equation 8.18}$$

Further, Equation 8.11 for j = 2 is:

$$\alpha^{1}C^{1}+\beta^{2}C^{2}+\gamma^{3}C^{3}=\delta^{2} \qquad \textbf{Equation 8.19}$$

and using Equation 8.18 to replace C^1 gives:

$$\alpha^{1}\frac{\left(r^{0}-q^{2}C^{2}\right)}{p^{1}}+\beta^{2}C^{2}+\gamma^{3}C^{3}=\delta^{2} \qquad \textbf{Equation 8.20}$$

and since r^0 is known it is moved to the right-hand side and the like terms are collected, and substituting for Equation 8.18:

$$p^{2}C^{2}+q^{3}C^{3}=r^{1} \qquad \textbf{Equation 8.21}$$

It follows that, for j = 3:

$$p^{3}C^{3}+q^{4}C^{4}=r^{2} \qquad \textbf{Equation 8.22}$$

And by analogy, Equation 8.11 for j = $N - 1$ can be written as:

$$p^{N-2}C^{N-2}+q^{N-1}C^{N-1} = r^{N-3} \qquad \textbf{Equation 8.23}$$

However, C^{N-1} is known from the upper transverse boundary and thus C^{N-2} can be solved as:

$$C^{N-2} = \frac{r^{N-3} - q^{N-1}C^{N-1}}{p^{N-2}} \qquad \textbf{Equation 8.24}$$

Note that in the above derivation the subscripts on the concentrations have been dropped since they are all at the same longitudinal location i.e. the i^{th} slice.

8.5.2 First modification

The first modification is to set the lateral boundary condition dC/dy = 0. Therefore, instead of specifying C^0, dC/dy_0 = 0 is specified. By using "dummy" nodes at j-2 and setting $C^{j-2} = C^j$, the double sweep algorithm is then modified below. Equation 8.11 for j = 0 is:

$$\alpha^{-1}C^{-1}+\beta^0C^0+\gamma^1C^1 = \delta^0 \qquad \textbf{Equation 8.25}$$

Since $C^{-1} = C^1$ for this boundary condition;

$$\beta^0C^0+\left(\alpha^{-1}+\gamma^1\right)C^1 = \delta^0 \qquad \textbf{Equation 8.26}$$

and for j = 1, Equation 8.11 becomes;

$$\alpha^0C^0+\beta^1C^1+\gamma^2C^2 = \delta^1 \qquad \textbf{Equation 8.27}$$

Replacing C^0 from Equation 8.26 gives;

$$\alpha^0\left[\delta^0-\left(\alpha^{-1}+\gamma^1\right)C^1\right]/\beta^0+\beta^1C^1+\gamma^2C^2 = \delta^1 \qquad \textbf{Equation 8.28}$$

and;

$$-\alpha^0\left(\alpha^{-1}+\gamma^1\right)C^1/\beta^0+\beta^1C^1+\gamma^2C^2 = \delta^1 - \frac{\alpha^0\delta^0}{\beta^0} \qquad \textbf{Equation 8.29}$$

where:

$$p^1C^1+q^2C^2 = r^0 \qquad \textbf{Equation 8.30}$$

but now,

$$p^1 = -\alpha^0 \frac{\left(\alpha^{-1}+\gamma^1\right)}{\beta^0} + \beta^1 \qquad \textbf{Equation 8.31}$$

$$r^0 = \delta^1 - \frac{\alpha^0 \delta^0}{\beta^0} \qquad \textbf{Equation 8.32}$$

The basic algorithm is unchanged, but there is an additional modification at the upper boundary.

Now for the upper boundary condition, C^{N-1} is instead specified as $dC/dy_{N-1} = 0$ and by using a dummy node at N and setting $C^N = C^{N-2}$, the final two forward sweep equations are:

$$p^{N-2} C^{N-2} + q^{N-1} C^{N-1} = r^{N-3} \qquad \textbf{Equation 8.33}$$

$$p^{N-1} C^{N-1} + q^N C^N = r^{N-2} \qquad \textbf{Equation 8.34}$$

Since $C^N = C^{N-2}$ for this boundary condition, C^{N-2} can be eliminated and solved for C^{N-1}:

$$p^{N-2} \left[r^{N-2} - p^{N-1} C^{N-1}\right] / q^N + q^{N-1} C^{N-1} = r^{N-3} \qquad \textbf{Equation 8.35}$$

$$-\frac{p^{N-2} p^{N-1}}{q^N} C^{N-1} + q^{N-1} C^{N-1} = r^{N-3} - \frac{p^{N-2} r^{N-2}}{q^N} \qquad \textbf{Equation 8.36}$$

$$C^{N-1} \left(-\frac{p^{N-2} p^{N-1}}{q^N} + q^{N-1} \right) = r^{N-3} - \frac{p^{N-2} r^{N-2}}{q^N} \qquad \textbf{Equation 8.37}$$

Solving for C^{N-1}:

$$C^{N-1} = \frac{q^N r^{N-3} - p^{N-2} r^{N-2}}{-p^{N-2} p^{N-1} + q^N q^{N-1}} \qquad \textbf{Equation 8.38}$$

and for $C^{N-2;}$

$$C^{N-1} = \frac{r^{N-3} - q^{N-1} C^{N-1}}{p^{N-2}} \qquad \textbf{Equation 8.39}$$

This is then solved successively for C^{N-3} to C^1. Finally, C^0 comes from Equation 8.26, $C^0 = [\delta^0 - (\alpha^{-1}+\gamma^1)C^1]/\beta^0$. And since $C^{-1} = C^1$ then $\alpha^{-1} = \alpha^1$, $\gamma^{-1} = \gamma^1$, $h^{-1} = h^1$ and $D^{-1} = D^1$.

8.6 Appendix VI: Finite Difference Fitting Results

This appendix provides the optimized profiles of transverse mixing coefficient using the finite difference model. The model was developed in increasingly complexity. As such, the appendix provides the optimized line, step, triangle and Gaussian functional forms of $D_y(y)$ along with the best fit downstream predicted transverse concentration distribution. The results for each vegetation type are arranged in order of flow discharge where the chart titles show the discharge value. Sensitivity analysis to the value of $D_y(y)$ is also provided with each set of figures.

Full vegetation – spatially constant optimization

Figures 2.1 to 2.3 on the accompanying disc give the upstream and downstream steady-state concentration distributions; the best fit downstream prediction; the optimized value of $D_y(y)$; and the sensitivity of the quality of fit to the value of $D_y(y)$ for the high and low density artificial and winter and summer *typha* full vegetation, line optimization.

Partial vegetation – spatially constant mixing optimization

Figures 2.4 to 2.7 on the accompanying disc give the upstream and downstream steady-state concentration distributions; the best fit downstream prediction; the optimized value of $D_y(y)$; and the sensitivity of the quality of fit to the value of $D_y(y)$ for the high and low density artificial and winter and summer *typha* partial vegetation, line optimization.

Partial vegetation –transverse discontinuity optimization

Figures 2.8 to 2.11 on the accompanying disc give the upstream and downstream steady-state concentration distributions; the best fit downstream prediction; the optimized value of $D_y(y)$; and the sensitivity of the quality of fit to the value of $D_y(y)$ for the high and low density artificial and winter and summer *typha* partial vegetation, step optimization.

Partial vegetation – triangle optimization

Figures 2.12 to 2.15 on the accompanying disc give the upstream and downstream steady-state concentration distributions; the best fit downstream prediction; the optimized value of $D_y(y)$; and the sensitivity of the quality of fit to the value of $D_y(y)$ for the high and low density artificial and winter and summer *typha* partial vegetation, triangle optimization.

Partial vegetation – Gaussian optimization

Figures 2.16 to 2.19 on the accompanying disc give the upstream and downstream steady-state concentration distributions; the best fit downstream prediction; the optimized value of $D_y(y)$; and the sensitivity of the quality of fit to the value of $D_y(y)$ for the high and low density artificial and winter and summer *typha* partial vegetation, Gaussian optimization.

Partial vegetation – unconstrained triangle optimization

Figure 2.20 to 2.23 on the accompanying disc give the upstream and downstream steady-state concentration distributions; the best fit downstream prediction; the optimized value of $D_y(y)$; and the sensitivity of the quality of fit to the value of $D_y(y)$ for the high and low density artificial and winter and summer *typha* partial vegetation, unconstrained triangle optimization.

Partial vegetation – unconstrained Gaussian optimization

Figures 2.24 to 2.27 on the accompanying disc give the upstream and downstream steady-state concentration distributions; the best fit downstream prediction; the optimized value of $D_y(y)$; and the sensitivity of the quality of fit to the value of $D_y(y)$ for the high and low density artificial and winter and summer *typha* partial vegetation, unconstrained Gaussian optimization.

Partial vegetation – ten parameter optimization

Figures 2.28 to 2.31 on the accompanying disc give the upstream and downstream steady-state concentration distributions; the best fit downstream prediction; the optimized value of $D_y(y)$;

and the sensitivity of the quality of fit to the value of $D_y(y)$ for the high and low density artificial and winter and summer *typha* partial vegetation, ten parameter optimization.